UCLA
UCLA Electronic Theses and Dissertations

Title

From discrete LiDAR footprints to landscape-scale insights: tropical forest structure, biomass, and mapping potential

Permalink

https://escholarship.org/uc/item/38g3330h

ISBN

9798173794154

Author

Dean, Morgan

Publication Date

2026-11-17

Peer reviewed|Thesis/dissertation

eScholarship.org Powered by the California Digital Library
University of California

UNIVERSITY OF CALIFORNIA

Los Angeles

From discrete LiDAR footprints to landscape-scale insights: tropical forest structure, biomass, and mapping potential

A dissertation submitted in partial satisfaction of the

requirements for the degree Doctor of Philosophy in Biology

by

Morgan Dean

2026

© Copyright by

Morgan Dean

2026

ABSTRACT OF THE DISSERTATION

From discrete LiDAR footprints to landscape-scale insights: tropical forest structure, biomass, and mapping potential

by

Morgan Dean

Doctor of Philosophy in Biology

University of California, Los Angeles, 2026

Professor Elsa M. Ordway, Chair

Three-dimensional tropical forest structure underpins estimates of aboveground biomass, yet reliably mapping it across broad scales remains difficult. Remote sensing through LiDAR platforms such as Global Ecosystem Dynamics Investigation (GEDI) and airborne laser scanning (ALS) has expanded our capacity to measure forest structure, but how accurately these sparse data can support continuous, high-resolution mapping across the tropics remains uncertain. This dissertation evaluates the relationship between forest structural diversity and biomass using non-continuous LiDAR, and assesses the feasibility and limits of scaling these derived measurements into wall-to-wall datasets. Chapter 1 examines structural diversity-biomass relationships across the Congo Basin using two GEDI-derived structural metrics: richness and evenness. These relationships varied by land cover class, with richness and evenness operating largely

independently, indicating that they encode distinct ecological signals and may complement traditional species-based diversity metrics. However, because these metrics were derived from discrete GEDI measurements, analyses were spatially discontinuous, whereas carbon monitoring requires spatially continuous information. To assess the scalability of GEDI-derived structural metrics, Chapter 2 evaluates the predictability of three GEDI-derived structural attributes: relative canopy height (RH), foliage height diversity (FHD), and plant area index (PAI). I assess their suitability for continuous landscape mapping while accounting for spatial resolution, extreme error, and spatial autocorrelation. Predictive performance followed a consistent hierarchy (RH, FHD, then PAI), reflecting differences in attribute derivation and alignment with available predictors. Chapter 3 characterizes the error structure of such wall-to-wall maps, evaluating a 1 m global canopy height product against ALS data across the Congo Basin, Amazon, and Borneo. Error was predominantly systematic, with the magnitude of mean error reaching 58-75% of mean absolute error. A correction model trained in the Congo Basin transferred to the other two regions without retraining and achieved lower mean absolute error than the pixelwise height-and-slope corrections. Improvement held in canopies taller than roughly 16-19 m and reversed in shorter canopies, including within the Congo Basin. Much of this error is therefore shared across structurally distinct forests and reducible from single-region reference data. These findings show where LiDAR-derived structure can reliably inform tropical carbon assessments.

The dissertation of Morgan Dean is approved.

António Ferraz

Fabian D. Schneider

Yongwei Sheng

Victoria L. Sork

Felipe Zapata

Elsa M. Ordway, Committee Chair

University of California, Los Angeles

2026

CONTENTS

ABSTRACT OF THE DISSERTATION ii

LIST OF FIGURES vii

LIST OF TABLES x

ACKNOWLEDGEMENTS xi

BIOGRAPHICAL SKETCH xiii

INTRODUCTION 1

Chapter 1: Context-dependent effects of tropical forest structural diversity on aboveground biomass 6

- Abstract 6
- Introduction 7
- Data and methods 16
- Results 25
- Discussion 32
- Conclusion 41
- Supplementary Material 43

Chapter 2: Comparative predictability of GEDI-derived forest structural attributes in the tropics 59

- Abstract 59
- Introduction 60
- Study site and datasets 65
- Methods 71
- Results 78

Discussion 86
Conclusion 91
Supplementary Material 93
Chapter 3: Characterizing and correcting systematic bias in canopy height models across tropical forests 114
Abstract 114
Introduction 115
Data 120
Methods 122
Results 132
Discussion 139
Conclusion 146
Supplementary Material 147
REFERENCES 157

LIST OF FIGURES

Figure 1.1. (a) Structural richness is represented by curves showing differences in the span of occupied values, as indicated by horizontal arrows. The lack of a y-axis emphasizes that richness depends on the range of attribute values rather than their frequency, and maximal richness would span the full range of the x-axis. (b) Structural evenness is represented by the distribution of values, with the dashed line indicating a uniform distribution corresponding to maximal evenness. Side-view forest stand silhouettes above each set of curves illustrate examples of low and high structural richness and evenness. 12

Figure 1.2. Maps of GEDI-derived metrics across the study area: (a) biomass, (b) structural richness, and (c) structural evenness. 18

Figure 1.3. Map of the study site classified by the land cover classes under study. Dots denote locations where biomass and structural diversity metrics were sampled. An inset highlights an example area where the less spatially abundant degraded and forest regrowth classes are more clearly visible. Data source: TMF (Vancutsem et al., 2021). 23

Figure 1.4. Point estimates and 95% confidence intervals of additive (green) and interaction (blue) model coefficients for a) structural richness and b) structural evenness across land cover classes. Coefficients are elasticities and indicate the percent change in aboveground biomass per 1% change in each structural metric. Positive values indicate that increasing richness or evenness is associated with higher biomass, while negative values indicate lower biomass. 26

Figure 1.5. Comparison of additive (green) and interaction (blue) smooth model curves. Each smooth line represents the predicted relationship between biomass and the focal structural metric with the non-focal metric held at its mean, enabling standardized comparisons of slope and saturation across predictors and land cover classes. In additive models, this represents the average partial effect of the focal metric, whereas in interaction models, it represents a conditional effect given the mean of the other metric. Triangles denote points of maximum slope, and circles indicate saturation points where additional increases in the predictor produce little to no further change in biomass. Asterisks denote cases where smooths were statistically significant in both additive and interaction models. 31

Figure 2.1. Conceptual representation of GEDI-derived forest structural metrics: relative height (RH), foliage height diversity (FHD), and plant area index (PAI). Forest profiles are shown alongside their corresponding GEDI waveforms. Forest profiles are not to scale or footprint-accurate, but reflect general structural differences inferred from the waveform metrics. Waveform figures made using rGEDI (Silva et al., 2022). 65

Figure 2.2. Map of land cover types across the DRC overlaid on a shaded relief base derived from the Copernicus 30 m digital elevation model. The nine generalized forest categories illustrate broad patterns of vegetation across varying terrain. Data source: Tropical Moist Forest (Vancutsem et al., 2021). 67

Figure 2.3. Illustration of GEDI shots collected from 2019-2022 across the Democratic Republic of Congo, including invalid data points identified through visual inspection.

This figure highlights example regions where extreme error in relative height is spatially concentrated. 73

Figure 2.4. a) Aggregated mean R^2 and normalized RMSE (nRMSE) for both resolutions per structural metric: relative height (RH), foliage height diversity (FHD), and plant area index (PAI). These statistics were averaged across each structural metric's eight optimized model configurations. b) The same statistics averaged across each structural metric's four optimized model configurations per spatial resolution. 80

Figure 2.5. Proportion of pairwise comparisons favoring models with additional invalid data handling as assessed via the sign test and grouped by cross-validation strategy. The success rate represents the proportion of cases where these models outperformed their baseline counterparts (i.e., no additional invalid data handling). Bars are marked as statistically significant with an asterisk (*) if their sign test p-value < 0.05 and colored based on the Wilcoxon effect size in favor of invalid data handling. 82

Figure 2.6. Moran's I values for relative height (RH), foliage height diversity (FHD), and plant area index (PAI) across the 30 m and 1 km test datasets. Each point represents an aggregated Moran's I value calculated across data with and without additional invalid data handling. 83

Figure 2.7. Comparison of continuous maps of 1 km relative height (RH) generated using a) random cross-validation and b) spatial cross-validation. RH values were constrained between 0 – 35 m as more than 90% of the target values were within this range. 86

Figure 3.1. Bias field correction and transfer evaluation workflow. a) The residual between the evaluated canopy height model (H_{eval}) and Global Canopy Atlas airborne laser scanning (ALS) heights (H_{GCA}) was smoothed to form the bias field used as the training target. b) A U-Net was trained on Congo Basin tiles to predict this field from H_{eval} and slope. We fit two baselines, a mean offset and a linear regression, to the same data. c) Each model's predicted bias field was subtracted from H_{eval} to produce corrected height maps across both the held-out in-domain (ID) Congo Basin and out-of-domain (OOD) Amazon and Borneo regions without fine-tuning. The result was evaluated against H_{GCA} using mean absolute error (MAE) and mean error (ME). Magenta points mark ALS tile acquisitions. 120

Figure 3.2. Map of the pantropical study domain, showing in-domain (Congo Basin) and out-of-domain (Amazon and Borneo) forest extents. Magenta points mark the airborne laser scanning (ALS) acquisition footprints that make up the Global Canopy Atlas (GCA) reference dataset used for evaluation. 122

Figure 3.3. Architecture of the U-Net bias field correction model. The encoder downsamples the input evaluated canopy height model (H_{eval}) through three stages to a 256-map bottleneck at 8×8, and the decoder mirrors this with three upsampling stages, each concatenating the corresponding encoder skip connection (dashed arrows). Slope is not passed through the encoder. It is instead compressed by a small fully connected network into a 32-dimensional embedding and injected into the decoder at the final upsampling stage, then again before the final 1×1 convolution. The network outputs a single-channel predicted bias field. 128

Figure 3.4. Example of bias field correction on a held-out tile from the in-domain Congo Basin test set: a) original evaluated canopy height model: H_{eval}, b) the smoothed bias field used as a target for training: B, c) canopy height with the estimated bias field removed: $H_{corr} = H_{eval} - \hat{B}$ (Eq. (5)), and d) the estimated bias field $\hat{B}$ with positive values indicating where canopy height was increased. All panel units are in meters, and panels a and c share a color scale. 130

Figure 3.5. Regional performance of the pre-correction evaluated canopy height (H_{eval}) in grey and the three correction methods (mean baseline - orange, linear regression baseline - green, U-Net - navy), evaluated against Global Canopy Atlas ground truth (H_{GCA}) in the Congo Basin (in-domain), Amazon, and Borneo (out-of-domain). (a) Mean absolute error (MAE) by region and method. (b) Mean error (ME) by region and method. 134

Figure 3.6. (a) Mean absolute error (MAE) by slope bin (0-5°, 5-15°, 15-30°, ≥30°), for each region, pre-correction and after three correction methods, pooled across canopy height. (b-d) Change in MAE after U-Net correction (U-Net MAE minus pre-correction MAE) for the Congo Basin, Amazon, and Borneo respectively, jointly stratified by canopy height and slope bins. Negative values (blue) indicate improved MAE after correction, positive values (red) indicate worsened MAE, and color saturation reflects the size of the change. 137

LIST OF TABLES

Table 3.1. Mean absolute error (MAE) in meters (m) between canopy height estimates and reference canopy height (H_{GCA}) before and after three bias-correction methods, stratified by region and canopy height bin. Pre-correction is the MAE between the evaluated canopy height model (H_{eval}) and H_{GCA}, computed prior to any bias correction. The remaining three columns report MAE after applying each of this study's bias-correction methods ($H_{corr} = H_{eval} - \hat{B}$, Eq. (5) where $\hat{B}$ is the estimated bias field). Bold values indicate the lowest MAE among the three corrected methods within each row. 135

ACKNOWLEDGEMENTS

I would first like to thank my advisor, Dr. Elsa Ordway, for her empathy and patient guidance. She believed in my capacity to become a researcher, set the bar high, and encouraged me to push beyond my comfort zone, supporting me the whole way and believing in me when I did not. She fostered an environment where I was able to learn from my mistakes and grow, and for that I will always be grateful. Seriously, I cannot express that enough. I'd also like to thank my wonderful lab mates, Ary Amaya, Carissa DeRanek, Anna Ongjoco, Natalie Queally, Hannah Stouter, and Nidhi Vinod, who brought curiosity and warmth to every discussion. I learned a great deal from each of them, and I am better for it.

Prior to my PhD, I had the great fortune of working closely with Drs. António Ferraz, Fabian Schneider, and Ryan Pavlick at NASA Jet Propulsion Laboratory. Their mentorship shaped my technical skills and subject knowledge, and their humor made the more challenging moments easier to navigate. Drs. Ferraz and Schneider continued as mentors into my PhD, joining Drs. Elsa Ordway, Yongwei Sheng, Victoria Sork, and Felipe Zapata on my committee. I am grateful for their thoughtful feedback and incisive questions. They challenged me to think more critically, and this dissertation is stronger for it.

Beyond academia, my parents made this work possible long before my time at UCLA. Their sacrifices enabled me to pursue higher education, and I carry forward their lessons and resilience, which have helped me reach this milestone.

I would also like to acknowledge all others who were a positive part of my life throughout my PhD journey: mentors, colleagues, and friends. There were many who

shared laughs with me and cheered me on, with a special shoutout to Tim, Oli, and Daniel. My time at UCLA shaped me in ways both expected and unexpected. I am thankful for the full range of experiences, including the challenges and the triumphs, that have led me to this accomplishment.

Chapter 1 is currently being prepared for submission for publication of the material. Dean, Morgan; Schneider, Fabian D.; Ferraz, António; Ordway, Elsa M., 2026. The dissertation author was the primary researcher and author of this paper.

Chapter 2 has been submitted for publication of the material as it may appear in Science of Remote Sensing, 2026. Dean, Morgan; Ferraz, António; Schneider, Fabian D.; Ordway, Elsa M. The dissertation author was the primary researcher and author of this paper.

Chapter 3 is currently being prepared for submission for publication of the material. Dean, Morgan; Keyes, Daniel J.; Stocker, Olivier; Ferraz, António; Schneider, Fabian D.; Ordway, Elsa M., 2026. The dissertation author was the primary researcher and author of this paper.

Financial support for my work was provided by the University of California, Los Angeles and the NASA GEDI Science Team grant #80NSSC21K0202 (NNH20ZDA001N-GEDIST). The research carried out at the Jet Propulsion Laboratory, California Institute of Technology, was under a contract with the National Aeronautics and Space Administration (80NM0018D0004). Government sponsorship is acknowledged.

BIOGRAPHICAL SKETCH

EDUCATION

2022 Master of Science in Geospatial Data Sciences, University of Michigan

2019 Bachelor of Arts in Mathematical Sciences, University of Illinois, Springfield

SELECTED EXPERIENCE

Graduate Student Researcher, UCLA 2022 – 2026

Graduate Researcher, NASA Jet Propulsion Laboratory 2021 – 2022

DEVELOP Systems Scientist, NASA Ames Research Center 2022

Graduate Student Instructor, University of Michigan, Ann Arbor 2021

Remote Sensing Intern, Pacific Gas and Electric Co. 2021

PUBLICATIONS

Berman, L.M., Schneider, F.D., Pavlick, R.P., Stenglein, J., Bemowski, R., **Dean, M.**, Townsend, P.A., 2024. Fractional Richness: An index for camera trap networks. Ecological Indicators 166, 112266. https://doi.org/10.1016/j.ecolind.2024.112266

Russo, N.J., Takuo, J.M., Tegebong, V., LeBreton, M., **Dean, M.**, Ferraz, A., Barbier, N., Wikelski, M., Ordway, E.M., Saatchi, S., Smith, T.B., 2025. Spaceborne and UAV-LiDAR reveal hammer-headed bat preference for intermediate canopy height and diverse structure in a Central African rainforest. Mov Ecol 13, 30. https://doi.org/10.1186/s40462-025-00552-7

Schneider, F.D., **Dean, M.**, Ordway, E.M., Libalah, M.B., Ferraz, A., 2026. Mapping the structural diversity of Central African and Western US forests using GEDI. Remote Sensing of Environment 334, 115215. https://doi.org/10.1016/j.rse.2025.115215

Weeks, B.C., Zhou, Z., O'Brien, B.K., Darling, R., **Dean, M.**, Dias, T., Hassena, G., Zhang, M., Fouhey, D.F., 2023. A deep neural network for high-throughput measurement of functional traits on museum skeletal specimens. Methods in Ecology and Evolution 14, 347–359. https://doi.org/10.1111/2041-210X.13864

PRESENTATIONS

Dean, M., 2021. Can avian museum specimens guide conservation interventions by estimating population connectivity? November 4, 2021. The Wildlife Society 2021 Annual Conference. Poster Presentation.

INTRODUCTION

Tropical forests support high levels of primary productivity and play a disproportionate role in terrestrial carbon storage and in global ecological functioning (Artaxo et al., 2022; Beer et al., 2010; Bonan, 2008; Lewis et al., 2009; Malhi, 2012; Silva Dias et al., 2002). These functions are closely linked to their three-dimensional vegetation structure, which influences light interception, water-use efficiency, and productivity (Malhi et al., 2011; Montgomery and Chazdon, 2001; Murphy et al., 2022; Poorter et al., 2006). Yet despite its importance, tropical forest structure remains difficult to characterize across broad spatial extents. Consequently, remote sensing has become increasingly important for measuring forest structure at ecosystem, continental, and global scales, with LiDAR offering a unique capacity to directly characterize vegetation structural attributes (Dubayah and Drake, 2000; Lefsky et al., 2002). Over the past two decades, advances in LiDAR platforms have expanded opportunities to study tropical forest structure across increasingly large regions. Airborne laser scanning can capture highly detailed three-dimensional representations of forests (Asner et al., 2013, 2012; Mascaro et al., 2011; Murphy and Bowman, 2012; Yang et al., 2016), while spaceborne systems such as the Global Ecosystem Dynamics Investigation (GEDI) extend structural observations across continental and pantropical scales (Dubayah et al., 2020). These broad scale observations have transformed our ability to examine structural variation in forests where field observations remain sparse (Lang et al., 2022; Potapov et al., 2021; Xu et al., 2017).

Forest structure is also multidimensional, and separate structural characteristics may reflect distinct ecological processes and measurement constraints. For example,

canopy height, foliage height diversity, and leaf area index do not necessarily encode the same information about ecosystem organization or biomass (Asner and Mascaro, 2014; Fang et al., 2019; MacArthur and MacArthur, 1961), nor are they necessarily equally predictable or observable across landscapes. Consequently, understanding the ecological effects of forest structure requires evaluating how different dimensions of structure relate to biomass, how reliably these variables can be estimated across heterogeneous environments, and how uncertainty emerges when models are applied beyond the conditions in which they were developed. These challenges are becoming increasingly important as machine learning and deep learning approaches are more frequently incorporated into forest remote sensing studies. While modern predictive models can generate detailed representations of forest structure across large areas (Lang et al., 2022; Potapov et al., 2021; Schwartz et al., 2024a; Tolan et al., 2024), strong overall performance metrics may obscure substantial spatial variation in model reliability. In structurally diverse systems such as tropical forests (Banin et al., 2012b; Corlett and Primack, 2006; S. Liu et al., 2025; Loubota Panzou et al., 2021; Sullivan et al., 2017), models may encounter domain shift, where relationships learned from one region do not transfer uniformly to another. As a result, prediction error may become systematic rather than random, producing geographically structured bias that influences ecological interpretation and downstream estimates of biomass and carbon storage. Together, these interconnected knowledge gaps, spanning how forest structural diversity relates to biomass beyond plot scales, how predictability differs among structural attributes, and the degree to which mapped error transfers between regions,

limit how confidently LiDAR-derived structure can be used to infer ecological relationships and estimate carbon across tropical forests.

This dissertation addresses these gaps by tackling a central question of how LiDAR-derived forest structure can be used to understand and map tropical aboveground biomass, and where the limits of that inference lie. I examine the relationship between tropical forest structure and aboveground biomass in Chapter 1, as well as the scalability of structural metrics in Chapters 2 and 3. All three chapters are anchored in the Congo Basin. Despite containing the world's second largest contiguous tropical forest, high carbon density, and diverse vegetation types (Mayaux et al., 2013; Sullivan et al., 2017; Vancutsem et al., 2021; Xu et al., 2017), the Congo Basin remains a relatively understudied tropical region (White et al., 2021). In Chapter 1, I investigate relationships between structural diversity and biomass using GEDI-derived measures of structural richness and evenness across different land cover types. In Chapter 2, I evaluate the predictability of several GEDI-derived structural attributes representing different dimensions of canopy complexity. I also assess their suitability for continuous landscape-scale prediction while accounting for spatial resolution, extreme error, and spatial autocorrelation. In Chapter 3, I investigate systematic bias and spatial transferability in a very high resolution, deep learning-derived canopy height product. To do so, I develop a framework designed to learn and correct this bias in canopy height estimates and evaluate the extent to which learned error structures generalize across canopy height conditions and land cover classes. While model development is centered in the Congo Basin, I test out-of-domain performance across tropical forests in the Amazon and Borneo.

The chapters are designed to build sequentially. Chapter 1 demonstrates that GEDI-derived structural diversity carries ecologically meaningful information about biomass, but GEDI samples forests as discrete footprints, leaving most of the landscape unobserved and restricting such analyses to coarse gridded summaries. Extending these insights to continuous, finer-scale maps requires predicting structure where it was not measured, which raises the question addressed in Chapter 2: which structural attributes can be predicted reliably from wall-to-wall satellite data, and at what spatial resolution? Chapter 2 shows that canopy height is the most predictable of the attributes examined, while also revealing that prediction error is spatially structured rather than random. These two findings motivate Chapter 3, which focuses on canopy height products specifically and asks whether their systematic, spatially structured errors can be learned and corrected, and whether a correction developed in one region transfers to others. Across the three chapters, the spatial scale of analysis moves from 1 km aggregates of GEDI footprints, to 30 m and 1 km predictive maps, to very-high-resolution canopy height, tracing the path from sparse structural observation to continuous structural mapping.

Collectively, these findings indicate that LiDAR-derived structure is neither uniformly informative nor uniformly reliable. Structure-biomass relationships differed across land cover and disturbance classes (Chapter 1), predictability differed among structural attributes and produced spatially structured error (Chapter 2), and mapped canopy height carried systematic error that varied with canopy height (Chapter 3), differences that pooled analyses and aggregate accuracy metrics would obscure. Future research should therefore focus on where and under what conditions mapped

structure can support ecological and carbon inference. This includes characterizing reliability by forest condition rather than by a single accuracy value and directing new reference data toward conditions where reliability is lowest, such as shorter, open, and disturbed vegetation. A further priority is testing whether biomass estimates and ecological relationships derived from mapped structure match those derived from direct LiDAR observations.

Chapter 1: Context-dependent effects of tropical forest structural diversity on aboveground biomass

Abstract

Tropical forests store a disproportionate amount of global aboveground biomass relative to their area, making them essential for climate change mitigation, yet the ecological drivers of variability in these carbon stocks remain poorly resolved. Species and functional trait diversity may drive productivity through niche complementarity and selection effects, but species-level data are rarely available at broad scales. Remote sensing-derived structural diversity metrics instead capture canopy architecture variability as a spatially continuous proxy for functional heterogeneity. We use Global Ecosystem Dynamics Investigation (GEDI) derived structural richness and evenness with generalized additive models to evaluate their additive and interactive relationships with aboveground biomass across undisturbed, degraded, regrowth moist tropical forests, and mixed open-canopy savanna woodland in the Congo Basin, the world's second largest contiguous tropical forest. Additive and interaction models yielded broadly similar patterns, indicating largely complementary but context-dependent relationships between richness and evenness. Structural richness predicted biomass across land cover classes, with positive associations saturating at low richness in undisturbed forests and mixed open-canopy savanna woodland but increasing across the observed range in degraded and regrowth forests. Structural evenness exhibited pronounced context dependence, with negative associations in undisturbed and degraded forests, positive associations in mixed open-canopy savanna woodland, and no clear pattern in regrowth forests. Interpreted through niche complementarity and

selection effects, these results suggest that structural diversity-biomass relationships vary with disturbance history and canopy composition. These findings extend diversity-biomass relationships from plot to regional scales and inform how structural diversity links to ecosystem functioning in tropical forests under ongoing change.

Introduction

Tropical forests cover only 7-10% of the global land area but account for nearly one-third of the planet's total terrestrial metabolic activity and store a disproportionately large share of aboveground biomass (Lewis et al., 2009; Malhi, 2012; Pan et al., 2024, 2011). Because these terrestrial ecosystems represent a major and uncertain component of the global carbon budget (Friedlingstein et al., 2022; Hubau et al., 2020; Liu et al., 2017; Rowland et al., 2015), quantifying the mechanisms that govern ecosystem productivity and carbon storage in tropical forests at large scales is critical for improving predictions of carbon dynamics and feedbacks to climate change. Studies have evaluated biodiversity's role in these processes through classical frameworks such as biodiversity-ecosystem functioning theory, which posits that species richness, composition, and functional trait diversity influence ecosystem productivity in forests (Finegan et al., 2015; Schnabel et al., 2019; Sullivan et al., 2017; Zhang et al., 2012). Niche complementarity and the selection effect are among the most commonly examined mechanisms, with additional processes such as facilitation also recognized in shaping ecosystem functioning (Ammer, 2019). Niche complementarity posits that greater species diversity enhances ecosystem functioning by partitioning resources and minimizing competition, leading to greater collective ecosystem efficiency (Hector et al., 1999; Loreau and Hector, 2001). In contrast, the selection effect proposes that

communities with more species have a higher likelihood of including particularly productive or resilient species that disproportionately drive ecosystem processes (Huston, 1997; Loreau and Hector, 2001).

Together, these mechanisms provide a conceptual basis for linking biodiversity to ecosystem functioning through primary productivity and biomass accumulation, processes that underlie carbon storage and serve as core ecosystem functions. Productivity measures the rate at which ecosystems assimilate carbon and generate organic matter, while biomass reflects this accumulated carbon as shaped through species longevity and turnover (Keeling and Phillips, 2007). Although productivity and biomass are not directly equivalent, biomass provides an integrative measure of productivity over time and is often used as a surrogate or functional outcome in biodiversity-ecosystem functioning studies (Ma et al., 2023; Vargas-Larreta et al., 2021; Wu et al., 2015; Zhang et al., 2026). As such, biomass provides a practical way to assess ecosystem functioning, although determining how biodiversity shapes carbon accumulation in tropical forests remains challenging due to their large spatial scales and limited species and trait data (Kattge et al., 2020; Slik et al., 2015). Where such data are available, tree species richness is often positively related to biomass within small plots, but these relationships weaken or become inconsistent at larger spatial scales (Chisholm et al., 2013; Sullivan et al., 2017), complicating efforts to scale diversity-carbon relationships across tropical landscapes.

Advances in active remote sensing, particularly spaceborne LiDAR from the Global Ecosystem Dynamics Investigation (GEDI) mission, provide broad scale measurements of three-dimensional vegetation at sub-hectare resolution across the

tropics (Dubayah et al., 2020). These measurements enable the derivation of metrics that characterize the volumetric capacity, spatial arrangement, and structural attributes of biotic components within ecosystems (LaRue et al., 2023a; Schneider et al., 2026a, 2020). As structural, functional, and compositional attributes of forests have been found to be interdependent, structural attributes have been used as surrogates for functional and compositional variation (Ferris and Humphrey, 1999; Franklin et al., 2002; McElhinny et al., 2005; Noss, 1990). A synthesis of remote sensing studies has likewise suggested that plant diversity and vegetation structural complexity are generally positively related (Coverdale and Davies, 2023). Structural attributes have also been shown to be strong predictors of productivity, performing comparably to species-based measurements and at times outperforming them, with their importance varying across spatial extents, climate contexts, and successional stages (Hwang and Zhai, 2026; LaRue et al., 2023b; Schneider et al., 2023; Silva Pedro et al., 2017). Among the structural metrics evaluated in relation to productivity are measures of canopy architecture, which can mediate pathways by which forest structure influences light distribution and water-use efficiency within the canopy (Montgomery and Chazdon, 2001; Murphy et al., 2022; Poorter et al., 2006; Schneider et al., 2023). For example, vertical crown stratification can increase total leaf area, enhancing light capture and supporting higher growth rates (Yachi and Loreau, 2007; Zhang and Chen, 2015), while differences in leaf area index and leaf angle distributions can substantially alter canopy-level carbon and water fluxes (Ponce De León and Bailey, 2024). Through their influence on light capture, water use, and resource partitioning, structural attributes like canopy architecture provide a functional link between vegetation structure and

ecosystem processes. Thus, canopy structure has been interpreted both as a potential driver and outcome of biodiversity-ecosystem functioning mechanisms without relying on species identity, offering a means of examining these relationships where species-level data are sparse (Deng et al., 2025a; Storch et al., 2023; Zhao et al., 2023). GEDI's capacity to characterize canopy structure consistently across large areas has begun to make such analyses possible at broad scales. Across forest inventory plots in the United States, GEDI-derived foliage height diversity explained more variation in aboveground carbon storage than tree species diversity (Crockett et al., 2023), while across the tropics, a GEDI-derived index of forest structure was more strongly associated with gross primary productivity than mapped tree species richness (Zhang et al., 2024).

While individual structural attributes can provide valuable insights into canopy functioning, they represent single dimensions of forest structure, motivating the use of integrative structural diversity metrics that summarize complexity across multiple canopy attributes. To meet this challenge, multivariate metrics of structural diversity, such as structural richness and evenness, have been developed to quantify variation across multiple canopy structural attributes simultaneously (LaRue et al., 2023b; Schneider et al., 2017). Structural richness captures the range of canopy structural configurations in an area, with higher values indicating greater horizontal variation in canopy structure and, by extension, a larger set of potential resource-use opportunities (Figure 1.1a). In contrast, low structural richness emerges in ecosystems with homogeneous horizontal canopy structure, such as forests dominated by species with similar crown structure at similar heights, or forest plantations. Meanwhile, structural

evenness measures the distribution of abundance among varying canopy structural configurations (Figure 1.1b). Understanding the co-variation in structural evenness and biomass could indicate whether biomass is concentrated within a small range of canopy structural configurations or more evenly distributed across them. Together, structural richness and evenness capture the potential for resource partitioning among canopy structural configurations and the influence of dominant structures that may disproportionately drive carbon storage.

While studies focused on species richness have provided evidence for both niche complementarity and selection effects (Cardinale et al., 2007; Cavanaugh et al., 2014), incorporating evenness metrics and ecosystem structure may yield new insights into the mechanisms shaping diversity-biomass relationships. Evidence from species-based studies also indicates that richness and evenness may be negatively correlated, respond differently to environmental factors, or be shaped by distinct ecological processes across sites (Bock et al., 2007; Ma, 2005; Wilsey et al., 2005). These patterns suggest that richness alone provides an incomplete representation of diversity, particularly in heterogeneous tropical forests where the long tail of rare species may produce highly uneven communities (Cooper et al., 2024; Hordijk et al., 2023). Focusing on richness alone may therefore obscure how biomass is distributed across canopy structural configurations. For example, even where structural richness is high, biomass may be concentrated within a few dominant configurations as represented through low structural evenness, dampening the productivity gains that complementarity might otherwise predict. Meanwhile, high evenness could amplify richness effects by ensuring that a broader range of structural niches contributes meaningfully to carbon storage.

Evaluating both metrics together is thus critical for understanding how structural diversity shapes biomass accumulation across tropical forests.

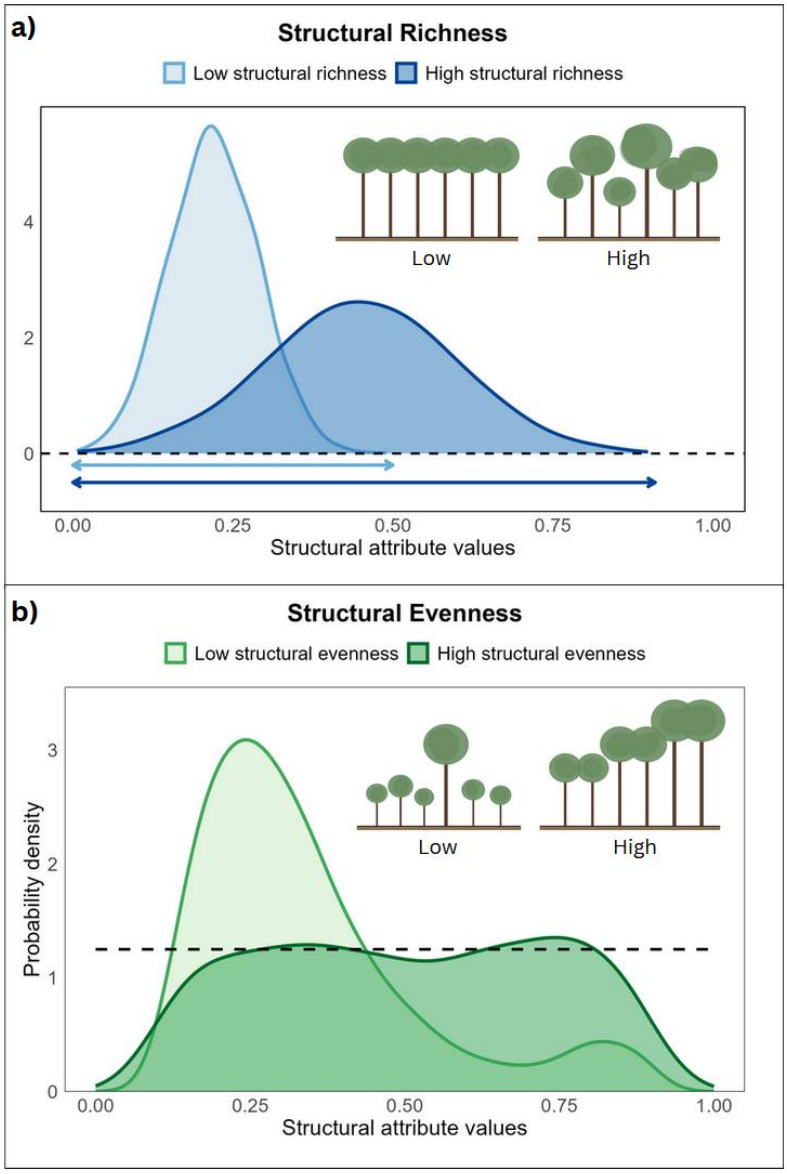


Figure 1.1. (a) Structural richness is represented by curves showing differences in the span of occupied values, as indicated by horizontal arrows. The lack of a y-axis emphasizes that richness depends on the range of attribute values rather than their frequency, and maximal richness would span the full range of the x-axis. (b) Structural evenness is represented by the distribution of values, with the dashed line indicating a uniform distribution corresponding to maximal evenness. Side-view forest stand silhouettes above each set of curves illustrate examples of low and high structural richness and evenness.

The relationship between structural richness and evenness and their influence on carbon storage may also be context-dependent, with their respective influences on biomass varying across land cover classes. In undisturbed, structurally mature tropical forests, long-term competitive interactions can create complex vertical layering, with variation in tree height, crown shape, and leaf distribution shaping light availability across the canopy (Montgomery and Chazdon, 2001). These interactions may create conditions in which taller canopies capture a disproportionate share of light and contribute substantially to aboveground biomass (Ali et al., 2019b; Goodman et al., 2014), while variation in crown architecture and vertical position among coexisting species may also facilitate more efficient canopy packing and light-use complementarity, enhancing the potential of carbon storage (Deng et al., 2025b; Williams et al., 2017; Xu et al., 2022). By contrast, degraded or regenerating forests can be more likely to exhibit simplified or transient vertical structure and rapid structural turnover, with vertical canopy layering reassembling decades after disturbances (Clark et al., 2021; Montgomery and Chazdon, 2001). Under such dynamic conditions, whether ecosystem-scale variation in biomass primarily reflects transient canopy configurations or longer-term structural organization remains unclear. In addition, outside of moist tropical forest systems, open or seasonally dry tropical ecosystems, including savannas and open woodlands, are typically less light-limited than closed-canopy forests and strongly structured by low precipitation and recurrent disturbance. For example, process-based modeling in an African savanna system suggests that frequent or intense fires can create demographic bottlenecks that limit tree size and aboveground biomass (Saito et al., 2014). Despite these conditions, these ecosystems remain

relatively stable because they are driven and maintained by long-term disturbance regimes (Cirezi et al., 2022; Sankaran et al., 2005; Silva Pedro et al., 2016). Relative to moist tropical forests, these climatic and disturbance regimes define a contrasting context in which biomass accumulates.

Together, these patterns suggest that structural richness and evenness are variably associated with biomass across intact forests, regenerating systems, and open-canopy land cover classes, potentially reflecting the roles of niche complementarity and selection effects. In this study, we use GEDI-derived structural diversity metrics to quantify how broad scale patterns of structural richness and evenness relate to aboveground biomass across land cover types within the Congo Basin. Despite being understudied relative to tropical forests in the Amazon, Central America, and Southeast Asia (White et al., 2021), this region is the world's second largest contiguous tropical forest and is notable for its high carbon density and broad range of vegetation types (Mayaux et al., 2013; Sullivan et al., 2017; Vancutsem et al., 2021; Xu et al., 2017). Beyond broad-scale land cover types, including expansive savanna regions influenced by fire and climatic extremes (Andela et al., 2017; Ramo et al., 2021; Sankaran et al., 2005), we also evaluate structural diversity along a gradient of forest intactness as shaped by anthropogenic disturbance (Watson et al., 2018). Disturbance-driven structural shifts suggest that structural diversity-biomass relationships are unlikely to be constant across space, motivating the following research questions:

1. How are structural richness and structural evenness, separately and in interaction, associated with aboveground biomass across the Congo Basin?

2. How do these relationships vary across differing levels of forest intactness and closed-canopy versus open-canopy tropical ecosystems?

As this study is observational, our analyses focus on quantifying structural diversity-biomass patterns, which we then interpret in the context of niche complementarity and selection effects across land cover classes. We first hypothesize that (H_1) structural richness and evenness jointly shape aboveground biomass but capture largely separate aspects of canopy structure. The expectation is that their contributions will be primarily additive, though some interaction may occur under specific forest conditions. Building on this, we hypothesize that (H_2) structural richness will generally be positively associated with aboveground biomass, as higher richness may reflect expanded vertical and horizontal niche space and create additional opportunities for complementary resource use. However, this structural richness-biomass relationship is expected to saturate quickly in structurally intact forests, where canopy space and light are already largely occupied, so additional structural configurations add little. Our third hypothesis is that (H_3) the influence of structural evenness on biomass is more variable than richness and strongly contingent on forest conditions. In mature, undisturbed forests, lower structural evenness is expected to be associated with higher biomass as richness increases, consistent with strong selection effects, while in degraded, regrowth, or mixed open-canopy systems, higher evenness may allow the niche opportunities created by high structural richness to be more fully realized. In evaluating these questions, this study provides a large-scale assessment of how structural diversity relates to aboveground biomass in a major but understudied tropical forest region, distinguishing the contributions of structural richness and evenness and testing how

they change with disturbance history and between closed and open-canopy ecosystems.

Data and methods

Remote sensing data

We used aboveground biomass density (hereafter referred to as biomass) as the dependent variable and structural richness and evenness as independent variables in the modeling framework (Figure 1.2). We obtained biomass estimates from the GEDI L4B version 2.1 product based on observations collected from April 2019 to March 2023 (Dubayah et al., 2023b). The GEDI L4B biomass product was generated from footprint-level parametric models calibrated with a global set of field and airborne LiDAR data and stratified by plant functional type and geographic region. Relative height metrics derived from GEDI waveforms were used as predictors, with square root transformations of both biomass and height applied to improve model fit across strata (Duncanson et al., 2022). Structural richness and evenness metrics were derived from GEDI L2A and L2B products over the same period (2019 – 2023) using methods independent of the biomass estimates, described in detail in Schneider et al. (2026a, 2026b). These two metrics provide complementary perspectives on forest structure and combine GEDI-derived relative canopy height, foliage height diversity, and canopy cover into a probability density-based, multivariate index of structural richness and evenness following Carmona et al. (2016), and modified by Schneider et al. (2020, 2026a) (Figures 1.1a – 1.1b). To evaluate potential collinearity among predictors, pairwise correlations were calculated using Pearson's r and Spearman's ρ (Tables S1.1 – S1.2). Because our inference framework focuses on proportional responses, we log-

transformed biomass, structural richness, and evenness so model coefficients can be interpreted as elasticities. On this scale, correlations between structural richness and evenness were all below |0.4| and well below common collinearity thresholds (Dormann et al., 2013), supporting the inclusion of richness and evenness as independent predictors in our modeling framework.

To assess the spatial variability of structural diversity-biomass relationships, we defined land cover classes via the Tropical Moist Forest (TMF) transition map product (Vancutsem et al., 2021). The TMF transition map depicts the spatial distribution of Congo Basin vegetation and its sequential dynamics from 1990 through 2024. The original data were 30 m resolution, which we regridded to match the 1 km biomass data using nearest-neighbor resampling. For our analyses, we retained the following TMF classes: undisturbed forest, degraded forest, regrowth, and the broader 'other land cover' class, which we henceforth refer to as mixed open-canopy savanna woodland. Undisturbed forests correspond to closed-canopy evergreen or semi-deciduous tropical forest without observed disturbance throughout the entire 1990-2024 observation range. Degraded forest represents temporarily disturbed forest (maximum 2.5 years) with the last disruption observation recorded at the latest in 2023. Forest regrowth includes previously deforested areas that have shown sustained recovery for at least three years. A regional analysis by Tyukavina et al. (2018) indicates that a substantial portion of forest disturbance in the Congo Basin is attributable to human activities such as smallholder clearing and selective logging. These classes therefore encompass forests with different levels of intactness, with only about 0.13% of the total forest loss area attributed to natural disturbance (Tyukavina et al., 2018). Meanwhile, mixed open-

canopy savanna woodland areas include savannas, woodlands, grasslands, and shrublands, which store less aboveground biomass than closed-canopy systems but support natural vegetation and structural variation across the Congo Basin.

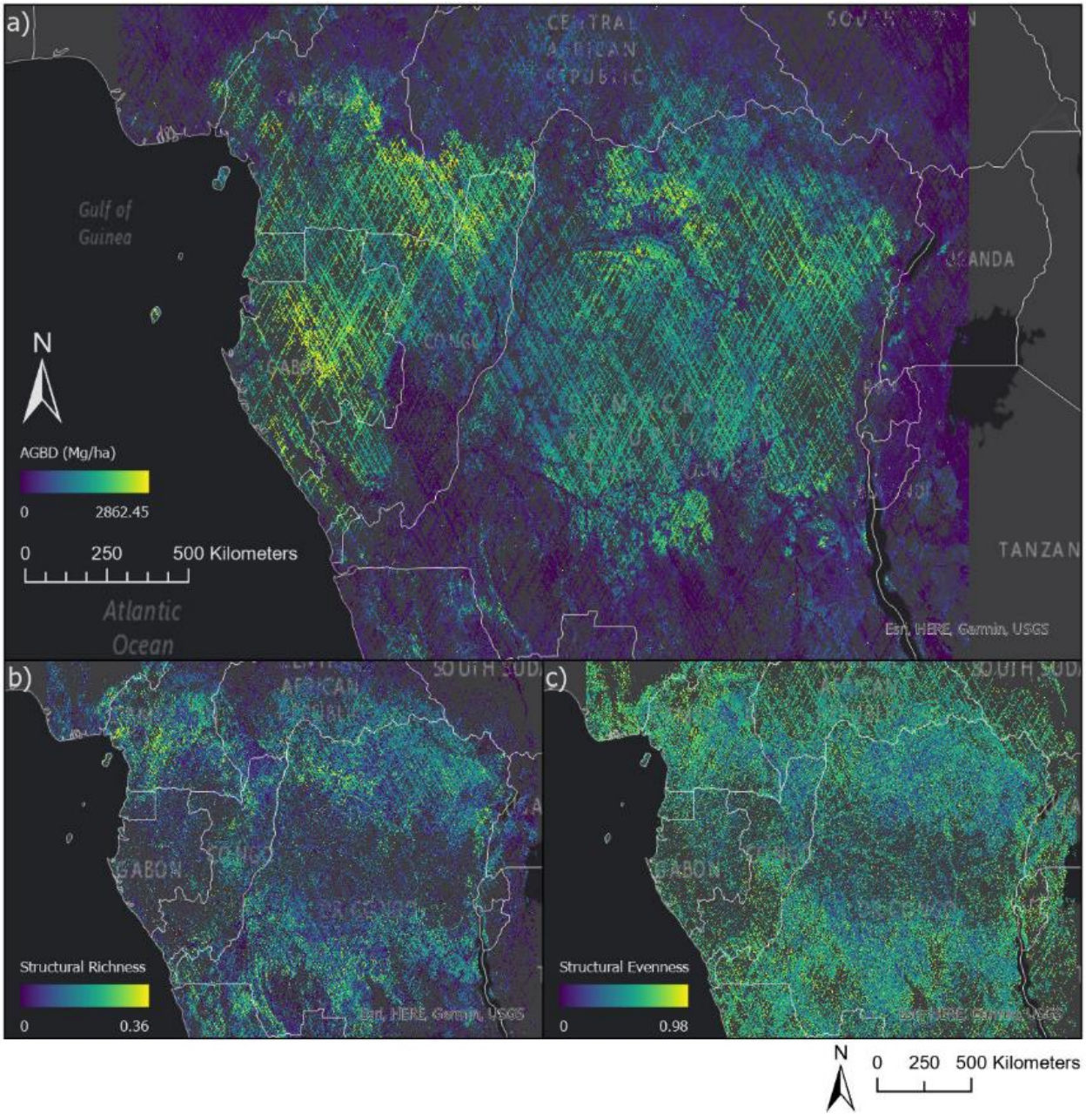


Figure 1.2. Maps of GEDI-derived metrics across the study area: (a) biomass, (b) structural richness, and (c) structural evenness.

We further refined our dataset by excluding deforested areas, ongoing disturbances, and permanent or seasonal water body classes. Deforested areas represent complete conversion from tropical forest to non-forest land uses or plantations. Ongoing disturbance was removed because it represents disturbances that began between 2022 and 2024 and cannot yet be distinguished as either temporary degradation or permanent deforestation. This uncertainty arises because the monitoring window is too short to determine whether these recent disturbances will recover and thus qualify as degraded forest or persist as forest loss. In contrast, the degraded forest class explicitly includes disturbances with ≤ 2.5 years duration with the last disruption observed no later than 2023, which ensures consistency with the temporal extent of our GEDI dataset (2019 - 2023). Excluding the ongoing disturbance class therefore avoids conflating uncertain trajectories with the more well-characterized degradation state and maintains temporal alignment with GEDI-derived biomass and structure estimates. Permanent and seasonal water bodies were also excluded. This approach ensured that our analysis targeted regions where forest structure metrics were ecologically meaningful across the landscape.

Data sampling

All 1 km data layers were compiled as a raster stack. To account for the spatial structure of remote sensing data, we designed a sampling strategy that maximized independence among points and minimized spatial autocorrelation. Sampling grids were generated at intervals from 10 km to 30 km, in 5 km increments, across the study area. Values were extracted for biomass, structural richness, structural evenness, and each land cover class, resulting in one dataset per interval. Each sampled dataset was then

evaluated to confirm adequate representation of the distribution and variance of the remote sensing variables. Finally, because the logarithm of zero is undefined, all zero values were replaced with a small constant (1e-6) before log transformation.

Generalized additive model specifications

We implemented generalized additive models (GAMs) using the mgcv package in R (Wood, 2017) to flexibly capture nonlinear relationships between aboveground biomass and structural diversity. Biomass, structural richness, and evenness were first log-transformed to facilitate interpretation such that coefficients represent proportional changes in biomass on the original scale. All models assumed a Gaussian error distribution with an identity link on log-transformed biomass. To account for residual spatial dependence after threshold sampling, we included a two-dimensional smooth of geographic coordinates (i.e., longitude, latitude), allowing for the modeling of broad-scale spatial variation. The basis dimension of the spatial smooth (k = 60) was chosen through an iterative process, adjusting k until residuals showed no significant spatial autocorrelation based on Moran's I across the full dataset.

Additive and interaction terms in generalized additive models

These GAMs were applied separately within each land cover class to assess the partial (additive) and conditional (interactive) contributions of structural richness and evenness to aboveground biomass across environmental conditions. As a first step, we fit additive linear models in which structural richness and evenness were included as separate predictors. This approach provides a clear baseline for understanding the average scaling relationships between each component of structural diversity and biomass via partial effects. Then, to examine whether the effect of one structural

diversity component is modified by the other, we also fitted interaction linear models, which incorporate a multiplicative term between richness and evenness to calculate a conditional effect. This specification captures how the combined variation across both structural diversity metrics influences biomass beyond partial effects, allowing us to distinguish conditional relationships from purely additive ones.

Additive and interaction smooth models

To explore nonlinear effects and potential saturation in structural diversity-biomass relationships, we modified the linear GAMs by modeling richness and evenness with smooth functions for each land cover class. The additive smooth models included separate smooths for each predictor, while the interaction smooth models used tensor-product smooths to capture the joint nonlinear influence of both structural diversity metrics. Unlike linear GAMs, which assume a constant effect across the predictor range, these smooth models allow the effect of richness and evenness on biomass to vary, revealing non-monotonic or saturating patterns that linear models cannot capture. Predictions were evaluated at 200 evenly spaced values across the observed range of each predictor within each land cover class to ensure full coverage of the structural diversity gradient. To summarize each fitted smooth, we derived two slope-based metrics: the maximum-slope point, indicating where biomass responds most strongly to changes in the predictor, and the saturation point, defined as the predictor value where the slope falls below 5% of its maximum, indicating negligible additional biomass gain. Finally, we quantified overall relationship strength using proportional area under the curve (AUC) as computed through trapezoidal integration. All metrics were derived from model predictions back-transformed to the original scale

of both biomass and the predictor, and expressed as proportions of the original-scale predictor range to allow comparison across land cover classes.

Model selection and evaluation

After fitting the linear and smooth GAMs across datasets sampled using 10 to 30 km thresholds, we evaluated model assumptions and selected the dataset that balanced maximal data retention with appropriate residual behavior. Residuals were required to be approximately normal, homoscedastic, and free of meaningful spatial autocorrelation, consistent with the GAM framework's Gaussian identity link specification. The models associated with the 20 km sampling threshold (n = 3413 pixels) were ultimately selected (Figure 1.3), as this dataset was the largest that met all evaluation criteria. Across all models associated with this sampling threshold, spatial smooths were statistically significant, indicating that broad spatial patterns not captured by the predictors were modeled. After accounting for the two-dimensional spatial smooth, Moran's I was calculated on the full dataset to assess residual spatial structure. Residual spatial autocorrelation was statistically significant but small in magnitude (Moran's $I < 0.05$; $p < 0.05$), supporting the adequacy of the spatial terms (Table S1.3). While the calculation could be performed reliably at this level due to sufficient spatial coverage, individual land cover classes were smaller and more spatially separated, which limited neighbor relationships and precluded robust per-class Moran's I calculations.

Diagnostic checks showed that model assumptions were adequately met for inference across land cover types. Residual variance was stable across fitted values for all categories, with the dense core of residuals generally centered near zero (Figures

S1.1 – S1.4). Q-Q plots confirmed approximate normality with deviations limited primarily to the tails of distributions (Figures S1.5 – S1.8). The full dataset and high-sample categories showed consistent variance and minimal systematic patterns. However, the forest regrowth class showed more variable residual patterns, likely reflecting the lower sample size and potential within-category heterogeneity (Tables S1.4 – S1.5), though no severe violations of model assumptions were observed.

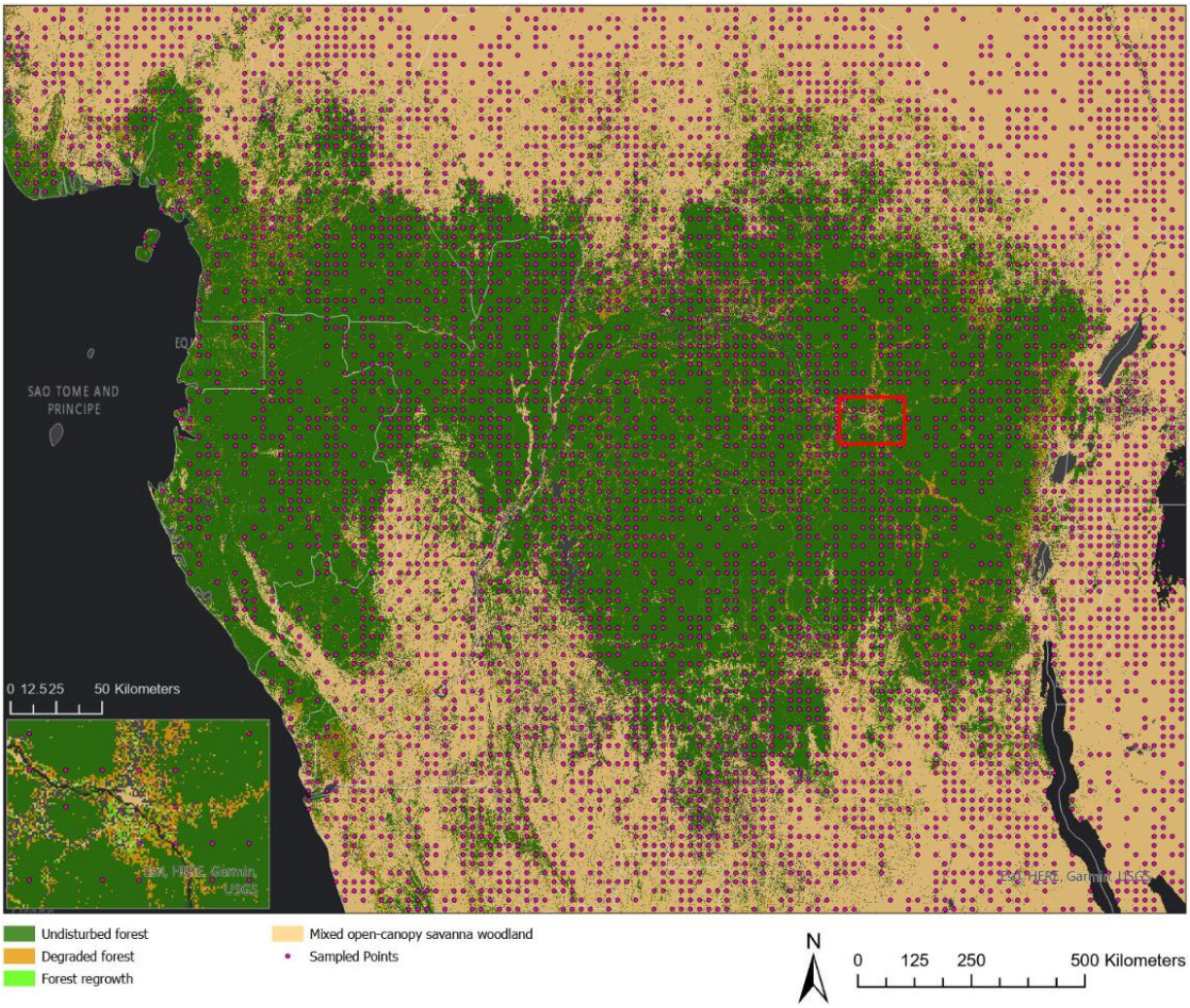


Figure 1.3. Map of the study site classified by the land cover classes under study. Dots denote locations where biomass and structural diversity metrics were sampled. An inset highlights an example area where the less spatially abundant degraded and forest regrowth classes are more clearly visible. Data source: TMF (Vancutsem et al., 2021).

From this set of models, we quantified the partial linear and interaction-modified, conditional effects of structural richness and evenness on biomass accumulation. Partial effects were assessed using the additive models in which the linear model provided average, baseline estimates via interpretable β coefficients. Conditional effects were evaluated using the interaction linear models, which allow the linear effect of one structural metric to vary with the level of the other. We quantified shifts in linear effect estimates for richness and evenness to assess how accounting for joint variation altered their apparent influence.

To evaluate nonlinear responses, we examined the smooth GAMs. Because smooth terms are not summarized by single coefficients, we assessed nonlinear effects using predictions in which the non-focal structural metric was held at its mean. In the additive smooth models, the shape and magnitude of each predicted smooth term represents an average partial effect that does not vary with the value of the non-focal predictor. In the interaction smooth models, holding the non-focal predictor at its mean defines a conditional effect corresponding to a specific slice through the fitted response surface. As a result, the metrics derived from the model predictions are expected to vary across predictors and land cover classes. Using standardized predictions from both additive and interaction smooth models, we quantified how accounting for joint variation altered inferred nonlinear effects by comparing derived metrics, which included differences in proportional AUC (ΔAUC), maximum-slope points, and saturation points. Together, these comparisons allowed us to assess whether structural diversity-biomass relationships are best characterized by partial effects, conditional effects, or a combination of both, and how their relative contributions vary across land cover classes.

Results

The baseline effects of richness and evenness on biomass

Across additive linear land cover-specific GAMs, the spatial smooth term was statistically significant in all cases except forest regrowth, indicating that spatial variation across land cover classes contributed meaningfully to relationships between biomass and structural diversity across the Congo Basin. The partial effects of structural richness and evenness on biomass differed across land cover classes, highlighting the context-dependent nature of structural diversity-biomass relationships (Figure 1.4). In undisturbed forests (n = 1548 pixels), structural richness had a slightly negative partial effect on biomass (β = -0.17, $p < 0.001$), while evenness exhibited a stronger negative effect (β = -1.31, $p < 0.001$). In other words, higher structural evenness or richness in undisturbed forests was associated with lower biomass. In contrast, degraded forests (n = 252 pixels) showed a positive relationship between richness and biomass (β = 0.35, $p < 0.001$), whereas evenness remained negatively associated with biomass (β = -1.18, p = 0.010). Forest regrowth sites (n = 66 pixels) followed the degraded forest richness-evenness pattern, with richness positively influencing biomass (β = 0.38, p = 0.002), although the effect of evenness was not statistically significant (β = -0.063, p = 0.95). Within the mixed open-canopy savanna woodland class (n = 1547 pixels), both richness and evenness were positively associated with biomass (β = 0.31, $p < 0.001$ and 0.89, $p < 0.001$, respectively) (Table S1.4).

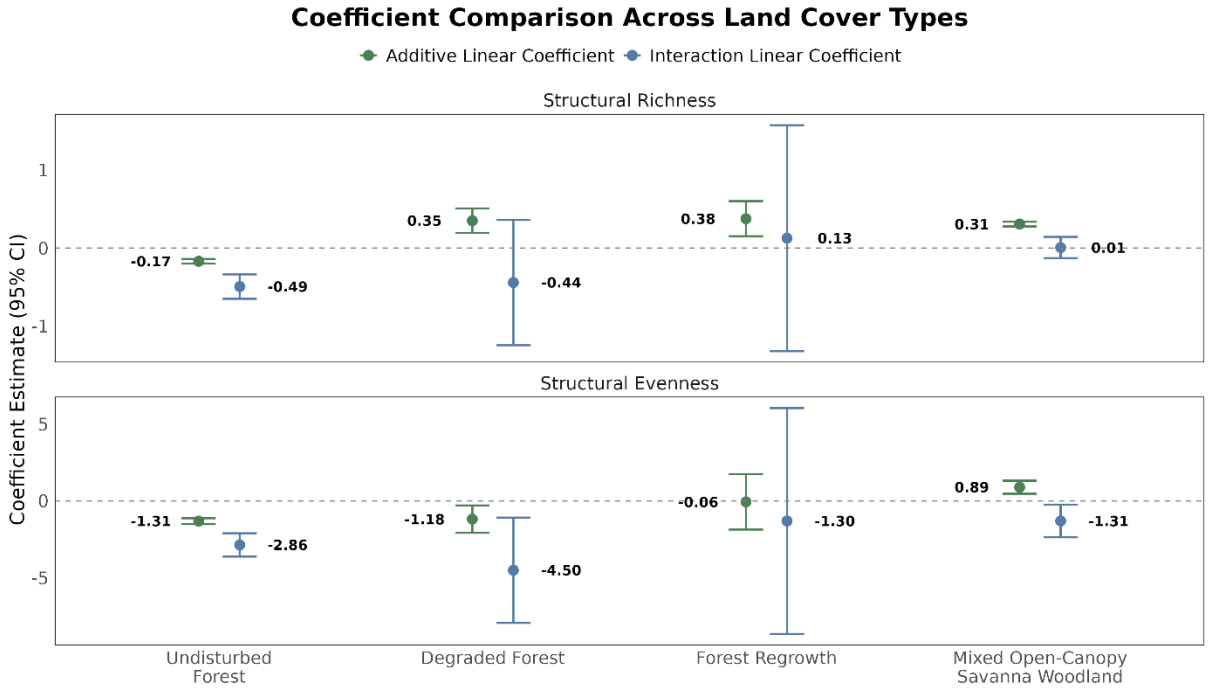


Figure 1.4. Point estimates and 95% confidence intervals of additive (green) and interaction (blue) model coefficients for a) structural richness and b) structural evenness across land cover classes. Coefficients are elasticities and indicate the percent change in aboveground biomass per 1% change in each structural metric. Positive values indicate that increasing richness or evenness is associated with higher biomass, while negative values indicate lower biomass.

Although the additive models quantify the partial effects of structural richness and evenness on biomass, these effects represent overall trends rather than detailed nonlinear responses. To capture these responses, we next evaluated the predictions from the additive smooth GAMs to quantify maximum-slope points and to identify saturation points across land cover classes, all of which exhibited statistically significant spatial smooths except the forest regrowth model (Table S1.4).

We first examined structural richness, whose additive smooth terms were statistically significant across all models. Undisturbed forests' positive maximum-slope point occurred extremely early at only 0.53% of its range, indicating that the strongest gains in biomass with structural richness are associated with low richness levels.

However, this relationship was unique as the only structural metric and land cover class combination with a non-monotonic slope; this steep increase in biomass gains was then followed by a decline and stabilization (Figure 1.5a). Biomass reached a saturation point at just 2.53% of the richness range, marking the level beyond which additional richness no longer led to substantial biomass increases. In contrast, degraded forests and areas of forest regrowth displayed more gradual but sustained increases, with maximum slopes occurring later (i.e., at 1.71% and 7.31% of their respective richness ranges) (Figures 1.5c and 1.5e). These increases continued until richness values approached their saturation points at the upper end of their range, indicating that biomass increased steadily across nearly the entire predictor range and showed no evidence of saturation within the observed richness values. Meanwhile, the mixed open-canopy savanna woodland class exhibited the shallowest and weakest relationships, with its maximum slope occurring almost immediately at 0.0010% of the richness range. Biomass gains also reached saturation quickly at just 7.54% of the richness range (Figure 1.5g).

In contrast to the generally positive richness-biomass relationships, the additive smooth models revealed structural evenness-biomass slopes were largely negative across land cover classes, suggesting that a more even distribution of canopy structural configurations tends to correspond to areas with lower aboveground biomass. For undisturbed forests, the negative slope of the evenness-biomass relationship reached its greatest absolute magnitude at 74.39% of the predictor range, indicating that declines in biomass became most pronounced at relatively high evenness values. The relationship continued to decline toward the end of the predictor range with no evidence of saturation (Figure 1.5b). Degraded forests followed a similar pattern, although the

point of maximum slope occurred earlier at 56.87% of the predictor range. Despite this shift, the overall trajectory remained negative (Figure 1.5d). Forest regrowth sites also exhibited a broadly similar pattern, as the strongest negative slope appeared at 65.30% of the range (Figure 1.5f), although the relationship was not statistically significant ($p = 0.78$). The mixed open-canopy savanna woodland class was the sole exception to this overall trend. Here, the evenness-biomass relationship was positive throughout the predictor range. Mixed open-canopy savanna woodland was also the only class in which the evenness coefficient exceeded that of richness (Figure 1.4; Table S1.4). Overall, negative maximum-slope points tended to emerge in the mid to late portions of the evenness range, with no clear evidence of saturation within observed values.

Biomass shifts due to interaction effects

Including the interaction between structural richness and evenness in the GAMs allowed us to assess how the effect of one predictor varies with the other across varying levels of intactness and by vegetated ecosystem type. The interaction coefficients were negative across all classes, indicating that the effect of one component decreases as the other increases, and were statistically significant in undisturbed ($\beta = -0.53$, $p < 0.001$), degraded ($\beta = -1.30$, $p < 0.05$), and mixed open-canopy savanna woodland ($\beta = -0.59$, $p < 0.001$) systems, but not in forest regrowth areas ($\beta = -0.44$, $p = 0.73$) (Table S1.5).

To determine the degree to which structural richness and evenness effects were additive or conditional on average, we compared coefficients between the additive and interaction linear models ($\Delta\beta_{linear} = \beta_{interactive} - \beta_{additive}$). For structural richness, $\Delta\beta$ values were negative in all classes and largely non-statistically significant as conditional main

effects in the interaction linear models (Figure S1.9). Only undisturbed forests retained a statistically significant richness coefficient in its interaction linear model ($p < 0.001$) (Table S1.5), making this the only class where richness remained significant once accounting for interactions with evenness, and enabling a comparison against the additive coefficients ($\Delta\beta = -0.32$). Meanwhile, structural evenness $\Delta\beta$ values were consistently negative (Figure S1.9), indicating that the conditional effect of evenness decreased when accounting for the interaction and were about four to seven times greater in magnitude than those for richness (undisturbed $\Delta\beta = -1.54$, degraded $\Delta\beta = -3.32$, mixed open-canopy savanna woodland $\Delta\beta = -2.19$, regrowth $\Delta\beta = -1.24$). In the interaction linear models, the corresponding evenness coefficients were statistically significant in all classes except forest regrowth ($p = 0.73$; Table S1.5).

To assess how interaction effects altered the shape and intensity of structural diversity-biomass relationships, we compared predictions from the additive and interaction smooth models ($\Delta\beta_{smooth} = \beta_{interaction\ smooth} - \beta_{additive\ smooth}$). We focused only on comparisons between land cover classes for which both the smooth term for the structural diversity metric and the interaction tensor were statistically significant; this included all classes except forest regrowth.

For structural richness, ΔAUC values increased slightly in undisturbed ($\Delta = 2.70\%$) and degraded forests ($\Delta = 3.50\%$) whereas the change in mixed open-canopy savanna woodland systems was negligible ($\Delta = -0.57\%$) and the position of maximum slope was stable ($\Delta = 0$). Meanwhile, there were minor positive saturation shifts in undisturbed forests ($\Delta = 1.00\%$). Structural evenness had similarly low differences in ΔAUC, with values near zero across classes (undisturbed = -0.36%, degraded =

0.25%), indicating minimal change in the overall strength of the relationships. And although the change in position of maximum slope was largely negligible across land cover classes, maximum slope shifted towards substantially lower evenness values in undisturbed forests (Δ = -25.35%), indicating that variation in biomass becomes most sensitive to reductions in evenness within structurally complex systems (Table S1.6 and Figure S1.10).

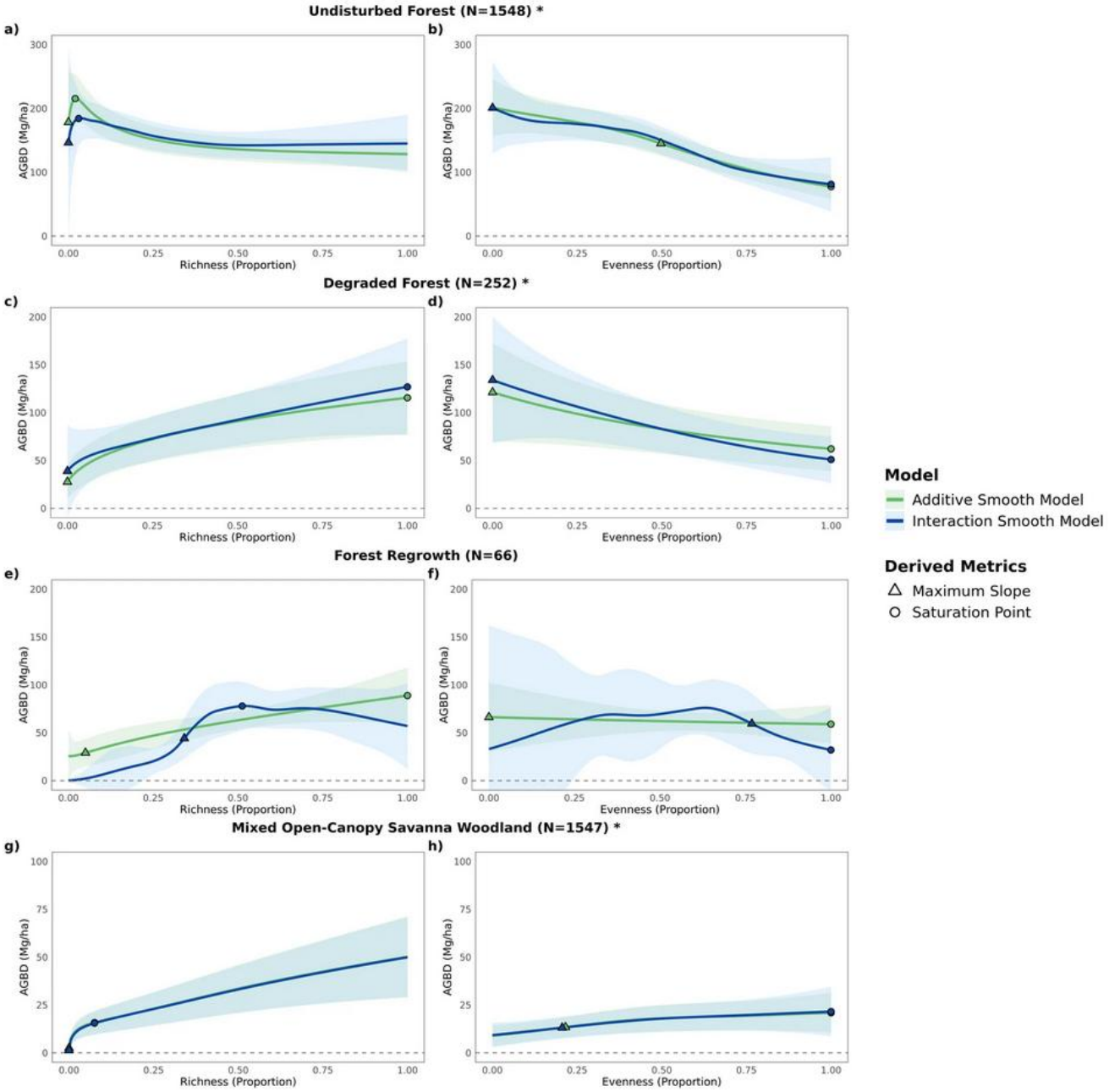


Figure 1.5. Comparison of additive (green) and interaction (blue) smooth model curves. Each smooth line represents the predicted relationship between biomass and the focal structural metric with the non-focal metric held at its mean, enabling standardized comparisons of slope and saturation across predictors and land cover classes. In additive models, this represents the average partial effect of the focal metric, whereas in interaction models, it represents a conditional effect given the mean of the other metric. Triangles denote points of maximum slope, and circles indicate saturation points where additional increases in the predictor produce little to no further change in biomass. Asterisks denote cases where smooths were statistically significant in both additive and interaction models.

Discussion

While species-based diversity metrics are classically linked to carbon storage via niche complementarity and selection effects, growing evidence suggests that structural diversity captures complementary dimensions of ecosystem organization that are also strongly associated with aboveground biomass accumulation (Aponte et al., 2020; Guo et al., 2025; LaRue et al., 2023b). Our results are consistent with these studies and extend them to the forests and savannas of the Congo Basin, providing general support for H_1 and H_2, and partial support for H_3. In the additive GAMs, which indicate general, average relationships, structural richness was a statistically significant predictor of biomass across all land cover classes, whereas structural evenness was significant in most classes except regrowth forests (H_1). Although the interaction term was statistically significant in three of four land cover classes, accounting for it only modestly altered the overall shape of the predicted structural diversity-biomass relationships. Consistent with previous studies, this suggests that richness and evenness largely capture complementary aspects of canopy structure (Hordijk et al., 2023; Stirling and Wilsey, 2001; Wilsey et al., 2005). As hypothesized, structural richness was also generally positively associated with biomass (H_2). Although the additive model for undisturbed forests yielded a slight negative richness coefficient, the nonlinear analysis revealed an initial positive relationship that leveled off and, at higher richness values, declined slightly, reflecting the sole non-monotonic relationship. In contrast, structural evenness exhibited context-dependent effects for its statistically significant terms (H_3), being

negatively associated with biomass in undisturbed and degraded forests and positively associated in mixed open-canopy savanna woodland systems. The differences between additive and interaction model coefficients were also substantially larger for evenness than for richness, suggesting that structural richness provides the outer bounds for structural niche potential as evenness determines how effectively this potential is realized, underscoring the value of analyzing the two components separately.

Although the additive models provide an overview of structural diversity-biomass relationships across land cover classes, the interaction models better enabled us to evaluate how structural diversity shapes spatial variation in aboveground biomass across different levels of intactness and types of ecosystems, providing insight beyond the average effects as captured by additive models. For example, in undisturbed forests, richness and evenness coefficients were more negative in the interaction models than in the additive models, indicating that their marginal effects diminish when considered jointly, particularly at high structural richness. This pattern may indicate structural saturation where canopy space and light resources are largely occupied, and consequently additional canopy structure types are constrained in their ability to functionally contribute. Such saturation likely reflects long-term structural filtering where competition and spatial constraints result in the selection of dominant, highly productive canopy structural configurations (Jucker et al., 2015; Williams et al., 2017). Statistically, this is reflected in the redistribution of shared explanatory power to the interaction term, showing that once an optimal range of canopy structural configurations is present, biomass variation is increasingly associated with skewed structural dominance rather than additional forms or more even representation. This potential of functional

redundancy alongside greater variation in canopy structure may connect with why species-, trait-, or evolutionary-based diversity often fail to predict biomass at large spatial scales and how diversity-biomass relationships can weaken or disappear in more established forests (Borges et al., 2024; Finegan et al., 2015; Lasky et al., 2014; Sullivan et al., 2017). The nonlinear smooths from both the additive and interaction models further illustrate these dynamics, as biomass is initially associated with increases with the addition of new canopy structural configurations at low richness, but the slope diminishes and stabilizes as dominant forms emerge. Notably, undisturbed forests were the only land cover class to retain a statistically significant richness coefficient in the interaction linear model ($p < 0.001$), suggesting that richness contributes to biomass independently of evenness. Together, these patterns indicate that biomass is maintained primarily by dominant canopy structural configurations in undisturbed forests, which may reflect structural selection effects.

Meanwhile, the degraded and regrowth land cover classes exhibited contrasting structural diversity-biomass relationships. These contrasts may reflect differences in disturbance attributes such as timing (Miller et al., 2012), severity (Shea et al., 2004), and land cover histories (Chazdon, 2003; Pyles et al., 2018). In the degraded forests class, where disturbances did not result in long-term canopy removal and forest cover persisted over multiple years, disturbance severity can be characterized as low to moderate, involving partial and short-duration impacts. Within this system, the interaction model revealed that structural evenness retained a negative relationship with biomass and became stronger relative to the additive model, whereas richness was no longer significant, suggesting that biomass is driven more by how canopy structural

variation is distributed than by the range of structural configurations present. In line with tropical forest disturbance research suggesting community composition to lean towards faster growing species with more acquisitive traits (Carreño-Rocabado et al., 2012), early successional stages may be dominated by a small subset of fast-growing, functionally similar canopy species whose traits and regeneration patterns allow them to disproportionately contribute to biomass before structural and compositional stabilization occurs, while slower growing species become more abundant later (Chazdon et al., 2010; Lohbeck et al., 2014). Thus, the strengthening of the negative evenness-biomass relationship in degraded forests could be explained by selection-driven processes observed during early successional stages, although this mechanistic connection is a hypothesis that warrants further investigation.

Meanwhile, in more severely disturbed regrowth forests, structural diversity-biomass relationships differed fundamentally from those observed in the undisturbed or degraded moist tropical forest classes. Regrowth forest was the only forest type for which the interaction term between structural richness and evenness was not statistically significant. It was also the only class whose additive model suggested evenness itself did not significantly explain biomass variation. One possible contributor is that structural diversity and biomass may differ in their rates of recovery. Across secondary forest sites in the Neotropics and West Africa, structural heterogeneity recovered at an intermediate pace, whereas aboveground biomass recovered much more slowly (Poorter et al., 2021). If similar dynamics apply here, structural diversity in regrowth forests may approach mature levels while biomass is still accumulating. However, interpretation of the regrowth class is highly uncertain because of its small

sample size and its heterogeneous composition, which likely spans regrowing closed-canopy moist tropical forests as well as woodland expansion into savannas within the forest-savanna transition zone, a dynamic ecotone shaped by interacting constraints, which include water availability, natural and anthropogenic disturbance, and soil heterogeneity (Andela et al., 2017; Cardoso et al., 2021; Oliveras and Malhi, 2016). Despite this uncertainty, one interpretation of the observed patterns is that canopy development may proceed through the progressive accumulation of multiple vegetation strata, with middle and lower layers contributing increasingly to canopy cover and biomass as canopy closure advances. This may be analogous to the progressive occupation of newly created shaded understory environments by shade-adapted woody species observed during canopy closure in savanna-forest transitions (Veenendaal et al., 2015). In this scenario, variation in aboveground biomass may be driven primarily by the incremental addition of multiple canopy structures rather than through abrupt shifts in dominance from a specific set of canopy structural configurations. This interpretation also aligns with observations from young tropical secondary forests, where increases in tree density and structural diversity correspond to high aboveground biomass through the cumulative contribution of multiple canopy-forming strategies and complementary use of space and resources without strong selection effects favoring a narrow subset of dominant competitors (Lasky et al., 2014; Matsuo et al., 2025). However, further research is needed to assess whether these patterns represent general mechanisms of recovery, given the uncertainty regarding the ecological contexts represented within this land cover class.

In contrast to the three moist tropical forest classes (undisturbed, degraded, and regrowth), the mixed open-canopy savanna woodland class stands out as both structural richness and evenness contributed meaningfully to variation in biomass. Notably, structural evenness had a stronger association with biomass than richness, a distinctive feature of this class compared to the others studied. The interaction model also revealed that richness contributes to biomass primarily when evenness is low, suggesting the benefit of having greater variation in canopy structural configurations declines as these types become more evenly distributed. Higher structural richness and evenness may therefore function as stabilizing mechanisms in these high-disturbance ecosystems (Cirezi et al., 2022; Sankaran et al., 2005), buffering aboveground biomass against environmental variability and ultimately promoting structural complementarity. These patterns are consistent with evidence from mixed savanna ecosystems spanning grassland to woodland gradients where increased species or functional richness stabilizes productivity and distributes aboveground biomass across coexisting plant forms rather than allowing a single type to dominate (Isbell et al., 2009; Lloyd et al., 2008; Polley et al., 2013). Moreover, repeated disturbances in these systems can allow vegetation to re-establish multiple times across the landscape, maintaining high structural richness while preventing dominance by a single canopy form (Cole et al., 2014). Consequently, this dynamic creates periods in which reduced disturbance permits dominant forms to develop, while severe disturbance maintains open canopies (Murphy and Bowman, 2012). Together, these dynamics suggest that mixed open-canopy savanna woodland systems exhibit both niche complementarity and selection effects.

While GEDI-derived structural richness and evenness enable the quantification of broad scale structural diversity-biomass patterns, they do not capture the processes that regulate biomass, but rather the emergent structural patterns from which ecological drivers are inferred. These limitations are partially reflected in the moderate proportion of biomass variation explained by the models (adjusted R^2 = 0.49 to 0.52 for the additive and interaction models, respectively, trained across all data; Tables S1.4 – S1.5), indicating our models could not fully reconcile the impact of factors such as species identity, functional traits, disturbance regimes, and abiotic influences. Because climate, soils, and species composition can influence both structural diversity and biomass (Ali et al., 2019a; Bastin et al., 2015; Ehbrecht et al., 2021; S. Liu et al., 2025; Nunes et al., 2026), they may confound the relationships observed here. Fitting separate models for each land cover class partially addresses this, as it prevents differences among classes from driving the estimated relationships. The two-dimensional spatial smooth can also reduce bias from environmental gradients that vary more broadly than structural diversity, such as regional climate (Paciorek, 2010). Although finer-scale factors such as topography and soil properties are not represented, future work could incorporate them explicitly. Doing so will require accounting for the differing resolutions, acquisition methods, and uncertainties of available products, as systematic measurement errors can bias estimated relationships in inconsistent directions (Van Cleemput et al., 2025), a consideration that informed our decision to restrict predictors to structural metrics derived from the same GEDI observations. Future work will also likely require integration with process-based modeling or field experiment approaches (e.g., Huang et al., 2020; Longo et al., 2020; Niklaus et al., 2017). Recent work also demonstrates that

assimilating GEDI-derived canopy structure into dynamic vegetation models can meaningfully alter predictions of biomass trajectories by constraining these underlying processes (Chang et al., 2025). In this context, structural richness and evenness may provide complementary information on vertical organization and the heterogeneity of canopy structure in future data-model fusion efforts, particularly if combined with functional trait data from imaging spectroscopy to better parameterize variation in plant functional strategies (Cavender-Bares et al., 2022).

Spatial autocorrelation was also statistically significant and substantial in our models without the use of spatial smooths, warranting further investigation into the potential of generalizability across tropical forests. Tropical forests are known to differ in their species diversity, carbon density, dominant allometric relationships, environmental predictors, and the nature and intensity of disturbances (Banin et al., 2012b; Corlett and Primack, 2006; S. Liu et al., 2025; Sullivan et al., 2017), raising the question as to how generalizable the relationships observed here may be across other tropical forest regions. Furthermore, disturbance events may temporarily alter canopy structural diversity, either by creating new canopy structure types (e.g., through gap formation) or by shifting their relative contributions, complicating interpretation of structural diversity-biomass relationships in recently disturbed forests. Because we aggregated our data into a single temporal snapshot, we cannot fully disentangle the longer-term effects of niche complementarity or selection from the immediate structural consequences of recent disturbance. Further research could leverage longitudinal GEDI observations across tropical forests to assess the generalizability and temporal stability of the structural diversity-biomass relationships observed here.

GEDI also constrains the structural metrics derived from it, as its sampling is sparsely distributed across the landscape and is influenced by terrain steepness and canopy sparsity due to variable ground energy returns (Liu et al., 2021; Wang et al., 2022). While this issue is less problematic in dense, relatively flat moist tropical forests, it is particularly relevant in the expansive mixed open-canopy savanna woodland class, which contains substantial stretches of sparse vegetation (i.e., grasslands and savanna) where ground-canopy signal separation may be challenging (Schneider et al., 2026a). Beyond these data quality concerns, sparse sampling limits the representation of structurally important but spatially rare features such as large-sized trees, obscuring their potentially disproportionate contributions to aboveground biomass (Kearsley et al., 2019). Furthermore, the structural diversity metrics used here reflect horizontal variation among 25 m GEDI footprints rather than vertical canopy complexity or volumetric properties (e.g., gap size distributions), which are more fully resolved by airborne or terrestrial laser scanning. This limitation is particularly important in intact forests with dense, multi-layered crown packing where GEDI-derived structural diversity could be complemented with products more strongly focused on vertical canopy complexity (e.g., De Conto et al., 2024). In light of these issues, future work should prioritize both quantifying and reducing uncertainties in GEDI data and developing approaches that better incorporate vertical as well as horizontal variation in canopy structure across gradients of vegetation cover and topography.

Despite these challenges, GEDI-derived structural richness was a significant predictor of aboveground biomass in every land cover class, and structural evenness in all but regrowth forests, across both dense canopy forests and the more open, sparsely

vegetated savanna-dominated landscapes of the Congo Basin. This suggests that GEDI-derived structural diversity metrics may capture important aspects of canopy structure that influence aboveground carbon storage at broad spatial scales. For management and restoration in the Congo Basin, structural richness may be a useful indicator for monitoring biomass recovery, while in intact forests, maintaining existing structural patterns could contribute to sustaining high biomass. Collectively, this study demonstrates that structural diversity metrics offer a scalable way to assess biomass variation across tropical forests under ongoing change.

Conclusion

Our results demonstrate that GEDI-derived structural richness and evenness exhibit context-dependent relationships with aboveground biomass across the Congo Basin. These patterns are broadly interpretable through the lenses of niche complementarity and selection effects, which illustrate the potential of GEDI-based structural metrics for examining structural diversity-biomass relationships beyond traditional plot scales. Although additional work is needed to quantify uncertainties in GEDI data and to validate these patterns experimentally, the observed relationships provide benchmarks for parameterizing process-based models and for designing field experiments across intactness gradients and ecosystem types. Moreover, GEDI's near-global coverage enables these analyses to be extended to other tropical forest regions, providing opportunities to assess how structural diversity relates to carbon storage and ecosystem resilience under ongoing global change, while integration with imaging spectroscopy missions could disentangle how plant functional composition mediates structural diversity-biomass relationships. By establishing that remotely sensed

structural diversity metrics can capture diversity-biomass relationships at broad spatial scales, this work advances their use for understanding and monitoring tropical forest structure and carbon dynamics.

Supplementary Material

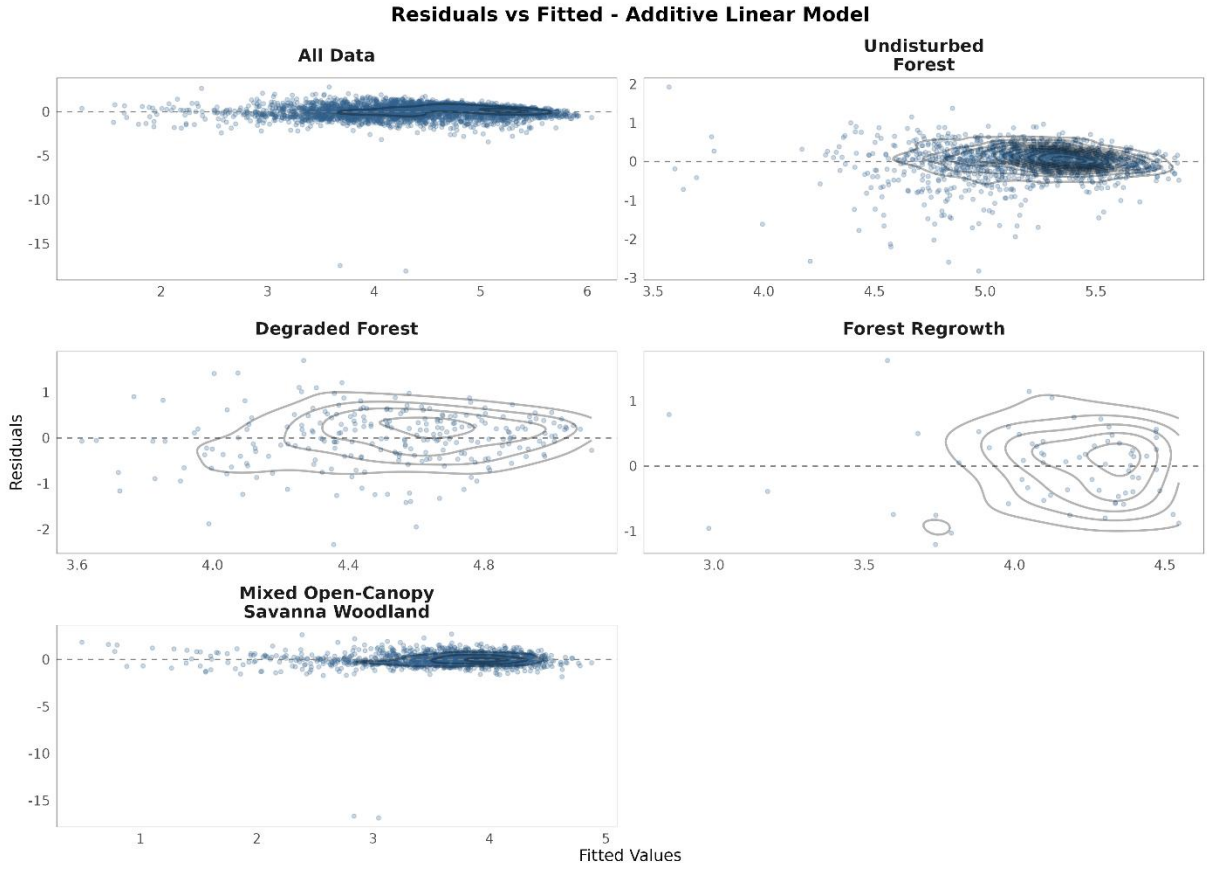


Figure S1.1. Residuals versus fitted values for additive linear models fitted using the dataset sampled at a 20,000 m spacing. Point transparency and 2D density contours reveal observation density, with darker regions and contour lines indicating areas of higher point concentration.

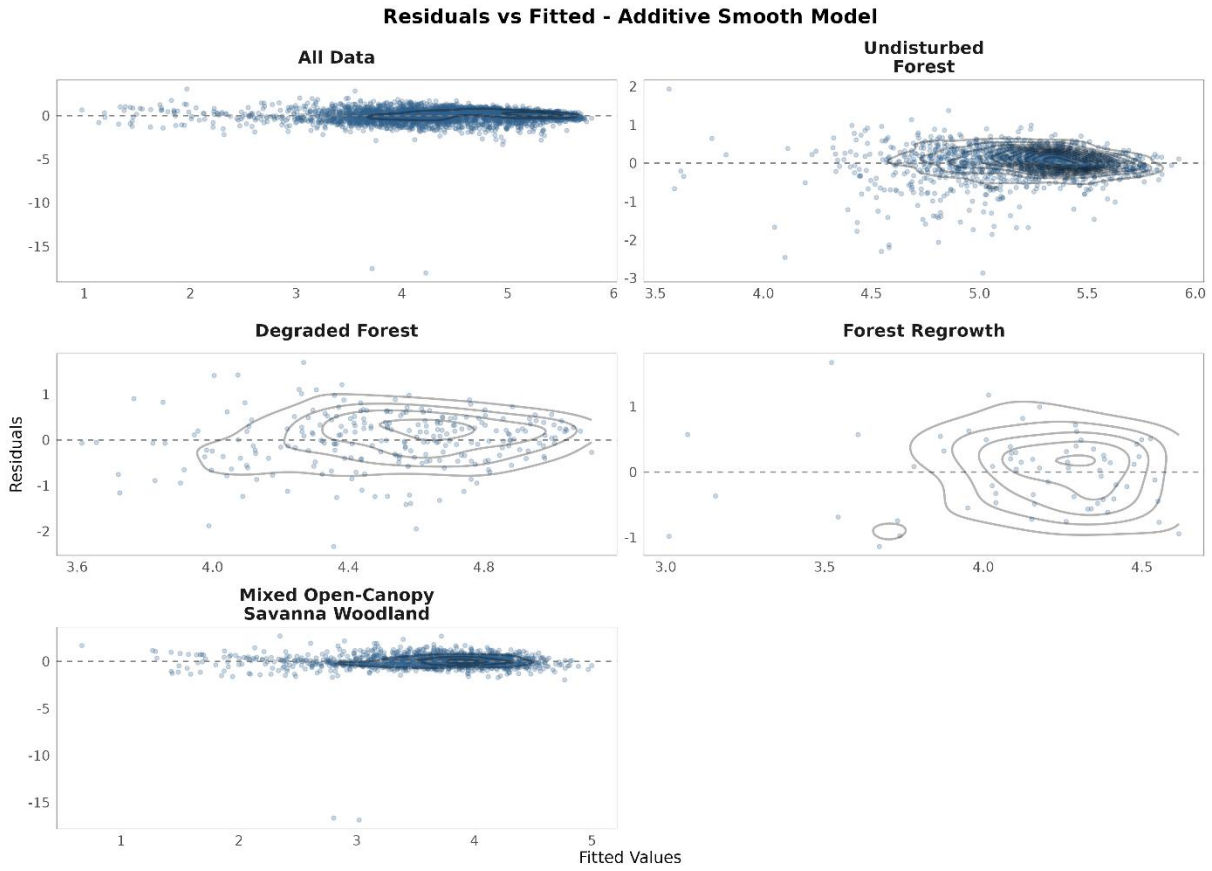


Figure S1.2. Residuals versus fitted values for additive smooth models fitted using the dataset sampled at a 20,000 m spacing. Point transparency and 2D density contours reveal observation density, with darker regions and contour lines indicating areas of higher point concentration.

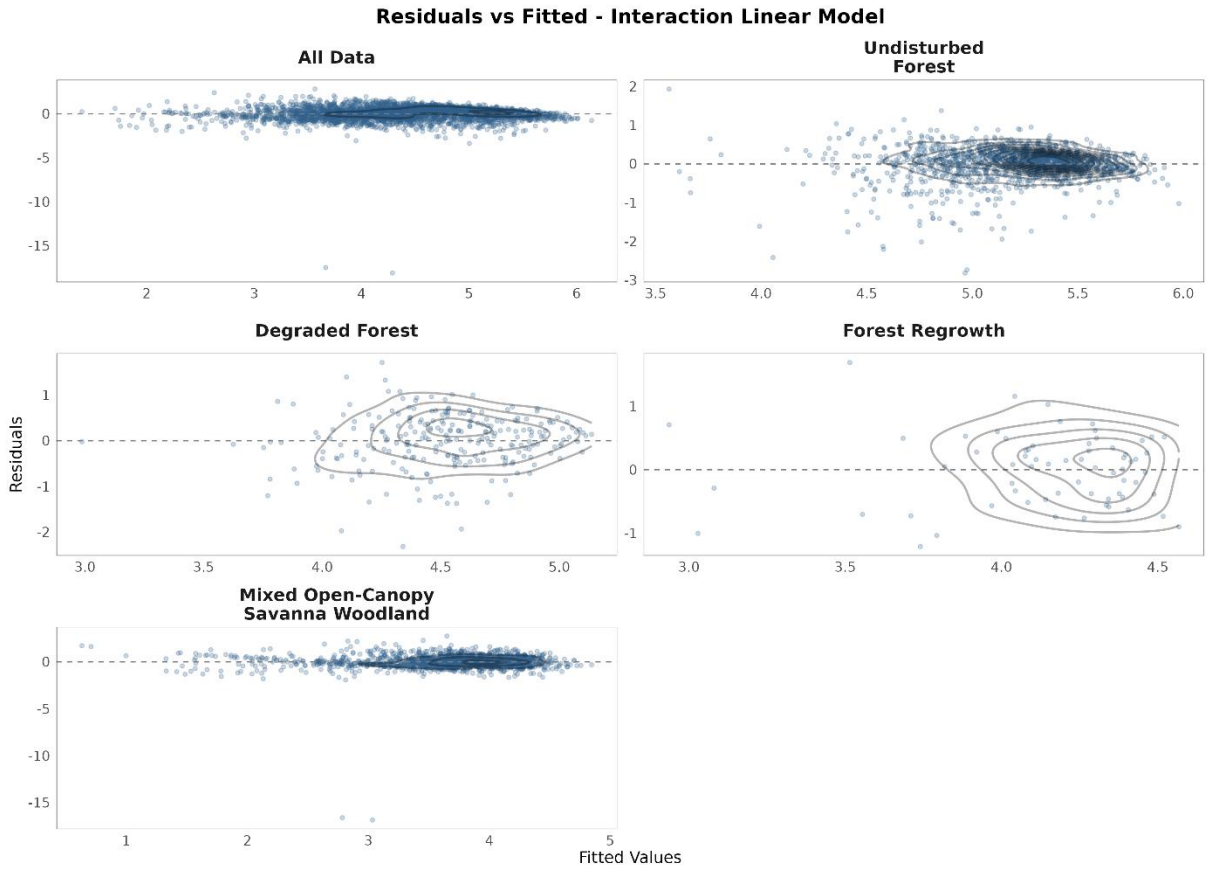


Figure S1.3. Residuals versus fitted values for interaction linear models fitted using the dataset sampled at a 20,000 m spacing. Point transparency and 2D density contours reveal observation density, with darker regions and contour lines indicating areas of higher point concentration.

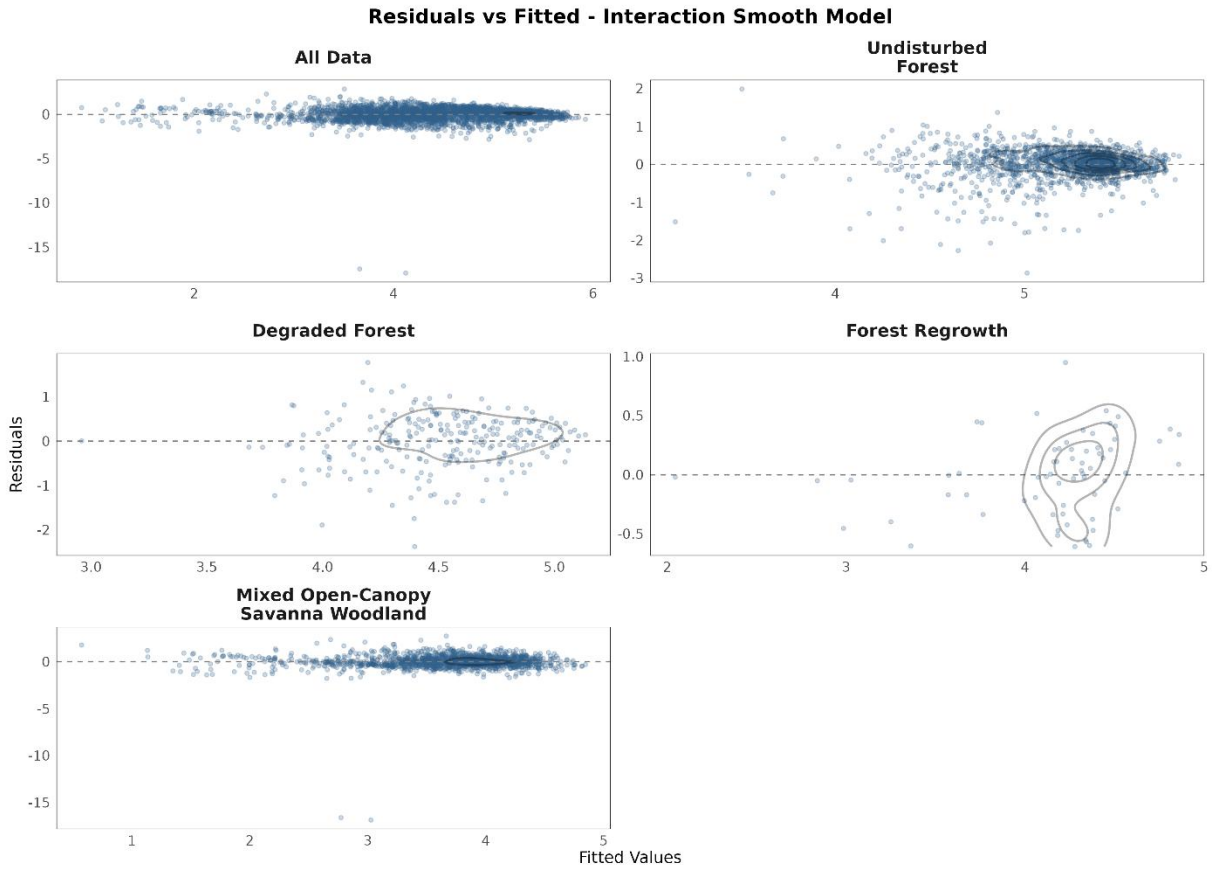


Figure S1.4. Residuals versus fitted values for interaction smooth models fitted using the dataset sampled at a 20,000 m spacing. Point transparency and 2D density contours reveal observation density, with darker regions and contour lines indicating areas of higher point concentration.

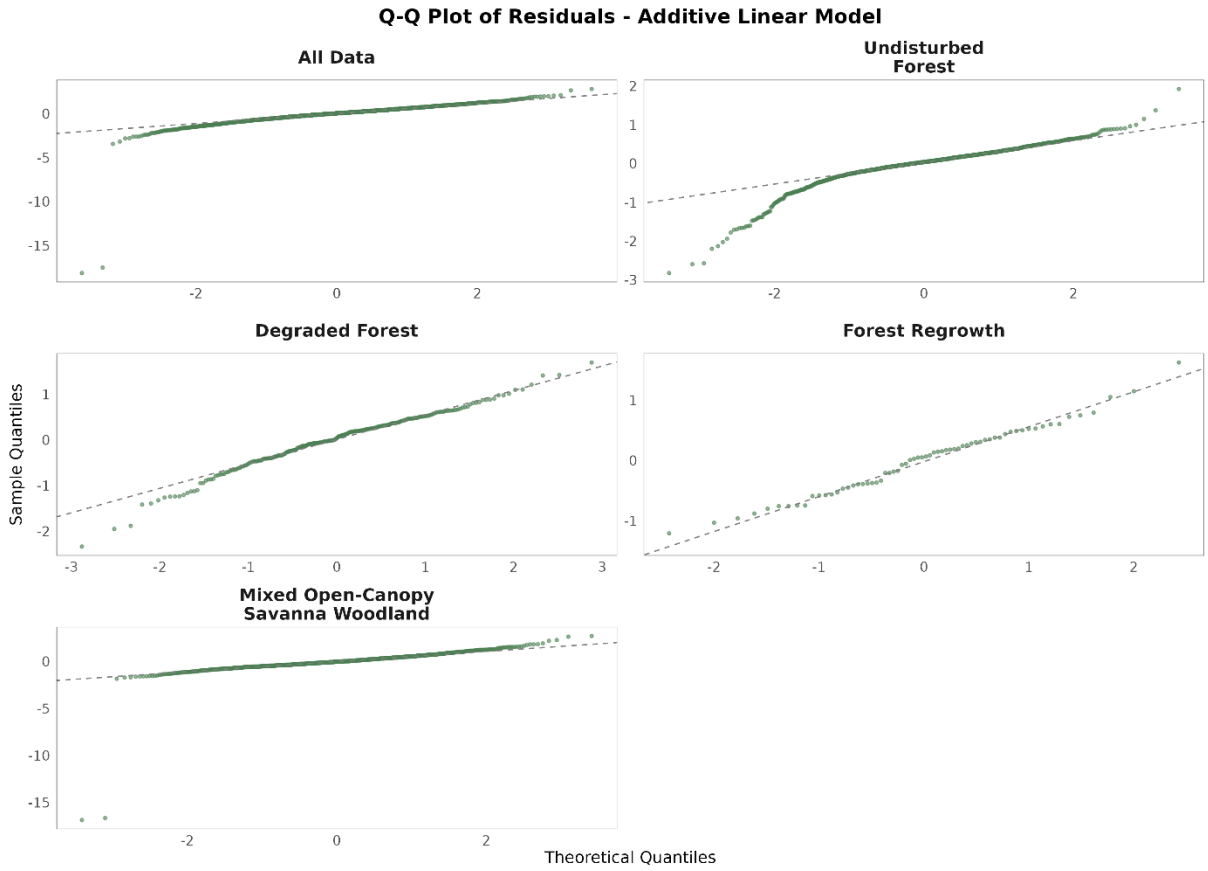


Figure S1.5. Q-Q plots of residuals for additive linear models fitted using the dataset sampled at a 20,000 m spacing. Points closely following the diagonal line indicate approximate normality.

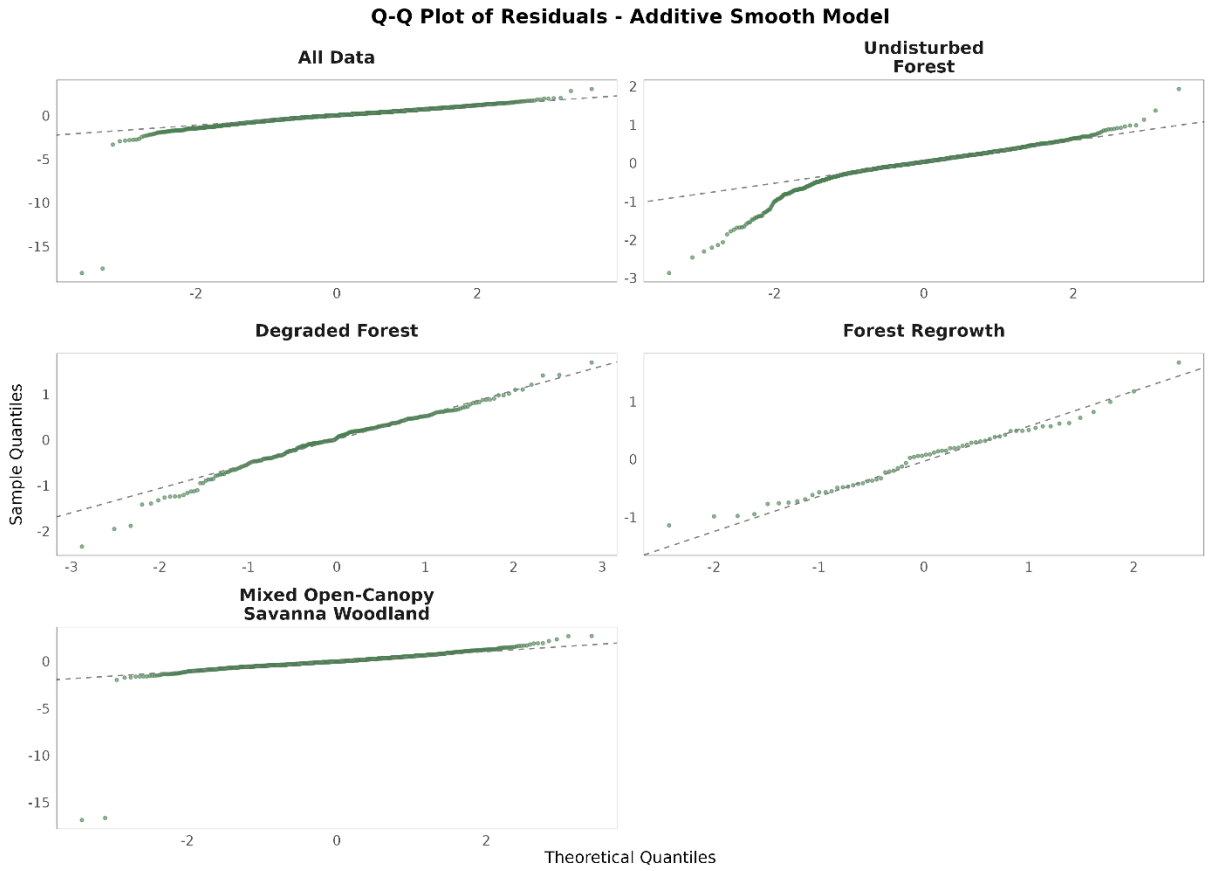


Figure S1.6. Q-Q plots of residuals for additive smooth models fitted using the dataset sampled at a 20,000 m spacing. Points closely following the diagonal line indicate approximate normality.

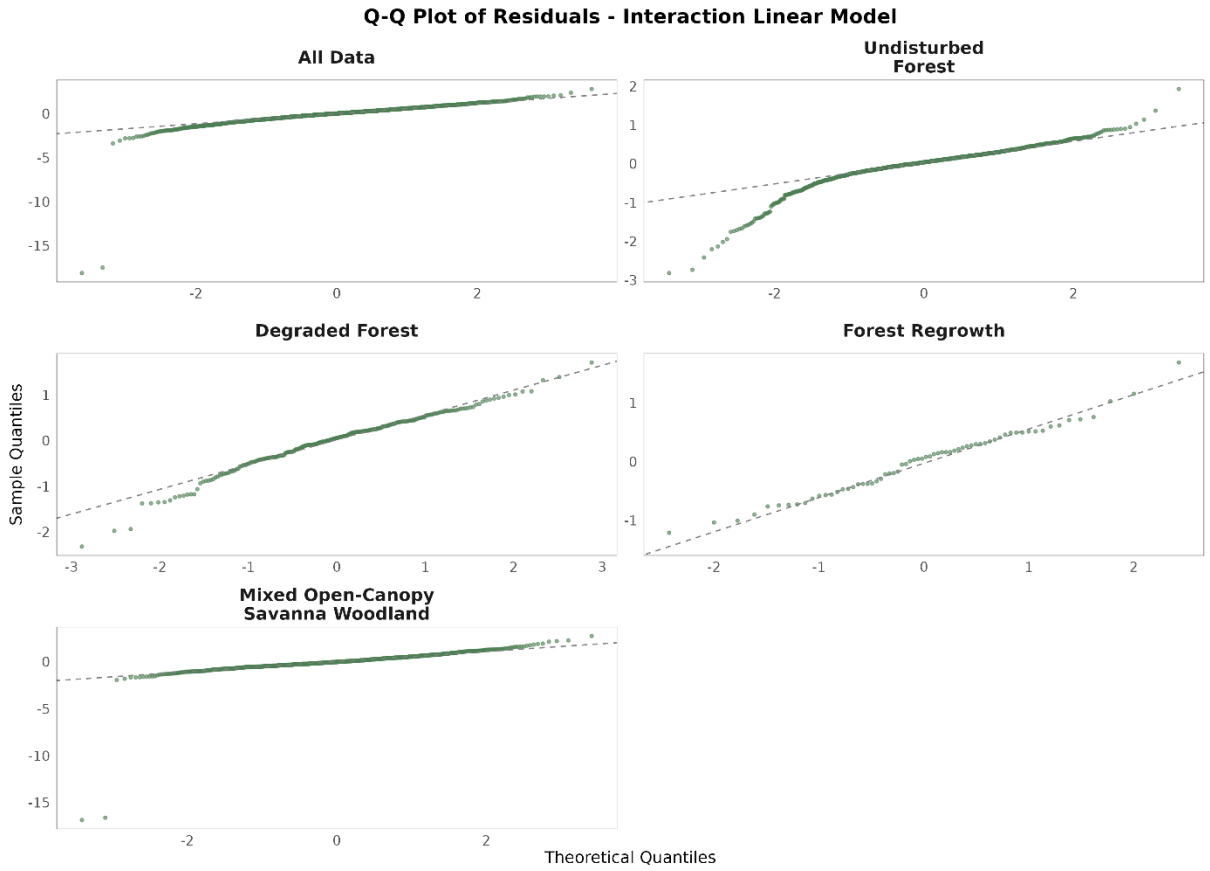


Figure S1.7. Q-Q plots of residuals for interaction linear models fitted using the dataset sampled at a 20,000 m spacing. Points closely following the diagonal line indicate approximate normality.

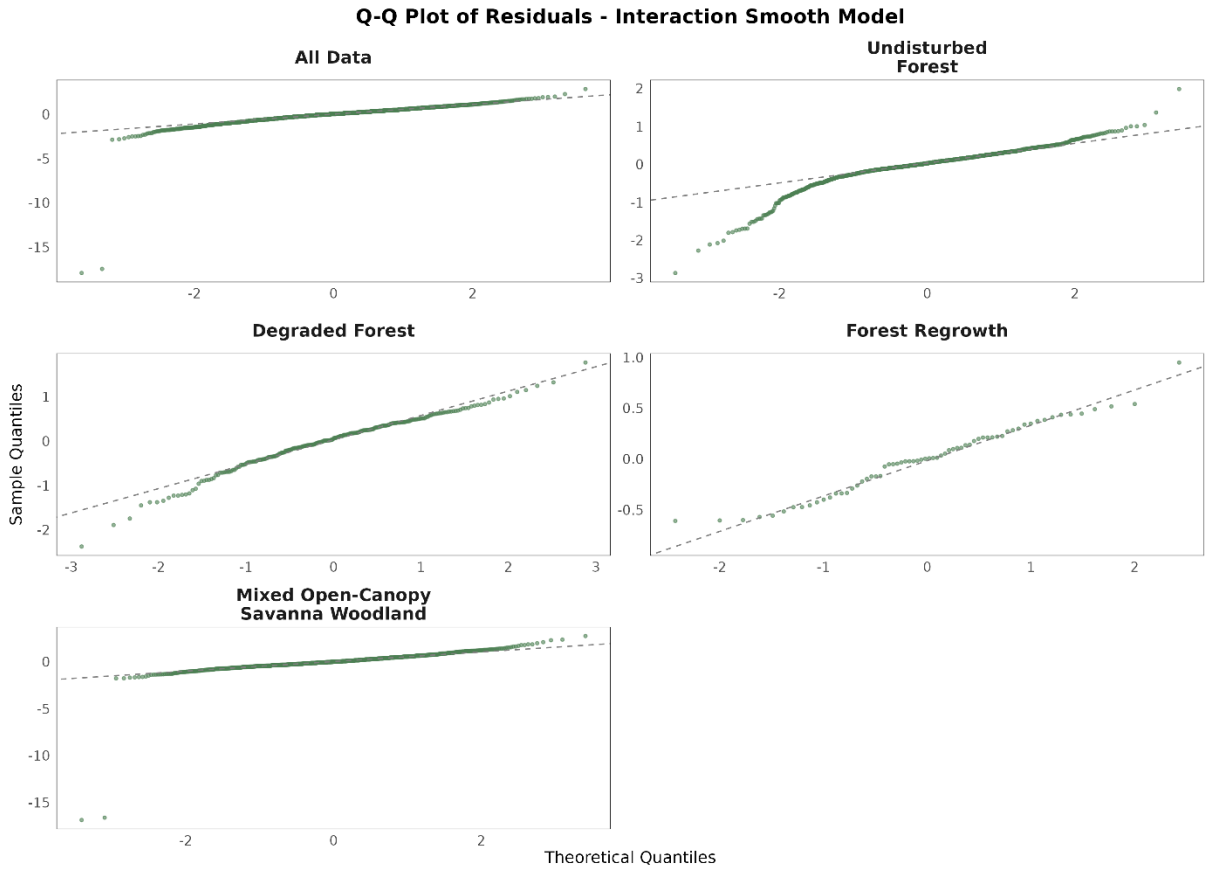


Figure S1.8. Q-Q plots of residuals for interaction smooth models fitted using the dataset sampled at a 20,000 m spacing. Points closely following the diagonal line indicate approximate normality.

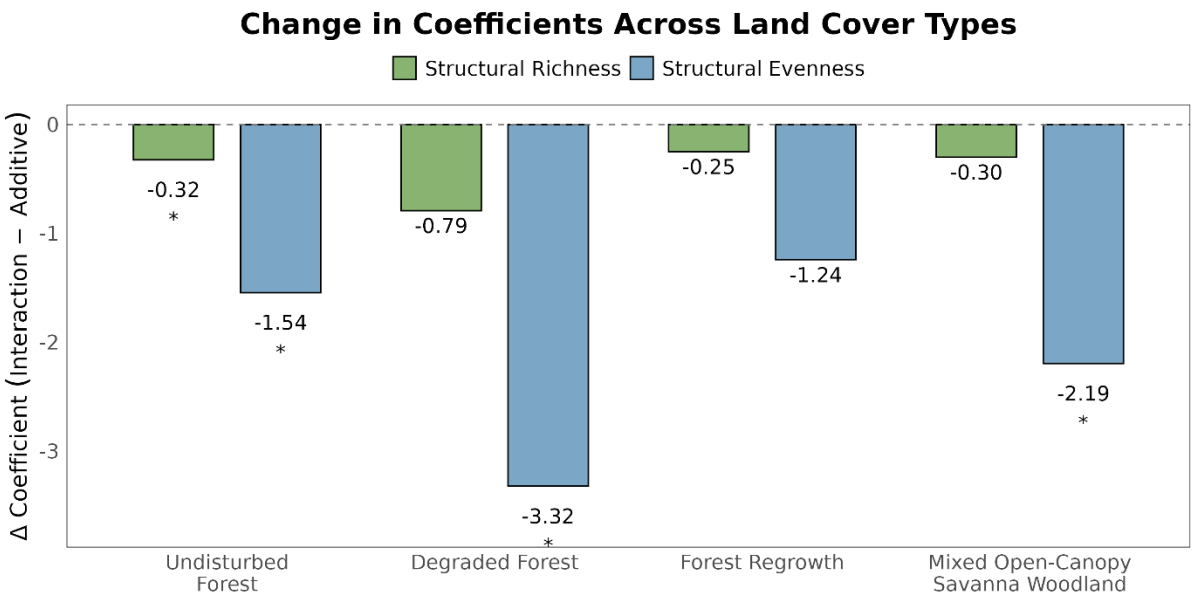


Figure S1.9. Differences between interaction and additive model coefficients ($\Delta\beta_{linear}$ = $\beta_{interaction\ linear}$ - $\beta_{additive\ linear}$) are shown for structural richness and structural evenness across land cover classes. An asterisk indicates cases where the linear model β coefficient was statistically significant in both the interaction and additive models.

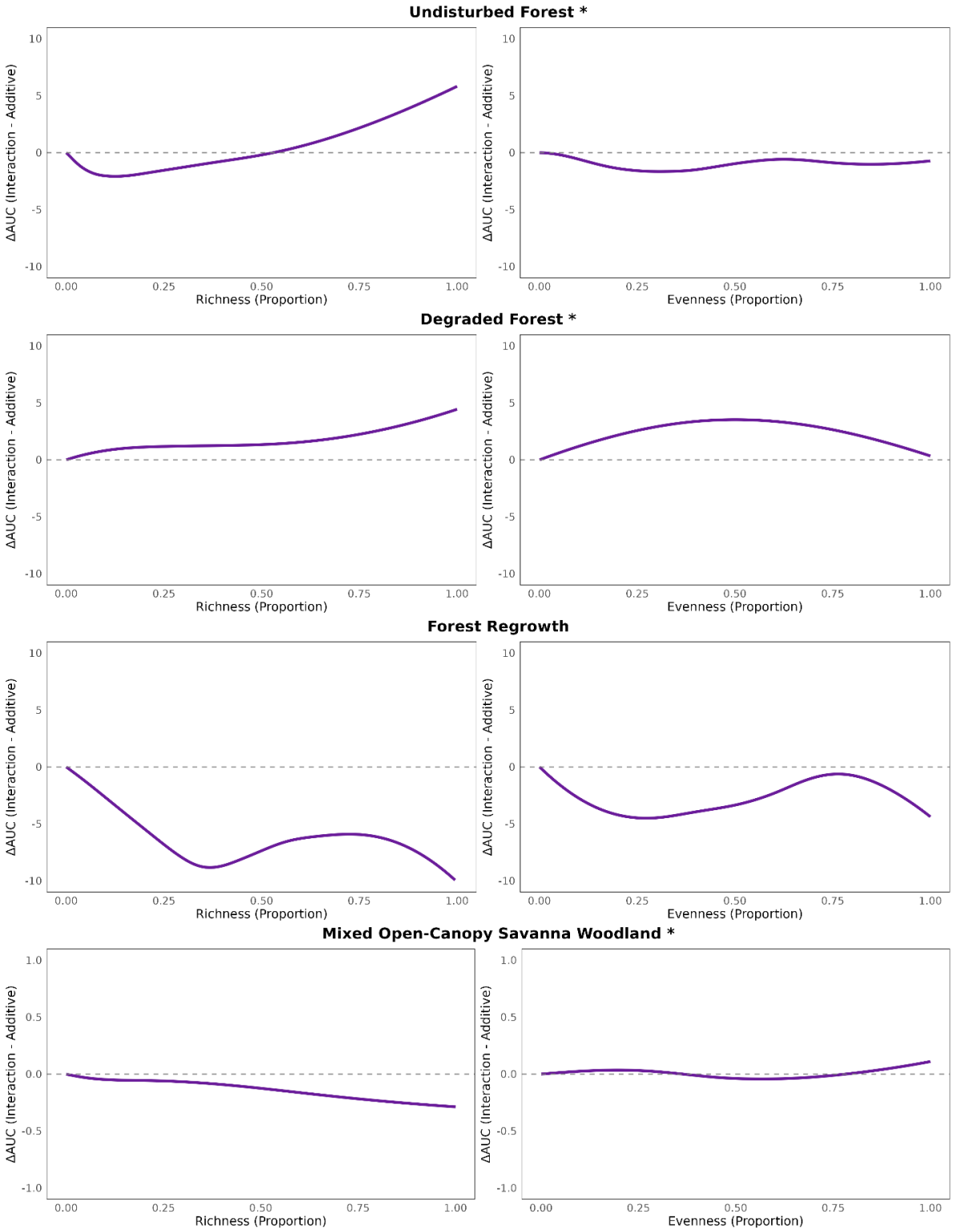


Figure S1.10. Differences in cumulative area under the curve (ΔAUC) of aboveground biomass across structural diversity gradients for each land cover class. Asterisks mark land cover classes where both the interaction and additive models were statistically significant.

Table S1.1. Pearson's correlation coefficients among log transformed biomass, structural richness, and evenness, as derived from the 20,000 m threshold spacing.

Land Cover Class	log(Biomass)-log(Richness)	log(Biomass)-log(Evenness)	log(Richness)-log(Evenness)
All Data	0.37	-0.32	-0.21
Undisturbed Forest	-0.25	-0.28	-0.12
Degraded Forest	0.21	-0.12	0.28
Regrowth Forest	0.46	0.04	0.14
Mixed open-canopy savanna woodland	0.47	0.01	-0.22

Table S1.2. Spearman's correlation coefficients among log transformed biomass, structural richness, and evenness, as derived from the 20,000 m threshold spacing.

Land Cover Class	log(Biomass)-log(Richness)	log(Biomass)-log(Evenness)	log(Richness)-log(Evenness)
All Data	0.15	-0.39	-0.08
Undisturbed Forest	-0.32	-0.26	-0.04
Degraded Forest	0.13	-0.2	0.34
Regrowth Forest	0.26	-0.05	0.14
Mixed open-canopy savanna woodland	0.49	-0.01	-0.17

Table S1.3. Moran's I values and associated p-values for models estimated using the entire dataset.

Model Type	Moran's I	p-value
Additive Linear	0.0467	<2.2e-16
Additive Smooth	0.0441	3.17E-15
Interaction Linear	0.0458	3.02E-16
Interaction Smooth	0.0371	2.48E-11

Table S1.4. Results from additive models evaluating partial relationships between structural diversity metrics and biomass. Green column headers correspond to additive linear model results and blue column headers correspond to additive smooth model results.

Land Cover Class	Number of Samples	Term	Coefficient Estimate	p-value	p-value (Lat/Lon Smooth)	R^2 (adj)	Term	p-value	R^2 (adj)
All Data	3413	log(Richness)	0.20	<2e-16		0.49	s(log(Richness))	<2e-16	0.50
All Data	3413	log(Evenness)	-1.00	0.0000		0.49	s(log(Evenness))	<2e-16	0.50
All Data	3413	s(Longitude, Latitude)			<2e-16	0.49	s(Longitude, Latitude)	<2e-16	0.50
Undisturbed Forest	1548	log(Richness)	-0.17	<2e-16		0.39	s(log(Richness))	<2e-16	0.40
Undisturbed Forest	1548	log(Evenness)	-1.31	<2e-16		0.39	s(log(Evenness))	<2e-16	0.40
Undisturbed Forest	1548	s(Longitude, Latitude)			<2e-16	0.39	s(Longitude, Latitude)	<2e-16	0.40
Degraded Forest	252	log(Richness)	0.35	0.0000		0.23	s(log(Richness))	0.0000	0.23
Degraded Forest	252	log(Evenness)	-1.18	0.0096		0.23	s(log(Evenness))	0.0096	0.23
Degraded Forest	252	s(Longitude, Latitude)			0.0005	0.23	s(Longitude, Latitude)	0.0005	0.23
Forest Regrowth	66	log(Richness)	0.38	0.0017		0.22	s(log(Richness))	0.0064	0.21
Forest Regrowth	66	log(Evenness)	-0.06	0.9454		0.22	s(log(Evenness))	0.7826	0.21
Forest Regrowth	66	s(Longitude, Latitude)			0.0946	0.22	s(Longitude, Latitude)	0.1028	0.21
Mixed open-canopy savanna woodland	1547	log(Richness)	0.31	<2e-16		0.34	s(log(Richness))	<2e-16	0.35
Mixed open-canopy savanna woodland	1547	log(Evenness)	0.89	0.0000		0.34	s(log(Evenness))	0.0010	0.35
Mixed open-canopy savanna woodland	1547	s(Longitude, Latitude)			<2e-16	0.34	s(Longitude, Latitude)	<2e-16	0.35

Table S1.5. Results from interaction models evaluating the joint effects of structural diversity metrics on biomass. Green column headers correspond to interaction linear model results, and blue column headers correspond to interaction smooth model results.

Land Cover Class	Number of Samples	Term	Coefficient Estimate	p-value	p-value (Lat/Lon Smooth)	R^2 (adj)	Term	p-value	R^2 (adj)
All Data	3413	log(Richness)	0.06	0.2651		0.49			
All Data	3413	log(Evenness)	-1.88	0.0000		0.49			
All Data	3413	log(Richness): log(Evenness)	-0.27	0.0050		0.49	te(log_fRic,log_fEve)	<2e-16	0.52
All Data	3413	s(Longitude, Latitude)			<2e-16	0.49	s(Longitude, Latitude)	<2e-16	0.52
Undisturbed Forest	1548	log(Richness)	-0.49	0.0000		0.39			
Undisturbed Forest	1548	log(Evenness)	-2.86	0.0000		0.39			
Undisturbed Forest	1548	log(Richness): log(Evenness)	-0.53	0.0000		0.39	te(log_fRic,log_fEve)	<2e-16	0.43
Undisturbed Forest	1548	s(Longitude, Latitude)			<2e-16	0.39	s(Longitude, Latitude)	<2e-16	0.43
Degraded Forest	252	log(Richness)	-0.44	0.2829		0.24			
Degraded Forest	252	log(Evenness)	-4.50	0.0104		0.24			
Degraded Forest	252	log(Richness): log(Evenness)	-1.30	0.0499		0.24	te(log_fRic,log_fEve)	0.0005	0.24
Degraded Forest	252	s(Longitude, Latitude)			0.0005	0.24	s(Longitude, Latitude)	0.0013	0.24
Forest Regrowth	66	log(Richness)	0.13	0.8640		0.21			
Forest Regrowth	66	log(Evenness)	-1.30	0.7286		0.21			
Forest Regrowth	66	log(Richness): log(Evenness)	-0.44	0.7333		0.21	te(log_fRic,log_fEve)	0.9620	0.59
Forest Regrowth	66	s(Longitude, Latitude)			0.1130	0.21	s(Longitude, Latitude)	0.1700	0.59

Mixed open-canopy savanna woodland	1547	log(Richness)	0.01	0.9141		0.35			
Mixed open-canopy savanna woodland	1547	log(Evenness)	-1.31	0.0153		0.35			
Mixed open-canopy savanna woodland	1547	log(Richness):log(Evenness)	-0.59	0.0000		0.35	te(log_fRic,log_fEve)	<2e-16	0.36
Mixed open-canopy savanna woodland	1547	s(Longitude, Latitude)			<2e-16	0.35	s(Longitude, Latitude)	<2e-16	0.36

Table S1.6. Changes in GAM-derived structural diversity-biomass metrics across smooth models for each land cover class and predictor. For each case, we report percent changes in proportion of maximum area under the curve (AUC), maximum-slope point, and saturation point. Absolute differences in median biomass are also included as a reference for changes in the central tendency of biomass across observations.

Land Cover Class	Predictor	ΔAUC (Proportion)	ΔMax-Slope Point (Proportion)	ΔSaturation Point (Proportion)	ΔMedian Biomass
All Data	log(Evenness)	-7.19%	-1.13%	0.00%	-7.44
All Data	log(Richness)	-0.72%	0.50%	1.51%	-3.02
Undisturbed Forest	log(Evenness)	-0.36%	-25.35%	0.00%	5.08
Undisturbed Forest	log(Richness)	2.70%	0.00%	1.00%	8.53
Degraded Forest	log(Evenness)	0.25%	0.00%	0.00%	0.01
Degraded Forest	log(Richness)	3.50%	0.00%	0.00%	1.35
Forest Regrowth	log(Evenness)	-5.75%	26.68%	0.00%	-0.18
Forest Regrowth	log(Richness)	-11.35%	28.44%	-47.57%	1.52
Mixed open-canopy savanna woodland	log(Evenness)	0.51%	-0.57%	0.00%	-0.14
Mixed open-canopy savanna woodland	log(Richness)	-0.57%	0.00%	0.00%	-0.37

Chapter 2: Comparative predictability of GEDI-derived forest structural attributes in the tropics

Abstract

Understanding spatial variation in forest structure is essential for accurately estimating carbon storage and fluxes, yet the remote sensing approaches used in their quantification, such as spaceborne LiDAR, provide only discrete samples, requiring predictive models to map spatial gaps. To date, evaluation of the variation in predictive performance among structural attributes remains limited. Here, we assess the predictability of tropical forest canopy height (relative height, RH), foliage height diversity (FHD), and plant area index (PAI) from GEDI spaceborne LiDAR at 30 m and 1 km across the Democratic Republic of Congo, examining how spatial autocorrelation, resolution, and invalid data affect mapping outcomes. RH consistently showed the strongest performance (R^2 = 0.83 at 1 km, 0.61 at 30 m; nRMSE = 0.28 at 1 km, 0.43 at 30 m), likely reflecting its more direct waveform derivation and stronger alignment with available predictors. FHD showed moderate predictability, while PAI was the most challenging to model, particularly at the finer 30 m resolution. Coarser 1 km models consistently outperformed 30 m models for all attributes, highlighting the influence of residual geolocation error and fine-scale structural heterogeneity. Additional invalid data handling improved spatial reliability across all attributes, with RH demonstrating the greatest sensitivity to extreme error, with only negligible differences in R^2 and RMSE. Overall, the consistent predictive performance ranking of RH, FHD, and PAI reflects systematic differences in derivation complexity, feature alignment, and spatial context. Our findings suggest that the limits of predictive mapping are not merely technical but

intrinsic to each structural attribute, underscoring that robust large-scale carbon estimation depends as much on attribute choice and spatial context as on model sophistication.

Introduction

The three-dimensional structural composition of tropical forests is vital to their functioning across scales, contributing to biogeochemical processes such as gas exchange, respiration, and cloud formation, which influence global carbon, water, and energy cycles (Artaxo et al., 2022; Silva Dias et al., 2002). Complex vertical and horizontal vegetation structure also fosters biodiversity by providing a range of habitat spaces and niches with variable microclimates that support diverse ecological interactions (Gardner et al., 2009) and provide ecosystem services crucial to human well-being, including water regulation, climate moderation, and food provisioning (Chiabai, 2015; Pattanayak, 2004). Variation in forest structure also directly underpins heterogeneity in aboveground carbon storage (Lefsky et al., 2002) and carbon fluxes (Malhi et al., 2011; Rödig et al., 2018; Thomas et al., 2008), making the capture of its spatial variation across broad scales essential. Remote sensing technologies like LiDAR (light detection and ranging) are pivotal to characterizing patterns of tropical forest structural variation at broad scales (Murphy and Bowman, 2012; Yang et al., 2016).

A key limitation of LiDAR is its spatial coverage, as measurements are collected along only specific flight paths or orbital tracks. As a result, gaps between sampled areas must be predicted to generate spatially continuous maps. These maps enable researchers and decision-makers to assess forest conditions across entire landscapes rather than within scattered footprints (Lang et al., 2022; Potapov et al., 2021; Xu et al.,

2017). However, there has been little systematic evaluation of how broad-scale predictive mapping performance varies across vegetation structural attributes and spatial contexts (e.g., spatial autocorrelation), leaving uncertainties about the conditions under which predictive modeling capacity varies. As a result, there is a potential overestimation of model accuracy and a mismatch between perceived and actual product quality, especially when assessed at local scales.

Addressing these uncertainties to better understand the ecological function of tropical forests first requires broad, ecosystem scale data acquisitions. In 2018, the launch of NASA's Global Ecosystem Dynamics Investigation (GEDI) mission, which was explicitly designed to capture vegetation structure using full-waveform LiDAR from the International Space Station, enabled extensive characterization of ecosystem structure across the tropics (Dubayah et al., 2020). GEDI samples the Earth's surface between 51.6° N and S latitude in discrete, ~25 m diameter laser footprints spaced ~60 m apart along-track and ~600 m across-track, resulting in spatially irregular coverage. A variety of forest structural attributes have been derived from these footprints, including canopy height, foliage height diversity, and plant area index, which are essential for capturing the heterogeneity of forest canopies (Fahey et al., 2019). Canopy height provides a measure of the vertical distance from the highest point in the canopy to the ground, serving as an important input for estimating biomass (Asner and Mascaro, 2014; Fayolle et al., 2016; Ferraz et al., 2018; Jucker et al., 2017). Foliage height diversity reflects the vertical distribution of foliage across canopy layers, offering insights into habitat complexity and ecological niches (MacArthur and MacArthur, 1961). Plant area index is a proxy of leaf area index, which quantifies the amount of leaf area per unit of horizontal

ground surface area. This metric is critical for scaling leaf-level processes to the ecosystem-scale, including photosynthesis and respiration (Fang et al., 2019). However, it is difficult to distinguish between leaves and small branches in the canopy through GEDI, and leaf area index is instead approximated and referred to as plant area index (Tang and Armston, 2019).

The availability of GEDI data has spurred a surge of efforts in generating spatially continuous predictions of forest structural metrics with the integration of irregularly sampled GEDI footprints. These efforts encompass a variety of approaches, including statistical models, physics-based radar-GEDI fusion methods, and machine learning-based spatial prediction (e.g., Chen et al., 2021; Lang et al., 2022; Potapov et al., 2021; Schlund et al., 2023; Tolan et al., 2024). In particular, machine learning studies have used GEDI-derived metrics as training targets and modeled their relationships with geospatial features which include optical imagery, climate variables, and topographic data. This predictive mapping approach allows for the estimation of forest structural attributes across landscapes, including locations not directly sampled by GEDI. However, most existing GEDI predictive mapping studies focus on canopy height (referred to as relative height in GEDI products), which may be more directly observable in waveform data through distinct signal returns from the canopy top and ground. In contrast, foliage height diversity and plant area index require more complex calculations, as they are derived from vertical foliage profiles and the estimated distribution of plant material (Tang and Armston, 2019), making them inherently noisier targets and potentially more challenging to predict. As a result, variable predictability from these metrics can arise from two main sources of uncertainty: (1) noisy or

uncertain training targets, where the GEDI-derived values themselves are less precisely estimated; and (2) low predictive power due to feature space limitations where the available predictor variables may not strongly align with the target variable.

These sources of uncertainty may further interact with spatial structure, the resolution of data aggregation, and attribute-specific sensitivities to influence predictive performance. Spatial autocorrelation is the tendency for nearby observations to be more similar than those farther apart, which poses a challenge for standard validation approaches (Nikparvar and Thill, 2021). Conventional cross-validation techniques assume observations in a sample are independent and identically distributed, which is an assumption that is violated in the presence of spatial autocorrelation. As a result, evaluation metrics do not truly reflect model generalizability (Ploton et al., 2020). In addition to spatial autocorrelation, statistical outcomes can also change with the spatial resolution at which data are aggregated, introducing scale-dependent effects that influence model performance (Jelinski and Wu, 1996). In GEDI-based predictive mapping, this occurs when GEDI observations are aggregated at different resolutions. For example, aggregating GEDI data to a 1 km grid reduces sampling variance and stabilizes model-based biomass estimates relative to footprint-level values (Patterson et al., 2019). Uncertainty in both input remote sensing features and GEDI-derived attributes further complicates forest structure mapping, particularly in humid tropical forests with persistent cloud cover and high humidity (Asner, 2001; Frankenberg et al., 2024; Hansen et al., 2008).

The overall goal of this study is to evaluate the relative predictability of canopy height (hereafter, relative height), foliage height diversity, and plant area index data

across the Democratic Republic of Congo (DRC) in Central Africa. This region represents a useful testbed for this analysis not only due to its vast tropical forest extent, but also due to its structural diversity (Mayaux et al., 1999; Schneider et al., 2026a; Xu et al., 2017). This variation, combined with the availability of high-density airborne LiDAR validation data across the country, makes the DRC an ideal region to explore the predictability of forest structural attributes as derived from GEDI. In this study, we seek to answer two questions: (1) How does predictive performance vary across GEDI-derived relative height (RH), foliage height diversity (FHD), and plant area index (PAI)? (2) How do spatial autocorrelation, spatial resolution, and sensitivity to noise shape differences in predictability among these GEDI-derived attributes? We hypothesize that relative height, which represents the top of canopy height, will be the most predictable metric across modeling scenarios, partially because its derivation method is the least complex of the three. RH is calculated by identifying the height at which a specified upper quantile of cumulative returned energy is reached, which is typically where return amplitudes are stronger and less prone to interference. FHD is expected to follow, as it is correlated with RH but incorporates information about how foliage is distributed vertically. This adds complexity, as the metric depends on the shape of the entire return profile rather than a single point, making it more sensitive to vegetation structure variation. PAI is anticipated to be the most difficult to predict, as it reflects the total amount of plant material in the canopy and requires detailed information about canopy volume and layering, including through contributions from the mid-canopy and understory (Figure 2.1).

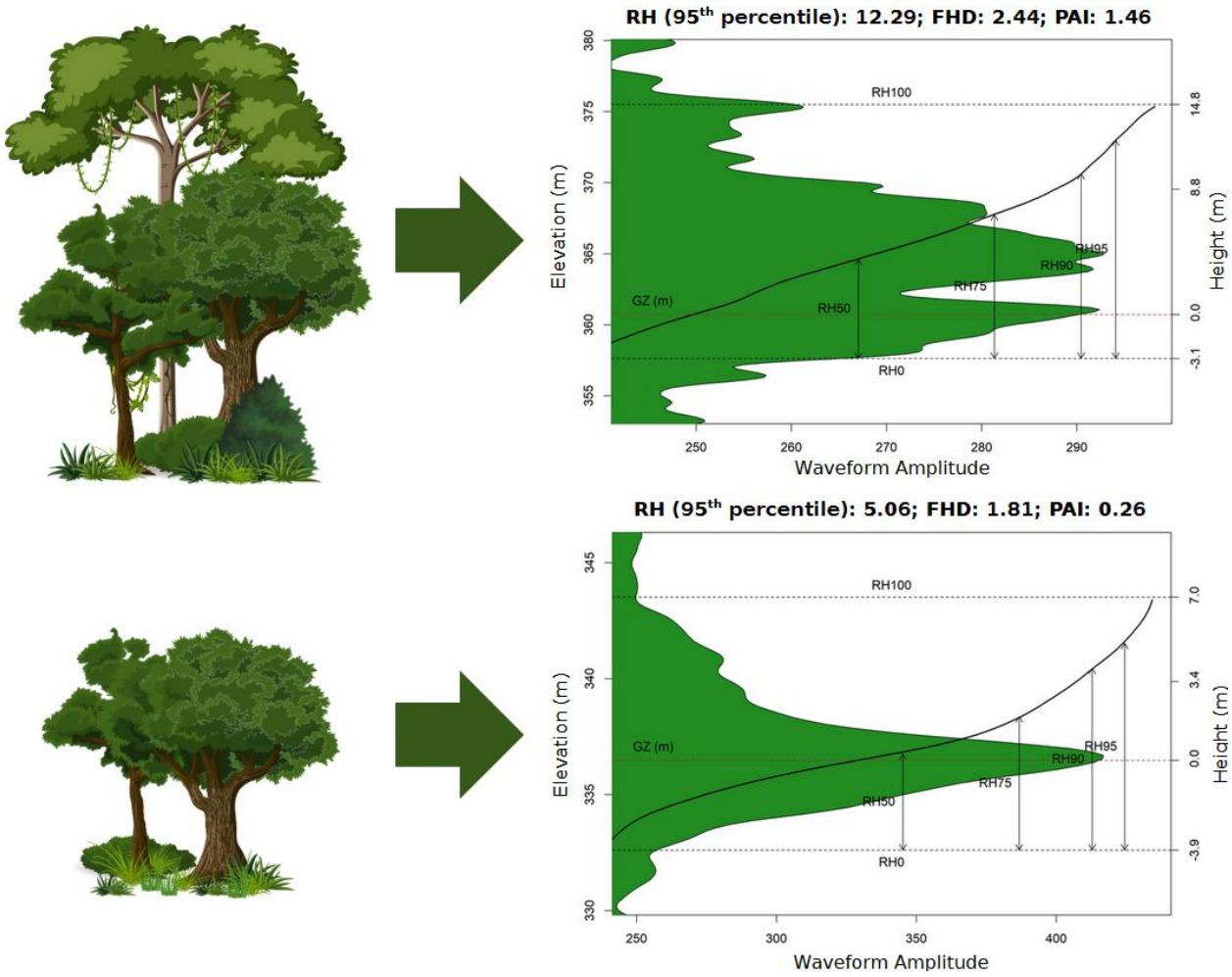


Figure 2.1. Conceptual representation of GEDI-derived forest structural metrics: relative height (RH), foliage height diversity (FHD), and plant area index (PAI). Forest profiles are shown alongside their corresponding GEDI waveforms. Forest profiles are not to scale or footprint-accurate, but reflect general structural differences inferred from the waveform metrics. Waveform figures made using rGEDI (Silva et al., 2022).

Study site and datasets

Study site

The DRC encompasses approximately 60% of the Congo Basin, which is situated within Central Africa, home to the world's second largest contiguous tropical forest (Mayaux et al., 2013). These tropical forests exhibit high structural diversity, encompassing a range of forest types, including closed evergreen forests, swamp

forests, and deciduous woodlands (Vancutsem et al., 2009; Xu et al., 2017), each contributing to the region's ecological complexity. Despite its ecological importance, the Congo Basin remains relatively understudied compared to other tropical forests in the Amazon, Central America, or Southeast Asia (White et al., 2021). The DRC served as the focal area for this study due to its complex, heterogeneous, and extensive forest cover as well as the availability of high-density airborne laser scanning (ALS) point cloud data sampled throughout the country using a stratified sampling technique (Xu et al., 2017), which enabled the evaluation and validation of GEDI measurements (Figure 2.2).

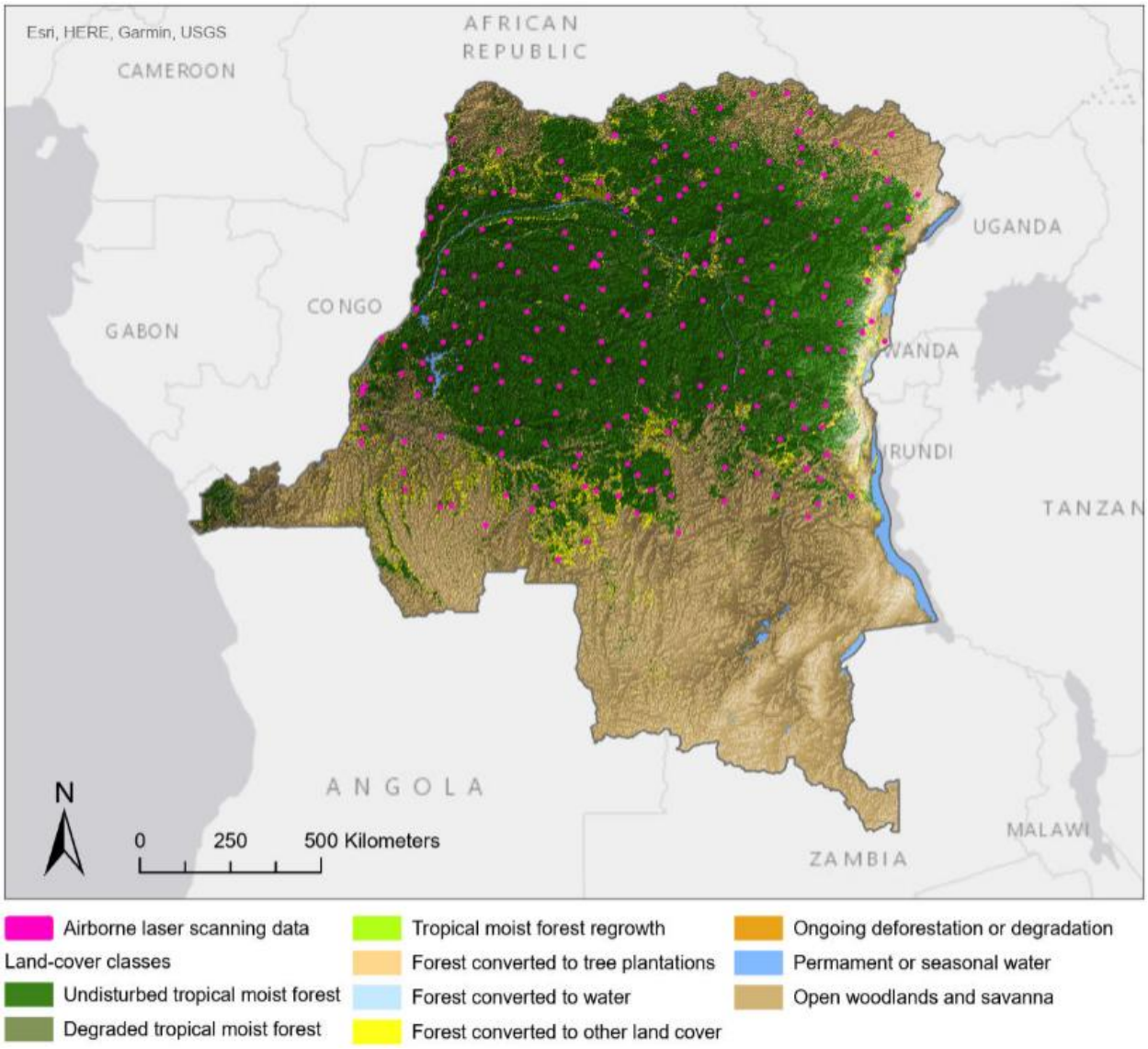


Figure 2.2. Map of land cover types across the DRC overlaid on a shaded relief base derived from the Copernicus 30 m digital elevation model. The nine generalized forest categories illustrate broad patterns of vegetation across varying terrain. Data source: Tropical Moist Forest (Vancutsem et al., 2021).

ALS Data

ALS data, sourced from Xu et al. (2017), were acquired through an airborne LiDAR survey across the DRC. The survey, conducted between June 2014 and February 2015, used an Optech ALTM 3100 LiDAR scanner. The resulting LiDAR point cloud dataset consists of 216 1 km^2 datasets clipped from flightlines and collected from

randomized transect locations within a systematic grid with an average density of 4 points per square meter (Xu et al., 2017). The preprocessing of these data included trajectory calculation and LiDAR point calibration. However, because these ALS data predate the GEDI mission, a temporal mismatch exists between the two datasets. While localized disturbances or gradual forest dynamics (e.g., growth) may introduce additional variability, all three structural attributes evaluated are derived from the same GEDI waveforms. As a result, temporal effects should affect all three metrics similarly, preserving the validity of their relative predictability.

GEDI data

This study utilized GEDI Level 2A (L2A) and 2B (L2B) version 2 data spanning 2019 to 2022 (Dubayah et al., 2020). These datasets served as the basis for generating continuous forest structure maps. We selected RH from the L2A dataset and PAI and FHD from the L2B dataset. The RH metric, as well as its accompanying quality and sensitivity flags, was calculated using six different ground-finding algorithms, each applying distinct threshold and smoothing settings to interpret the waveform and determine the ground location. This variation allows flexibility to optimize ground detection under different conditions and waveform complexities (Hofton and Blair, 2019). Quality flags indicated whether the data met energy, amplitude, and real-time surface tracking quality requirements. Sensitivity flags, also specific to each algorithm, represented the minimum detectable ground return pulse energy.

Remote Sensing Features

Environmental features included a combination of spectral, radar, and elevation data from multiple sources: Landsat-8 (Bands 2–7), ALOS PALSAR-2/PALSAR

(Polarizations HH and HV), Sentinel-1 (Polarizations VV and VH), and the Copernicus Digital Elevation Model (DEM). To explore how changes in spatial aggregation affect predictive performance, all datasets were processed at two resolutions: 30 m and 1 km. The finer scale (30 m) preserved the native resolution of most input layers while the coarser scale (1 km) followed the GEDI science team's sampling design for their published Distributed Active Archive Center (DAAC) gridded products, which aggregates footprint-level observations into 1 km grid cells to support statistically robust estimation of forest structural properties within observational constraints (Dubayah et al., 2023a; Patterson et al., 2019). All data were processed and aggregated in Google Earth Engine (GEE) to generate wall-to-wall feature stacks at both 30 m and 1 km resolution, then aligned with the 2019-2022 study period and clipped to the DRC boundary.

Landsat-8 bands 2-7 were aggregated by calculating the median surface reflectance value across all images in the GEE collection from 2019 to 2022. Cloud masking was applied to remove cloud-contaminated pixels, although gaps caused by persistent cloud cover necessitated additional gap-filling. The gap-filling utilized the quality mosaic function in GEE, which selects the pixel with the maximum Normalized Difference Vegetation Index (NDVI) value for each cloud-removed or null-value pixel across the time series. This process helped fill persistent gaps with the greenest available observations from the time series. While these pixels are not guaranteed to be cloud-free or from peak productivity periods, selecting by maximum NDVI helps reduce the influence of low-quality observations and partially controls for phenological variability across a region that spans closed-canopy moist evergreen forests to drought-deciduous

forests and open woodlands (Kearsley et al., 2024; Verhegghen et al., 2012). Additionally, a near-infrared reflectance of vegetation (NIRv) band was calculated using Landsat-8 by multiplying the near-infrared reflectance band by NDVI. We chose NIRv over more common vegetation indices because it more directly represents the proportion of near-infrared light reflected by vegetation, providing a stronger and more interpretable physical basis (Badgley et al., 2017). Consequently, NIRv functions as an integrative metric of light capture that reflects canopy architecture (Badgley et al., 2019), making it a valuable feature for modeling GEDI-derived variables.

ALOS PALSAR-2/PALSAR data from 2019 to 2022 were supplied by JAXA as annual mosaics in decibel units (Shimada et al., 2014). Pixels with values of zero corresponded to no valid radar return and were masked, and the remaining valid observations were averaged for both HH and HV polarizations to reduce speckle and interannual variability. These L-band radar data penetrate deeper into forest canopies than shorter-wavelength sensors and are sensitive to woody structure through volume and double-bounce scattering mechanisms (Nesha et al., 2020; Villard et al., 2016), making them complementary for mapping ecosystem structure alongside optical data. Similarly, C-band Sentinel-1 data (VV and VH polarizations, in decibels), with no-data pixels masked, were aggregated by mean across 2019 – 2022 to provide additional radar-based features of vegetation structure. Due to its relatively shorter wavelength, C-band backscatter is especially sensitive to upper crown characteristics (Kuenzer et al., 2011; Oon et al., 2019), providing information complementary to deeper-penetrating L-band observations. Finally, the Copernicus DEM was also included to account for

elevation, which is associated with variation in tropical forest structure (Ediriweera et al., 2008; Robinson et al., 2018).

Methods

Filtering GEDI data based on ALS data

ALS derived RH (i.e., canopy height) correlates well with field measurements and can be more accurate than field measured height, especially in areas where the top of the canopy might not be visible from the ground (Andersen et al., 2006; Hirschmugl et al., 2023; Wang and Fang, 2020). We used the DRC country-wide ALS dataset to filter GEDI shots based on relative height percentiles, quality, and sensitivity flags, following a method that has been used to remove unusable GEDI data in past research (Li et al., 2023; Rishmawi et al., 2021). The ALS data were used to create canopy height models at 2 m spatial resolution, selected to align with the point density of the ALS data, by calculating the maximum elevation of all laser returns above the ground surface for each grid cell. GEDI L2A shot locations were converted to point vectors and buffered to 25 m to match the GEDI footprint. All 2 m canopy height model pixels within each footprint were summarized using both the mean and median for comparison with GEDI shot-level RH. We then compared ALS-derived canopy height with GEDI RH across all algorithm groups (Table S2.1). For top-of-canopy RH (RH 95, RH 98, RH 100), we tested three sensitivity ranges (0.9 – 1, 0.95 – 1, 0.98 – 1) after applying a quality flag of 1, evaluating each combination using R^2 and RMSE. RH 95 generated by Algorithm 5 with sensitivity 0.9 – 1 provided the best overall agreement with ALS canopy height and was therefore used in subsequent analyses. PAI and FHD were then filtered using the same quality flag and sensitivity range (0.9 – 1).

Additional GEDI invalid data handling

After the initial filtering scheme, we created an additional core dataset of target variables per metric to evaluate the impacts of anomalous measurements that remained after GEDI metadata filtering (i.e., quality flag and sensitivity). We first tested an automated z-score filtering approach on RH to remove values conspicuously deviating from surrounding measurements (i.e., extreme error). However, this statistical outlier approach could not reliably distinguish these erroneous measurements from legitimate observations and over-aggressively removed data. Instead, we manually removed remaining invalid RH data by identifying spatially coherent extreme error along single GEDI overpasses (Figure 2.3). This additional invalid data handling was implemented to examine how the targeted removal of extreme, spatially structured error influences spatial predictions rather than eliminate all remaining uncertainty. To facilitate this, RH shots were aggregated to a 600 m raster, enabling visualization of conspicuously irregular patterns, such as orbital lines that appeared unusually bright or dark, corresponding to extreme high or low values relative to their surrounding areas (Figure S2.1). These problematic shots were hand delineated and removed from the core RH dataset. The corresponding PAI and FHD shots were also excluded because all three metrics are derived from the same underlying waveforms. RH was used as the primary basis for this cleaning because it is calculated directly from the waveform's vertical energy distribution, making it a clearer indicator of structural anomalies, and thus extreme error, than PAI or FHD. Only a small fraction of GEDI shots met our criteria for extreme error (hereafter referred to as invalid data) and were excluded (~0.2%; Figure S2.2). Importantly, however, these targeted removals allowed us to evaluate model

sensitivity to extreme error while retaining the broader distribution of valid forest structural variability.

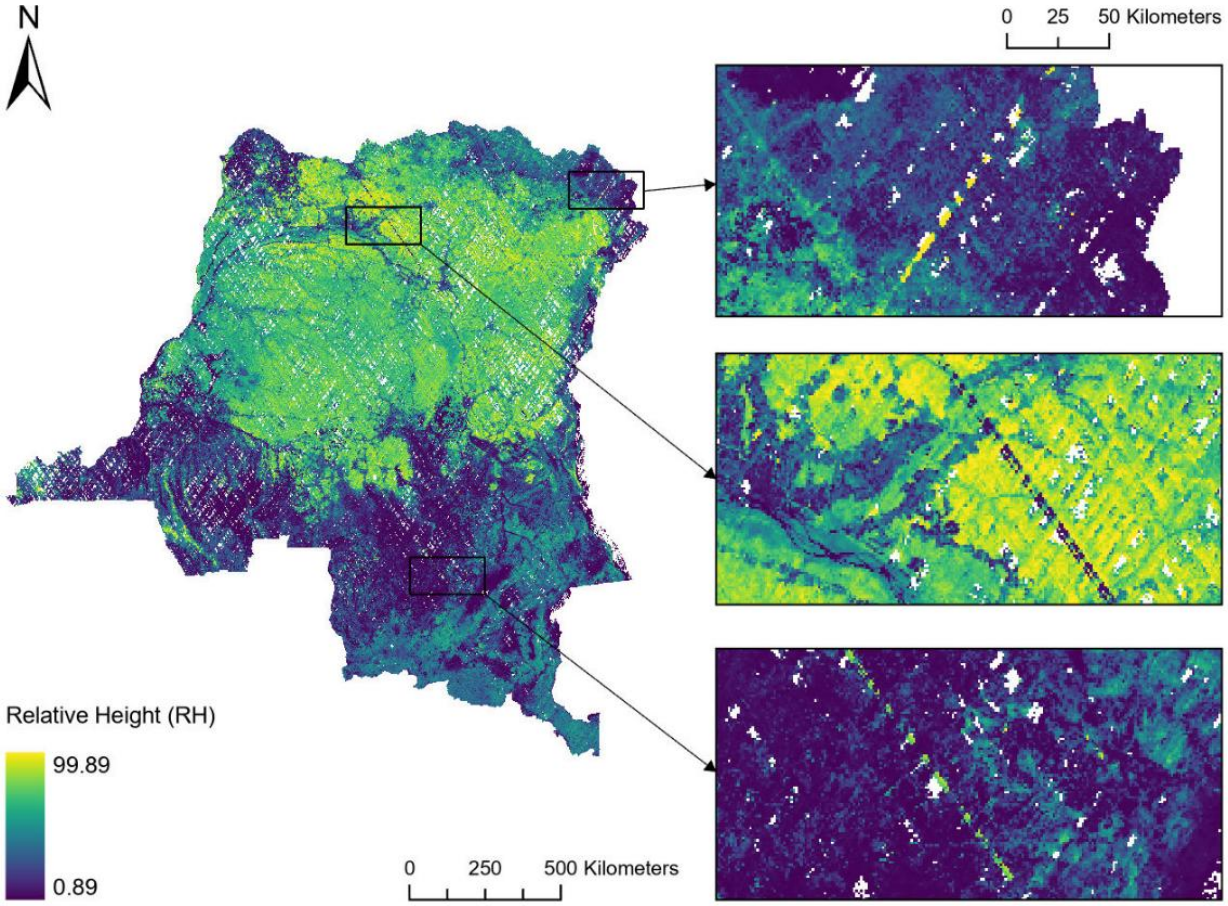


Figure 2.3. Illustration of GEDI shots collected from 2019-2022 across the Democratic Republic of Congo, including invalid data points identified through visual inspection. This figure highlights example regions where extreme error in relative height is spatially concentrated.

Creating machine learning training datasets

To construct the machine learning datasets, GEDI shots were aligned based on reference grids matching the spatial resolution of two datasets: a 30 m grid derived from Landsat data and a 1 km grid corresponding to the grid of published GEDI science team products (Dubayah et al., 2020). The data were aggregated and rasterized to these grids, stacked alongside the feature rasters, and sampled at each GEDI shot location to

create the tabular training datasets. To evaluate the influence of invalid data on model performance, we generated two versions of each dataset, one using the GEDI data as filtered through comparison with the ALS data, and another incorporating the additional invalid shot removal described above. This comparison allowed us to assess sensitivity to error across structural metrics. To examine the effects of data aggregation across resolutions, each filtering level was produced at both the 30 m and 1 km resolutions. This design yielded four training datasets per structural attribute, two filtering levels at two spatial resolutions, for a total of twelve datasets (Figure S2.3).

Machine learning models

To evaluate the impacts of the data aggregation across resolutions, spatial autocorrelation, and invalid data on model performance, we implemented Random Forest regression models for each dataset, a method chosen for its interpretability, reliability, and stability (Chen et al., 2018; Filippi et al., 2019; Garcia-Martí et al., 2017). Hyperparameter tuning was performed systematically using grid search via the scikit-learn library, enabling an exhaustive search over a hyperparameter grid to optimize model performance. All models incorporated bootstrapping, which supported model robustness and contributed to uncertainty estimation through ensemble prediction variance. Using this bootstrapping approach, we also generated maps where each pixel represents the standard deviation of the ensemble predictions at that location, providing a spatially explicit measure of predictive uncertainty (Figure S2.4).

To assess sensitivity to spatial autocorrelation, two cross-validation strategies were employed per dataset. The first strategy used a traditional 5-fold cross-validation approach where the data were randomly partitioned into five subsets. Each subset

served as a validation set once, while the remaining four were used for training, ensuring that every sample contributed to both training and validation at some point. The second strategy similarly employed 5-fold cross-validation but also incorporated a spatial block sampling approach (Roberts et al., 2017). Here, the study area was divided into folds defined by hexagon blocks, each covering approximately 90,000 km^2, aligning with the median province area in the DRC (Figure S2.5). Although somewhat arbitrary, this spatial scale helped structure the sizing of the folds in a way that aligned with broader environmental and municipal gradients without enforcing artificial administrative boundaries. Additionally, to ensure the effects of spatial autocorrelation were not masked, all modeling strategies excluded regularization. Under this strategy, each fold assigned approximately 70% of the hexagons to training and 15% to validation, with a 30 km buffer between sets to prevent adjacent folds from containing spatially dependent data to minimize the influence of spatial autocorrelation. The remaining 15% of hexagons were excluded entirely from both training and validation and designated as a holdout set and withheld as independent evaluation data for every model, including those using random k-fold cross-validation (Figure S2.5). This split aligned with the subdivision of spatial blocks and ensured a consistent basis for model comparison regardless of cross-validation strategy.

Evaluating spatial autocorrelation in the data

We also assessed whether spatial structure within the test data could influence performance metrics by using the spatially independent holdout sets reserved for final model evaluation. Spatial autocorrelation was quantified using Moran's I, which measures the degree to which similar values cluster or disperse across space. We

selected Moran's I over variogram-based approaches because it does not require second-order stationarity (i.e., constant mean and variance across space), an assumption unlikely to hold across our large and heterogeneous study region (Gringarten and Deutsch, 2001). Moran's I was calculated within each test set grid cell to characterize underlying spatial autocorrelation, providing context for interpreting subsequent results by illustrating how spatial autocorrelation decays with distance. The primary parameter in Moran's I is the spatial threshold, which defines the neighborhood distance used to measure autocorrelation. Due to computational constraints, we limited the number of spatial thresholds evaluated for each dataset, choosing three progressively larger distances relative to each dataset's resolution to examine how spatial autocorrelation decays across scales. For the 30 m resolution datasets, we evaluated Moran's I at 50 m, 1 km, and 3 km thresholds. The 50 m threshold captures very fine-scale spatial structure, while the 1 km threshold corresponds to distances on the order of hundreds of meters over which forest structure has been studied to exhibit spatial dependence (Hardiman et al., 2018; Réjou-Méchain et al., 2014). The 3 km threshold represents the largest extent relative to the 30 m resolution, allowing us to assess the degree to which autocorrelation persists and decays at multi-kilometer distances. For the 1 km resolution datasets, we assessed Moran's I at 3 km, 10 km, and 30 km thresholds. The 3 km threshold was included for a direct comparison of spatial autocorrelation across both 30 m and 1 km resolution datasets at a common scale, as it represents the least common multiple of both. The 10 km and 30 km thresholds were used to further evaluate how spatial autocorrelation declines across progressively larger distances, without implying ecological breakpoints.

Model evaluation

Model performance was initially evaluated on the full test set using R^2 and normalized RMSE (nRMSE), the latter providing a unit-agnostic measure of error that facilitates a direct comparison across different target variables. This normalization was performed by dividing the RMSE by the mean of the observed target values in the test set. However, performance metrics derived from a single aggregated test set may obscure how errors are distributed across the data range, particularly when observations are unevenly distributed. The overall datasets are highly clustered, leading to disproportionate representation of central values in both the training and test sets (Figure S2.2). For instance, the 90th percentile of RH is approximately 33 m, meaning that most observations represent vegetation below this height. PAI and FHD exhibit similar clustering, with the majority of values concentrated within relatively narrow ranges. Consequently, R^2 and nRMSE are dominated by densely sampled regions and may underrepresent errors in less common values.

Because aggregate R^2 and nRMSE can mask how differences between models are distributed across samples, we evaluated the significance of differences in overall model performance by conducting hypothesis testing to determine whether observed differences in model performance could be explained by data variability. We employed the Wilcoxon signed-rank test, a non-parametric method suited for comparing paired sample-level prediction errors when distributions are skewed, heavy-tailed, or otherwise deviate from normality (Whitley and Ball, 2002). For each pair of models, we computed the difference between absolute prediction residuals for every test sample and applied the Wilcoxon test to this vector of paired error differences. By relying on the ranks of

differences rather than raw magnitudes, the test provides an assessment of whether one model systematically outperforms another across individual test observations without relying on mean differences, which can be distorted by skew or outliers. While the Wilcoxon test can be interpreted as a test of median differences when distributions have similar shape and spread, our goal was to assess whether one model systematically produces smaller residuals across paired samples. Although it does not correct for data clustering and is influenced by the densely sampled central regions of our target data, it provides a rank-based, conservative evaluation of paired model errors across the full test dataset.

To further explore these performance differences, we also implemented the sign test, a complementary non-parametric test that considers the direction of paired differences. This enabled us to assess whether one model consistently outperformed the other. To enhance our interpretation of model outputs, we then calculated Shapley Additive Explanations (SHAP) values, which quantify each feature's contribution to model predictions while accounting for interactions among variables. Given the large size of the test datasets and the computational demands of SHAP analysis, we utilized random sampling capped at a maximum of 5,000 samples to limit processing time. This sampling approach yields an approximately representative subset of each input dataset's overall distribution.

Results

Predictive performance across structural metrics

Based on test statistics aggregated across all eight model configurations per structural metric, RH performed the best overall (mean R^2 across all configurations =

0.72, mean nRMSE = 0.36), followed by FHD (mean R^2 = 0.43, mean nRMSE = 0.10), then PAI (mean R^2 = 0.30, mean nRMSE = 0.38) (Figure 2.4a). Aggregate SHAP values indicated that ALOS PALSAR HV was the most influential predictor for all three structural metrics. Secondary predictors varied by metric: RH depended strongly on Landsat-8 RGB bands, FHD showed greater importance of red-green-NIR features, and PAI relied more on Sentinel-1 VV and Copernicus DEM (Tables S2.7 – S2.9).

Resolution played a substantial role in influencing model performance across all structural metrics (Figure 2.4b). For every structural metric evaluated, R^2 values were consistently higher in the 1 km models compared to their 30 m counterparts. RH showed the highest R^2 overall (1 km: 0.83; 30 m: 0.61), followed by FHD (1 km: 0.53; 30 m: 0.32), and then PAI (1 km: 0.50; 30 m: 0.11). However, patterns in nRMSE diverged from the R^2 results. For FHD and PAI, despite their 30 m models having lower R^2, there was no practical difference in nRMSE when compared against their 1 km counterparts. This suggests that the 30 m resolution models explain less variance but result in predictions with similar accuracy on average. In contrast, for RH the 1 km model had both a higher R^2 (1 km: 0.83; 30 m: 0.61) and lower nRMSE (1 km: 0.28; 30 m: 0.43), indicating that model performance for RH consistently benefited from coarser resolution (Table S2.2). Furthermore, when comparing training and testing performance, the 1 km models generally showed larger discrepancies between train and test R^2 values compared to the 30 m models, particularly for FHD and PAI, and error metrics similarly reflected these trends (Table S2.3).

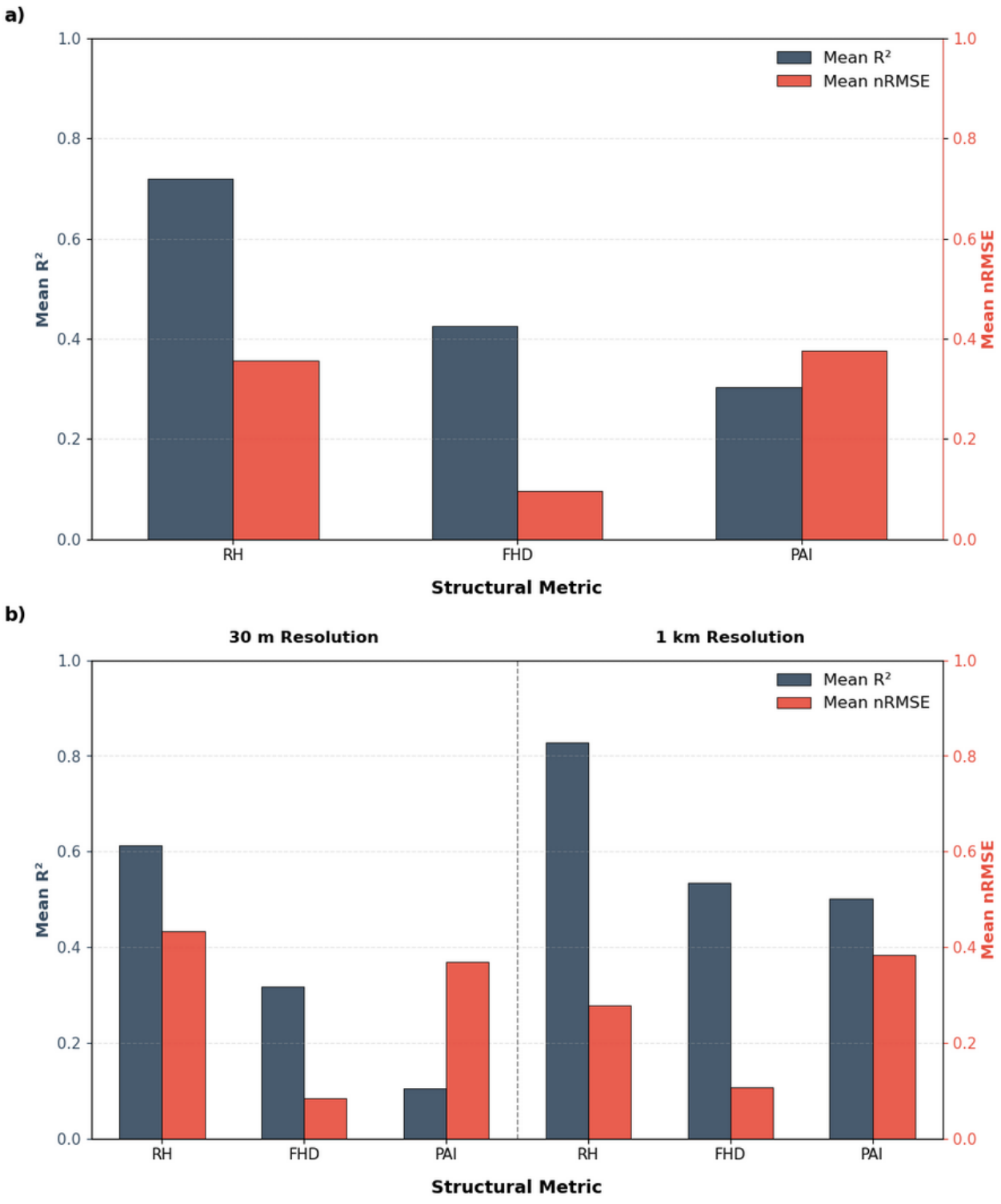


Figure 2.4. a) Aggregated mean R^2 and normalized RMSE (nRMSE) for both resolutions per structural metric: relative height (RH), foliage height diversity (FHD), and plant area index (PAI). These statistics were averaged across each structural metric's eight optimized model configurations. b) The same statistics averaged across each structural metric's four optimized model configurations per spatial resolution.

Impacts of invalid data on the prediction of structural metrics

To evaluate the sensitivity of individual metrics to invalid data, we compared models trained on data with and without additional invalid data handling within the same treatment group (i.e., spatial or random cross-validation). All reported results are based on differences that were statistically significant for both the Wilcoxon (Table S2.4) and sign tests (Table S2.5) at both resolutions (i.e., 1 km and 30 m). The only sign test that favored the base model (without additional invalid data handling) was the 1 km PAI comparison under random cross-validation ($p = 0.035$). Among all variables, RH results showed the greatest positive improvement with the addition of invalid data handling. The sign test favored this configuration in 65.39% of cases at 1 km and 62.00% at 30 m. R^2 and nRMSE differences consistently indicated improved numerical accuracy for models with additional invalid data handling (1 km: $\Delta R^2 = 0.0018$, ΔnRMSE = 0.0018; 30 m: $\Delta R^2 = 0.0008$, ΔnRMSE = 0.0005). Wilcoxon effect sizes were substantially stronger for RH than for other variables ($r = 0.34$ at 1 km; $r = 0.25$ at 30 m), indicating a robust and consistent advantage. Among all variables, RH showed the clearest and most consistent performance gains under the invalid data handling model, even if the effect magnitudes were small.

Model performance for FHD revealed minimal but statistically significant differences between models that incorporated additional invalid data handling and those that did not. At the 1 km resolution, the sign test indicated that the additional invalid data handling model outperformed the base model in 53.52% of cases. At 30 m, this decreased slightly to 52.44%. R^2 and nRMSE differences were negligible but favored the base model at both resolutions (1 km: $\Delta R^2 = 0.0068$, ΔnRMSE = 0.0008; 30 m: ΔR^2

= 0.0002, ΔnRMSE = 0.0000). Wilcoxon effect sizes were small but also in favor of additional invalid data handling (r = 0.10 at 1 km; r = 0.06 at 30 m). For PAI, the model that accounted for invalid data handling showed a modest and consistent advantage as the sign test indicated better performance in 54.36% of cases at 1 km and 53.06% at 30 m. Likewise, nRMSE values were marginally lower and R^2 values higher for the additional invalid data handling model at both resolutions (1 km: $\Delta R^2 = 0.0017$, ΔnRMSE = 0.0007; 30 m: $\Delta R^2 = 0.0003$, ΔnRMSE = 0.0001). Wilcoxon effect sizes were small but in favor of additional invalid data handling (r = 0.11 at 1 km; r = 0.08 at 30 m), aligning with the direction of other metrics (Figure 2.5).

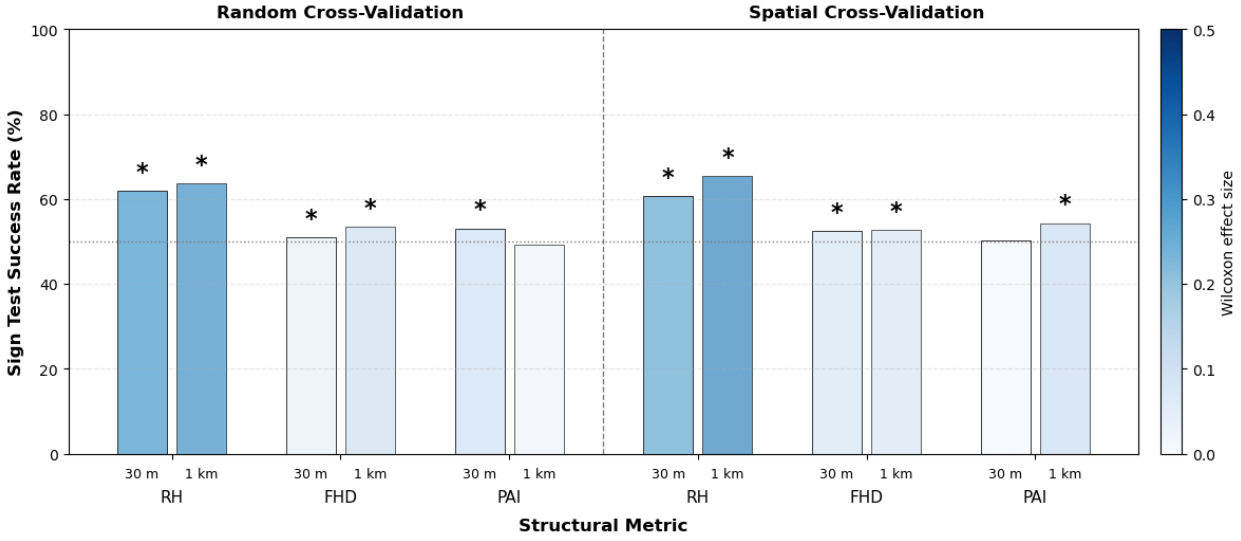


Figure 2.5. Proportion of pairwise comparisons favoring models with additional invalid data handling as assessed via the sign test and grouped by cross-validation strategy. The success rate represents the proportion of cases where these models outperformed their baseline counterparts (i.e., no additional invalid data handling). Bars are marked as statistically significant with an asterisk (*) if their sign test p-value < 0.05 and colored based on the Wilcoxon effect size in favor of invalid data handling.

Variation in spatial autocorrelation across structural metrics and resolutions

Moran's I values calculated using spatial thresholds ranging from 50 m to 30 km show that RH consistently exhibited the strongest spatial autocorrelation, followed by

FHD then PAI. At the smallest shared threshold (3 km), RH had a Moran's I of 0.24 at 30 m and 0.51 at 1 km. This resolution-dependence in spatial autocorrelation was also observed for FHD (increasing from 0.17 to 0.4) and PAI (increasing from 0.09 to 0.35). Across all metrics, spatial autocorrelation decreased as the spatial threshold increased, although RH maintained the highest Moran's I values (Figure 2.6).

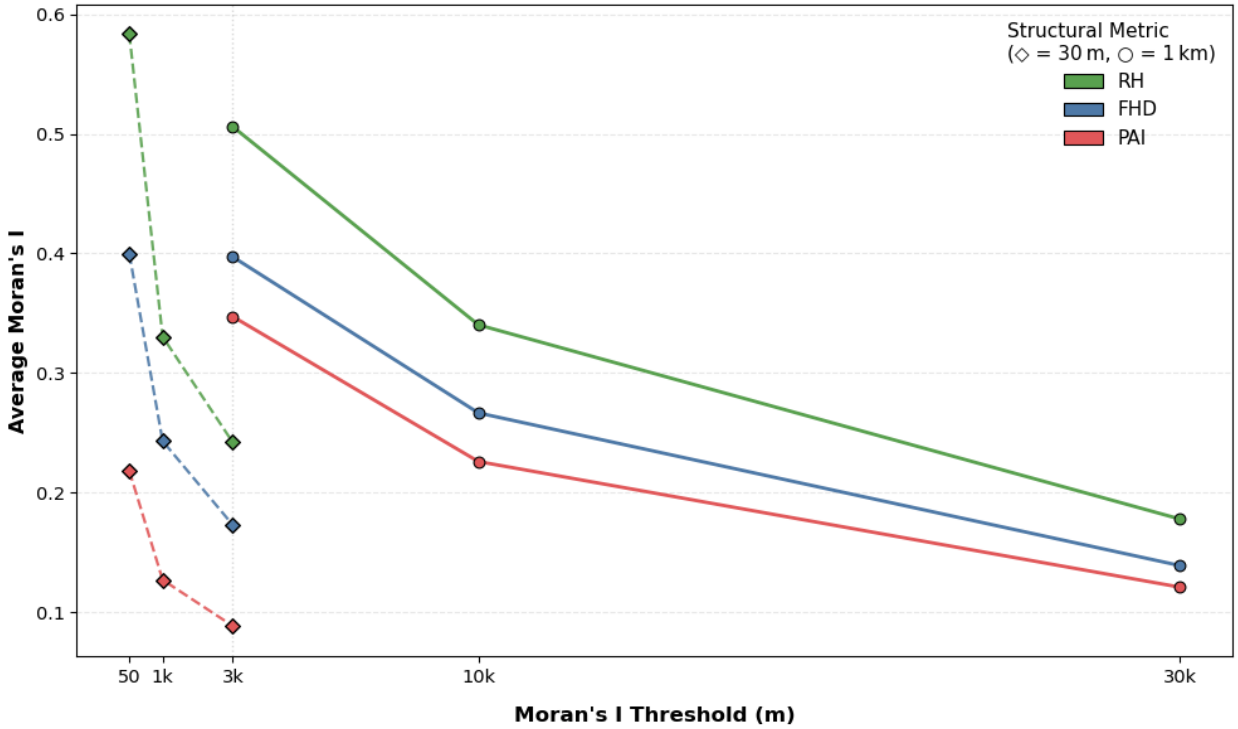


Figure 2.6. Moran's I values for relative height (RH), foliage height diversity (FHD), and plant area index (PAI) across the 30 m and 1 km test datasets. Each point represents an aggregated Moran's I value calculated across data with and without additional invalid data handling.

Impacts of spatial autocorrelation on the prediction of structural metrics

To assess the impact of spatial autocorrelation on structural attribute predictions, we compared spatial and random cross-validation models while keeping the type of invalid data handling consistent. The results presented in this section focus exclusively on comparisons in which both models applied invalid data handling, as these yielded

statistically significant differences according to both Wilcoxon and sign tests at 1 km and 30 m. Comparisons conducted without invalid data handling are reported in Tables S2.4 and S2.5 and show similar directional trends but weaker statistical support.

Of the three structural metrics evaluated, RH showed the clearest performance differences between models evaluating spatial autocorrelation and a clear resolution effect (Figure 2.7). At the 1 km scale, spatial cross-validation outperformed random cross-validation in 63.68% of sign test comparisons, while R^2 and nRMSE differences also favored the spatial model ($\Delta R^2 = 0.0054$, ΔnRMSE = 0.0054). Although the Wilcoxon effect size (r = 0.33) favored random sampling, this reflects that the fewer cases where random sampling performed better involved larger error differences. At 30 m, random sampling achieved lower error in 51.90% of sign test cases. However, the effect size (r = 0.06) was smaller than at 1 km, and nRMSE and R^2 differences ($\Delta R^2 = 0.0146$, ΔnRMSE = 0.0101) now favored random cross-validation in numerical accuracy (Figure S2.6).

Model comparisons for FHD revealed mixed results between spatial and randomly sampled models. At the 1 km scale, the random cross-validation model outperformed the spatial cross-validation model in 54.25% of samples according to the sign test. While this reflects a slight edge, the Wilcoxon effect size (r = 0.10) indicates that the gains were relatively small. The nRMSE and R^2 differences ($\Delta R^2 = 0.0027$, ΔnRMSE = 0.0003) marginally favored spatial cross-validation in terms of numerical accuracy. At 30 m, the spatial model showed stronger spatial reliability, outperforming the randomly sampled model in 63.66% of samples as the most decisive sign test result for this metric. Despite this, the Wilcoxon effect size remained in favor of the randomly

sampled model (r = 0.28), suggesting generally lower error. Numerical metrics once again favored the random cross-validation model ($\Delta R^2 = 0.1425$, $\Delta nRMSE = 0.0134$), indicating better fit quality at 30 m.

For PAI, differences between cross-validation models were small but consistent. Spatial models at 1 km outperformed randomly sampled models in 53.06% of samples according to the sign test, indicating a mild spatial advantage. However, the Wilcoxon effect size (r = 0.10) again favored random sampling, suggesting that when random sampling outperformed spatial sampling, improvements were small. nRMSE and R^2 differences ($\Delta R^2 = 0.0087$, $\Delta nRMSE = 0.0036$) also favored spatial cross-validation, reflecting slightly better numerical accuracy. This was reversed at 30 m, with random cross-validation outperforming spatial cross-validation in 52.68% of samples and producing a smaller Wilcoxon effect size (r = 0.07). However, numerical performance differences were negligible at this scale ($\Delta R^2 = 0.0004$, $\Delta nRMSE = 0.0001$).

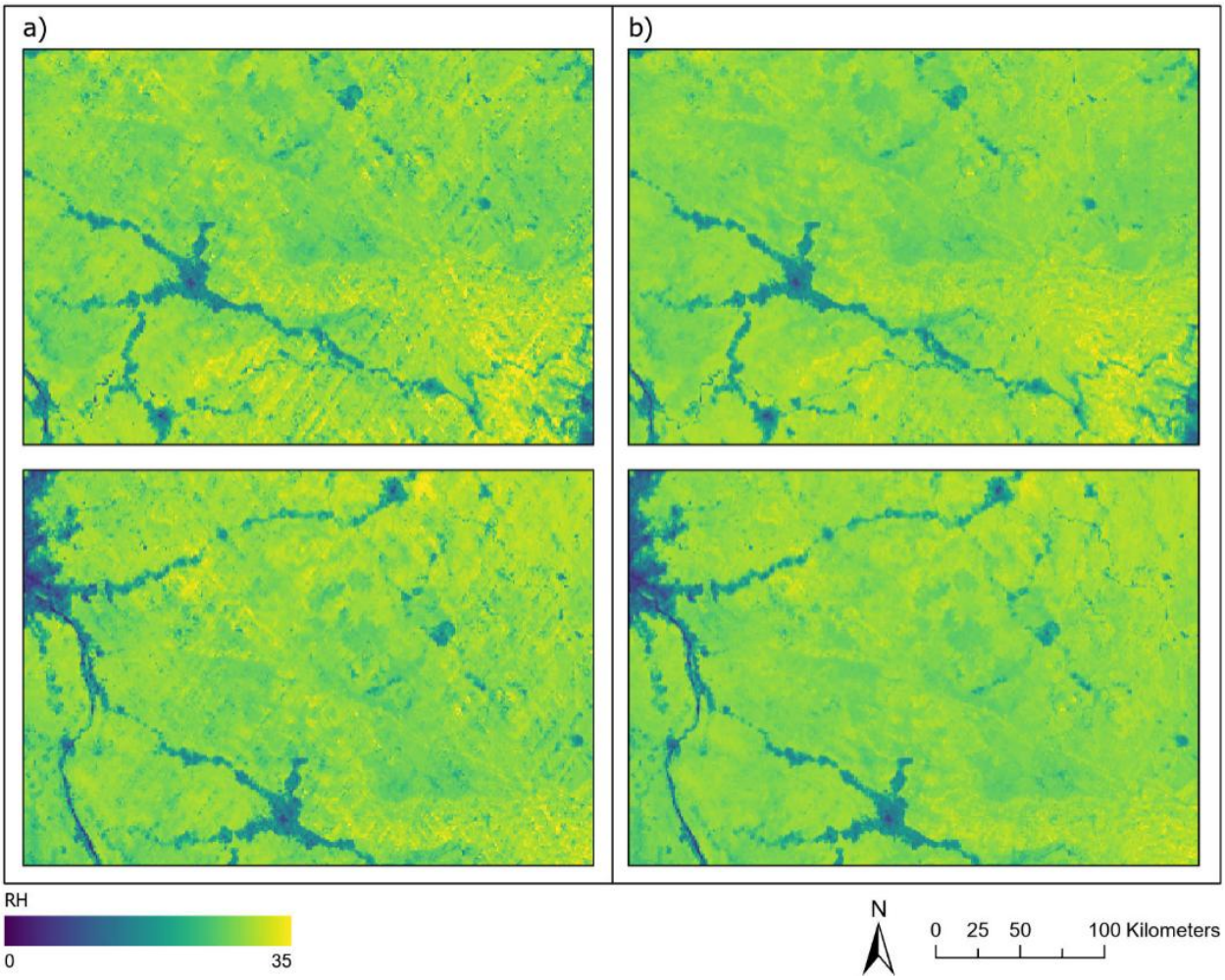


Figure 2.7. Comparison of continuous maps of 1 km relative height (RH) generated using a) random cross-validation and b) spatial cross-validation. RH values were constrained between 0 – 35 m as more than 90% of the target values were within this range.

Discussion

A central question motivating this study was whether differences in predictability among GEDI-derived attributes stem from the characteristics being estimated or the confounded influence of resolution, region, and modeling approach, which vary simultaneously across prior work (e.g., Lang et al., 2022; Potapov et al., 2021; Tolan et al., 2024). By holding the feature space, spatial extent, and modeling framework consistent across RH, FHD, and PAI, we isolate the attribute-level differences in

predictability from these confounding factors. The resulting pattern, in which RH was most predictable, is broadly consistent with expectations grounded in GEDI's sensor design (Dubayah et al., 2020; Tang and Armston, 2019). However, the relative ordering of FHD and PAI has not been established in prior work, which has generally treated these attributes individually rather than comparing them directly under shared conditions. While GEDI-derived RH, FHD, and PAI have occasionally been mapped within the same study (e.g., Burns et al., 2024; Cardenas-Martinez et al., 2025), these efforts have not systematically varied resolution, spatial cross-validation strategy, or noise handling to test whether sensitivity to these analytical choices varies by attribute.

The predictability ranking likely reflects differences in both signal strength and derivation complexity. First, RH's higher predictability may stem in part from its greater variation across the study area. Of the three structural attributes examined, RH showed the highest coefficient of variation (Table S2.6), reflecting a stronger signal available for predictive modeling. Because RH has a relatively direct derivation from the GEDI waveform, this variation more likely reflects meaningful ecological heterogeneity rather than noise. Second, the attributes differ in derivation complexity. Unlike RH, which is calculated relatively directly from the waveform, FHD requires calculation of the vertical plant area distribution and is normalized by PAI. Meanwhile, PAI's derivation presents its own complexities, as it represents total plant area, which requires corrections for factors such as canopy clumping and woody contributions for translation into true leaf area index (Chen et al., 2005; Kalacska et al., 2005; Pisek et al., 2015). The necessary ancillary data for these corrections are not available globally at GEDI's footprint scale (Tang and Armston, 2019), and accounting for these variables remains a source of

uncertainty that varies with environmental conditions, including seasonal variability, vegetation type, and topography (Fang et al., 2014; Garrigues et al., 2008; Richardson et al., 2011; Spadavecchia et al., 2008). To maintain comparability across metrics, we did not incorporate these ancillary corrections, and our analysis represents baseline predictability for the standard GEDI PAI product.

Predictability also depended on how effectively each structural attribute was represented in the available feature space. The SHAP analysis ranked ALOS PALSAR-2 HV backscatter as the most influential predictor across all three structural metrics, which is consistent with evidence that L-band SAR is more sensitive to forest biomass and vertical structure than shorter wavelengths such as C-band (Imhoff, 1995; Ranson and Guoqing Sun, 1994). Meanwhile, the strong performance of the HV channel aligns with prior studies demonstrating that cross-polarized backscatter is more sensitive to volumetric canopy scattering and aboveground biomass than HH polarization, even in tropical forests (Gupta and Sharma, 2022; Yu and Saatchi, 2016). Feature importance patterns nonetheless diverged among metrics. RH depended strongly on Landsat-8 green, red, and blue bands, similar to prior work demonstrating that RGB-based canopy height models, when corrected with GEDI, capture structural variation effectively even without extra spectral or structural inputs (Fischer et al., 2025a; Tolan et al., 2024). For FHD, importance shifted toward red-green-NIR features, indicating partial convergence towards the spectral sensitivities characteristic of leaf area. In contrast, PAI models relied more strongly on Sentinel-1 VV and Copernicus DEM than on optical reflectance despite the central role of red and NIR bands in global leaf area index and PAI retrieval frameworks (Baret et al., 2007; Xiao et al., 2014; Yan et al., 2018). The comparatively

lower importance of optical predictors for GEDI-derived PAI may partially reflect uncertainty in the PAI target itself, reducing the relative contribution of those predictors within the feature space.

We also found that spatial resolution influences predictive accuracy, with consistently higher model performance at 1 km resolution than at 30 m. This is likely due in part to scale-dependent uncertainties, including GEDI footprint geolocation errors, which reduce the effective signal-to-noise ratio at finer resolutions. Although this study uses Version 2 data, which improves positional accuracy relative to Version 1 and more consistently approaches the mission's 10 m geolocation target (Dubayah et al., 2020; Li et al., 2024; Shannon et al., 2024; Tang et al., 2023), residual error on the order of 10 m remains substantial when relating 25 m footprints to 30 m feature pixels. At 30 m resolution, even modest horizontal offsets can shift a footprint across heterogeneous canopy conditions, reducing the effective signal-to-noise ratio of pixel-level training data, whereas aggregation to 1 km attenuated these effects by averaging positional discrepancies and fine-scale structural variability. Consequently, the improved performance across the coarser 1 km resolution models reflects reduced sensitivity to residual geolocation uncertainty. These findings emphasize the importance of considering resolution and positional uncertainty in GEDI-based wall-to-wall mapping and reinforce the need for continued geolocation refinement and expanded calibration-validation efforts, particularly in understudied regions such as the Congo Basin where initiatives such as AfriSAR are critical for strengthening reference data (Fatoyinbo et al., 2021; White et al., 2021).

Interestingly, although invalid observations (i.e., extreme error) comprised a very small fraction of the dataset, their treatment had measurable effects on model performance, albeit with variable improvements across metrics and resolutions. These adjustments were most effective at 1 km, likely because invalid shots were concentrated along entire orbital tracks (Figure 2.3), biasing whole 1 km grid cells rather than isolated footprints. Of the three structural attributes, RH benefited most from these corrections, as the greater variability among its valid observations made the model more sensitive to invalid data. The impact of these corrections was modest but noticeable across models despite removing only ~0.2% of observations via invalid data handling (Figure S2.2). Their consistent influence emphasizes the value of integrating error detection and invalid data handling into GEDI wall-to-wall structural mapping workflows. However, manual delineation alone cannot eliminate all erroneous observations, and while GEDI data flag filtering is commonly applied (Dwiputra et al., 2023; Kashongwe et al., 2023; Li et al., 2023), residual uncertainties may propagate into the resulting analyses and associated data products. Although factors such as cloud cover, solar radiation, and terrain are known to impact GEDI data quality (Adam et al., 2020; Fayad et al., 2021b; Li et al., 2024; Urbazaev et al., 2022), these influences remain challenging to fully accommodate in GEDI workflows due to their complex and context-dependent effects. As a result, a future direction may include the development of statistical or modeling approaches that explicitly account for these confounding factors.

Spatial autocorrelation further influenced model outcomes in ways not fully captured by R^2 and nRMSE alone. Although spatial cross-validation was intended to reduce overfitting by enforcing spatial independence between folds, it yielded lower R^2

and higher nRMSE than random cross-validation when evaluated on the same spatially segmented test set, a pattern also supported by Wilcoxon signed-rank tests. However, these numerical differences masked contrasts in spatial reliability. At 1 km resolution, RH predictions from random cross-validation exhibited structured striping aligned with GEDI orbital tracks, indicating the leakage of location-specific information between training and validation sets (Figure 2.7). Spatial cross-validation reduced this leakage, as supported by the sign test, producing RH maps that better captured ecologically plausible gradients. The reduction in spatial artifacts was only evident for RH at 1 km, as its combination of high variability and spatial autocorrelation accentuated ecological gradients, making track-aligned artifacts more visually detectable. In contrast, FHD and PAI showed fewer visible differences between validation approaches. This apparent lack of differences between predictions may have been supported by Moran's I, which showed that spatial dependence declined rapidly with distance (Figure 2.6), indicating that the 30 km buffer and ~90,000 km² blocks exceeded the autocorrelation range for all structural metrics. The oversized blocks removed large contiguous training regions, likely increasing prediction variance and contributing to the lower R^2 and higher nRMSE under spatial cross-validation. However, block size was set to the median province area for consistency across structural attributes and computational feasibility in the DRC. Future users imputing these GEDI-derived structural attributes for their own applications could align block size and buffer distance with empirical spatial autocorrelation, or adopt strategies such as weighted cross-validation or alternative block assignments (De Bruin et al., 2022; Roberts et al., 2017; Sarafian et al., 2021).

Conclusion

In conclusion, RH consistently exhibited the highest predictive performance among the GEDI-derived structural attributes we evaluated, followed by FHD and PAI, reflecting differences in attribute derivation complexity, ecological variability, and feature-space alignment. This higher predictive accuracy associated with RH was consistent across resolutions and validation strategies, and remained evident whether or not invalid data handling was applied, highlighting that some structural attributes are inherently more learnable, though still sensitive to extreme error. Specifically, RH models had the highest R^2 values, lowest errors, and were the most spatially reliable, indicating that it is the best-suited attribute of the three for mapping using widely available Landsat-8, ALOS PALSAR, Sentinel-1, and Copernicus DEM features. FHD showed moderate predictability with relatively consistent performance across scales, whereas PAI was the most challenging to model, particularly at finer resolutions where limited variability, increased noise, and geolocation uncertainty constrained the model's ability to learn and predict spatial patterns. These findings highlight how attribute properties, methodological choices, and spatial context jointly influence the predictability of GEDI-derived structural attributes, with strong implications for the accuracy and interpretation of GEDI-derived data products.

Supplementary Material

GEDI Data Filtering, Comparison, and Selection Based on ALS Reference Data

To determine the most reliable GEDI relative height (RH) metric for comparison with ALS-derived canopy height models (CHMs), we conducted an exhaustive evaluation of RH values generated by all six GEDI algorithms across three relative height thresholds, RH95, RH98, and RH100. Each RH product was compared against mean and median ALS-based 30 m CHM aggregations using linear regression. We filtered the GEDI data using combinations of quality flag = 1 and sensitivity thresholds (0.95–1.0, 0.98–1.0, and 0.9–1.0), consistent with filtering schemes used in prior GEDI validation studies. For each combination of RH metric, ALS aggregation method, and sensitivity threshold, we calculated the coefficient of determination (R^2), root mean square error (RMSE), and sample size. This comparative analysis revealed that RH 95 values from Algorithm 5 filtered with a sensitivity between 0.9 and 1.0 consistently produced the highest R^2 values and lowest RMSE across both CHM aggregation methods. Therefore, we selected this RH metric and filtering scheme for our main analysis.

Anomalous Data Detection

To filter out anomalous, invalid data from the GEDI dataset, we attempted a statistical approach by calculating z-scores for relative height (RH) metrics—specifically Algorithm 5's RH95, RH98, and RH100—under the assumption that statistical outliers may correspond to low-quality or invalid measurements. These z-scores were computed for each RH metric across the entire dataset, and multiple thresholds (i.e., $|z| > 1, 2, 3$) were evaluated to determine the proportion and distribution of potential outliers.

However, this approach proved ineffective at distinguishing high-quality from low-quality GEDI shots when compared against ALS data. Furthermore, the z-score method discarded a substantial number of shots that were well-aligned with ALS data but were outside the core cluster of data points, as most points fell within a narrow range. Most RH values were concentrated within the 40th to 60th percentiles (11.26–18.05 m), resulting in a narrow distribution. The z-score method characterized shot values outside this range as outliers, omitting a large fraction of the data that was still strongly correlated with the ALS data. Consequently, the method classified many legitimate data points, particularly those in the distribution's tails (e.g., 0–10th and 90–100th percentiles), as outliers. Since 90% of the GEDI data across the entire study region falls below 32.58 m, shots corresponding to less common, but nonetheless valid taller canopies were often flagged erroneously as outliers. Due to these limitations, we ultimately resorted to manually delineating anomalous data by visually identifying areas where extreme and clearly invalid RH values were spatially concentrated.

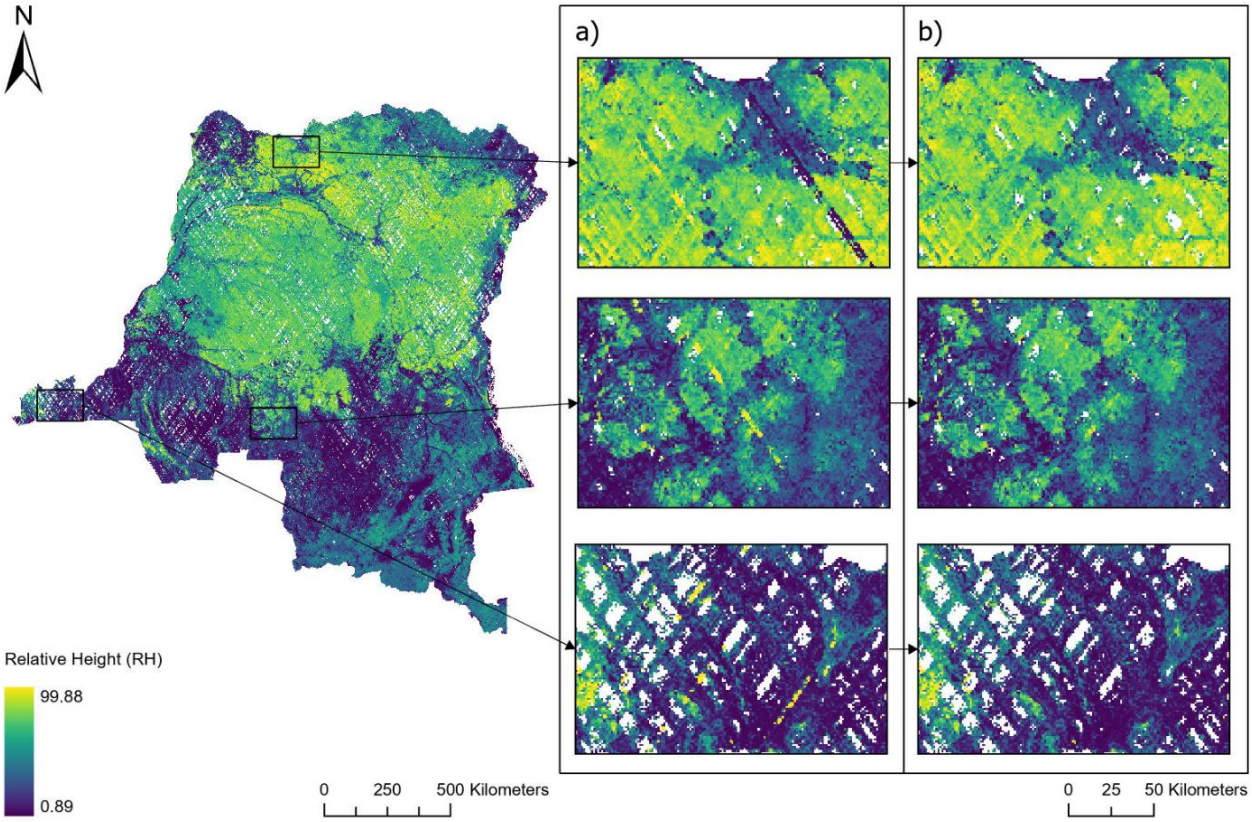


Figure S2.1. a) Locations with examples of anomalous, invalid relative height data. b) The same locations post invalid data handling.

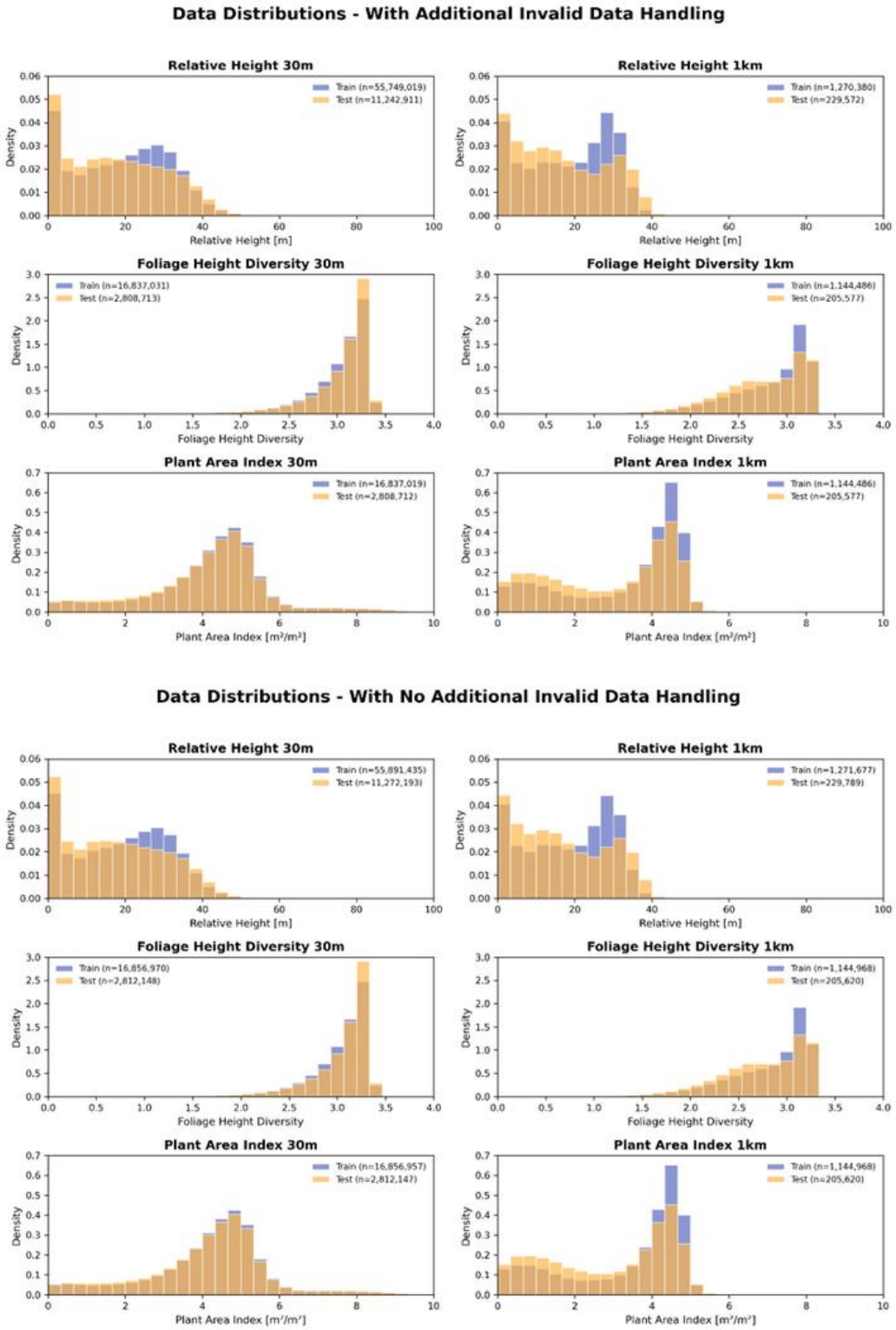


Figure S2.2. Distributions of all datasets across the study resolutions (30 m and 1 km) for the target variables: relative height (RH), foliage height diversity (FHD), and plant area index (PAI). Distributions are shown for both data with and without additional invalid data handling applied.

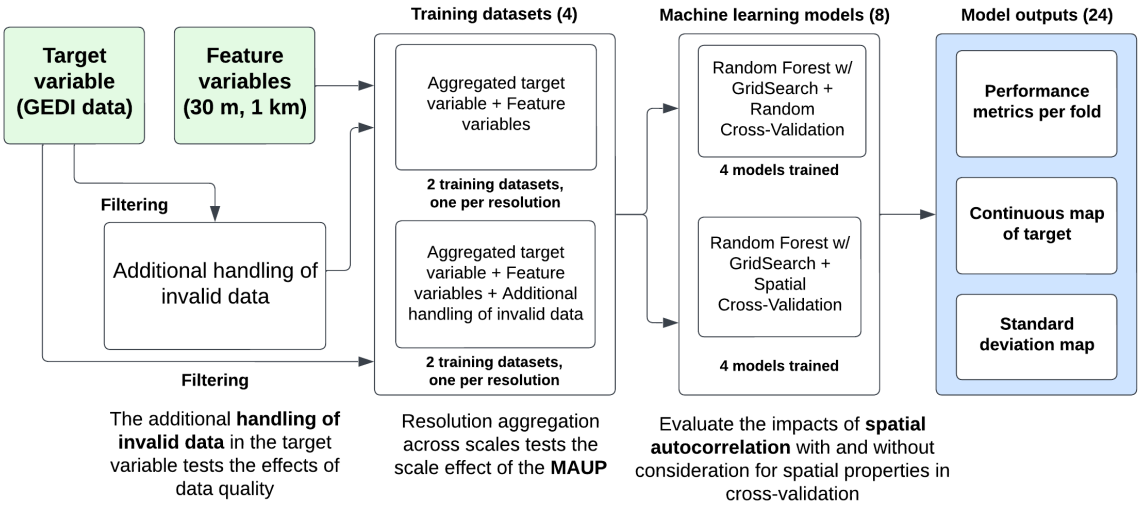


Figure S2.3. Machine learning workflow diagram demonstrating the systematic approach taken to test the impacts of the scale effect of the modifiable areal unit problem (MAUP), sensitivity to anomalous data, and spatial autocorrelation. This workflow illustrates this process for a single structural metric.

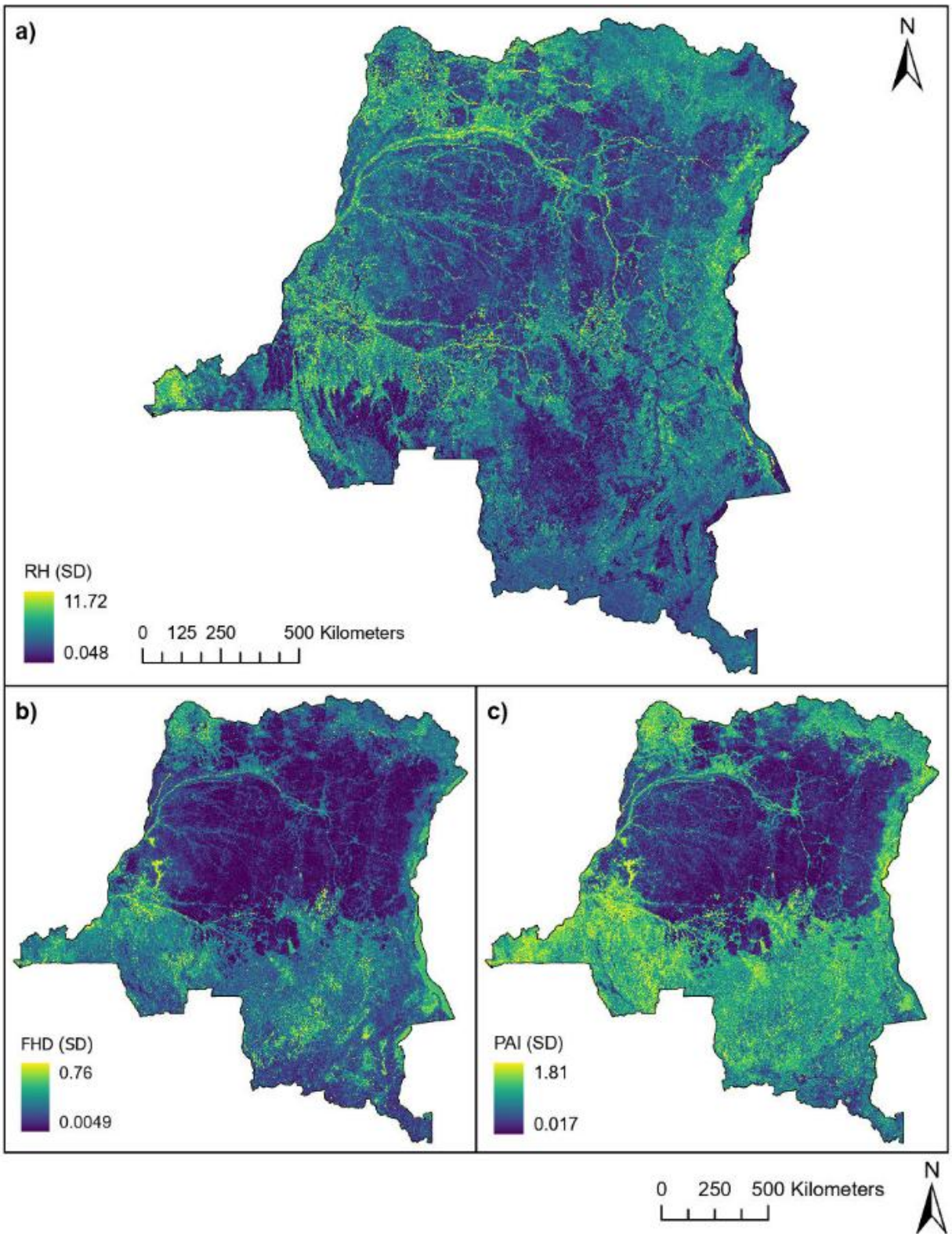


Figure S2.4. Predictive uncertainty maps based on the standard deviation of bootstrapped Random Forest predictions. Each pixel indicates uncertainty for (a) RH, (b) FHD, and (c) PAI.

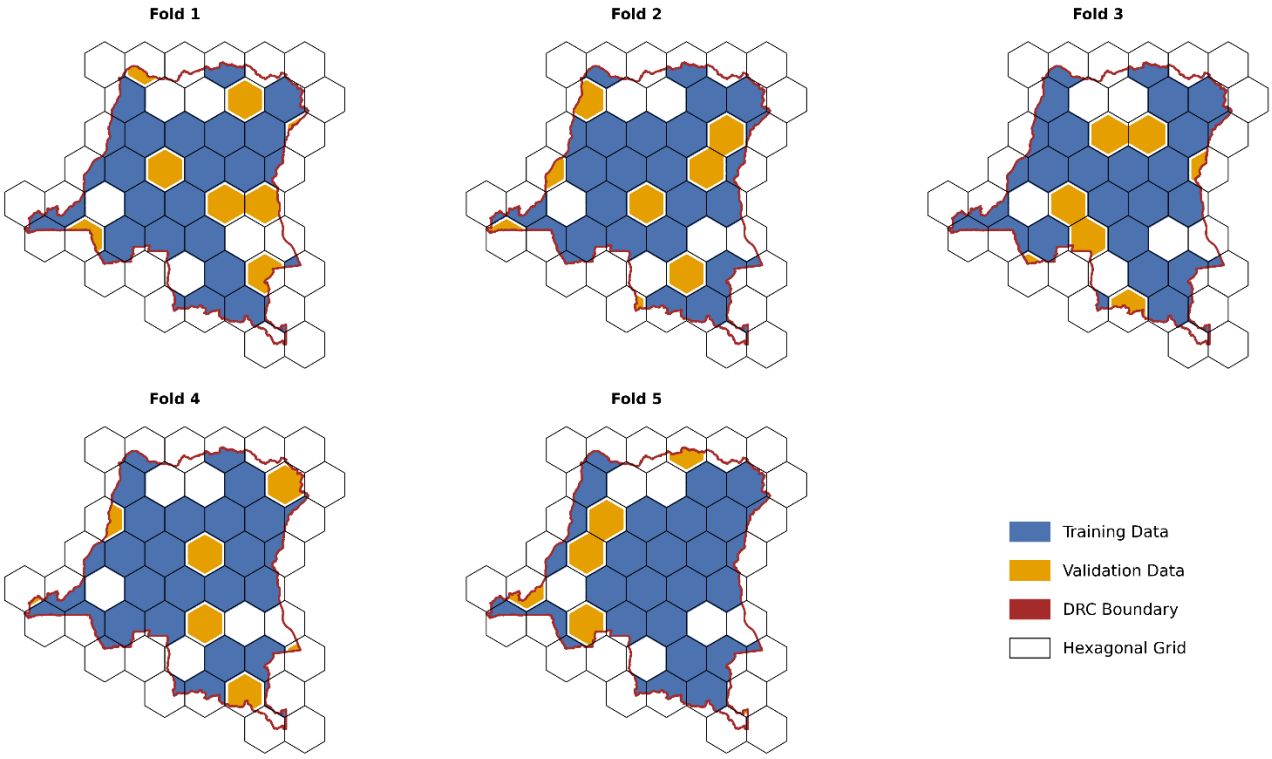


Figure S2.5. Spatial distribution of training and validation samples across five folds used for model evaluation. Each subplot corresponds to one of the five cross-validation folds, which were consistent across all models. Sample assignments were derived using spatial units defined by the hexagonal grid, and the test data were retained as holdout prior to the creation of these folds.

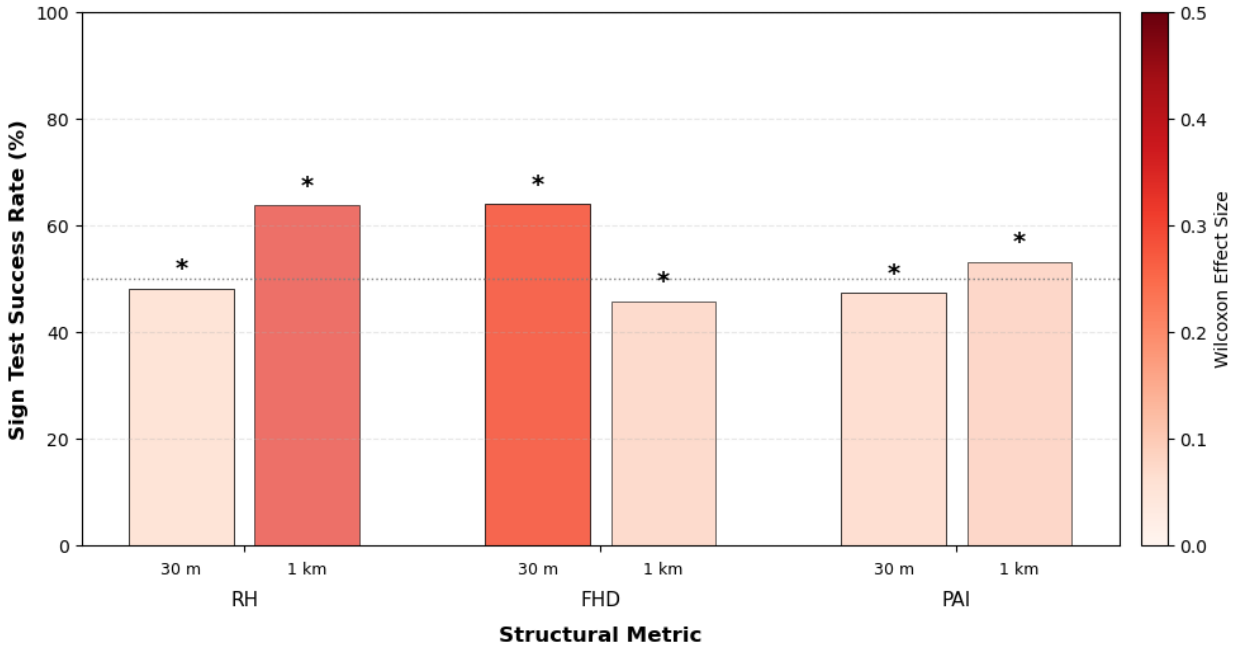


Figure S2.6. Proportion of pairwise comparisons favoring models using spatial cross-validation as assessed by the sign test. All models include additional invalid data handling in this figure. The success rate represents the percentage of cases where spatial cross-validation models outperformed their random cross-validation counterparts. Bars are marked as statistically significant with an asterisk (*) if their sign test p-value < 0.05.

Table S2.1. Performance statistics for all tested combinations of GEDI algorithm flags for relative height (RH) metrics compared against airborne laser scanning derived canopy height models.

Algorithm and Relative Height	CHM Metric	Sensitivity Range	R2	RMSE	Sample Size
Algorithm 5, RH 95	CHM (Mean)	0.9-1	0.40	9.15	705
Algorithm 5, RH 95	CHM (Median)	0.9-1	0.40	9.45	705
Algorithm 5, RH 98	CHM (Mean)	0.9-1	0.39	9.49	705
Algorithm 5, RH 98	CHM (Median)	0.9-1	0.39	9.76	705
Algorithm 5, RH 95	CHM (Mean)	0.98-1	0.38	9.81	174
Algorithm 5, RH 95	CHM (Median)	0.98-1	0.38	10.01	174
Algorithm 5, RH 100	CHM (Mean)	0.9-1	0.37	10.02	705
Algorithm 5, RH 98	CHM (Mean)	0.98-1	0.37	10.69	174
Algorithm 5, RH 100	CHM (Median)	0.9-1	0.37	10.25	705
Algorithm 5, RH 98	CHM (Median)	0.98-1	0.37	10.87	174
Algorithm 5, RH 100	CHM (Mean)	0.98-1	0.36	11.90	174
Algorithm 5, RH 95	CHM (Mean)	0.95-1	0.35	9.25	495
Algorithm 5, RH 95	CHM (Median)	0.95-1	0.35	9.49	495
Algorithm 5, RH 100	CHM (Median)	0.98-1	0.35	12.04	174
Algorithm 5, RH 98	CHM (Mean)	0.95-1	0.34	9.71	495
Algorithm 5, RH 98	CHM (Median)	0.95-1	0.34	9.91	495
Algorithm 2, RH 95	CHM (Median)	0.98-1	0.33	8.95	174
Algorithm 5, RH 100	CHM (Mean)	0.95-1	0.33	10.38	495
Algorithm 2, RH 95	CHM (Mean)	0.98-1	0.32	8.60	174
Algorithm 5, RH 100	CHM (Median)	0.95-1	0.32	10.54	495
Algorithm 2, RH 98	CHM (Median)	0.98-1	0.31	9.17	174
Algorithm 2, RH 98	CHM (Mean)	0.98-1	0.31	8.84	174
Algorithm 2, RH 100	CHM (Mean)	0.98-1	0.30	9.40	174
Algorithm 2, RH 100	CHM (Median)	0.98-1	0.30	9.70	174
Algorithm 2, RH 95	CHM (Median)	0.9-1	0.29	10.61	705
Algorithm 2, RH 95	CHM (Mean)	0.9-1	0.29	10.26	705
Algorithm 2, RH 98	CHM (Median)	0.9-1	0.28	10.54	705
Algorithm 2, RH 98	CHM (Mean)	0.9-1	0.28	10.21	705
Algorithm 2, RH 100	CHM (Median)	0.9-1	0.27	10.62	705
Algorithm 2, RH 100	CHM (Mean)	0.9-1	0.26	10.31	705
Algorithm 2, RH 95	CHM (Median)	0.95-1	0.25	10.45	495

Algorithm and Relative Height	CHM Metric	Sensitivity Range	R2	RMSE	Sample Size
Algorithm 2, RH 95	CHM (Mean)	0.95-1	0.24	10.15	495
Algorithm 2, RH 98	CHM (Median)	0.95-1	0.24	10.40	495
Algorithm 2, RH 98	CHM (Mean)	0.95-1	0.23	10.12	495
Algorithm 6, RH 95	CHM (Median)	0.9-1	0.23	11.42	705
Algorithm 2, RH 100	CHM (Median)	0.95-1	0.22	10.53	495
Algorithm 6, RH 95	CHM (Mean)	0.9-1	0.22	11.06	705
Algorithm 2, RH 100	CHM (Mean)	0.95-1	0.22	10.28	495
Algorithm 6, RH 98	CHM (Median)	0.9-1	0.22	11.35	705
Algorithm 6, RH 98	CHM (Mean)	0.9-1	0.21	11.01	705
Algorithm 6, RH 95	CHM (Median)	0.98-1	0.21	10.07	174
Algorithm 6, RH 95	CHM (Mean)	0.98-1	0.20	9.76	174
Algorithm 6, RH 100	CHM (Median)	0.9-1	0.20	11.42	705
Algorithm 6, RH 98	CHM (Median)	0.98-1	0.20	10.32	174
Algorithm 6, RH 100	CHM (Mean)	0.9-1	0.20	11.10	705
Algorithm 6, RH 98	CHM (Mean)	0.98-1	0.19	10.01	174
Algorithm 6, RH 100	CHM (Median)	0.98-1	0.19	10.84	174
Algorithm 6, RH 100	CHM (Mean)	0.98-1	0.18	10.58	174
Algorithm 6, RH 95	CHM (Median)	0.95-1	0.17	11.49	495
Algorithm 6, RH 95	CHM (Mean)	0.95-1	0.16	11.18	495
Algorithm 6, RH 98	CHM (Median)	0.95-1	0.16	11.44	495
Algorithm 6, RH 98	CHM (Mean)	0.95-1	0.15	11.15	495
Algorithm 6, RH 100	CHM (Median)	0.95-1	0.15	11.56	495
Algorithm 6, RH 100	CHM (Mean)	0.95-1	0.14	11.29	495
Algorithm 3, RH 95	CHM (Median)	0.9-1	0.10	13.76	705
Algorithm 3, RH 95	CHM (Mean)	0.9-1	0.09	13.33	705
Algorithm 3, RH 98	CHM (Median)	0.9-1	0.09	13.52	705
Algorithm 3, RH 98	CHM (Mean)	0.9-1	0.09	13.09	705
Algorithm 1, RH 95	CHM (Median)	0.9-1	0.08	14.38	705
Algorithm 1, RH 95	CHM (Mean)	0.9-1	0.08	13.97	705
Algorithm 4, RH 95	CHM (Median)	0.98-1	0.08	14.62	174
Algorithm 1, RH 95	CHM (Median)	0.98-1	0.08	13.99	174
Algorithm 3, RH 100	CHM (Median)	0.9-1	0.08	13.38	705
Algorithm 1, RH 98	CHM (Median)	0.9-1	0.08	14.08	705
Algorithm 3, RH 100	CHM (Mean)	0.9-1	0.08	12.96	705

Algorithm and Relative Height	CHM Metric	Sensitivity Range	R2	RMSE	Sample Size
Algorithm 1, RH 98	CHM (Mean)	0.9-1	0.08	13.66	705
Algorithm 4, RH 98	CHM (Median)	0.98-1	0.07	14.23	174
Algorithm 1, RH 98	CHM (Median)	0.98-1	0.07	13.48	174
Algorithm 4, RH 100	CHM (Median)	0.98-1	0.07	13.89	174
Algorithm 1, RH 100	CHM (Median)	0.9-1	0.07	13.87	705
Algorithm 1, RH 95	CHM (Mean)	0.98-1	0.07	13.64	174
Algorithm 4, RH 95	CHM (Mean)	0.98-1	0.07	14.28	174
Algorithm 1, RH 100	CHM (Median)	0.98-1	0.07	13.06	174
Algorithm 1, RH 100	CHM (Mean)	0.9-1	0.07	13.46	705
Algorithm 4, RH 95	CHM (Median)	0.9-1	0.07	15.71	705
Algorithm 1, RH 98	CHM (Mean)	0.98-1	0.07	13.13	174
Algorithm 4, RH 95	CHM (Mean)	0.9-1	0.07	15.29	705
Algorithm 4, RH 98	CHM (Mean)	0.98-1	0.06	13.89	174
Algorithm 3, RH 95	CHM (Median)	0.98-1	0.06	13.06	174
Algorithm 4, RH 98	CHM (Median)	0.9-1	0.06	15.50	705
Algorithm 4, RH 100	CHM (Mean)	0.98-1	0.06	13.55	174
Algorithm 1, RH 100	CHM (Mean)	0.98-1	0.06	12.71	174
Algorithm 4, RH 98	CHM (Mean)	0.9-1	0.06	15.07	705
Algorithm 3, RH 98	CHM (Median)	0.98-1	0.06	12.74	174
Algorithm 4, RH 100	CHM (Median)	0.9-1	0.06	15.33	705
Algorithm 3, RH 95	CHM (Median)	0.95-1	0.06	14.12	495
Algorithm 3, RH 95	CHM (Mean)	0.98-1	0.06	12.68	174
Algorithm 4, RH 100	CHM (Mean)	0.9-1	0.06	14.91	705
Algorithm 1, RH 95	CHM (Median)	0.95-1	0.06	14.90	495
Algorithm 3, RH 95	CHM (Mean)	0.95-1	0.05	13.71	495
Algorithm 3, RH 98	CHM (Mean)	0.98-1	0.05	12.36	174
Algorithm 3, RH 100	CHM (Median)	0.98-1	0.05	12.56	174
Algorithm 3, RH 98	CHM (Median)	0.95-1	0.05	13.84	495
Algorithm 1, RH 95	CHM (Mean)	0.95-1	0.05	14.51	495
Algorithm 1, RH 98	CHM (Median)	0.95-1	0.05	14.52	495
Algorithm 3, RH 98	CHM (Mean)	0.95-1	0.05	13.43	495
Algorithm 3, RH 100	CHM (Mean)	0.98-1	0.05	12.19	174
Algorithm 1, RH 98	CHM (Mean)	0.95-1	0.05	14.13	495
Algorithm 4, RH 95	CHM (Median)	0.95-1	0.05	16.17	495

Algorithm and Relative Height	CHM Metric	Sensitivity Range	R2	RMSE	Sample Size
Algorithm 3, RH 100	CHM (Median)	0.95-1	0.05	13.65	495
Algorithm 1, RH 100	CHM (Median)	0.95-1	0.04	14.24	495
Algorithm 3, RH 100	CHM (Mean)	0.95-1	0.04	13.26	495
Algorithm 4, RH 95	CHM (Mean)	0.95-1	0.04	15.76	495
Algorithm 4, RH 98	CHM (Median)	0.95-1	0.04	15.91	495
Algorithm 1, RH 100	CHM (Mean)	0.95-1	0.04	13.86	495
Algorithm 4, RH 98	CHM (Mean)	0.95-1	0.04	15.50	495
Algorithm 4, RH 100	CHM (Median)	0.95-1	0.04	15.71	495
Algorithm 4, RH 100	CHM (Mean)	0.95-1	0.04	15.30	495

Table S2.2. Summary statistics comparing predicted versus observed values on test data for the three structural metrics at two spatial resolutions (1 km and 30 m), using both mean and median aggregation methods.

Structural Metric	Resolution	Statistic	R2	Normalized RMSE	Normalized MAE	Normalized MSE	Normalized ME
FHD	1 km	Mean	0.53	0.11	0.08	0.01	0.01
FHD	30 m	Mean	0.32	0.08	0.06	0.01	0.01
PAI	1 km	Mean	0.50	0.38	0.29	0.15	-0.01
PAI	30 m	Mean	0.11	0.37	0.27	0.14	-0.01
RH	1 km	Mean	0.83	0.28	0.21	0.08	0.04
RH	30 m	Mean	0.61	0.43	0.32	0.19	0.04
FHD	1 km	Median	0.53	0.11	0.08	0.01	0.01
FHD	30 m	Median	0.32	0.08	0.06	0.01	0.01
PAI	1 km	Median	0.50	0.38	0.29	0.15	-0.01
PAI	30 m	Median	0.11	0.37	0.27	0.14	-0.01
RH	1 km	Median	0.83	0.28	0.21	0.08	0.04
RH	30 m	Median	0.61	0.43	0.32	0.19	0.04

Table S2.3. Performance of the optimized random forest models for FHD, PAI, and RH.

Structural Metric	Resolution	Additional Invalid Data Handling?	Spatial cross-validation?	Train R^2	Validation R^2	Test R^2	Train RMSE	Validation RMSE	Test RMSE	Units
FHD	1 km	No	No	0.8949	0.6995	0.5342	0.1361	0.2302	0.2935	-
FHD	1 km	No	Yes	0.8217	0.6335	0.5353	0.1772	0.2507	0.2931	-
FHD	1 km	Yes	No	0.8961	0.7023	0.5335	0.1354	0.2292	0.2937	-
FHD	1 km	Yes	Yes	0.8234	0.6379	0.5342	0.1765	0.2493	0.2934	-
FHD	30 m	No	No	0.4170	0.3407	0.2697	0.2428	0.2582	0.2668	-
FHD	30 m	No	Yes	0.4084	0.2914	0.2697	0.2445	0.2638	0.2668	-
FHD	30 m	Yes	No	0.4175	0.3413	0.2705	0.2428	0.2581	0.2667	-
FHD	30 m	Yes	Yes	0.4201	0.2921	0.2704	0.2421	0.2637	0.2667	-
PAI	1 km	No	No	0.8144	0.6325	0.5024	0.6653	0.9360	1.1190	m^2/m^2
PAI	1 km	No	Yes	0.7622	0.5511	0.5026	0.7522	1.0067	1.1188	m^2/m^2
PAI	1 km	Yes	No	0.8769	0.6342	0.5002	0.5420	0.9344	1.1216	m^2/m^2
PAI	1 km	Yes	Yes	0.7633	0.5535	0.5028	0.7507	1.0046	1.1187	m^2/m^2
PAI	30 m	No	No	0.2140	0.1392	0.1044	1.3784	1.4425	1.5226	m^2/m^2
PAI	30 m	No	Yes	0.2144	0.1082	0.1044	1.3779	1.4589	1.5226	m^2/m^2
PAI	30 m	Yes	No	0.2895	0.1412	0.1058	1.3108	1.4411	1.5217	m^2/m^2
PAI	30 m	Yes	Yes	0.2149	0.1085	0.1049	1.3778	1.4589	1.5225	m^2/m^2
RH	1 km	No	No	0.9359	0.8423	0.8141	2.7648	4.3364	4.8943	m
RH	1 km	No	Yes	0.8912	0.8096	0.8143	3.5978	4.6608	4.8908	m
RH	1 km	Yes	No	0.9434	0.8557	0.8274	2.5814	4.1221	4.7016	m
RH	1 km	Yes	Yes	0.8994	0.8232	0.8274	3.4373	4.4599	4.7019	m
RH	30 m	No	No	0.6479	0.6212	0.5954	7.2745	7.5451	8.0241	m
RH	30 m	No	Yes	0.6495	0.6038	0.5954	7.2531	7.6267	8.0241	m
RH	30 m	Yes	No	0.6568	0.6304	0.6045	7.1347	7.4042	7.9008	m
RH	30 m	Yes	Yes	0.6584	0.6129	0.6045	7.1142	7.4895	7.9008	m

Table S2.4. Results of Wilcoxon signed-rank tests comparing paired models across all structural metrics at 30 m and 1 km resolutions. Models are categorized by cross-validation type ('SAC' for spatial cross-validation and 'No-SAC' for random cross-validation) and by the application of additional invalid data handling ('IDH' vs. 'No-IDH'). Reported values include the differences in normalized RMSE (∆nRMSE) and R^2 (ΔR^2), calculated as the metric of the first model in each pair minus that of the second.

Structural Metric	Resolution	Model 1 SAC-Type	Model 1 IDH-Type	Model 2 SAC-Type	Model 2 IDH-Type	Total Number of Points	∆nRMSE	ΔR^2	Wilcoxon P-Value	Wilcoxon r
FHD	1 km	No-SAC	IDH	No-SAC	No-IDH	20557	0.0008	-0.0068	0.000	-0.10
FHD	1 km	No-SAC	IDH	SAC	IDH	20557	0.0003	-0.0027	0.000	-0.10
FHD	1 km	No-SAC	IDH	SAC	No-IDH	20557	0.0009	-0.0080	0.000	-0.17
FHD	1 km	No-SAC	No-IDH	SAC	IDH	20557	-0.0005	0.0041	0.153	-0.01
FHD	1 km	No-SAC	No-IDH	SAC	No-IDH	20557	0.0001	-0.0013	0.000	-0.06
FHD	1 km	SAC	IDH	SAC	No-IDH	20557	0.0006	-0.0053	0.000	-0.08
PAI	1 km	No-SAC	IDH	No-SAC	No-IDH	20557	0.0032	-0.0076	0.001	-0.02
PAI	1 km	No-SAC	IDH	SAC	IDH	20557	0.0036	-0.0087	0.000	-0.10
PAI	1 km	No-SAC	IDH	SAC	No-IDH	20557	0.0029	-0.0070	0.005	-0.02
PAI	1 km	No-SAC	No-IDH	SAC	IDH	20557	0.0004	-0.0011	0.000	-0.10
PAI	1 km	No-SAC	No-IDH	SAC	No-IDH	20557	-0.0002	0.0006	0.737	0.00
PAI	1 km	SAC	IDH	SAC	No-IDH	20557	-0.0007	0.0017	0.000	-0.11
RH	1 km	No-SAC	IDH	No-SAC	No-IDH	22957	-0.0047	0.0047	0.000	-0.32
RH	1 km	No-SAC	IDH	SAC	IDH	22957	0.0054	-0.0054	0.000	-0.33
RH	1 km	No-SAC	IDH	SAC	No-IDH	22957	0.0036	-0.0036	0.004	-0.02
RH	1 km	No-SAC	No-IDH	SAC	IDH	22957	0.0102	-0.0101	0.000	-0.51
RH	1 km	No-SAC	No-IDH	SAC	No-IDH	22957	0.0083	-0.0083	0.000	-0.34
RH	1 km	SAC	IDH	SAC	No-IDH	22957	-0.0018	0.0018	0.000	-0.34
FHD	30 m	No-SAC	IDH	No-SAC	No-IDH	280871	0.0000	0.0000	0.000	-0.03
FHD	30 m	No-SAC	IDH	SAC	IDH	280871	-0.0134	0.1425	0.000	-0.28
FHD	30 m	No-SAC	IDH	SAC	No-IDH	280871	-0.0133	0.1423	0.000	-0.27
FHD	30 m	No-SAC	No-IDH	SAC	IDH	280871	-0.0134	0.1425	0.000	-0.28
FHD	30 m	No-SAC	No-IDH	SAC	No-IDH	280871	-0.0133	0.1423	0.000	-0.27
FHD	30 m	SAC	IDH	SAC	No-IDH	280871	0.0000	-0.0002	0.000	-0.06
PAI	30 m	No-SAC	IDH	No-SAC	No-IDH	280871	-0.0001	0.0003	0.000	-0.08
PAI	30 m	No-SAC	IDH	SAC	IDH	280871	-0.0001	0.0004	0.000	-0.07

Structural Metric	Resolution	Model 1 SAC-Type	Model 1 IDH-Type	Model 2 SAC-Type	Model 2 IDH-Type	Total Number of Points	ΔnRMSE	ΔR^2	Wilcoxon P-Value	Wilcoxon r
PAI	30 m	No-SAC	IDH	SAC	No-IDH	280871	0.0000	0.0002	0.000	-0.08
PAI	30 m	No-SAC	No-IDH	SAC	IDH	280871	0.0000	0.0001	0.000	-0.01
PAI	30 m	No-SAC	No-IDH	SAC	No-IDH	280871	0.0000	-0.0001	0.037	0.00
PAI	30 m	SAC	IDH	SAC	No-IDH	280871	0.0001	-0.0002	0.001	-0.01
RH	30 m	No-SAC	IDH	No-SAC	No-IDH	1124291	-0.0005	0.0008	0.000	-0.25
RH	30 m	No-SAC	IDH	SAC	IDH	1124291	-0.0101	0.0146	0.000	-0.06
RH	30 m	No-SAC	IDH	SAC	No-IDH	1124291	-0.0103	0.0149	0.000	-0.15
RH	30 m	No-SAC	No-IDH	SAC	IDH	1124291	-0.0096	0.0138	0.012	0.00
RH	30 m	No-SAC	No-IDH	SAC	No-IDH	1124291	-0.0098	0.0141	0.000	-0.10
RH	30 m	SAC	IDH	SAC	No-IDH	1124291	-0.0002	0.0003	0.000	-0.22

Table S2.5. Results of sign tests comparing paired models across all structural metrics at 30 m and 1 km resolutions. Models are categorized by cross-validation type ('SAC' for spatial cross-validation and 'No-SAC' for random cross-validation) and by the application of additional invalid data handling ('IDH' vs. 'No-IDH').

Structural Metric	Resolution	Model 1 SAC-Type	Model 1 IDH-Type	Model 2 SAC-Type	Model 2 IDH-Type	Total Number of Points	Sign P-Value	Sign Test Success Rate – Model 1	Sign Test Success Rate – Model 2
FHD	1 km	No-SAC	IDH	No-SAC	No-IDH	20557	0.000	53.52	46.48
FHD	1 km	No-SAC	IDH	SAC	IDH	20557	0.000	54.25	45.75
FHD	1 km	No-SAC	IDH	SAC	No-IDH	20557	0.000	57.01	42.99
FHD	1 km	No-SAC	No-IDH	SAC	IDH	20557	0.147	50.51	49.49
FHD	1 km	No-SAC	No-IDH	SAC	No-IDH	20557	0.000	52.92	47.08
FHD	1 km	SAC	IDH	SAC	No-IDH	20557	0.000	52.71	47.29
PAI	1 km	No-SAC	IDH	No-SAC	No-IDH	20557	0.035	49.26	50.74
PAI	1 km	No-SAC	IDH	SAC	IDH	20557	0.000	46.94	53.06
PAI	1 km	No-SAC	IDH	SAC	No-IDH	20557	0.220	50.43	49.57
PAI	1 km	No-SAC	No-IDH	SAC	IDH	20557	0.000	46.88	53.12
PAI	1 km	No-SAC	No-IDH	SAC	No-IDH	20557	0.503	50.24	49.76
PAI	1 km	SAC	IDH	SAC	No-IDH	20557	0.000	54.36	45.64
RH	1 km	No-SAC	IDH	No-SAC	No-IDH	22957	5e-324	63.61	36.39
RH	1 km	No-SAC	IDH	SAC	IDH	22957	5e-324	36.32	63.68
RH	1 km	No-SAC	IDH	SAC	No-IDH	22957	0.000	51.84	48.16
RH	1 km	No-SAC	No-IDH	SAC	IDH	22957	5e-324	27.53	72.47
RH	1 km	No-SAC	No-IDH	SAC	No-IDH	22957	5e-324	36.30	63.70
RH	1 km	SAC	IDH	SAC	No-IDH	22957	5e-324	65.39	34.61
FHD	30 m	No-SAC	IDH	No-SAC	No-IDH	280871	0.000	50.96	49.04
FHD	30 m	No-SAC	IDH	SAC	IDH	280871	1.5e-323	36.03	63.97
FHD	30 m	No-SAC	IDH	SAC	No-IDH	280871	1.5e-323	36.54	63.46
FHD	30 m	No-SAC	No-IDH	SAC	IDH	280871	1.5e-323	35.89	64.11
FHD	30 m	No-SAC	No-IDH	SAC	No-IDH	280871	1.5e-323	36.34	63.66
FHD	30 m	SAC	IDH	SAC	No-IDH	280871	0.000	52.44	47.56

Structural Metric	Resolution	Model 1 SAC-Type	Model 1 IDH-Type	Model 2 SAC-Type	Model 2 IDH-Type	Total Number of Points	Sign P-Value	Sign Test Success Rate – Model 1	Sign Test Success Rate – Model 2
PAI	30 m	No-SAC	IDH	No-SAC	No-IDH	280871	0.000	53.06	46.94
PAI	30 m	No-SAC	IDH	SAC	IDH	280871	0.000	52.68	47.32
PAI	30 m	No-SAC	IDH	SAC	No-IDH	280871	0.000	52.89	47.11
PAI	30 m	No-SAC	No-IDH	SAC	IDH	280871	0.006	49.74	50.26
PAI	30 m	No-SAC	No-IDH	SAC	No-IDH	280871	0.426	49.92	50.08
PAI	30 m	SAC	IDH	SAC	No-IDH	280871	0.007	50.26	49.74
RH	30 m	No-SAC	IDH	No-SAC	No-IDH	1124291	2.5e-323	62.00	38.00
RH	30 m	No-SAC	IDH	SAC	IDH	1124291	2.5e-323	51.90	48.11
RH	30 m	No-SAC	IDH	SAC	No-IDH	1124291	2.5e-323	56.95	43.05
RH	30 m	No-SAC	No-IDH	SAC	IDH	1124291	2.5e-323	47.63	52.37
RH	30 m	No-SAC	No-IDH	SAC	No-IDH	1124291	2.5e-323	53.27	46.73
RH	30 m	SAC	IDH	SAC	No-IDH	1124291	2.5e-323	60.70	39.30

Table S2.6. Coefficient of variation and related descriptive statistics for each dataset.

Structural Metric	Resolution	Additional Invalid Data Handling?	Split	Mean	Median	Standard Deviation	Coefficient of Variation
FHD	1 km	No	Train + Val	2.83	2.98	0.42	0.15
FHD	1 km	No	Test	2.76	2.84	0.43	0.16
FHD	1 km	Yes	Train + Val	2.82	2.98	0.42	0.15
FHD	1 km	Yes	Test	2.76	2.84	0.43	0.16
FHD	30 m	No	Train + Val	3.03	3.12	0.32	0.11
FHD	30 m	No	Test	3.05	3.16	0.31	0.10
FHD	30 m	Yes	Train + Val	3.02	3.12	0.32	0.11
FHD	30 m	Yes	Test	3.05	3.16	0.31	0.10
PAI	1 km	No	Train + Val	3.33	4.05	1.54	0.46
PAI	1 km	No	Test	2.92	3.39	1.59	0.54
PAI	1 km	Yes	Train + Val	3.33	4.05	1.54	0.46
PAI	1 km	Yes	Test	2.92	3.39	1.59	0.54
PAI	30 m	No	Train + Val	4.18	4.43	1.55	0.37
PAI	30 m	No	Test	4.12	4.38	1.61	0.39
PAI	30 m	Yes	Train + Val	4.18	4.43	1.56	0.37
PAI	30 m	Yes	Test	4.12	4.38	1.61	0.39
RH	1 km	No	Train + Val	18.66	19.97	10.92	0.59
RH	1 km	No	Test	16.85	15.21	11.35	0.67
RH	1 km	Yes	Train + Val	18.60	19.92	10.85	0.58
RH	1 km	Yes	Test	16.87	15.24	11.32	0.67
RH	30 m	No	Train + Val	19.58	20.31	12.26	0.63
RH	30 m	No	Test	18.07	16.99	12.62	0.70
RH	30 m	Yes	Train + Val	19.53	20.28	12.18	0.62
RH	30 m	Yes	Test	18.07	17.01	12.56	0.70

Table S2.7. Mean SHAP values averaged across all model configurations for RH, indicating each feature's contribution to the prediction.

Target	Feature	Mean SHAP Value
RH	ALOS HV	5.89
RH	L8 B3	2.05
RH	L8 B4	1.34
RH	L8 B2	0.71
RH	COP DEM	0.69
RH	COP DEM Slope	0.60
RH	S1 VV	0.48
RH	L8 NIRv	0.20
RH	L8 B7	0.17
RH	L8 B6	0.16
RH	ALOS HH	0.16
RH	L8 B5	0.16
RH	S1 VH	0.11
RH	COP DEM Aspect	0.03

Table S2.8. Mean SHAP values averaged across all model configurations for FHD, indicating each feature's contribution to the prediction.

Target	Feature	Mean SHAP Value
FHD	ALOS HV	0.11
FHD	L8 B3	0.05
FHD	COP DEM	0.03
FHD	L8 B4	0.03
FHD	L8 B5	0.03
FHD	L8 B2	0.02
FHD	S1 VV	0.02
FHD	COP DEM Slope	0.01
FHD	L8 B7	0.01
FHD	S1 VH	0.01
FHD	L8 B6	0.01
FHD	ALOS HH	0.01
FHD	L8 NIRv	0.01
FHD	COP DEM Aspect	0.00

Table S2.9. Mean SHAP values averaged across all model configurations for PAI, indicating each feature's contribution to the prediction.

Target	Feature	Mean SHAP Value
PAI	ALOS HV	0.34
PAI	S1 VV	0.18
PAI	COP DEM	0.18
PAI	L8 B3	0.16
PAI	L8 B7	0.10
PAI	L8 B5	0.08
PAI	L8 B2	0.07
PAI	L8 B4	0.04
PAI	S1 VH	0.04
PAI	L8 NIRv	0.04
PAI	ALOS HH	0.03
PAI	COP DEM Slope	0.02
PAI	L8 B6	0.02
PAI	COP DEM Aspect	0.01

Chapter 3: Characterizing and correcting systematic bias in canopy height models across tropical forests

Abstract

Canopy height is a primary predictor of aboveground biomass, and global products now map it at meter scale across the tropics. These products are trained on sparse reference data, and independent evaluations show their errors are large and systematically biased. Because such errors do not cancel when maps are aggregated, they propagate into regional carbon estimates. Whether that error is correctable beyond the calibration domain depends on how much of the error structure is shared geographically across forests, which residual comparisons alone cannot establish. To address this, we characterized the error structure of one such product and evaluated its geographic transferability in the Congo Basin, Amazon, and Borneo, using an independent tropical airborne laser scanning dataset from the Global Canopy Atlas. Before correction, the magnitude of mean error (ME) reached 58-75% of mean absolute error (MAE) in all three regions, indicating predominantly systematic error. We trained a modified U-Net on Congo Basin data alone to predict the bias field, then applied it to the other regions without retraining. Correction reduced ME from -4.09 to -0.88 m (Congo Basin), -3.68 to -0.90 m (Amazon), and -6.68 to -3.54 m (Borneo), and lowered MAE by 0.7-1.1 m. To evaluate the approach, we compared it with two simpler corrections, a constant mean offset and a linear regression on canopy height and slope, which brought ME closer to zero but reduced MAE less than the U-Net in every region, suggesting that height and slope capture the average bias but not its pixel-to-pixel variation. Correction reduced MAE where canopy height exceeded 16-19 m, depending

on region, and increased it in shorter vegetation. This pattern holds at nearly every slope bin, even within the training region. Much of this product's error is therefore shared across structurally distinct tropical forests, and correctable well beyond the region where reference data exist.

Introduction

Tropical forests cover only 7-10% of the global land area but account for nearly one-third of the planet's total terrestrial metabolic activity, thus storing a disproportionately large share of aboveground biomass (Lewis et al., 2009; Malhi, 2012; Pan et al., 2011). Yet within this outsized carbon reservoir, biomass is unevenly distributed at fine spatial scales, varying considerably across short distances even within the same forest and forest type (Chave et al., 2003; Culmsee et al., 2010; Kearsley et al., 2013). While field inventories and airborne laser scanning (ALS) can capture such variation with high fidelity, the logistical and financial constraints of deploying these methods continuously across the tropics restrict pantropical coverage of the forest structure that underpins variation in aboveground biomass (Asner et al., 2014; Ometto et al., 2023; Xu et al., 2017). Capturing this variation at a pantropical scale therefore requires methods that can resolve biomass as a continuous spatial field at high spatial resolutions.

One way to bridge fine-scale structural variation with the need for pantropical coverage is to map forest attributes that are both ecologically meaningful and remotely retrievable. Among these, canopy height stands out as a primary predictor in allometric estimation (Banin et al., 2012a; Feldpausch et al., 2011; Hunter et al., 2013), and its importance as a structural intermediary has motivated the use of LiDAR-derived canopy

height to supervise machine learning models, which are applied to spaceborne imagery for continuous mapping at broad scales (Lang et al., 2022; Potapov et al., 2021; Schwartz et al., 2024a; Tolan et al., 2024). Although applied globally, these training data are unlikely to adequately represent the structural diversity of tropical forests, where canopy architecture varies considerably across regions, reflecting differences in topography, disturbance histories, dominant allometric relationships, and species diversity (Banin et al., 2012b; Corlett and Primack, 2006; S. Liu et al., 2025; Loubota Panzou et al., 2021; Sullivan et al., 2017). Because these models learn how imagery relates to canopy height from a limited set of forests, that relationship may not hold in forests with different crown sizes, canopy layering, or height allometry. Consistent with this, regional evaluations of these global canopy height products report large errors when applied to forests unlike those represented in their training data, and those errors are biased rather than merely noisy (Moudrý et al., 2024a; Wagner et al., 2026).

Several components of this error are already documented, as both the LiDAR-derived height targets and the spaceborne imagery used as model inputs carry known systematic error. Geolocation uncertainty, acquisition angle differences, and temporal mismatch between ALS reference data and spaceborne signals introduce noise into the training relationship (Réjou-Méchain et al., 2019). Terrain and illumination geometry also distort the radiometric properties of a scene (Chen et al., 2014; Wang et al., 2024), while vertical error in the digital terrain model (DTM) underlying ALS-derived height propagates directly into the height estimate (Hyyppä et al., 2008; Tinkham et al., 2012). A further well-characterized artifact is the tendency of LiDAR-supervised canopy height models (CHM) to underestimate the tallest trees and overestimate the shortest, arising

from spatial averaging in coarse reference data that skews the training sample toward the middle of the height distribution (Dong et al., 2025; A. Liu et al., 2025; Moudrý et al., 2024a). Because these errors are directionally consistent, they do not cancel when predictions are aggregated, and even a small, uncorrected offset accumulates linearly across predictions, producing large error in aggregate estimates despite low pixel-level error (Igel and Oehmcke, 2023). The systematic component should therefore be isolated and corrected before these products are used for regional estimates, including biomass totals.

A bias field separates the systematic component of these known artifacts from the fine-scale, unmodeled error component. Rather than modeling the residuals between predicted and reference canopy heights, the low-frequency component of these residuals can be isolated as a spatial bias field, a continuous surface describing systematic departures between predictions and observations while suppressing local, high-frequency variation. This field is obtained by spatially aggregating and smoothing the residuals before model training, so that the low-frequency component becomes the modeling target while high-frequency error is left unmodeled (Habib et al., 2014; Juntu et al., 2005; Maraun, 2013). Despite the structural complexity that varies among tropical forests, the systematic causes of error described above are not specific to any single region, and may produce a comparable error pattern wherever a canopy height product is deployed. However, the magnitude of that error may not be constant across regions, since domain shift among structurally distinct tropical forests can alter how strongly each source of error affects height estimates from one forest to the next (e.g., from montane forests to lowland tropical forests, or between compositionally and structurally

distinct lowland tropical forests). Unexpected error propagation has direct consequences for downstream use of these products, including estimates of tropical forest carbon stocks and emissions that underpin carbon-market projects and monitoring, reporting, and verification.

In this study, we characterize the error structure of a globally deployed CHM across structurally distinct tropical forests in the Amazon, Congo Basin, and Borneo, asking what fraction of the data product's error is a consistent directional offset, how that systematic component varies with average canopy height and slope, and how much of that error structure is shared across forests. We predict the bias field rather than the raw residual because it represents the systematic error that does not cancel upon aggregation and drives error in landscape- and regional-scale estimates, even where pixel-level error is small. We trained the correction in the Congo Basin because its canopy heights are intermediate among the three regions (Banin et al., 2012a; S. Liu et al., 2025), so applying the model to the Amazon and Borneo tests transfer toward both shorter and taller canopies rather than in a single direction away from one extreme. The 1 m canopy height model product by Tolan et al. (2024), hereafter referred to as the evaluated CHM (H_{eval}), serves as the test case because of its high resolution and because it was trained on ALS data from the United States, then corrected using globally available GEDI data between 51° N and 51° S. None of the three tropical forests evaluated here is therefore closer to the product's training data than the others, so differences in how well our correction transfers among them should reflect structural differences between the forests.

We trained a modified U-Net on Congo Basin data to predict a spatial bias field derived from the difference between H_{eval} and the CHM from the Global Canopy Atlas (GCA), an ALS-derived dataset compiled across multiple forest regions (Fischer et al., 2025b), hereafter H_{GCA}. We then compared the modified U-Net's bias field predictions with two baseline models: a constant mean offset and a linear regression, fit on the same in-domain (ID) Congo Basin data. We evaluated all three corrections on held-out Congo Basin data and, without retraining, in the out-of-domain (OOD) Amazon and Borneo (Figure 3.1). We then identified the canopy heights and slopes at which correction increased rather than reduced error. Together, these results show how consistently a product's error structure generalizes across the tropics and whether that generalization can be expressed as a function of available covariates, which bears directly on downstream applications like carbon stock estimation.

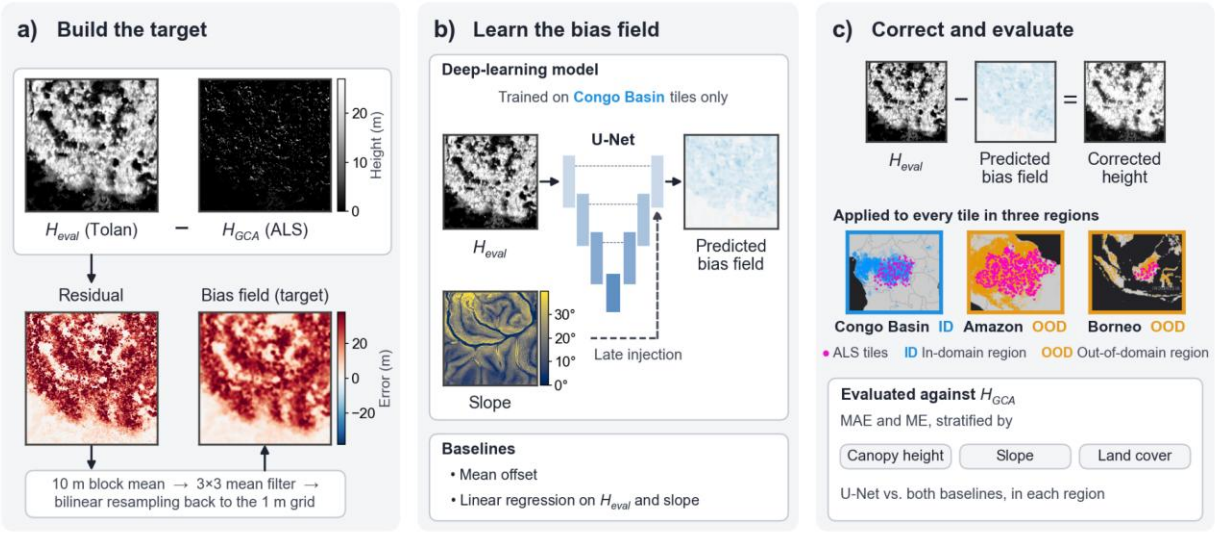


Figure 3.1. Bias field correction and transfer evaluation workflow. a) The residual between the evaluated canopy height model (H_{eval}) and Global Canopy Atlas airborne laser scanning (ALS) heights (H_{GCA}) was smoothed to form the bias field used as the training target. b) A U-Net was trained on Congo Basin tiles to predict this field from H_{eval} and slope. We fit two baselines, a mean offset and a linear regression, to the same data. c) Each model's predicted bias field was subtracted from H_{eval} to produce corrected height maps across both the held-out in-domain (ID) Congo Basin and out-of-domain (OOD) Amazon and Borneo regions without fine-tuning. The result was evaluated against H_{GCA} using mean absolute error (MAE) and mean error (ME). Magenta points mark ALS tile acquisitions.

Data

CHM and DTM data from the GCA dataset served as the base reference for ground truth calculations and slope product derivation (Fischer et al., 2025b). These data were sampled pantropically across the Congo Basin, the Amazon, and Borneo, with acquisition dates ranging from 2014 to 2018 (Figure 3.2). The CHM data were generated using a locally adaptive variant of the spikefree algorithm (Fischer et al., 2024; Khosravipour et al., 2016), ensuring methodological consistency across sites and mitigating variability introduced by different algorithms. The DTMs were derived using the standard ground classification algorithm in LAStools but refined on steep slopes (≥40 degrees) (Fischer et al., 2025b). Because some areas were captured through

repeat or overlapping LiDAR acquisitions, we divided the acquisition footprints into tiles to produce a single, non-overlapping spatial reference shapefile for both the CHM and DTM. We accessed canopy height data from Tolan et al. (2024) using Google Earth Engine, clipped at their native resolution (~1 m) to the GCA footprint shapefile. To represent the variability in pantropical vegetation, we filtered data with the 2019 version of the Copernicus Global Land Service land cover map (Buchhorn et al., 2020). This dataset distinguishes open and closed canopy forest types with deciduous broadleaf, evergreen broadleaf, and unknown subcategories, while non-forested classes include shrubs, herbaceous vegetation, wetlands, and cropland. We excluded pixels in land cover classes with no meaningful vegetation structure, such as open sea, permanent water bodies, and urban areas.

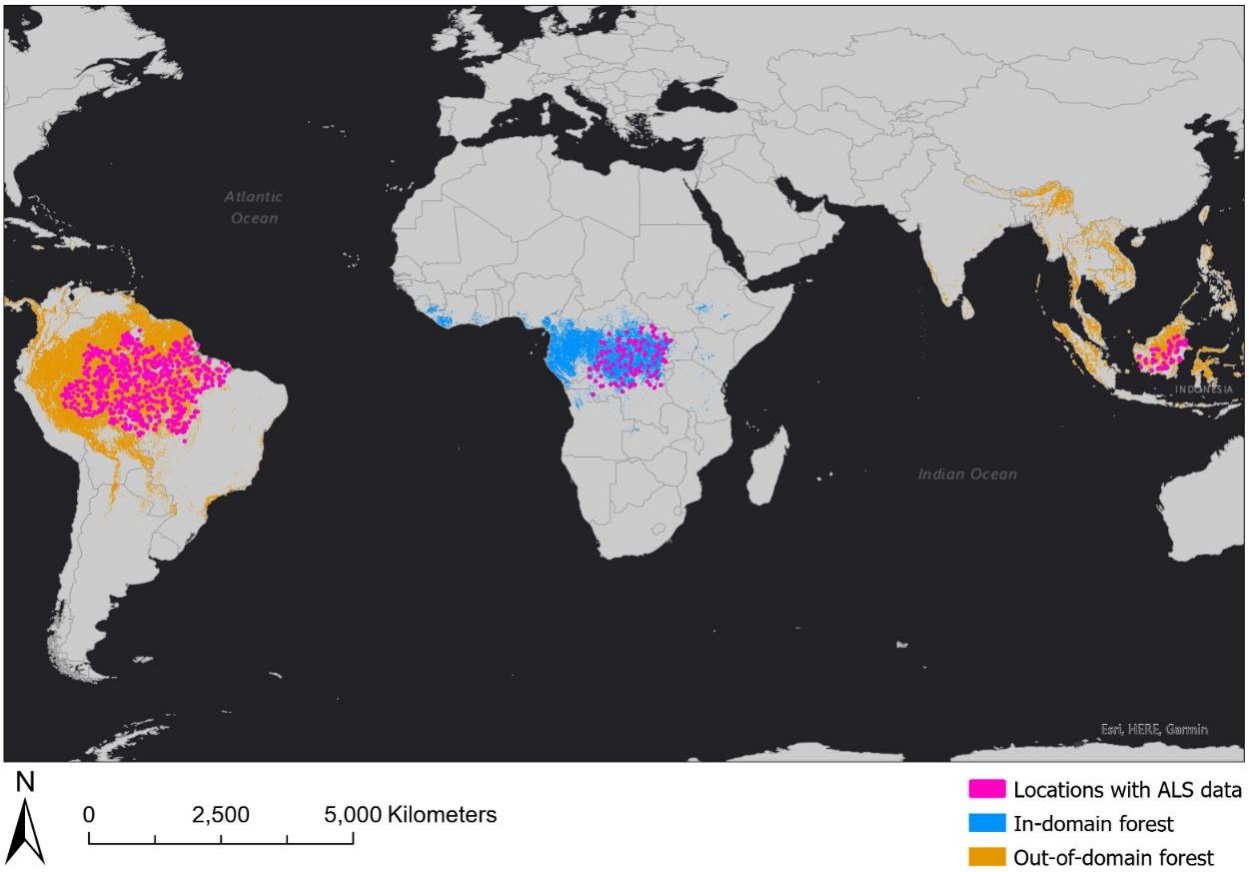


Figure 3.2. Map of the pantropical study domain, showing in-domain (Congo Basin) and out-of-domain (Amazon and Borneo) forest extents. Magenta points mark the airborne laser scanning (ALS) acquisition footprints that make up the Global Canopy Atlas (GCA) reference dataset used for evaluation.

Methods

Data pre-processing

Prior to analysis, we co-registered H_{GCA} and the GCA DTMs to the H_{eval} grid to ensure geometric consistency between datasets. Although both products have a native resolution of 1 m, their raster origins differ slightly due to independent tiling conventions. The GCA is spatially limited to discrete ALS footprints across the pantropics and was therefore co-registered to the H_{eval} grid to ensure compatibility with the broader dataset.

Where multiple ALS acquisitions contributed to the same pixel within a spatial reference footprint, we summarized the CHM and DTM by computing their per-pixel

median. We then derived slope from the median DTMs in degrees using the Horn (1981) algorithm. Because both the residual target and the slope conditioning variable came from GCA products, we also evaluated their correlation using Pearson's r. H_{GCA} and GCA-derived slope were only weakly correlated across Congo Basin pixels (Pearson's r = 0.017), indicating little linear association between canopy height and slope.

Calculating residuals

For each region, we computed residuals as the pixelwise difference between H_{eval} and H_{GCA} at 1 m resolution. For a pixel at row-column position (*i*, *j*) on this grid, we define the residual R_{pre} as

$$R_{\mathrm{pre}}(i,j) = H_{\mathrm{eval}}(i,j) - H_{\mathrm{GCA}}(i,j) \quad (1)$$

so that negative values indicate underestimation by H_{eval}. To reduce the influence of fine-scale variation while preserving spatially coherent bias structure, we first aggregated residuals to 10 m resolution by taking the mean across non-missing pixels within each aggregation window, giving a 10 m residual raster $\bar{R}_{pre}$. We chose this scale to account for the potential spatial and temporal mismatch between ALS and satellite-derived canopy height products, and to match the 10 m geolocation target of the GEDI L2A Version 2 shots used in the post-processing correction step of H_{eval} (Dubayah et al., 2020; Li et al., 2024; Shannon et al., 2024; Tang et al., 2023). The aggregated raster was then smoothed using a 3×3 mean focal kernel,

$$\tilde{R}_{\mathrm{pre}}(u,v) = \frac{1}{|N(u,v)|}\sum_{(u\prime,v\prime)\in N(u,v)} \overline{R}_{\mathrm{pre}}(u',v') \quad (2)$$

where (*u*, *v*) denote the row and column indices of a cell on the 10 m aggregated grid and *N(u, v)* is the set of cells with valid data in the 3×3 window centered on (*u, v*). We then resampled the smoothed raster $\tilde{R}_{pre}$ back to the original 1 m grid via bilinear interpolation to produce a spatial bias field, *B(i, j)*, representing the low-frequency component of the residual surface, which we used as the training target.

Dataset creation

Within the Congo Basin, we identified the spatial overlap among H_{eval}, GCA-derived slope, and residual target layers, and retained only the tiles falling within this common extent. We then constructed a joint validity mask by requiring each pixel across all layers to be free of missing or invalid data and, for H_{eval} specifically, to fall within a range of 0-100 m. Because the mask was the intersection of all per-layer masks, any pixel excluded on the basis of canopy height was also excluded from slope and all other variables. This joint masking approach ensures that statistics and model inputs were computed on a consistent set of physically plausible pixels across all variables. From each tile, non-overlapping 64×64 pixel patches were extracted and retained only if at least 95% of pixels passed the joint validity mask. We computed a representative canopy height for each tile as the median of its patch-level mean H_{eval} heights, and assigned tiles to one of four bins defined by quantiles of this value. We split tiles into train, validation, and test splits in nominal proportions of 70%, 15%, and 15%, respectively, within each bin, so all three shared a similar canopy height distribution. We

used this stratification only to construct the splits, whereas patches were sampled uniformly at random during training to preserve the height distribution of the training set. This procedure yielded 110 tiles and 361,882 patches in total, distributed as training: 245,172; validation: 51,855; and testing: 64,855.

Modeling approach

Baseline models

Two baseline models were first developed to test whether the U-Net captures error structure beyond what a simple, closed-form function of canopy height and slope would predict: a mean baseline and a pixel-wise linear regression baseline. The mean baseline was calculated as the mean of the bias field target across all valid training set pixels, yielding a single constant value,

$$\hat{B}_{\text{mean}} = \frac{1}{N} \sum_{(i,j)\in \text{train}} B(i,j) \tag{3}$$

where $\hat{B}_{mean}$ is the mean baseline's predicted bias field, B(*i, j*) is the bias field target at the pixel in row *i* and column *j* of the 1 m grid, and train is the set of *N* valid pixels in the training split. The linear regression baseline was fit via ordinary least squares, regressing the bias field target on H_{eval} and slope across the same training set pixels,

$$\hat{B}_{\text{lin}}(i,j) = \beta_0 + \beta_1 H_{\text{eval}}(i,j) + \beta_2 S(i,j) \tag{4}$$

where β_0, β_1 and β_2 are the ordinary least squares coefficients estimated over the same training pixels and *S* denotes slope. H_{eval}, H_{GCA}, *B* and all predicted bias fields are in

meters, while S is in degrees. $\hat{B}_{mean}$ is therefore a single number applied identically to every pixel, while $\hat{B}_{lin}(i, j)$ takes a distinct value at each pixel.

Bias field correction model

The bias field correction model was implemented as a modified U-Net trained to predict the low-frequency component of the difference between H_{eval} and H_{GCA} (Ronneberger et al., 2015). Such architectures are used widely for dense prediction, where the output must be produced at input resolution while drawing on spatial context beyond the individual pixel (Isensee et al., 2021; Siddique et al., 2021). Once trained, the model was applied to new tiles to predict their bias field, and this predicted bias field was subtracted from the input H_{eval} to generate a bias field corrected canopy height estimate,

$$H_{\mathrm{corr}}(i,j) = H_{\mathrm{eval}}(i,j) - \hat{B}(i,j) \tag{5}$$

where $\hat{B}$ denotes the predicted bias field of whichever method is being evaluated ($\hat{B}_{mean}$, $\hat{B}_{lin}$, or $\hat{B}_{U\text{-}Net}$ for the U-Net). The primary input to the network was H_{eval}, processed by a three-stage U-Net (Figure 3.3; full architectural specification in Supplementary Text). Slope was incorporated as a conditioning signal injected late in the decoder rather than as a standard input channel. Because slope was derived from the high-quality GCA DTM, it was expected to be a strong, low-noise predictor of canopy height bias. Late injection allowed slope information to contribute to the final correction while encouraging the network to learn the main feature representation from the evaluated canopy height model (H_{eval}). This design was motivated by evidence that multi-modal networks tend to rely disproportionately on whichever input is faster or easier to learn from, underutilizing

other inputs as a result (Wu et al., 2022), suggesting that a strong, low-noise predictor like slope could otherwise dominate learning at the expense of the more error-prone canopy height input if introduced without care. In preliminary experiments with a simpler architecture, introducing slope as an input channel led the network to overfit to the slope signal, motivating the late-injection design adopted here. To quantify the contribution of this conditioning signal, we carried out an ablation study in which an otherwise identical network was trained without slope injection, holding all hyperparameters at the values tuned for the primary model and evaluated on the held-out ID test set. Normalization to zero mean and unit variance was applied to improve optimization stability and convergence during network training (LeCun et al., 2012). Means and standard deviations were computed from the training set and applied unchanged to validation and test data to maintain a consistent input transformation across all model evaluations. The model was trained with L1 loss on a single Nvidia P4 GPU, with training taking approximately three days.

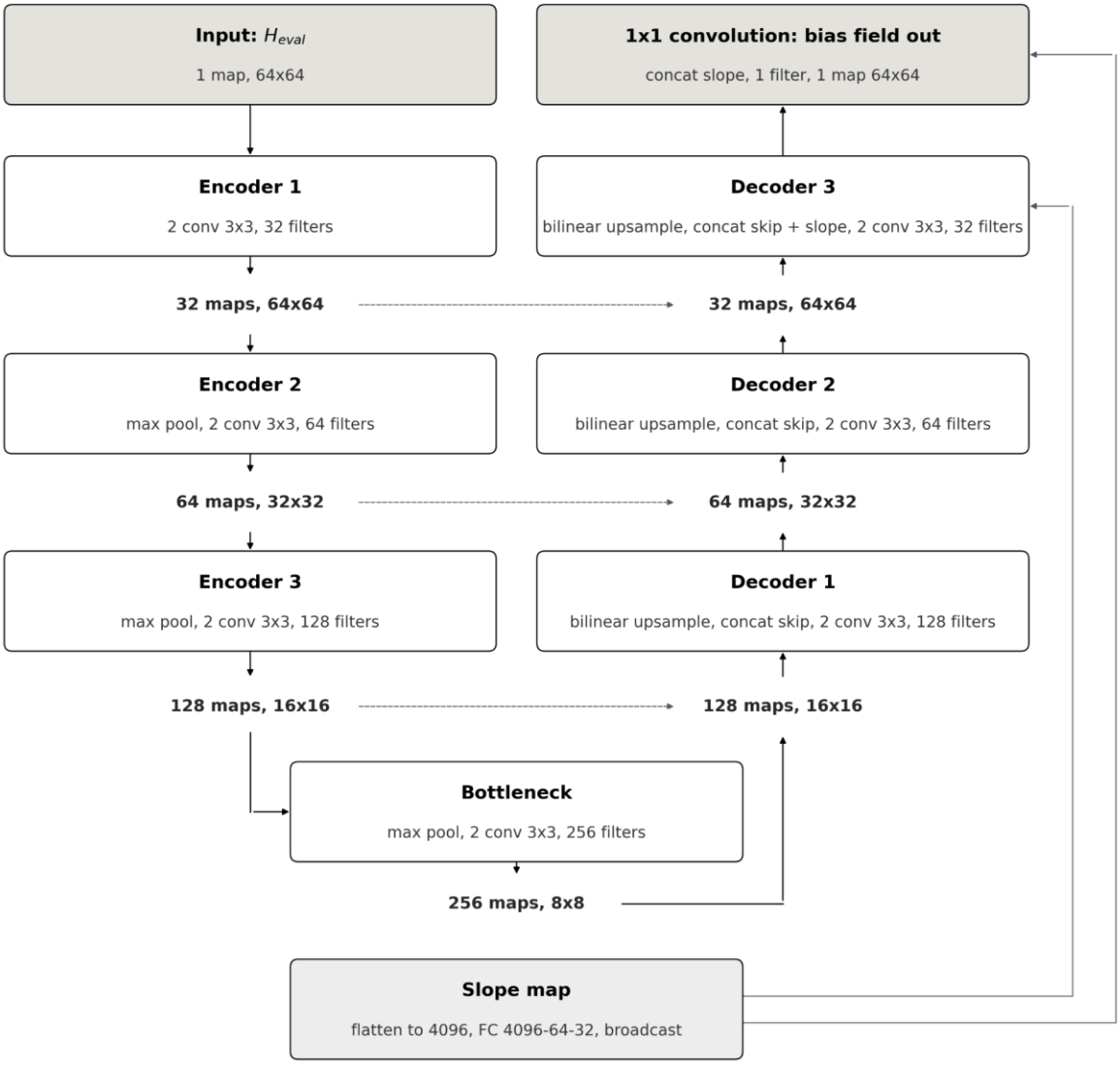


Figure 3.3. Architecture of the U-Net bias field correction model. The encoder downsamples the input evaluated canopy height model (H_{eval}) through three stages to a 256-map bottleneck at 8×8, and the decoder mirrors this with three upsampling stages, each concatenating the corresponding encoder skip connection (dashed arrows). Slope is not passed through the encoder. It is instead compressed by a small fully connected network into a 32-dimensional embedding and injected into the decoder at the final upsampling stage, then again before the final 1×1 convolution. The network outputs a single-channel predicted bias field.

Evaluation of bias field correction performance

After training on the Congo Basin tiles, we applied the U-Net to generate corrected canopy height maps across all three regions. Inference was run on the held-out Congo Basin tiles to evaluate ID correction performance, while the model was applied without any retraining or fine-tuning for Amazon and Borneo, as they served as OOD test cases for geographic transferability. Because the model was trained on 64×64 pixel patches, inference used a sliding-window approach in which successive 64×64 windows were extracted from each full resolution raster at a stride of 32 pixels along both row and column directions, yielding 50% overlap between adjacent windows. For each retained window, H_{eval} and slope were normalized using training set statistics before being passed through the model. The model returned a 64×64 predicted bias field patch in normalized units, which was subsequently rescaled using the training set statistics of the bias field target to recover the predicted bias field in meters. At this stride, each pixel was covered by up to four windows. To reduce edge-effects, overlapping predictions were combined using a two-dimensional Hann window, which assigns higher weights to predictions near the center of each window and lower weights near the edges (Pielawski and Wählby, 2020). The final bias field estimate at each pixel was calculated as the weighted mean across all overlapping windows. A pixel-level validity mask was then applied to the blended outputs, retaining only pixels for which H_{GCA} and slope were both finite and H_{GCA} fell within a plausible range (0-100 m). Corrected canopy height at each pixel was then obtained by subtracting the predicted bias field from H_{eval} following Eq. (5) (Figure 3.4). The mean and linear regression baselines were also applied to generate corrected canopy height estimates on the same

ID and OOD tiles, predicting the bias field independently at every pixel and following the same correction and masking procedure as the U-Net.

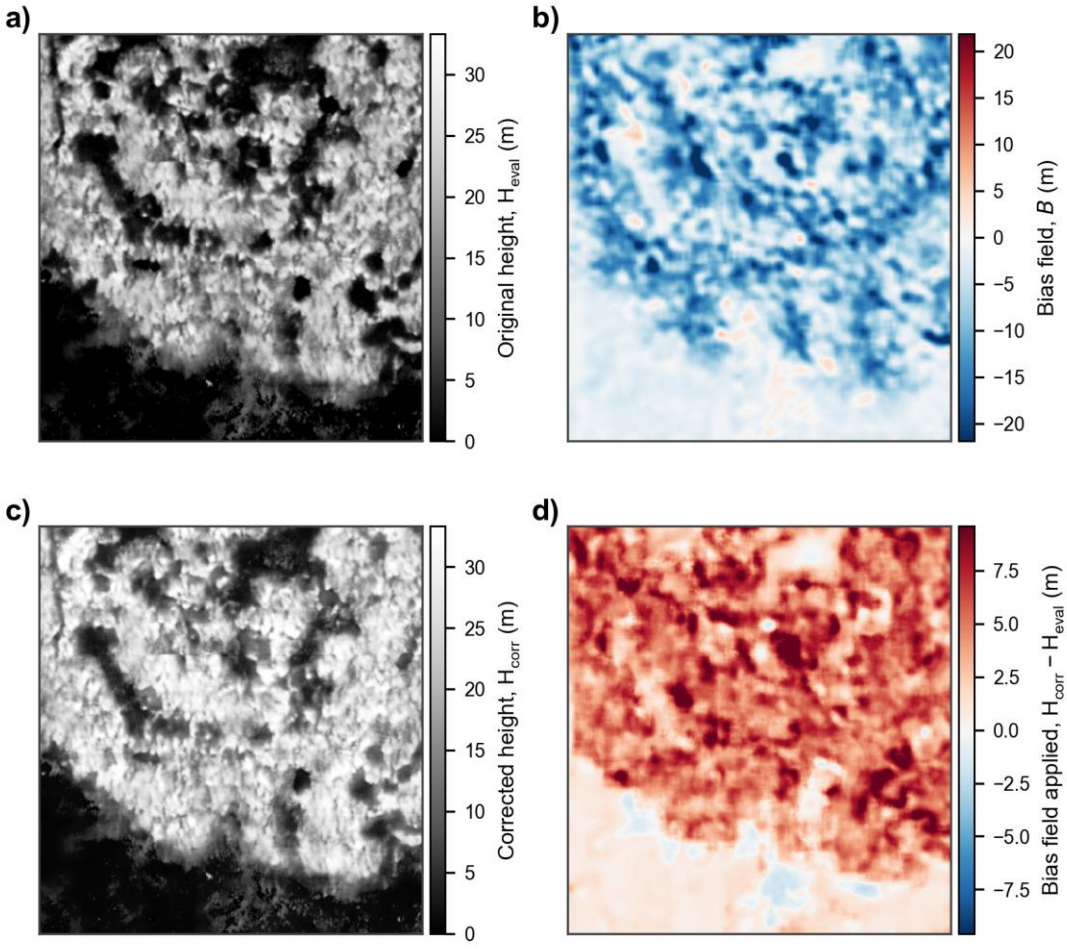


Figure 3.4. Example of bias field correction on a held-out tile from the in-domain Congo Basin test set: a) original evaluated canopy height model: H_{eval}, b) the smoothed bias field used as a target for training: B, c) canopy height with the estimated bias field removed: $H_{corr} = H_{eval} - \hat{B}$ (Eq. (5)), and d) the estimated bias field $\hat{B}$ with positive values indicating where canopy height was increased. All panel units are in meters, and panels a and c share a color scale.

To quantify the effect of primary U-Net bias field correction, the U-Net-corrected canopy height was compared pixelwise against H_{GCA} for each region, alongside the two baseline corrections (mean and linear regression), which served as a reference for

interpreting the U-Net's performance. This yielded a pre-correction residual R_{pre} (Eq. (1)) and a post-correction residual R_{post} for the U-Net and each baseline,

$$R_{\text{post}}(i,j) = H_{\text{corr}}(i,j) - H_{\text{GCA}}(i,j) = R_{\text{pre}}(i,j) - \hat{B}(i,j) \quad (6)$$

where $H_{corr}(i, j)$ is bias-corrected canopy height, $H_{GCA}(i, j)$ is GCA reference canopy height, $R_{pre}(i, j)$ is the pre-correction residual, and $\hat{B}(i, j)$ is the bias field predicted by the method being evaluated (i.e., mean baseline, linear regression baseline, or U-Net). This residual is equal in magnitude but opposite in sign to the bias field prediction error ($\varepsilon = \hat{B} - R_{pre}$, so that $R_{post} = -\varepsilon$) and is reported in canopy height units (m) to enable interpretable evaluation and consistency with conventions in evaluating canopy height predictions (e.g., Lang et al., 2022; Schwartz et al., 2024b; Tolan et al., 2024). Mean residuals (ME) were calculated for the pre-corrected H_{eval}, the U-Net-corrected product, and each baseline-corrected product, and summarized as area-weighted means within strata defined by region, canopy height, slope, canopy height and slope, and land cover class (Buchhorn et al., 2020).

For each stratum, the absolute error change was calculated as the difference between pre-correction and post-correction mean absolute error (MAE) for each correction method. MAE was used as the primary stratum-level statistic because it reflects pixel-level error magnitude directly, including the spread of individual pixel errors within a stratum. Canopy height was grouped into six bins (0-2 m, 2-10 m, 10-20 m, 20-30 m, 30-40 m, and ≥40 m) and slope into four bins (0-5°, 5-15°, 15-30°, and ≥30°). The 0-2 m canopy height boundary was set with reference to the empirical distribution of the Congo Basin training data (Figure S3.1), which is bimodal, with a

distinct low-height mode separated from the main canopy height mode. The remaining intervals use round, interpretable boundaries spanning the unimodal forest-canopy distribution and its upper tail, with the uppermost bin (≥40 m) isolating a comparatively rare set of pixels at the high end of the training distribution. To locate the transition between improved and worsened MAE more precisely than these fixed bins allow, MAE was also computed in 1 m canopy height bins over the same pixels and validity mask. For slope, bin boundaries reflect the documented decline in GEDI accuracy with increasing slope (Dhargay et al., 2022; Moudrý et al., 2024b), with steep terrain at ≥30° in particular posing a substantial challenge for canopy height retrieval (Liu et al., 2021). Pixels in the OOD Amazon and Borneo were assigned to these same fixed bins. Model performance was also evaluated using ME as a secondary metric, which isolates directional bias and can reveal cases where a method's average error is small despite comparatively large MAE. Because each region contains hundreds of millions to billions of spatially autocorrelated pixels (Table S3.1), conventional significance tests would flag even negligible differences as significant (Lin et al., 2013). Spatial autocorrelation compounds this, as neighboring pixels add little independent information yet inflate effective sample sizes, further overstating statistical significance (Dormann et al., 2007; Legendre, 1993). We therefore interpret differences by their magnitude and consistency across regions and bins rather than by p-values.

Results

Training was stable, with validation loss plateauing well within the 200-epoch budget (Figure S3.2). On the held-out ID Congo Basin set, the U-Net bias field correction model achieved the lowest MAE of the three correction methods, reducing

MAE from 6.37 m pre-correction to 5.34 m (mean baseline: 5.87 m; linear regression baseline: 5.84 m; Figure 3.5a). OOD, this advantage was retained: in the Amazon, the U-Net again produced the lowest MAE of the three correction methods, improving from 6.29 m to 5.59 m (mean baseline: 5.83 m; linear regression baseline: 5.81 m), and in Borneo it improved from 8.95 m to 7.84 m, once more the lowest (mean baseline: 8.25 m; linear regression baseline: 8.12 m). Whereas MAE measures average error magnitude, mean error (ME) measures directional bias. ME moved substantially toward zero across correction methods and regions (Figure 3.5b). For the U-Net, ME improved from -4.09 m to -0.88 m in the Congo Basin. OOD improvements were comparable: from -3.68 m to -0.90 m in the Amazon, nearly matching ID performance, and from -6.68 m to -3.54 m in Borneo. Pre-correction, the large magnitude of ME relative to MAE indicates substantial systematic underestimation of evaluated canopy height (H_{eval}) relative to H_{GCA}. Post-correction, the larger reductions in ME magnitude than in MAE indicate reduced systematic underestimation, although considerable negative bias remained in Borneo. Both baselines achieved ME closer to zero than the U-Net in every region (Figure 3.5b), indicating lower net bias, whereas the U-Net achieved the lowest MAE of the three corrected products, indicating smaller average errors overall.

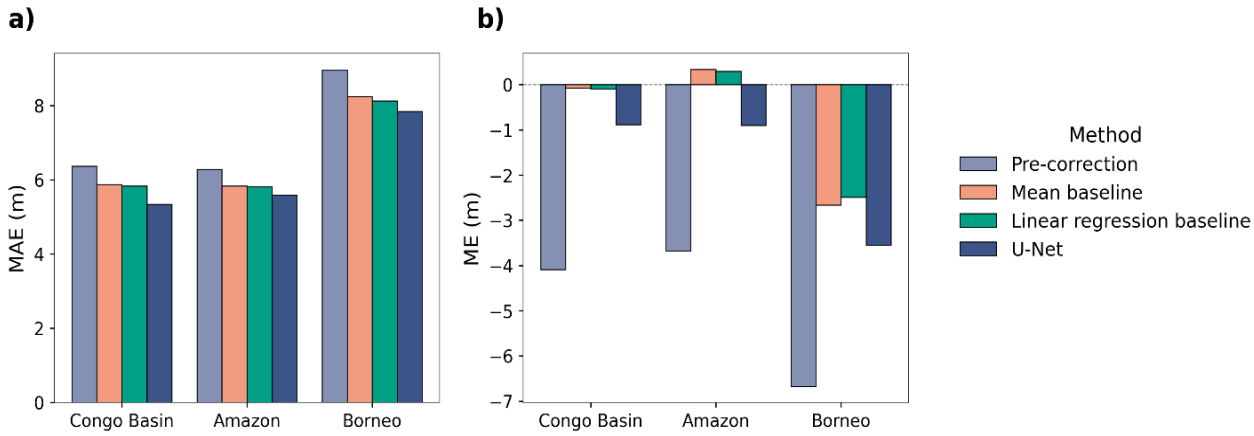


Figure 3.5. Regional performance of the pre-correction evaluated canopy height (H_{eval}) in grey and the three correction methods (mean baseline - orange, linear regression baseline - green, U-Net - navy), evaluated against Global Canopy Atlas ground truth (H_{GCA}) in the Congo Basin (in-domain), Amazon, and Borneo (out-of-domain). (a) Mean absolute error (MAE) by region and method. (b) Mean error (ME) by region and method.

Canopy height

Correction performance varied consistently with canopy height across regions: the U-Net reduced MAE in all bins ≥20 m but increased it in the three shorter bins (Table 3.1). In the 0-2 m bin, MAE increased from 1.31 to 2.21 m in the Congo Basin, 1.70 to 2.85 m in the Amazon, and 1.68 to 2.80 m in Borneo. MAE also increased in the 2-10 m bins in every region (4.86 to 5.57 m Congo Basin, 5.62 to 6.87 m Amazon, 5.27 to 5.85 m Borneo). However, the U-Net produced smaller errors than either baseline in both bins. In the 0-2 m bin, the U-Net's post-correction MAE was approximately half that of the mean baseline (4.51, 5.21, 4.96 m across the three regions for Congo Basin, Amazon, and Borneo respectively) and the linear regression baseline (4.37, 5.02, 4.79 m, respectively).

Table 3.1. Mean absolute error (MAE) in meters (m) between canopy height estimates and reference canopy height (H_{GCA}) before and after three bias-correction methods, stratified by region and canopy height bin. Pre-correction is the MAE between the evaluated canopy height model (H_{eval}) and H_{GCA}, computed prior to any bias correction. The remaining three columns report MAE after applying each of this study's bias-correction methods ($H_{corr} = H_{eval} - \hat{B}$, Eq. (5) where $\hat{B}$ is the estimated bias field). Bold values indicate the lowest MAE among the three corrected methods within each row.

Region	Height bin	Pre-correction	Mean baseline	Linear regression baseline	U-Net
Congo Basin	0-2 m	1.31	4.51	4.37	**2.21**
	2-10 m	4.86	6.11	6.08	**5.57**
	10-20 m	4.60	5.74	5.73	**5.19**
	20-30 m	6.32	**4.32**	4.34	4.42
	30-40 m	12.18	8.28	8.20	**8.06**
	≥40 m	20.42	16.40	16.22	**15.57**
Amazon	0-2 m	1.70	5.21	5.02	**2.85**
	2-10 m	5.62	7.67	7.61	**6.87**
	10-20 m	4.26	5.65	5.63	**4.93**
	20-30 m	6.01	**4.00**	4.01	4.23
	30-40 m	13.03	9.06	**9.02**	9.87
	≥40 m	23.67	19.66	**19.58**	20.15
Borneo	0-2 m	1.68	4.96	4.79	**2.80**
	2-10 m	5.27	6.32	6.33	**5.85**
	10-20 m	5.42	5.59	5.63	**5.52**
	20-30 m	8.34	**6.40**	6.40	6.85
	30-40 m	15.42	11.65	11.24	**11.23**
	≥40 m	27.87	23.85	23.27	**23.06**

The 10-20 m height bin marked the transition between worsened and improved MAE. U-Net MAE increased in the Congo Basin (4.60 to 5.19 m) and Amazon (4.26 to 4.93 m) and changed little in Borneo (5.42 to 5.52 m). ME revealed a different regional pattern. Correction shifted near-zero pre-correction bias toward overestimation in the Congo Basin (-0.28 to +2.79 m) and Amazon (-0.12 to +2.56 m), but reduced underestimation in Borneo (-2.14 to +0.38 m). Thus, lower net bias in Borneo did not translate into lower average error magnitude. Evaluation in 1 m height bins revealed the

transition to improved MAE at 18.9 m in the Congo Basin, 19.3 m in the Amazon, and 15.9 m in Borneo (Figure S3.3). Within the broader 10-20 m bin, the U-Net nevertheless achieved both the lowest MAE and the smallest ME magnitude of the three correction methods in every region.

In the 20-30 m height bin, U-Net correction reduced MAE relative to pre-correction H_{eval} from 6.32 to 4.42 m in the Congo Basin, 6.01 to 4.23 m in the Amazon, and 8.34 to 6.85 m in Borneo, while also moving ME closer to zero. This bin contained the largest proportion of evaluated pixels in the Congo Basin and Amazon, and the second-largest in Borneo (Table S3.1). Both baselines achieved slightly lower MAE than the U-Net in this bin, although differences were small, ranging from 0.1 to 0.5 m (Table 3.1, Figure S3.4).

The largest absolute MAE reductions occurred in the two tallest bins. In the 30-40 m bin, U-Net MAE decreased from 12.18 to 8.06 m in the Congo Basin, 13.03 to 9.87 m in the Amazon, and 15.42 to 11.23 m in Borneo. In the ≥40 m bin, MAE decreased from 20.42 to 15.57 m in the Congo Basin, 23.67 to 20.15 m in the Amazon, and 27.87 to 23.06 m in Borneo. Despite these improvements, the tallest bin retained the strongest negative ME post-correction, indicating substantial residual underestimation. The U-Net achieved lower MAE than both baselines in the two tallest bins in the Congo Basin and Borneo, whereas baselines performed better in the Amazon (Figure S3.4).

Overall, regional MAE improvements combined substantial gains in taller canopies with increased errors in shorter vegetation. The U-Net's lowest regional MAE therefore did not imply superior performance in every height bin.

Slope

When pooled across canopy heights, U-Net correction reduced MAE and moved ME closer to zero in every slope bin in all three regions relative to pre-correction H_{eval} (Figure 3.6a). Compared to the baselines, the U-Net achieved the lowest MAE in 9 of the 12 region-by-slope combinations. In the remaining combinations, it tied the linear regression baseline at the reported precision in the Amazon's 15-30° bin (6.61 m) and performed slightly worse in Borneo's 15-30° and ≥30° (10.61 vs. 10.58 m and 12.99 vs. 12.90 m, respectively) (Figure 3.6). The largest reductions in ME magnitude occurred on the steepest terrain (≥30°).

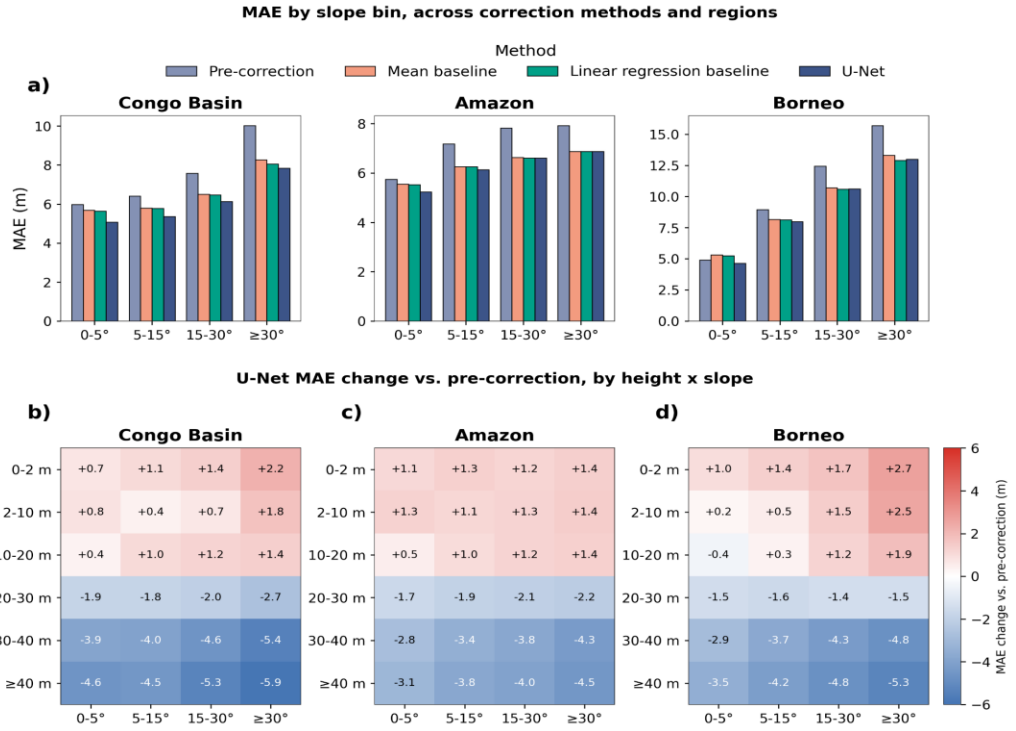


Figure 3.6. (a) Mean absolute error (MAE) by slope bin (0-5°, 5-15°, 15-30°, ≥30°), for each region, pre-correction and after three correction methods, pooled across canopy height. (b-d) Change in MAE after U-Net correction (U-Net MAE minus pre-correction MAE) for the Congo Basin, Amazon, and Borneo respectively, jointly stratified by canopy height and slope bins. Negative values (blue) indicate improved MAE after correction, positive values (red) indicate worsened MAE, and color saturation reflects the size of the change.

Joint stratification by canopy height and slope showed that these slope-level improvements concealed the same height-dependent pattern observed above (Figure 3.6b-d). U-Net correction increased MAE in the 0-2 m and 2-10 m bins at every slope bin in every region, with post-correction ME consistently positive. MAE also increased throughout the 10-20 m bin, except in 0-5° slopes in Borneo. By contrast, correction reduced MAE in every height-by-slope combination ≥20 m, although substantial underestimation remained in the ≥40 m bin.

Pre-correction ME magnitude increased monotonically with slope in 11 of the 18 region-by-height combinations, with most exceptions occurring in the Congo Basin. Thus, steeper terrain often carried greater initial bias, but canopy height more consistently distinguished where correction improved or worsened MAE. Removing slope conditioning modestly worsened performance against the bias-field target on the held-out ID set, measured as the predicted minus the target bias field (MAE: 3.16 to 3.29 m; ME: 0.88 to 0.90 m), indicating a small additional benefit from slope information.

Land cover

Land cover stratification was dominated by closed evergreen broadleaf forest, which accounted for 85.09% of the evaluated pixels in the Congo Basin, 94.61% in the Amazon, and 78.09% in Borneo (Table S3.1). Consequently, landscape-level results were largely determined by correction performance within this class. Within closed evergreen broadleaf forest, U-Net correction reduced MAE relative to pre-correction H_{eval} in all three regions, from 7.13 to 5.91 m in the Congo Basin, 6.52 to 5.76 m in the Amazon, and 10.01 to 8.62 m in Borneo. ME moved closer to zero but remained negative in every region. As in the regional comparison, the U-Net achieved the lowest

MAE of the three correction methods, whereas the baselines achieved ME closer to zero by 0.50-0.83 m (Table S3.2). The U-Net therefore reduced average error magnitude more effectively, but the baselines removed more net directional bias.

Closed forest of unknown type, accounting for 13.11% of evaluated pixels in Borneo, showed a similar pattern. U-Net MAE decreased from 7.16 to 6.66 m, compared with post-correction values of 7.31 m for the mean baseline and 7.22 m for the linear regression baseline. However, the U-Net retained greater ME magnitude (2.11 m) than either baseline (0.37-0.39 m).

Performance was less consistent in the remaining, less-represented land cover classes. In Borneo's herbaceous vegetation, open evergreen broadleaf forest, and shrub classes, and in Congo Basin herbaceous wetlands, correction increased both MAE and ME magnitude, indicating greater average errors and overestimation exceeding the original bias. Each of these classes represented less than 1% of its regional evaluation set (herbaceous vegetation (0.58%), open forest evergreen broad leaf (0.82%), and shrubs (0.07%) in Borneo, and herbaceous wetland (0.24%) in the Congo Basin). Regional improvements therefore primarily describe performance in closed canopy forests.

Discussion

Transferable correction, with substantial residual error

A bias-field model trained only in the Congo Basin reduced both average error magnitude and systematic underestimation in the Amazon and Borneo without retraining. Before correction, ME magnitude was 58-75% of MAE across the three regions, indicating substantial net underestimation rather than errors that largely

canceled in the regional average (Congo Basin: -4.09 m vs. 6.37 m; Amazon: -3.68 m vs. 6.29 m; Borneo: -6.68 m vs. 8.95 m). After U-Net correction, ME approached zero in the Congo Basin and Amazon, although considerable underestimation remained in Borneo. These results support a transferable component of the evaluated product's error, while showing that correction does not eliminate regional differences in fine-scale error, likely associated with substantial domain shift in canopy height and architecture among tropical forest regions (Banin et al., 2012b; S. Liu et al., 2025). This pattern may partly reflect the dominance of closed evergreen broadleaf forest, which comprised 78–95% of evaluated pixels and showed consistent MAE and ME improvement in every region. Because H_{eval} was derived from RGB imagery, the transferable component of the learned bias may reflect the recurring canopy texture of these relatively stable forest systems, which retain foliage year-round and are frequently identified as informative features in RGB-based canopy attribute estimation (J. Chen et al., 2023; Huang and Xia, 2019; Illarionova et al., 2022). Because closed evergreen broadleaf forest dominates all three regions, we cannot disentangle whether this shared bias comes from how the imagery captures these canopies or from the forests themselves being similar.

Comparison with baseline models

The baseline comparison reveals an important distinction between reducing average error magnitude and removing net bias. Both baselines achieved ME closer to zero than the U-Net in every region, whereas the U-Net achieved the lowest regional MAE. A low ME can result from positive and negative errors canceling and does not, by

itself, indicate accurate individual predictions. The U-Net's advantage was therefore smaller average absolute errors, not the most complete removal of regional bias.

This contrast may partly reflect how each model was fit. The mean baseline applies a constant offset, and the linear regression baseline varies the correction with pixel-level height and slope. Neither incorporates neighboring spatial context. Their mean-based and least-squares fitting procedures favor removal of training-set mean residuals. The U-Net instead minimizes an L1 loss against the smoothed bias-field target, an objective that need not produce zero mean residuals (Hastie et al., 2009). The small difference between the two baselines, together with the U-Net's lower MAE, suggests that spatial context and/or non-linear relationships contain useful correction information beyond the tested linear relationship. However, the comparison does not isolate spatial context from model flexibility and therefore cannot establish that this information is inaccessible to other pixelwise models.

Height-dependent limits to correction

Canopy height provided the clearest boundary between beneficial and detrimental correction. MAE decreased relative to pre-correction H_{eval} in every bin ≥20 m across all regions and slope bins, with the largest absolute reductions in the tallest bins. Below approximately 16-19 m, depending on the region, correction generally increased MAE. Because this pattern also occurred within the Congo Basin, geographic domain shift alone cannot explain the failure in shorter vegetation.

The U-Net nevertheless limited these increases more effectively than the baselines, achieving the lowest post-correction MAE in all three shorter height bins. Conversely, its regional advantage did not hold throughout the taller canopy. Both

baselines performed slightly better in the 20-30 m height bin in every region and in the two tallest Amazon bins. This may reflect a trade-off in model flexibility. With few parameters, the baselines are fit almost entirely to the most common conditions, which in the ID training data is the 20-30 m bin. The U-Net also fit rarer height bins and spatial contexts, where it generally outperformed the baselines. No correction method was therefore uniformly preferable across the height distribution.

Height may also act as a proxy for other structural attributes. Crown width and shape both scale with canopy height (Osunkoya et al., 2007; Sterck and Bongers, 2001), a relationship that may allow the U-Net to learn texture patterns relevant at a pantropical scale. Nevertheless, similar heights need not imply equivalent canopy structure, and learned representations can differ in their transferability across domains (Yosinski et al., 2014; Zhang et al., 2021). Height-stratified performance is therefore a useful diagnostic, but it does not identify the features responsible for transfer.

Several factors may contribute to poorer performance in shorter vegetation. These height bins encompass heterogeneous cover types with different spectral and structural properties (Huang et al., 2018), while the smoothed training target may suppress local differences important for their correction. Elevated uncertainty in GEDI-based canopy height retrievals over low-height vegetation associated with post-processing may also affect H_{eval} (Moudrý et al., 2024b). Interpretation is further complicated by defining height strata using H_{GCA}. Reference uncertainty and conditioning on reference height can affect the apparent distribution of signed errors within bins. These considerations warrant caution in attributing stratum-specific ME

entirely to model behavior, although the observed MAE increases still demonstrate poorer agreement with the reference after correction.

At the other extreme, large MAE reductions were achieved alongside substantial residual underestimation in the tallest canopies. Tall pixels were relatively uncommon in the evaluated Congo Basin data, and limited training representation may constrain correction magnitude. Very tall forests can also contain complex architecture with emergent crowns (Alves and Santos, 2002), while tall-canopy underestimation has been reported in other satellite-derived height products affected by reference LiDAR sampling density and spatial aggregation (e.g., Dong et al., 2025; A. Liu et al., 2025). Additional reference data spanning tall forests and short, heterogeneous vegetation (e.g., open canopy woodlands and savannas) would help distinguish sampling limitations from limitations of the correction model.

Slope as contextual information

Stratifying further by slope within each height bin revealed that the U-Net's height-dependent successes and failures persist across nearly every slope bin. Terrain steepness therefore did not determine where correction was beneficial as consistently as canopy height. Terrain-related errors may enter through both satellite-derived predictions and ALS reference heights. ALS-derived terrain models can lose accuracy with increasing slope and vegetation density, propagating terrain errors into canopy height estimates (Fradette et al., 2019; Hyyppä et al., 2008; Takeda, 2004; Tinkham et al., 2012). This may be compounded by solar incidence angle, atmospheric effects, and acquisition hardware motion in satellite imagery (Silva et al., 2018; Vicente-Serrano et al., 2008; Yu et al., 2016), the effects of which may be particularly consequential across

the varied terrain of tropical forests (Bellingham and Tanner, 2000; Jucker et al., 2018; Roberts et al., 2015; Takyu et al., 2002). An otherwise identical network trained without slope lost little accuracy on the ID test set, suggesting that slope is not itself the primary axis of correctable error. Slope thus appears to contribute contextual information that helps the model interpret height-driven residual patterns, rather than function as an independently correctable error axis, which is consistent with the coupling between topography, illumination geometry, and vegetation structure in remotely sensed canopy observations (R. Chen et al., 2023; Schaaf et al., 1994). The small ablation effect supports retaining slope as a useful covariate without treating it as the dominant explanation for correction performance.

Implications for canopy height estimation and downstream products

The evaluated residuals combine errors in H_{eval} with uncertainty in H_{GCA} and differences between acquisition dates. Vegetation growth, mortality, and disturbance between observations can contribute to differences treated here as a static residual field (Clark et al., 2022; Espírito-Santo et al., 2014; Jackson et al., 2024). Other remote sensing artifacts, including variation in observation geometry, bidirectional reflectance effects, and GEDI retrieval uncertainty may introduce additional region-specific error (Adam et al., 2020; Fayad et al., 2021a; Yalcin et al., 2021).

H_{GCA} is also not an error-free reference. ALS-derived canopy height products are sensitive to acquisition conditions, with point density typically named as the dominant driver of canopy height model quality, with additional bias from scanning angles and footprint size (Fischer et al., 2024; Keränen et al., 2016; LaRue et al., 2022; Roussel et al., 2018, 2017). Because the GCA dataset combines data from different campaigns,

these uncertainties may vary across regions. The learned field should therefore be interpreted as a correction toward the available ALS reference, not as an isolated estimate of error originating solely in H_{eval}.

Transfer was tested from only one training region to two external regions, with closed evergreen broadleaf forest dominating all three evaluation sets. Our results establish transfer across these sampled domains but cannot speak to transfer beyond them. Future research would benefit from testing additional training regions, land cover types, and independently derived terrain inputs to evaluate the generalizability of these results to other ecosystem types. Architectures that capture longer-range spatial context, such as attention-based or transformer backbones, may also better resolve the structural patterns that determine where correction succeeds.

Nevertheless, a correction trained in a single region removed much of this product's net bias in two other regions, indicating that its systematic error is largely shared across tropical forests and that corrections calibrated on local ALS data can extend beyond the reference region. However, as correction increased error in shorter vegetation, these regional gains do not justify applying such a correction uniformly. Application should distinguish the objective (e.g., reducing absolute errors or reducing net bias). This distinction matters for aggregated estimates because directional errors do not cancel as random errors may (Igel and Oehmcke, 2023). The approximately 16-19 m transition provides a useful diagnostic, but it was identified using reference canopy height and is not directly an operational threshold where ALS data are unavailable. Our approach offers a framework for developing a selection rule based on available predictors, and then validating the resulting selectively corrected product. Importantly,

improved canopy height estimates should not be assumed to yield equivalent improvements in live biomass or carbon density estimates without downstream evaluation.

Conclusion

In conclusion, canopy height error in H_{eval} is predominantly systematic across the three tropical regions examined here, with ME magnitude reaching 58-75% of MAE. The U-Net trained to predict the bias field error component in the Congo Basin transferred to the Amazon and Borneo without retraining and achieved lower MAE than corrections built as pixelwise functions of canopy height and slope, which reduced ME further but reduced MAE less. Improvement held above roughly 16 to 19 m of canopy height, depending on region, and correction degraded the product below that threshold, including within its training domain. A substantial fraction of this product's error is thus shared across structurally distinct tropical forests and removable from reference data in a single region, extending the range over which such maps can support quantitative use. How far that generalization extends will require training domains beyond the one tested here.

Supplementary Material

Supplementary Text: Network architecture and training configuration

The encoder consisted of three downsampling stages, each comprising two 3×3 convolutional layers with batch normalization and ReLU activation after each convolution, with 2D dropout (p = 0.1) applied after the first convolution. Spatial downsampling between stages was performed using 2×2 max pooling. The base number of feature channels was 32, doubling at each stage to yield feature maps of 32, 64, and 128 channels at spatial resolutions of 64×64, 32×32, and 16×16 pixels, followed by a bottleneck of 256 channels at 8×8 resolution. The decoder comprised three bilinear upsampling stages, each concatenating the corresponding encoder skip connection before passing through a convolutional block. Slope was incorporated via a two-layer fully connected network that flattened the 64×64 slope map and compressed it to a 64-dimensional intermediate representation, and then to a 32-dimensional embedding, with ReLU activation after each layer. This embedding was spatially broadcast and concatenated with decoder feature maps at the final decoding stage and again immediately before the final 1×1 convolution. The network produced a single-channel output corresponding to the predicted bias field.

Models were implemented in PyTorch and trained on 64×64 patches with a batch size of 64. Training augmentation consisted of random 90° rotations and horizontal and vertical flips applied consistently across all spatial inputs. Slope dropout was applied with probability 0.1 during training, randomly zeroing the slope input to discourage overreliance on this comparatively high-quality predictor. The model was trained for up to 200 epochs using the Adam optimizer with a learning rate of 2.5×10^{-4}, L1 loss, and gradient clipping at a maximum norm of 1.0. The learning rate was reduced by a factor of 0.5 following 50 epochs without validation-loss improvement, and training was terminated early if no improvement was observed after 100 epochs. The checkpoint achieving the lowest validation loss was retained as the final model for inference. Hyperparameters were selected by manual search over base filter count, slope embedding dimension, and learning rate, with the configuration reported achieving the lowest validation loss.

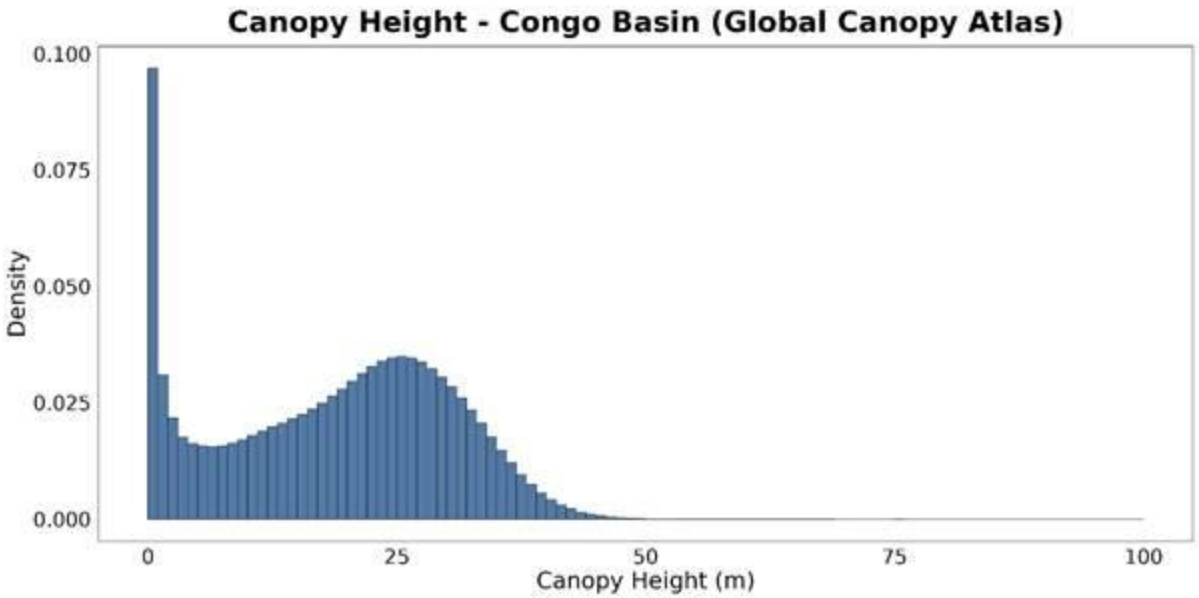


Figure S3.1. Density distribution of canopy height in meters (m) across the in-domain Congo Basin as derived from Global Canopy Atlas (Fischer et al., 2025b) canopy height model (H_{GCA}).

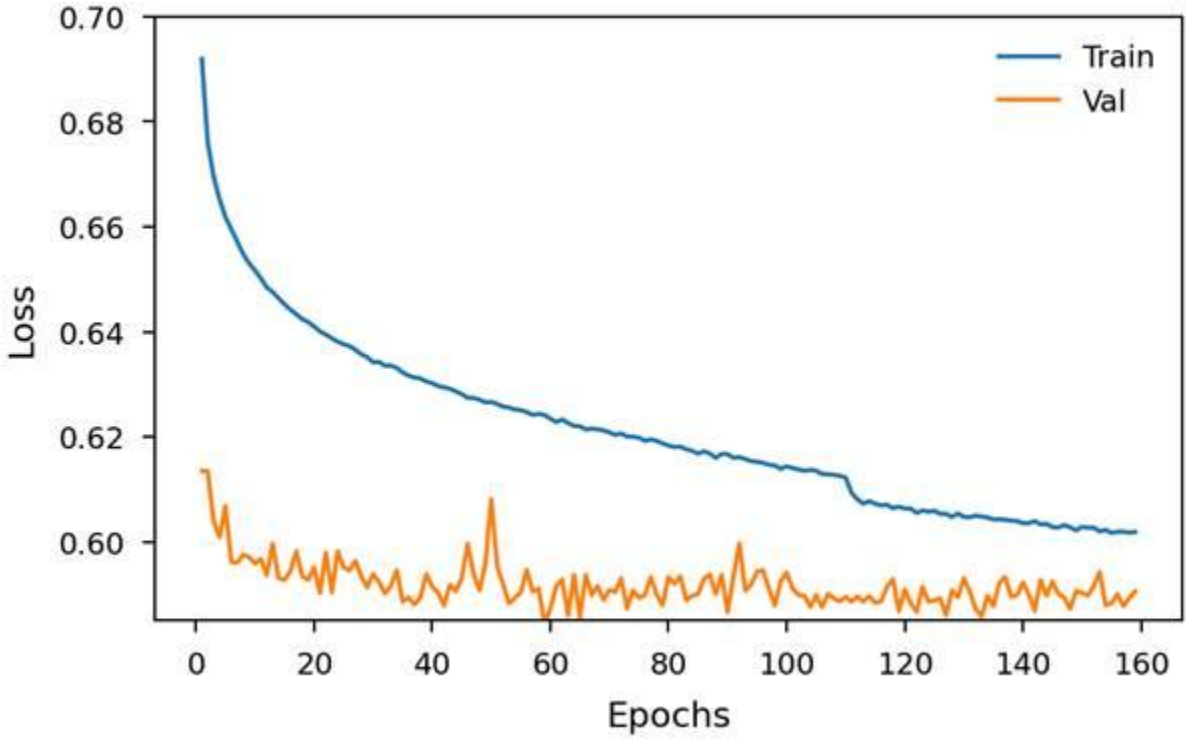


Figure S3.2. Training (blue) and validation (orange) loss over epochs for the bias field correction U-Net model.

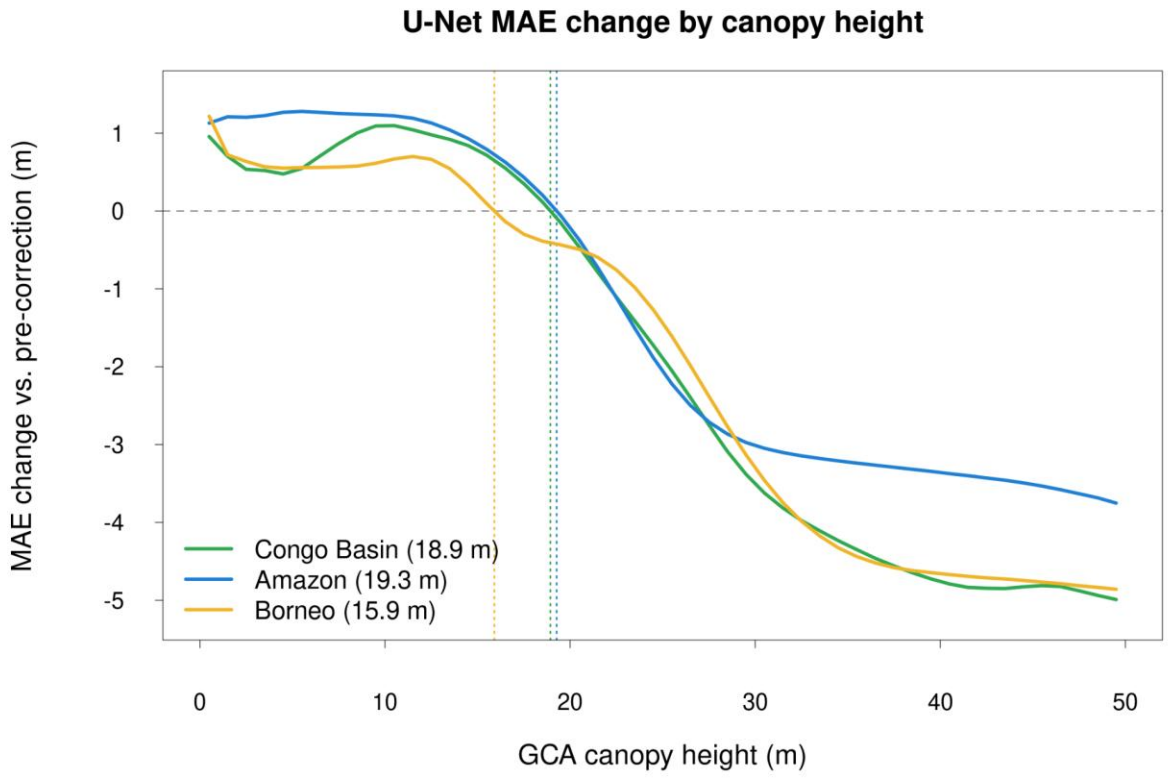


Figure S3.3. Changes in mean absolute error (MAE) after U-Net correction as a function of Global Canopy Atlas (GCA) canopy height (H_{GCA}). Values are MAE after correction minus MAE before, computed within 1 m height bins and plotted at bin midpoints. Negative values indicate that correction reduced error. The dashed horizontal line marks no change. Dotted vertical lines mark the height at which each region's curve crosses zero.

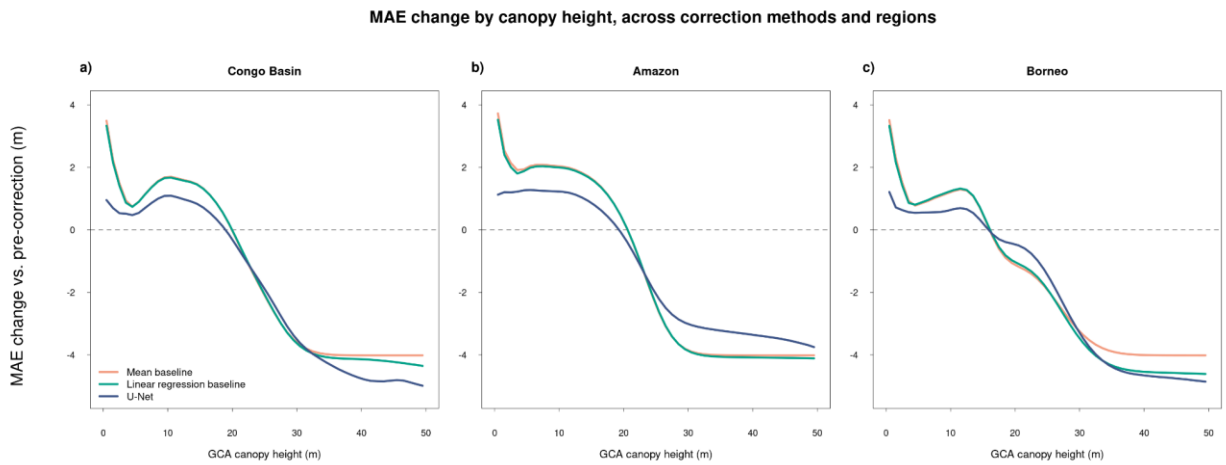


Figure S3.4. Changes in MAE after correction as a function of GCA canopy height (H_{GCA}) for three correction methods in a) the Congo Basin, b) the Amazon, and c) Borneo. Values are MAE after correction minus MAE before, computed within 1 m height bins and plotted at bin midpoints. Negative values indicate that correction reduced error. The dashed horizontal line marks no change.

Table S3.1. Percentage of valid analysis pixels in each region by canopy height, slope, their joint intersection, and land cover class, ranked by descending percentage within each stratum type.

Region	Stratum type	Bin/class	Pixel count	% of region
Congo Basin	**Canopy height**	20-30 m	83,795,113	30.64%
		10-20 m	65,765,522	24.04%
		30-40 m	45,150,598	16.51%
		0-2 m	36,175,518	13.23%
		2-10 m	35,851,703	13.11%
		≥40 m	6,783,245	2.48%
	Slope	0-5°	170,442,140	62.31%
		5-15°	69,033,730	25.24%
		15-30°	23,915,443	8.74%
		≥30°	10,130,386	3.70%
	Canopy height x slope	20-30 m x 0-5°	51,219,107	18.73%
		10-20 m x 0-5°	46,854,081	17.13%
		30-40 m x 0-5°	23,815,478	8.71%
		0-2 m x 0-5°	23,149,881	8.46%
		20-30 m x 5-15°	22,247,793	8.13%
		2-10 m x 0-5°	21,942,357	8.02%
		30-40 m x 5-15°	13,164,072	4.81%
		10-20 m x 5-15°	12,601,583	4.61%
		0-2 m x 5-15°	9,990,853	3.65%
		2-10 m x 5-15°	9,582,457	3.50%
		20-30 m x 15-30°	7,354,051	2.69%
		30-40 m x 15-30°	5,496,331	2.01%
		10-20 m x 15-30°	4,281,716	1.57%
		≥40 m x 0-5°	3,461,236	1.27%
		2-10 m x 15-30°	3,294,773	1.20%
		20-30 m x ≥30°	2,974,162	1.09%
		30-40 m x ≥30°	2,674,717	0.98%
		0-2 m x 15-30°	2,534,521	0.93%
		10-20 m x ≥30°	2,028,142	0.74%
		≥40 m x 5-15°	1,446,972	0.53%
		2-10 m x ≥30°	1,032,116	0.38%
		≥40 m x 15-30°	954,051	0.35%
		≥40 m x ≥30°	920,986	0.34%
		0-2 m x ≥30°	500,263	0.18%

	Land cover	Closed forest, evergreen, broad leaf	232,736,260	85.09%
		Closed forest, deciduous, broad leaf	10,900,403	3.99%
		Herbaceous vegetation	10,233,210	3.74%
		Open forest, unknown	8,605,583	3.15%
		Closed forest, unknown	7,004,687	2.56%
		Open forest, deciduous, broad leaf	2,200,214	0.80%
		Shrubs	735,022	0.27%
		Herbaceous wetland	656,174	0.24%
		Open forest, evergreen, broad leaf	359,651	0.13%
Amazon	**Canopy height**	20-30 m	1,362,860,125	38.49%
		10-20 m	1,132,908,093	32.00%
		30-40 m	421,107,459	11.89%
		2-10 m	401,013,052	11.33%
		0-2 m	171,537,237	4.84%
		≥40 m	51,463,948	1.45%
	Slope	0-5°	2,352,193,130	66.43%
		5-15°	837,634,992	23.66%
		15-30°	310,084,722	8.76%
		≥30°	40,977,070	1.16%
	Canopy height x slope	20-30 m x 0-5°	864,317,258	24.41%
		10-20 m x 0-5°	821,926,739	23.21%
		20-30 m x 5-15°	354,702,321	10.02%
		2-10 m x 0-5°	289,303,610	8.17%
		10-20 m x 5-15°	221,074,423	6.24%
		30-40 m x 0-5°	220,704,412	6.23%
		30-40 m x 5-15°	135,744,837	3.83%
		0-2 m x 0-5°	132,610,664	3.75%
		20-30 m x 15-30°	128,673,152	3.63%
		10-20 m x 15-30°	78,295,701	2.21%
		2-10 m x 5-15°	77,771,588	2.20%
		30-40 m x 15-30°	57,859,070	1.63%
		0-2 m x 5-15°	29,897,516	0.84%
		2-10 m x 15-30°	28,794,504	0.81%
		≥40 m x 0-5°	23,330,447	0.66%
		≥40 m x 5-15°	18,444,307	0.52%
		20-30 m x ≥30°	15,167,394	0.43%
		10-20 m x ≥30°	11,611,230	0.33%
		≥40 m x 15-30°	8,563,410	0.24%
		0-2 m x 15-30°	7,898,885	0.22%

		30-40 m x ≥30°	6,799,140	0.19%
		2-10 m x ≥30°	5,143,350	0.15%
		0-2 m x ≥30°	1,130,172	0.03%
		≥40 m x ≥30°	1,125,784	0.03%
	Land cover	Closed forest, evergreen, broad leaf	3,349,882,552	94.61%
		Herbaceous vegetation	65,456,026	1.85%
		Closed forest, unknown	49,280,354	1.39%
		Open forest, unknown	33,567,973	0.95%
		Herbaceous wetland	14,063,798	0.40%
		Shrubs	6,778,981	0.19%
		Open forest, evergreen, broad leaf	5,687,390	0.16%
		Closed forest, deciduous, broad leaf	52,103	0.00%
		Bare or sparse vegetation	31,963	0.00%
Borneo	**Canopy height**	10-20 m	271,021,568	27.99%
		20-30 m	221,953,839	22.92%
		30-40 m	140,309,275	14.49%
		0-2 m	137,285,702	14.18%
		2-10 m	113,100,340	11.68%
		≥40 m	84,662,915	8.74%
	Slope	0-5°	426,562,050	44.05%
		15-30°	205,024,794	21.17%
		5-15°	187,016,764	19.31%
		≥30°	149,730,031	15.46%
	Canopy height x slope	10-20 m x 0-5°	165,824,039	17.12%
		0-2 m x 0-5°	101,926,275	10.53%
		20-30 m x 0-5°	71,532,097	7.39%
		2-10 m x 0-5°	68,898,568	7.12%
		20-30 m x 15-30°	61,038,766	6.30%
		30-40 m x 15-30°	50,765,671	5.24%
		10-20 m x 5-15°	46,877,026	4.84%
		20-30 m x 5-15°	46,373,351	4.79%
		30-40 m x ≥30°	45,960,392	4.75%
		20-30 m x ≥30°	43,009,625	4.44%
		10-20 m x 15-30°	38,815,253	4.01%
		≥40 m x ≥30°	33,874,362	3.50%
		≥40 m x 15-30°	31,729,806	3.28%
		30-40 m x 5-15°	29,648,421	3.06%
		0-2 m x 5-15°	26,000,125	2.69%
		2-10 m x 5-15°	23,505,374	2.43%

		10-20 m x ≥30°	19,505,250	2.01%
		2-10 m x 15-30°	14,890,966	1.54%
		≥40 m x 5-15°	14,612,467	1.51%
		30-40 m x 0-5°	13,934,791	1.44%
		0-2 m x 15-30°	7,784,332	0.80%
		2-10 m x ≥30°	5,805,432	0.60%
		≥40 m x 0-5°	4,446,280	0.46%
		0-2 m x ≥30°	1,574,970	0.16%
	Land cover	Closed forest, evergreen, broad leaf	756,207,012	78.09%
		Closed forest, unknown	126,920,459	13.11%
		Open forest, unknown	50,836,584	5.25%
		Herbaceous wetland	9,734,699	1.01%
		Open forest, evergreen, broad leaf	7,988,395	0.82%
		Herbaceous vegetation	5,587,748	0.58%
		Shrubs	643,671	0.07%

Table S3.2. Mean absolute error (MAE) and mean error (ME) in meters (m) between canopy height estimates and reference canopy height (H_{GCA}) before and after three bias-correction methods, stratified by region and land cover class. Pre-correction is the error between the evaluated canopy height model (H_{eval}) and H_{GCA}, computed prior to any bias correction. The remaining columns in each group report error after applying each of this study's bias-correction methods ($H_{corr} = H_{eval} - \hat{B}$, Eq. (5) where $\hat{B}$ is the estimated bias field). Bold values indicate the best of the three corrected methods within each row: lowest MAE, and ME closest to zero.

Land cover class	MAE (m)				ME (m)			
	Pre-correction	Mean baseline	Linear reg. baseline	U-Net	Pre-correction	Mean baseline	Linear reg. baseline	U-Net
Congo Basin								
Closed forest, evergreen, broad leaf	7.13	6.22	6.19	**5.91**	-4.61	-0.59	**-0.58**	-1.09
Closed forest, deciduous, broad leaf	2.97	4.54	4.45	**3.09**	-0.92	3.10	3.00	**0.68**
Herbaceous vegetation	0.75	3.50	3.29	**0.76**	-0.72	3.29	3.06	**-0.14**
Open forest, unknown	1.76	3.69	3.56	**1.85**	-1.32	2.69	2.54	**0.35**
Closed forest, unknown	2.85	3.96	3.90	**2.81**	-1.87	2.14	2.06	**0.35**
Open forest, deciduous, broad leaf	1.71	3.57	3.50	**2.02**	-0.88	3.13	3.06	**0.63**
Shrubs	1.30	3.52	3.39	**1.34**	-1.12	2.90	2.74	**0.17**
Herbaceous wetland	2.42	3.83	3.64	**3.02**	-0.76	3.26	3.00	**1.50**
Open forest, evergreen, broad leaf	4.62	5.19	5.05	**4.19**	-3.61	0.41	**0.29**	-1.16
Amazon								
Closed forest, evergreen, broad leaf	6.52	5.92	5.90	**5.76**	-3.83	0.18	**0.15**	-0.98
Herbaceous vegetation	1.08	3.91	3.74	**1.54**	-0.60	3.42	3.23	**0.54**
Closed forest, unknown	4.08	4.99	4.92	**4.15**	-1.35	2.67	2.54	**0.79**
Open forest, unknown	2.67	4.17	4.08	**2.88**	-1.33	2.68	2.56	**0.38**
Herbaceous wetland	1.33	3.91	3.68	**1.52**	-0.85	3.17	2.91	**0.19**
Shrubs	1.99	3.67	3.53	**2.26**	-1.26	2.76	2.57	**0.36**
Open forest, evergreen, broad leaf	3.39	4.52	4.45	**3.44**	-1.93	2.09	2.00	**-0.15**
Closed forest, deciduous, broad leaf	6.59	9.51	9.42	**8.92**	5.24	9.25	9.16	**8.59**
Bare or sparse vegetation	0.80	4.15	3.88	**0.88**	-0.51	3.51	3.22	**0.15**
Borneo								
Closed forest, evergreen, broad leaf	10.01	8.82	8.70	**8.62**	-7.69	-3.68	**-3.44**	-4.24
Closed forest, unknown	7.16	7.31	7.22	**6.66**	-4.39	**-0.37**	-0.39	-2.11
Open forest, unknown	2.66	4.67	4.52	**2.94**	-1.22	2.80	2.63	**0.44**
Herbaceous wetland	1.79	3.87	3.65	**1.91**	-1.65	2.36	2.09	**-0.80**
Open forest, evergreen, broad leaf	1.46	4.24	4.02	**2.17**	-0.63	3.38	3.16	**1.02**
Herbaceous vegetation	2.30	4.99	4.85	**3.17**	-0.48	3.53	3.38	**1.35**
Shrubs	0.60	3.70	3.47	**1.22**	-0.53	3.49	3.25	**0.58**

REFERENCES

Adam, M., Urbazaev, M., Dubois, C., Schmullius, C., 2020. Accuracy Assessment of GEDI Terrain Elevation and Canopy Height Estimates in European Temperate Forests: Influence of Environmental and Acquisition Parameters. Remote Sensing 12, 3948. https://doi.org/10.3390/rs12233948

Ali, A., Chen, H.Y.H., You, W.-H., Yan, E.-R., 2019a. Multiple abiotic and biotic drivers of aboveground biomass shift with forest stratum. Forest Ecology and Management 436, 1–10. https://doi.org/10.1016/j.foreco.2019.01.007

Ali, A., Lin, S., He, J., Kong, F., Yu, J., Jiang, H., 2019b. Big-sized trees overrule remaining trees' attributes and species richness as determinants of aboveground biomass in tropical forests. Global Change Biology 25, 2810–2824. https://doi.org/10.1111/gcb.14707

Alves, L.F., Santos, F.A.M., 2002. Tree allometry and crown shape of four tree species in Atlantic rain forest, south-east Brazil. J. Trop. Ecol. 18, 245–260. https://doi.org/10.1017/S026646740200216X

Ammer, C., 2019. Diversity and forest productivity in a changing climate. New Phytologist 221, 50–66. https://doi.org/10.1111/nph.15263

Andela, N., Morton, D.C., Giglio, L., Chen, Y., Van Der Werf, G.R., Kasibhatla, P.S., DeFries, R.S., Collatz, G.J., Hantson, S., Kloster, S., Bachelet, D., Forrest, M., Lasslop, G., Li, F., Mangeon, S., Melton, J.R., Yue, C., Randerson, J.T., 2017. A human-driven decline in global burned area. Science 356, 1356–1362. https://doi.org/10.1126/science.aal4108

Andersen, H.-E., Reutebuch, S.E., McGaughey, R.J., 2006. A rigorous assessment of tree height measurements obtained using airborne lidar and conventional field methods. Canadian Journal of Remote Sensing 32, 355–366. https://doi.org/10.5589/m06-030

Aponte, C., Kasel, S., Nitschke, C.R., Tanase, M.A., Vickers, H., Parker, L., Fedrigo, M., Kohout, M., Ruiz-Benito, P., Zavala, M.A., Bennett, L.T., 2020. Structural diversity underpins carbon storage in Australian temperate forests. Global Ecol Biogeogr 29, 789–802. https://doi.org/10.1111/geb.13038

Artaxo, P., Hansson, H.C., Machado, L.A.T., Rizzo, L.V., 2022. Tropical forests are crucial in regulating the climate on Earth. PLOS Clim 1, e0000054. https://doi.org/10.1371/journal.pclm.0000054

Asner, G.P., 2001. Cloud cover in Landsat observations of the Brazilian Amazon. International Journal of Remote Sensing 22, 3855–3862. https://doi.org/10.1080/01431160010006926

Asner, G.P., Kellner, J.R., Kennedy-Bowdoin, T., Knapp, D.E., Anderson, C., Martin, R.E., 2013. Forest Canopy Gap Distributions in the Southern Peruvian Amazon. PLoS ONE 8, e60875. https://doi.org/10.1371/journal.pone.0060875

Asner, G.P., Knapp, D.E., Martin, R.E., Tupayachi, R., Anderson, C.B., Mascaro, J., Sinca, F., Chadwick, K.D., Higgins, M., Farfan, W., Llactayo, W., Silman, M.R., 2014. Targeted carbon conservation at national scales with high-resolution monitoring. Proc. Natl. Acad. Sci. U.S.A. 111. https://doi.org/10.1073/pnas.1419550111

Asner, G.P., Mascaro, J., 2014. Mapping tropical forest carbon: Calibrating plot estimates to a simple LiDAR metric. Remote Sensing of Environment 140, 614–624. https://doi.org/10.1016/j.rse.2013.09.023

Asner, G.P., Mascaro, J., Muller-Landau, H.C., Vieilledent, G., Vaudry, R., Rasamoelina, M., Hall, J.S., Van Breugel, M., 2012. A universal airborne LiDAR approach for tropical forest carbon mapping. Oecologia 168, 1147–1160. https://doi.org/10.1007/s00442-011-2165-z

Badgley, G., Anderegg, L.D.L., Berry, J.A., Field, C.B., 2019. Terrestrial gross primary production: Using NIR $_V$ to scale from site to globe. Global Change Biology 25, 3731–3740. https://doi.org/10.1111/gcb.14729

Badgley, G., Field, C.B., Berry, J.A., 2017. Canopy near-infrared reflectance and terrestrial photosynthesis. Sci. Adv. 3, e1602244. https://doi.org/10.1126/sciadv.1602244

Banin, L., Feldpausch, T.R., Phillips, O.L., Baker, T.R., Lloyd, J., Affum-Baffoe, K., Arets, E.J.M.M., Berry, N.J., Bradford, M., Brienen, R.J.W., Davies, S., Drescher, M., Higuchi, N., Hilbert, D.W., Hladik, A., Iida, Y., Salim, K.A., Kassim, A.R., King, D.A., Lopez-Gonzalez, G., Metcalfe, D., Nilus, R., Peh, K.S. -H., Reitsma, J.M., Sonké, B., Taedoumg, H., Tan, S., White, L., Wöll, H., Lewis, S.L., 2012a. What controls tropical forest architecture? Testing environmental, structural and floristic drivers. Global Ecology and Biogeography 21, 1179–1190. https://doi.org/10.1111/j.1466-8238.2012.00778.x

Banin, L., Feldpausch, T.R., Phillips, O.L., Baker, T.R., Lloyd, J., Affum-Baffoe, K., Arets, E.J.M.M., Berry, N.J., Bradford, M., Brienen, R.J.W., Davies, S., Drescher, M., Higuchi, N., Hilbert, D.W., Hladik, A., Iida, Y., Salim, K.A., Kassim, A.R., King, D.A., Lopez-Gonzalez, G., Metcalfe, D., Nilus, R., Peh, K.S.-H., Reitsma, J.M., Sonké, B., Taedoumg, H., Tan, S., White, L., Wöll, H., Lewis, S.L., 2012b. What controls tropical forest architecture? Testing environmental, structural and floristic drivers: Determinants of tropical forest architecture. Global Ecology and Biogeography 21, 1179–1190. https://doi.org/10.1111/j.1466-8238.2012.00778.x

Baret, F., Hagolle, O., Geiger, B., Bicheron, P., Miras, B., Huc, M., Berthelot, B., Niño, F., Weiss, M., Samain, O., Roujean, J.L., Leroy, M., 2007. LAI, fAPAR and

fCover CYCLOPES global products derived from VEGETATION. Remote Sensing of Environment 110, 275–286. https://doi.org/10.1016/j.rse.2007.02.018

Bastin, J.-F., Barbier, N., Réjou-Méchain, M., Fayolle, A., Gourlet-Fleury, S., Maniatis, D., De Haulleville, T., Baya, F., Beeckman, H., Beina, D., Couteron, P., Chuyong, G., Dauby, G., Doucet, J.-L., Droissart, V., Dufrêne, M., Ewango, C., Gillet, J.F., Gonmadje, C.H., Hart, T., Kavali, T., Kenfack, D., Libalah, M., Malhi, Y., Makana, J.-R., Pélissier, R., Ploton, P., Serckx, A., Sonké, B., Stevart, T., Thomas, D.W., De Cannière, C., Bogaert, J., 2015. Seeing Central African forests through their largest trees. Sci Rep 5, 13156. https://doi.org/10.1038/srep13156

Beer, C., Reichstein, M., Tomelleri, E., Ciais, P., Jung, M., Carvalhais, N., Rödenbeck, C., Arain, M.A., Baldocchi, D., Bonan, G.B., Bondeau, A., Cescatti, A., Lasslop, G., Lindroth, A., Lomas, M., Luyssaert, S., Margolis, H., Oleson, K.W., Roupsard, O., Veenendaal, E., Viovy, N., Williams, C., Woodward, F.I., Papale, D., 2010. Terrestrial Gross Carbon Dioxide Uptake: Global Distribution and Covariation with Climate. Science 329, 834–838. https://doi.org/10.1126/science.1184984

Bellingham, P.J., Tanner, E.V.J., 2000. The Influence of Topography on Tree Growth, Mortality, and Recruitment in a Tropical Montane Forest[1]. Biotropica 32, 378–384. https://doi.org/10.1111/j.1744-7429.2000.tb00484.x

Bock, C.E., Jones, Z.F., Bock, J.H., 2007. RELATIONSHIPS BETWEEN SPECIES RICHNESS, EVENNESS, AND ABUNDANCE IN A SOUTHWESTERN SAVANNA. Ecology 88, 1322–1327. https://doi.org/10.1890/06-0654

Bonan, G.B., 2008. Forests and Climate Change: Forcings, Feedbacks, and the Climate Benefits of Forests. Science 320, 1444–1449. https://doi.org/10.1126/science.1155121

Borges, E.R., Réjou-Méchain, M., Gourlet-Fleury, S., Vincent, G., Mortier, F., Bry, X., Cornu, G., Baya, F., Allah-Barem, F., Pélissier, R., 2024. Evolutionary diversity impacts tropical forest biomass and productivity through disturbance-mediated ecological pathways. Journal of Ecology 112, 2344–2358. https://doi.org/10.1111/1365-2745.14399

Buchhorn, M., Smets, B., Bertels, L., Roo, B.D., Lesiv, M., Tsendbazar, N.-E., Herold, M., Fritz, S., 2020. Copernicus Global Land Service: Land Cover 100m: collection 3: epoch 2019: Globe. https://doi.org/10.5281/ZENODO.3939050

Burns, P., Hakkenberg, C.R., Goetz, S.J., 2024. Multi-resolution gridded maps of vegetation structure from GEDI. Sci Data 11, 881. https://doi.org/10.1038/s41597-024-03668-4

Cardenas-Martinez, A., Pascual, A., Guisado-Pintado, E., Rodriguez-Galiano, V., 2025. Using airborne LiDAR and enhanced-geolocated GEDI metrics to map structural

traits over a Mediterranean forest. Science of Remote Sensing 11, 100195. https://doi.org/10.1016/j.srs.2025.100195

Cardinale, B.J., Wright, J.P., Cadotte, M.W., Carroll, I.T., Hector, A., Srivastava, D.S., Loreau, M., Weis, J.J., 2007. Impacts of plant diversity on biomass production increase through time because of species complementarity. Proc. Natl. Acad. Sci. U.S.A. 104, 18123–18128. https://doi.org/10.1073/pnas.0709069104

Cardoso, A.W., Oliveras, I., Abernethy, K.A., Jeffery, K.J., Glover, S., Lehmann, D., Edzang Ndong, J., White, L.J.T., Bond, W.J., Malhi, Y., 2021. A distinct ecotonal tree community exists at central African forest–savanna transitions. Journal of Ecology 109, 1170–1183. https://doi.org/10.1111/1365-2745.13549

Carmona, C.P., De Bello, F., Mason, N.W.H., Lepš, J., 2016. Traits Without Borders: Integrating Functional Diversity Across Scales. Trends in Ecology & Evolution 31, 382–394. https://doi.org/10.1016/j.tree.2016.02.003

Carreño-Rocabado, G., Peña-Claros, M., Bongers, F., Alarcón, A., Licona, J., Poorter, L., 2012. Effects of disturbance intensity on species and functional diversity in a tropical forest. Journal of Ecology 100, 1453–1463. https://doi.org/10.1111/j.1365-2745.2012.02015.x

Cavanaugh, K.C., Gosnell, J.S., Davis, S.L., Ahumada, J., Boundja, P., Clark, D.B., Mugerwa, B., Jansen, P.A., O'Brien, T.G., Rovero, F., Sheil, D., Vasquez, R., Andelman, S., 2014. Carbon storage in tropical forests correlates with taxonomic diversity and functional dominance on a global scale. Global Ecology and Biogeography 23, 563–573. https://doi.org/10.1111/geb.12143

Cavender-Bares, J., Schneider, F.D., Santos, M.J., Armstrong, A., Carnaval, A., Dahlin, K.M., Fatoyinbo, L., Hurtt, G.C., Schimel, D., Townsend, P.A., Ustin, S.L., Wang, Z., Wilson, A.M., 2022. Integrating remote sensing with ecology and evolution to advance biodiversity conservation. Nat Ecol Evol 6, 506–519. https://doi.org/10.1038/s41559-022-01702-5

Chang, L., Liu, S., Antonarakis, A.S., Longo, M., Tang, H., Armston, J.D., Dubayah, R., Moorcroft, P., 2025. Legacies of model initialization on predictions of future ecosystem dynamics in California's Sierra Nevada: insights from GEDI. New Phytologist 248, 2809–2832. https://doi.org/10.1111/nph.70657

Chave, J., Condit, R., Lao, S., Caspersen, J.P., Foster, R.B., Hubbell, S.P., 2003. Spatial and temporal variation of biomass in a tropical forest: results from a large census plot in Panama. Journal of Ecology 91, 240–252. https://doi.org/10.1046/j.1365-2745.2003.00757.x

Chazdon, R.L., 2003. Tropical forest recovery: legacies of human impact and natural disturbances. Perspectives in Plant Ecology, Evolution and Systematics 6, 51–71. https://doi.org/10.1078/1433-8319-00042

Chazdon, R.L., Finegan, B., Capers, R.S., Salgado-Negret, B., Casanoves, F., Boukili, V., Norden, N., 2010. Composition and Dynamics of Functional Groups of Trees During Tropical Forest Succession in Northeastern Costa Rica. Biotropica 42, 31–40. https://doi.org/10.1111/j.1744-7429.2009.00566.x

Chen, D., Shang, S., Wu, C., 2014. Shadow-based Building Detection and Segmentation in High-resolution Remote Sensing Image. JMM 9, 181–188. https://doi.org/10.4304/jmm.9.1.181-188

Chen, G., Wang, Y., Li, S., Cao, W., Ren, H., Knibbs, L.D., Abramson, M.J., Guo, Y., 2018. Spatiotemporal patterns of PM10 concentrations over China during 2005–2016: A satellite-based estimation using the random forests approach. Environmental Pollution 242, 605–613. https://doi.org/10.1016/j.envpol.2018.07.012

Chen, H., Cloude, S.R., White, J.C., 2021. Using GEDI Waveforms for Improved TanDEM-X Forest Height Mapping: A Combined SINC + Legendre Approach. Remote Sensing 13, 2882. https://doi.org/10.3390/rs13152882

Chen, J., Wang, L., Jucker, T., Da, H., Zhang, Z., Hu, J., Yang, Q., Wang, X., Qin, Y., Shen, G., Shu, L., Zhang, J., 2023. Detecting forest canopy gaps using unoccupied aerial vehicle imagery in a species-rich subtropical forest. Remote Sens Ecol Conserv 9, 671–686. https://doi.org/10.1002/rse2.336

Chen, J.M., Menges, C.H., Leblanc, S.G., 2005. Global mapping of foliage clumping index using multi-angular satellite data. Remote Sensing of Environment 97, 447–457. https://doi.org/10.1016/j.rse.2005.05.003

Chen, R., Yin, G., Zhao, W., Yan, K., Wu, S., Hao, D., Liu, G., 2023. Topographic Correction of Optical Remote Sensing Images in Mountainous Areas: A systematic review. IEEE Geosci. Remote Sens. Mag. 11, 125–145. https://doi.org/10.1109/MGRS.2023.3311100

Chiabai, A. (Ed.), 2015. Climate change impacts on tropical forests in Central America: an ecosystem service perspective. Routledge/Taylor & Francis Group, Milton Park, Abingdon, Oxon.

Chisholm, R.A., Muller-Landau, H.C., Abdul Rahman, K., Bebber, D.P., Bin, Y., Bohlman, S.A., Bourg, N.A., Brinks, J., Bunyavejchewin, S., Butt, N., Cao, H., Cao, M., Cárdenas, D., Chang, L., Chiang, J., Chuyong, G., Condit, R., Dattaraja, H.S., Davies, S., Duque, A., Fletcher, C., Gunatilleke, N., Gunatilleke, S., Hao, Z., Harrison, R.D., Howe, R., Hsieh, C., Hubbell, S.P., Itoh, A., Kenfack, D., Kiratiprayoon, S., Larson, A.J., Lian, J., Lin, D., Liu, H., Lutz, J.A., Ma, K., Malhi, Y., McMahon, S., McShea, W., Meegaskumbura, M., Mohd. Razman, S., Morecroft, M.D., Nytch, C.J., Oliveira, A., Parker, G.G., Pulla, S., Punchi-Manage, R., Romero-Saltos, H., Sang, W., Schurman, J., Su, S., Sukumar, R., Sun, I., Suresh, H.S., Tan, S., Thomas, D., Thomas, S., Thompson, J., Valencia,

R., Wolf, A., Yap, S., Ye, W., Yuan, Z., Zimmerman, J.K., 2013. Scale-dependent relationships between tree species richness and ecosystem function in forests. Journal of Ecology 101, 1214–1224. https://doi.org/10.1111/1365-2745.12132

Cirezi, N.C., Bastin, J.-F., Tshibasu, E., Lonpi, E.T., Chuma, G.B., Mugumaarhahama, Y., Sambieni, K.R., Karume, K.C., Lumbuenamo, R.S., Bogaert, J., 2022. Contribution of 'human induced fires' to forest and savanna land conversion dynamics in the Luki Biosphere Reserve landscape, western Democratic Republic of Congo. International Journal of Remote Sensing 43, 6406–6429. https://doi.org/10.1080/01431161.2022.2138622

Clark, D.B., Clark, D.A., Kellner, J.R., 2022. Spatial and temporal scales of canopy disturbance and recovery across an old-growth tropical rain forest landscape. Ecological Monographs 92, e01496. https://doi.org/10.1002/ecm.1496

Clark, D.B., Oberbauer, S.F., Clark, D.A., Ryan, M.G., Dubayah, R.O., 2021. Physical structure and biological composition of canopies in tropical secondary and old-growth forests. PLoS ONE 16, e0256571. https://doi.org/10.1371/journal.pone.0256571

Cole, L.E.S., Bhagwat, S.A., Willis, K.J., 2014. Recovery and resilience of tropical forests after disturbance. Nat Commun 5, 3906. https://doi.org/10.1038/ncomms4906

Cooper, D.L.M., Lewis, S.L., Sullivan, M.J.P., Prado, P.I., Ter Steege, H., Barbier, N., Slik, F., Sonké, B., Ewango, C.E.N., Adu-Bredu, S., Affum-Baffoe, K., De Aguiar, D.P.P., Ahuite Reategui, M.A., Aiba, S.-I., Albuquerque, B.W., De Almeida Matos, F.D., Alonso, A., Amani, C.A., Do Amaral, D.D., Do Amaral, I.L., Andrade, A., De Andrade Miranda, I.P., Angoboy, I.B., Araujo-Murakami, A., Arboleda, N.C., Arroyo, L., Ashton, P., Aymard C, G.A., Baider, C., Baker, T.R., Balinga, M.P.B., Balslev, H., Banin, L.F., Bánki, O.S., Baraloto, C., Barbosa, E.M., Barbosa, F.R., Barlow, J., Bastin, J.-F., Beeckman, H., Begne, S., Bengone, N.N., Berenguer, E., Berry, N., Bitariho, R., Boeckx, P., Bogaert, J., Bonyoma, B., Boundja, P., Bourland, N., Boyemba Bosela, F., Brambach, F., Brienen, R., Burslem, D.F.R.P., Camargo, J.L., Campelo, W., Cano, A., Cárdenas, S., Cárdenas López, D., De Sá Carpanedo, R., Carrero Márquez, Y.A., Carvalho, F.A., Casas, L.F., Castellanos, H., Castilho, C.V., Cerón, C., Chapman, C.A., Chave, J., Chhang, P., Chutipong, W., Chuyong, G.B., Cintra, B.B.L., Clark, C.J., Coelho De Souza, F., Comiskey, J.A., Coomes, D.A., Cornejo Valverde, F., Correa, D.F., Costa, F.R.C., Costa, J.B.P., Couteron, P., Culmsee, H., Cuni-Sanchez, A., Dallmeier, F., Damasco, G., Dauby, G., Dávila, N., Dávila Doza, H.P., De Alban, J.D.T., De Assis, R.L., De Canniere, C., De Haulleville, T., De Jesus Veiga Carim, M., Demarchi, L.O., Dexter, K.G., Di Fiore, A., Din, H.H.M., Disney, M.I., Djiofack, B.Y., Djuikouo, M.-N.K., Do, T.V., Doucet, J.-L., Draper, F.C., Droissart, V., Duivenvoorden, J.F., Engel, J., Estienne, V., Farfan-Rios, W., Fauset, S., Feeley, K.J., Feitosa, Y.O., Feldpausch, T.R., Ferreira, C., Ferreira,

J., Ferreira, L.V., Fletcher, C.D., Flores, B.M., Fofanah, A., Foli, E.G., Fonty, É., Fredriksson, G.M., Fuentes, A., Galbraith, D., Gallardo Gonzales, G.P., Garcia-Cabrera, K., García-Villacorta, R., Gomes, V.H.F., Gómez, R.Z., Gonzales, T., Gribel, R., Guedes, M.C., Guevara, J.E., Hakeem, K.R., Hall, J.S., Hamer, K.C., Hamilton, A.C., Harris, D.J., Harrison, R.D., Hart, T.B., Hector, A., Henkel, T.W., Herbohn, J., Hockemba, M.B.N., Hoffman, B., Holmgren, M., Honorio Coronado, E.N., Huamantupa-Chuquimaco, I., Hubau, W., Imai, N., Irume, M.V., Jansen, P.A., Jeffery, K.J., Jimenez, E.M., Jucker, T., Junqueira, A.B., Kalamandeen, M., Kamdem, N.G., Kartawinata, K., Kasongo Yakusu, E., Katembo, J.M., Kearsley, E., Kenfack, D., Kessler, M., Khaing, T.T., Killeen, T.J., Kitayama, K., Klitgaard, B., Labrière, N., Laumonier, Y., Laurance, S.G.W., Laurance, W.F., Laurent, F., Le, T.C., Le, T.T., Leal, M.E., Leão De Moraes Novo, E.M., Levesley, A., Libalah, M.B., Licona, J.C., Lima Filho, D.D.A., Lindsell, J.A., Lopes, A., Lopes, M.A., Lovett, J.C., Lowe, R., Lozada, J.R., Lu, X., Luambua, N.K., Luize, B.G., Maas, P., Magalhães, J.L.L., Magnusson, W.E., Mahayani, N.P.D., Makana, J.-R., Malhi, Y., Maniguaje Rincón, L., Mansor, A., Manzatto, A.G., Marimon, B.S., Marimon-Junior, B.H., Marshall, A.R., Martins, M.P., Mbayu, F.M., De Medeiros, M.B., Mesones, I., Metali, F., Mihindou, V., Millet, J., Milliken, W., Mogollón, H.F., Molino, J.-F., Mohd. Said, Mohd.N., Monteagudo Mendoza, A., Montero, J.C., Moore, S., Mostacedo, B., Mozombite Pinto, L.F., Mukul, S.A., Munishi, P.K.T., Nagamasu, H., Nascimento, H.E.M., Nascimento, M.T., Neill, D., Nilus, R., Noronha, J.C., Nsenga, L., Núñez Vargas, P., Ojo, L., Oliveira, A.A., De Oliveira, E.A., Ondo, F.E., Palacios Cuenca, W., Pansini, S., Pansonato, M.P., Paredes, M.R., Paudel, E., Pauletto, D., Pearson, R.G., Pena, J.L.M., Pennington, R.T., Peres, C.A., Permana, A., Petronelli, P., Peñuela Mora, M.C., Phillips, J.F., Phillips, O.L., Pickavance, G., Piedade, M.T.F., Pitman, N.C.A., Ploton, P., Popelier, A., Poulsen, J.R., Prieto, A., Primack, R.B., Priyadi, H., Qie, L., Quaresma, A.C., De Queiroz, H.L., Ramirez-Angulo, H., Ramos, J.F., Reis, N.F.C., Reitsma, J., Revilla, J.D.C., Riutta, T., Rivas-Torres, G., Robiansyah, I., Rocha, M., Rodrigues, D.D.J., Rodriguez-Ronderos, M.E., Rovero, F., Rozak, A.H., Rudas, A., Rutishauser, E., Sabatier, D., Sagang, L.B., Sampaio, A.F., Samsoedin, I., Satdichanh, M., Schietti, J., Schöngart, J., Scudeller, V.V., Seuaturien, N., Sheil, D., Sierra, R., Silman, M.R., Silva, T.S.F., Da Silva Guimarães, J.R., Simo-Droissart, M., Simon, M.F., Sist, P., Sousa, T.R., De Sousa Farias, E., De Souza Coelho, L., Spracklen, D.V., Stas, S.M., Steinmetz, R., Stevenson, P.R., Stropp, J., Sukri, R.S., Sunderland, T.C.H., Suzuki, E., Swaine, M.D., Tang, J., Taplin, J., Taylor, D.M., Tello, J.S., Terborgh, J., Texier, N., Theilade, I., Thomas, D.W., Thomas, R., Thomas, S.C., Tirado, M., Toirambe, B., De Toledo, J.J., Tomlinson, K.W., Torres-Lezama, A., Tran, H.D., Tshibamba Mukendi, J., Tumaneng, R.D., Umaña, M.N., Umunay, P.M., Urrego Giraldo, L.E., Valderrama Sandoval, E.H., Valenzuela Gamarra, L., Van Andel, T.R., Van De Bult, M., Van De Pol, J., Van Der Heijden, G., Vasquez, R., Vela, C.I.A., Venticinque, E.M., Verbeeck, H., Veridiano, R.K.A., Vicentini, A., Vieira, I.C.G., Vilanova Torre, E., Villarroel, D., Villa Zegarra, B.E., Vleminckx, J., Von Hildebrand, P., Vos, V.A., Vriesendorp, C., Webb, E.L., White, L.J.T., Wich, S., Wittmann, F., Zagt, R., Zang, R., Zartman, C.E., Zemagho, L., Zent, E.L., Zent,

S., 2024. Consistent patterns of common species across tropical tree communities. Nature 625, 728–734. https://doi.org/10.1038/s41586-023-06820-z

Corlett, R., Primack, R., 2006. Tropical rainforests and the need for cross-continental comparisons. Trends in Ecology & Evolution 21, 104–110. https://doi.org/10.1016/j.tree.2005.12.002

Coverdale, T.C., Davies, A.B., 2023. Unravelling the relationship between plant diversity and vegetation structural complexity: A review and theoretical framework. Journal of Ecology 111, 1378–1395. https://doi.org/10.1111/1365-2745.14068

Crockett, E.T.H., Atkins, J.W., Guo, Q., Sun, G., Potter, K.M., Ollinger, S., Silva, C.A., Tang, H., Woodall, C.W., Holgerson, J., Xiao, J., 2023. Structural and species diversity explain aboveground carbon storage in forests across the United States: Evidence from GEDI and forest inventory data. Remote Sensing of Environment 295, 113703. https://doi.org/10.1016/j.rse.2023.113703

Culmsee, H., Leuschner, C., Moser, G., Pitopang, R., 2010. Forest aboveground biomass along an elevational transect in Sulawesi, Indonesia, and the role of Fagaceae in tropical montane rain forests. Journal of Biogeography 37, 960–974. https://doi.org/10.1111/j.1365-2699.2009.02269.x

De Bruin, S., Brus, D.J., Heuvelink, G.B.M., Van Ebbenhorst Tengbergen, T., Wadoux, A.M.J.-C., 2022. Dealing with clustered samples for assessing map accuracy by cross-validation. Ecological Informatics 69, 101665. https://doi.org/10.1016/j.ecoinf.2022.101665

De Conto, T., Armston, J., Dubayah, R., 2024. Characterizing the structural complexity of the Earth's forests with spaceborne lidar. Nat Commun 15, 8116. https://doi.org/10.1038/s41467-024-52468-2

Deng, X., Schmid, B., Bruelheide, H., Chen, C., Li, Y., Li, S., Morsdorf, F., Ray, T., Schuman, M.C., Tang, T., Von Oheimb, G., Ma, K., Liu, X., 2025a. Forest biodiversity increases productivity via complementarity from greater canopy structural complexity. Proc. Natl. Acad. Sci. U.S.A. 122, e2506750122. https://doi.org/10.1073/pnas.2506750122

Deng, X., Schmid, B., Bruelheide, H., Chen, C., Li, Y., Li, S., Morsdorf, F., Ray, T., Schuman, M.C., Tang, T., Von Oheimb, G., Ma, K., Liu, X., 2025b. Forest biodiversity increases productivity via complementarity from greater canopy structural complexity. Proc. Natl. Acad. Sci. U.S.A. 122, e2506750122. https://doi.org/10.1073/pnas.2506750122

Dhargay, S., Lyell, C.S., Brown, T.P., Inbar, A., Sheridan, G.J., Lane, P.N.J., 2022. Performance of GEDI Space-Borne LiDAR for Quantifying Structural Variation in the Temperate Forests of South-Eastern Australia. Remote Sensing 14, 3615. https://doi.org/10.3390/rs14153615

Dong, H., Xu, Z., Wu, J., Lan, T., Wang, L., Shao, G., Tang, L., 2025. High-precision airborne LiDAR remains essential for urban forestry: Revealing the limitations of recent large-scale canopy height products in urban contexts. International Journal of Applied Earth Observation and Geoinformation 143, 104791. https://doi.org/10.1016/j.jag.2025.104791

Dormann, C.F., Elith, J., Bacher, S., Buchmann, C., Carl, G., Carré, G., Marquéz, J.R.G., Gruber, B., Lafourcade, B., Leitão, P.J., Münkemüller, T., McClean, C., Osborne, P.E., Reineking, B., Schröder, B., Skidmore, A.K., Zurell, D., Lautenbach, S., 2013. Collinearity: a review of methods to deal with it and a simulation study evaluating their performance. Ecography 36, 27–46. https://doi.org/10.1111/j.1600-0587.2012.07348.x

Dormann, C.F., McPherson, J., Araújo, M., Bivand, R., Bolliger, J., Carl, G., G. Davies, R., Hirzel, A., Jetz, W., Daniel Kissling, W., Kühn, I., Ohlemüller, R., R. Peres-Neto, P., Reineking, B., Schröder, B., M. Schurr, F., Wilson, R., 2007. Methods to account for spatial autocorrelation in the analysis of species distributional data: a review. Ecography 30, 609–628. https://doi.org/10.1111/j.2007.0906-7590.05171.x

Dubayah, R., Blair, J.B., Goetz, S., Fatoyinbo, L., Hansen, M., Healey, S., Hofton, M., Hurtt, G., Kellner, J., Luthcke, S., Armston, J., Tang, H., Duncanson, L., Hancock, S., Jantz, P., Marselis, S., Patterson, P.L., Qi, W., Silva, C., 2020. The Global Ecosystem Dynamics Investigation: High-resolution laser ranging of the Earth's forests and topography. Science of Remote Sensing 1, 100002. https://doi.org/10.1016/j.srs.2020.100002

Dubayah, R.O., Armston, J., Healey, S.P., Yang, Z., Patterson, P.L., Saarela, S., Stahl, G., Duncanson, L., Kellner, J.R., Bruening, J., Pascual, A., 2023a. Global Ecosystem Dynamics Investigation (GEDI)GEDI L4B Gridded Aboveground Biomass Density, Version 2.1. https://doi.org/10.3334/ORNLDAAC/2299

Dubayah, R.O., Armston, J., Healey, S.P., Yang, Z., Patterson, P.L., Saarela, S., Stahl, G., Duncanson, L., Kellner, J.R., Bruening, J.M., Pascual, A., 2023b. Global Ecosystem Dynamics Investigation (GEDI)GEDI L4B Gridded Aboveground Biomass Density, Version 2.1. https://doi.org/10.3334/ORNLDAAC/2299

Dubayah, R.O., Drake, J.B., 2000. Lidar Remote Sensing for Forestry. Journal of Forestry 98, 44–46. https://doi.org/10.1093/jof/98.6.44

Duncanson, L., Kellner, J.R., Armston, J., Dubayah, R., Minor, D.M., Hancock, S., Healey, S.P., Patterson, P.L., Saarela, S., Marselis, S., Silva, C.E., Bruening, J., Goetz, S.J., Tang, H., Hofton, M., Blair, B., Luthcke, S., Fatoyinbo, L., Abernethy, K., Alonso, A., Andersen, H.-E., Aplin, P., Baker, T.R., Barbier, N., Bastin, J.F., Biber, P., Boeckx, P., Bogaert, J., Boschetti, L., Boucher, P.B., Boyd, D.S., Burslem, D.F.R.P., Calvo-Rodriguez, S., Chave, J., Chazdon, R.L., Clark, D.B., Clark, D.A., Cohen, W.B., Coomes, D.A., Corona, P., Cushman, K.C., Cutler,

M.E.J., Dalling, J.W., Dalponte, M., Dash, J., de-Miguel, S., Deng, S., Ellis, P.W., Erasmus, B., Fekety, P.A., Fernandez-Landa, A., Ferraz, A., Fischer, R., Fisher, A.G., García-Abril, A., Gobakken, T., Hacker, J.M., Heurich, M., Hill, R.A., Hopkinson, C., Huang, H., Hubbell, S.P., Hudak, A.T., Huth, A., Imbach, B., Jeffery, K.J., Katoh, M., Kearsley, E., Kenfack, D., Kljun, N., Knapp, N., Král, K., Krůček, M., Labrière, N., Lewis, S.L., Longo, M., Lucas, R.M., Main, R., Manzanera, J.A., Martínez, R.V., Mathieu, R., Memiaghe, H., Meyer, V., Mendoza, A.M., Monerris, A., Montesano, P., Morsdorf, F., Næsset, E., Naidoo, L., Nilus, R., O'Brien, M., Orwig, D.A., Papathanassiou, K., Parker, G., Philipson, C., Phillips, O.L., Pisek, J., Poulsen, J.R., Pretzsch, H., Rüdiger, C., Saatchi, S., Sanchez-Azofeifa, A., Sanchez-Lopez, N., Scholes, R., Silva, C.A., Simard, M., Skidmore, A., Stereńczak, K., Tanase, M., Torresan, C., Valbuena, R., Verbeeck, H., Vrska, T., Wessels, K., White, J.C., White, L.J.T., Zahabu, E., Zgraggen, C., 2022. Aboveground biomass density models for NASA's Global Ecosystem Dynamics Investigation (GEDI) lidar mission. Remote Sensing of Environment 270, 112845. https://doi.org/10.1016/j.rse.2021.112845

Dwiputra, A., Coops, N.C., Schwartz, N.B., 2023. GEDI waveform metrics in vegetation mapping—a case study from a heterogeneous tropical forest landscape. Environ. Res. Lett. 18, 015007. https://doi.org/10.1088/1748-9326/acad8d

Ediriweera, S., Singhakumara, B.M.P., Ashton, M.S., 2008. Variation in canopy structure, light and soil nutrition across elevation of a Sri Lankan tropical rain forest. Forest Ecology and Management 256, 1339–1349. https://doi.org/10.1016/j.foreco.2008.06.035

Ehbrecht, M., Seidel, D., Annighöfer, P., Kreft, H., Köhler, M., Zemp, D.C., Puettmann, K., Nilus, R., Babweteera, F., Willim, K., Stiers, M., Soto, D., Boehmer, H.J., Fisichelli, N., Burnett, M., Juday, G., Stephens, S.L., Ammer, C., 2021. Global patterns and climatic controls of forest structural complexity. Nat Commun 12, 519. https://doi.org/10.1038/s41467-020-20767-z

Espírito-Santo, F.D.B., Gloor, M., Keller, M., Malhi, Y., Saatchi, S., Nelson, B., Junior, R.C.O., Pereira, C., Lloyd, J., Frolking, S., Palace, M., Shimabukuro, Y.E., Duarte, V., Mendoza, A.M., López-González, G., Baker, T.R., Feldpausch, T.R., Brienen, R.J.W., Asner, G.P., Boyd, D.S., Phillips, O.L., 2014. Size and frequency of natural forest disturbances and the Amazon forest carbon balance. Nat Commun 5, 3434. https://doi.org/10.1038/ncomms4434

Fahey, R.T., Atkins, J.W., Gough, C.M., Hardiman, B.S., Nave, L.E., Tallant, J.M., Nadehoffer, K.J., Vogel, C., Scheuermann, C.M., Stuart-Haëntjens, E., Haber, L.T., Fotis, A.T., Ricart, R., Curtis, P.S., 2019. Defining a spectrum of integrative trait-based vegetation canopy structural types. Ecology Letters 22, 2049–2059. https://doi.org/10.1111/ele.13388

Fang, H., Baret, F., Plummer, S., Schaepman-Strub, G., 2019. An Overview of Global Leaf Area Index (LAI): Methods, Products, Validation, and Applications. Reviews of Geophysics 57, 739–799. https://doi.org/10.1029/2018RG000608

Fang, H., Li, W., Wei, S., Jiang, C., 2014. Seasonal variation of leaf area index (LAI) over paddy rice fields in NE China: Intercomparison of destructive sampling, LAI-2200, digital hemispherical photography (DHP), and AccuPAR methods. Agricultural and Forest Meteorology 198–199, 126–141. https://doi.org/10.1016/j.agrformet.2014.08.005

Fatoyinbo, T., Armston, J., Simard, M., Saatchi, S., Denbina, M., Lavalle, M., Hofton, M., Tang, H., Marselis, S., Pinto, N., Hancock, S., Hawkins, B., Duncanson, L., Blair, B., Hansen, C., Lou, Y., Dubayah, R., Hensley, S., Silva, C., Poulsen, J.R., Labrière, N., Barbier, N., Jeffery, K., Kenfack, D., Herve, M., Bissiengou, P., Alonso, A., Moussavou, G., White, L.T.J., Lewis, S., Hibbard, K., 2021. The NASA AfriSAR campaign: Airborne SAR and lidar measurements of tropical forest structure and biomass in support of current and future space missions. Remote Sensing of Environment 264, 112533. https://doi.org/10.1016/j.rse.2021.112533

Fayad, I., Baghdadi, N., Alcarde Alvares, C., Stape, J.L., Bailly, J.S., Scolforo, H.F., Cegatta, I.R., Zribi, M., Le Maire, G., 2021a. Terrain Slope Effect on Forest Height and Wood Volume Estimation from GEDI Data. Remote Sensing 13, 2136. https://doi.org/10.3390/rs13112136

Fayad, I., Baghdadi, N., Riedi, J., 2021b. Quality Assessment of Acquired GEDI Waveforms: Case Study over France, Tunisia and French Guiana. Remote Sensing 13, 3144. https://doi.org/10.3390/rs13163144

Fayolle, A., Loubota Panzou, G.J., Drouet, T., Swaine, M.D., Bauwens, S., Vleminckx, J., Biwole, A., Lejeune, P., Doucet, J.-L., 2016. Taller trees, denser stands and greater biomass in semi-deciduous than in evergreen lowland central African forests. Forest Ecology and Management 374, 42–50. https://doi.org/10.1016/j.foreco.2016.04.033

Feldpausch, T.R., Banin, L., Phillips, O.L., Baker, T.R., Lewis, S.L., Quesada, C.A., Affum-Baffoe, K., Arets, E.J.M.M., Berry, N.J., Bird, M., Brondizio, E.S., De Camargo, P., Chave, J., Djagbletey, G., Domingues, T.F., Drescher, M., Fearnside, P.M., França, M.B., Fyllas, N.M., Lopez-Gonzalez, G., Hladik, A., Higuchi, N., Hunter, M.O., Iida, Y., Salim, K.A., Kassim, A.R., Keller, M., Kemp, J., King, D.A., Lovett, J.C., Marimon, B.S., Marimon-Junior, B.H., Lenza, E., Marshall, A.R., Metcalfe, D.J., Mitchard, E.T.A., Moran, E.F., Nelson, B.W., Nilus, R., Nogueira, E.M., Palace, M., Patiño, S., Peh, K.S.-H., Raventos, M.T., Reitsma, J.M., Saiz, G., Schrodt, F., Sonké, B., Taedoumg, H.E., Tan, S., White, L., Wöll, H., Lloyd, J., 2011. Height-diameter allometry of tropical forest trees. Biogeosciences 8, 1081–1106. https://doi.org/10.5194/bg-8-1081-2011

Ferraz, A., Saatchi, S., Xu, L., Hagen, S., Chave, J., Yu, Y., Meyer, V., Garcia, M., Silva, C., Roswintiart, O., Samboko, A., Sist, P., Walker, S., Pearson, T.R.H., Wijaya, A., Sullivan, F.B., Rutishauser, E., Hoekman, D., Ganguly, S., 2018. Carbon storage potential in degraded forests of Kalimantan, Indonesia. Environ. Res. Lett. 13, 095001. https://doi.org/10.1088/1748-9326/aad782

Ferris, R., Humphrey, J., 1999. A review of potential biodiversity indicators for application in British forests. Forestry 72, 313–328. https://doi.org/10.1093/forestry/72.4.313

Filippi, P., Jones, E.J., Wimalathunge, N.S., Somarathna, P.D.S.N., Pozza, L.E., Ugbaje, S.U., Jephcott, T.G., Paterson, S.E., Whelan, B.M., Bishop, T.F.A., 2019. An approach to forecast grain crop yield using multi-layered, multi-farm data sets and machine learning. Precision Agric 20, 1015–1029. https://doi.org/10.1007/s11119-018-09628-4

Finegan, B., Peña-Claros, M., De Oliveira, A., Ascarrunz, N., Bret-Harte, M.S., Carreño-Rocabado, G., Casanoves, F., Díaz, S., Eguiguren Velepucha, P., Fernandez, F., Licona, J.C., Lorenzo, L., Salgado Negret, B., Vaz, M., Poorter, L., 2015. Does functional trait diversity predict above-ground biomass and productivity of tropical forests? Testing three alternative hypotheses. Journal of Ecology 103, 191–201. https://doi.org/10.1111/1365-2745.12346

Fischer, F.J., Jackson, T., Vincent, G., Jucker, T., 2024. Robust characterisation of forest structure from airborne laser scanning—A systematic assessment and sample workflow for ecologists. Methods Ecol Evol 15, 1873–1888. https://doi.org/10.1111/2041-210X.14416

Fischer, F.J., Morgan, B., Jackson, T., Chave, J., Coomes, D., Cushman, K., Dalagnol, R., Dalponte, M., Duncanson, L., Saatchi, S., Seidl, R., Stereńczak, K., Laurin, G.V., Adu-Bredu, S., Aguirre-Gutiérrez, J., Antonielli, B., Armston, J.D., De Assis, M.L., Barbier, N., Burt, A., César, R.G., Cervenka, J., Coops, N., Cullen, L., Dalling, J.W., Davies, A., Demol, M., Ebenbeck, J., Fassnacht, F., Fatoyinbo, L., García, M., Gasparri, N.I., Gobakken, T., Goodbody, T.R.H., Görgens, E.B., Gorum, T., Gosper, C., Guan, H., Heiskanen, J., Heurich, M., Hobi, M., Höfle, B., Hooijer, A., Huth, A., Kedrov, A., Kellner, J.R., Koenig, S., Král, K., Krassovski, M., Kuechly, H., Krůček, M., Htoo, K.K., Labrière, N., Lai, D., Larson, J., Laudon, H., Lemke, D., Lenoir, J., Malhi, Y., Malik, O.A., Martin, M., McNicol, I., Milenkovic, M., Minor, D., Mitchard, E., Moudrý, V., Muller-Landau, H.C., Næsset, E., Nathalang, A., Ometto, J.P., Onishi, M., Onoda, Y., Pellikka, P., Persson, H., Ferreira, M.P., Ploton, P., Prober, S.M., Rahman, F., Rana, P., Réjou-Méchain, M., Schäfer, J., Senf, C., Shapiro, A., Schepaschenko, D., Shen, G., Silman, M., Silva, T., Singh, J., Slik, F., Stillhard, J., Subash, A., Takeshige, R., Tao, S., Tenorio, E., Tokola, T., Tompalski, P., Tripathi, N., Valbuena, R., Valentini, R., Vernimmen, R., Vincent, G., Wallerman, J., Jaafar, W.S.W.M., Wang, Y., Weiser, H., White, J., Winiwarter, L., Wulder, M., Yuan, Z., Zdunic, K.,

Zeng, Y., Zhang, H., Zhang, J., Zhang, Z., Jucker, T., 2025a. The Global Canopy Atlas: analysis-ready maps of 3D structure for the world's woody ecosystems. https://doi.org/10.1101/2025.08.31.673375

Fischer, F.J., Morgan, B., Jackson, T., Chave, J., Coomes, D., Dalagnol, R., Dalponte, M., Duncanson, L., Saatchi, S., Seidl, R., Stereńczak, K., Laurin, G.V., Adu-Bredu, S., Barbier, N., Burt, A., César, R.G., Cervenka, J., Cullen, L., Dalling, J.W., Davies, A., Fassnacht, F., Fatoyinbo, L., García, M., Gasparri, N.I., Gobakken, T., Goodbody, T.R.H., Görgens, E.B., Gorum, T., Guan, H., Heiskanen, J., Heurich, M., Hobi, M., Höfle, B., Hooijer, A., Huth, A., Kedrov, A., Kellner, J.R., Koenig, S., Král, K., Krassovski, M., Kuechly, H., Krůček, M., Htoo, K.K., Labrière, N., Lai, D., Larson, J., Laudon, H., Lemke, D., Lenoir, J., Malhi, Y., Malik, O.A., McNicol, I., Milenkovic, M., Minor, D., Mitchard, E., Muller-Landau, H.C., Onishi, M., Onoda, Y., Pellikka, P., Persson, H., Ferreira, P., Ploton, P., Prober, S.M., Rahman, F., Réjou-Méchain, M., Schäfer, J., Senf, C., Shapiro, A., Schepaschenko, D., Shen, G., Silman, M., Silva, T., Singh, J., Slik, F., Stillhard, J., Subash, A., Takeshige, R., Tao, S., Tokola, T., Tompalski, P., Tripathi, N., Valbuena, R., Vernimmen, R., Vincent, G., Wallerman, J., Wan, W.S., Jaafar, M., Wang, Y., Weiser, H., White, J., Winiwarter, L., Wulder, M., Yuan, Z., Zdunic, K., Zeng, Y., Zhang, H., Zhang, J., Zhang, Z., Jucker, T., 2025b. The Global Canopy Atlas: analysis-ready maps of 3D structure for the world's woody ecosystems.

Fradette, M.-S., Leboeuf, A., Riopel, M., Bégin, J., 2019. Method to Reduce the Bias on Digital Terrain Model and Canopy Height Model from LiDAR Data. Remote Sensing 11, 863. https://doi.org/10.3390/rs11070863

Frankenberg, C., Bar-On, Y.M., Yin, Y., Wennberg, P.O., Jacob, D.J., Michalak, A.M., 2024. Data Drought in the Humid Tropics: How to Overcome the Cloud Barrier in Greenhouse Gas Remote Sensing. Geophysical Research Letters 51, e2024GL108791. https://doi.org/10.1029/2024GL108791

Franklin, J.F., Spies, T.A., Pelt, R.V., Carey, A.B., Thornburgh, D.A., Berg, D.R., Lindenmayer, D.B., Harmon, M.E., Keeton, W.S., Shaw, D.C., Bible, K., Chen, J., 2002. Disturbances and structural development of natural forest ecosystems with silvicultural implications, using Douglas-fir forests as an example. Forest Ecology and Management 155, 399–423. https://doi.org/10.1016/S0378-1127(01)00575-8

Friedlingstein, P., O'Sullivan, M., Jones, M.W., Andrew, R.M., Gregor, L., Hauck, J., Le Quéré, C., Luijkx, I.T., Olsen, A., Peters, G.P., Peters, W., Pongratz, J., Schwingshackl, C., Sitch, S., Canadell, J.G., Ciais, P., Jackson, R.B., Alin, S.R., Alkama, R., Arneth, A., Arora, V.K., Bates, N.R., Becker, M., Bellouin, N., Bittig, H.C., Bopp, L., Chevallier, F., Chini, L.P., Cronin, M., Evans, W., Falk, S., Feely, R.A., Gasser, T., Gehlen, M., Gkritzalis, T., Gloege, L., Grassi, G., Gruber, N., Gürses, Ö., Harris, I., Hefner, M., Houghton, R.A., Hurtt, G.C., Iida, Y., Ilyina, T., Jain, A.K., Jersild, A., Kadono, K., Kato, E., Kennedy, D., Klein Goldewijk, K.,

Knauer, J., Korsbakken, J.I., Landschützer, P., Lefèvre, N., Lindsay, K., Liu, J., Liu, Z., Marland, G., Mayot, N., McGrath, M.J., Metzl, N., Monacci, N.M., Munro, D.R., Nakaoka, S.-I., Niwa, Y., O'Brien, K., Ono, T., Palmer, P.I., Pan, N., Pierrot, D., Pocock, K., Poulter, B., Resplandy, L., Robertson, E., Rödenbeck, C., Rodriguez, C., Rosan, T.M., Schwinger, J., Séférian, R., Shutler, J.D., Skjelvan, I., Steinhoff, T., Sun, Q., Sutton, A.J., Sweeney, C., Takao, S., Tanhua, T., Tans, P.P., Tian, X., Tian, H., Tilbrook, B., Tsujino, H., Tubiello, F., Van Der Werf, G.R., Walker, A.P., Wanninkhof, R., Whitehead, C., Willstrand Wranne, A., Wright, R., Yuan, W., Yue, C., Yue, X., Zaehle, S., Zeng, J., Zheng, B., 2022. Global Carbon Budget 2022. Earth Syst. Sci. Data 14, 4811–4900. https://doi.org/10.5194/essd-14-4811-2022

Garcia-Martí, I., Zurita-Milla, R., Swart, A., Van Den Wijngaard, K.C., Van Vliet, A.J.H., Bennema, S., Harms, M., 2017. Identifying Environmental and Human Factors Associated With Tick Bites using Volunteered Reports and Frequent Pattern Mining. Transactions in GIS 21, 277–299. https://doi.org/10.1111/tgis.12211

Gardner, T.A., Barlow, J., Chazdon, R., Ewers, R.M., Harvey, C.A., Peres, C.A., Sodhi, N.S., 2009. Prospects for tropical forest biodiversity in a human-modified world. Ecology Letters 12, 561–582. https://doi.org/10.1111/j.1461-0248.2009.01294.x

Garrigues, S., Lacaze, R., Baret, F., Morisette, J.T., Weiss, M., Nickeson, J.E., Fernandes, R., Plummer, S., Shabanov, N.V., Myneni, R.B., Knyazikhin, Y., Yang, W., 2008. Validation and intercomparison of global Leaf Area Index products derived from remote sensing data. J. Geophys. Res. 113, 2007JG000635. https://doi.org/10.1029/2007JG000635

Goodman, R.C., Phillips, O.L., Baker, T.R., 2014. The importance of crown dimensions to improve tropical tree biomass estimates. Ecological Applications 24, 680–698. https://doi.org/10.1890/13-0070.1

Gringarten, E., Deutsch, C.V., 2001. Teacher's Aide Variogram Interpretation and Modeling. Mathematical Geology.

Guo, Z., Tang, J., Lai, G., Liu, L., Wang, X., 2025. Structural diversity drives forest biomass along altitudinal gradients in subtropical forests. Journal Of Plant Ecology 18, rtaf100. https://doi.org/10.1093/jpe/rtaf100

Gupta, R., Sharma, L.K., 2022. Mixed tropical forests canopy height mapping from spaceborne LiDAR GEDI and multisensor imagery using machine learning models. Remote Sensing Applications: Society and Environment 27, 100817. https://doi.org/10.1016/j.rsase.2022.100817

Habib, E., Haile, A., Sazib, N., Zhang, Y., Rientjes, T., 2014. Effect of Bias Correction of Satellite-Rainfall Estimates on Runoff Simulations at the Source of the Upper Blue Nile. Remote Sensing 6, 6688–6708. https://doi.org/10.3390/rs6076688

Hansen, M.C., Roy, D.P., Lindquist, E., Adusei, B., Justice, C.O., Altstatt, A., 2008. A method for integrating MODIS and Landsat data for systematic monitoring of forest cover and change in the Congo Basin. Remote Sensing of Environment 112, 2495–2513. https://doi.org/10.1016/j.rse.2007.11.012

Hardiman, B.S., LaRue, E.A., Atkins, J.W., Fahey, R.T., Wagner, F.W., Gough, C.M., 2018. Spatial Variation in Canopy Structure across Forest Landscapes. Forests 9, 474. https://doi.org/10.3390/f9080474

Hastie, T., Tibshirani, R., Friedman, J., 2009. Overview of Supervised Learning, in: The Elements of Statistical Learning, Springer Series in Statistics. Springer New York, New York, NY, pp. 9–41. https://doi.org/10.1007/978-0-387-84858-7_2

Hector, A., Schmid, B., Beierkuhnlein, C., Caldeira, M.C., Diemer, M., Dimitrakopoulos, P.G., Finn, J.A., Freitas, H., Giller, P.S., Good, J., Harris, R., Högberg, P., Huss-Danell, K., Joshi, J., Jumpponen, A., Körner, C., Leadley, P.W., Loreau, M., Minns, A., Mulder, C.P.H., O'Donovan, G., Otway, S.J., Pereira, J.S., Prinz, A., Read, D.J., Scherer-Lorenzen, M., Schulze, E.-D., Siamantziouras, A.-S.D., Spehn, E.M., Terry, A.C., Troumbis, A.Y., Woodward, F.I., Yachi, S., Lawton, J.H., 1999. Plant Diversity and Productivity Experiments in European Grasslands. Science 286, 1123–1127. https://doi.org/10.1126/science.286.5442.1123

Hirschmugl, M., Lippl, F., Sobe, C., 2023. Assessing the Vertical Structure of Forests Using Airborne and Spaceborne LiDAR Data in the Austrian Alps. Remote Sensing 15, 664. https://doi.org/10.3390/rs15030664

Hofton, M., Blair, J.B., 2019. Algorithm Theoretical Basis Document (ATBD).

Hordijk, I., Maynard, D.S., Hart, S.P., Lidong, M., Ter Steege, H., Liang, J., de-Miguel, S., Nabuurs, G., Reich, P.B., Abegg, M., Adou Yao, C.Y., Alberti, G., Almeyda Zambrano, A.M., Alvarado, B.V., Esteban, A., Alvarez-Loayza, P., Alves, L.F., Ammer, C., Antón-Fernández, C., Araujo-Murakami, A., Arroyo, L., Avitabile, V., Aymard C, G.A., Baker, T., Bałazy, R., Banki, O., Barroso, J., Bastian, M.L., Bastin, J., Birigazzi, L., Birnbaum, P., Bitariho, R., Boeckx, P., Bongers, F., Bouriaud, O., Brancalion, P.H.S., Brandl, S., Brienen, R., Broadbent, E.N., Bruelheide, H., Bussotti, F., Cazzolla Gatti, R., César, R.G., Cesljar, G., Chazdon, R., Chen, H.Y.H., Chisholm, C., Cienciala, E., Clark, C.J., Clark, D.B., Colletta, G., Coomes, D., Cornejo Valverde, F., Corral-Rivas, J.J., Crim, P., Cumming, J., Dayanandan, S., De Gasper, A.L., Decuyper, M., Derroire, G., DeVries, B., Djordjevic, I., Iêda, A., Dourdain, A., Nestor Laurier, E.O., Enquist, B., Eyre, T., Fandohan, A.B., Fayle, T.M., Ferreira, L.V., Feldpausch, T.R., Finér, L., Fischer, M., Fletcher, C., Frizzera, L., Gamarra, J.G.P., Gianelle, D., Glick, H.B., Harris, D., Hector, A., Hemp, A., Hengeveld, G., Hérault, B., Herbohn, J., Hillers, A., Honorio Coronado, E.N., Hui, C., Cho, H., Ibanez, T., Bin Jung, I., Imai, N., Jagodzinski, A.M., Jaroszewicz, B., Johanssen,

V., Joly, C.A., Jucker, T., Karminov, V., Kartawinata, K., Kearsley, E., Kenfack, D., Kennard, D., Kepfer-Rojas, S., Keppel, G., Khan, M.L., Killeen, T., Kim, H.S., Kitayama, K., Köhl, M., Korjus, H., Kraxner, F., Laarmann, D., Lang, M., Lewis, S., Lu, H., Lukina, N., Maitner, B., Malhi, Y., Marcon, E., Marimon, B.S., Marimon-Junior, B.H., Marshall, A.R., Martin, E., Martynenko, O., Meave, J.A., Melo-Cruz, O., Mendoza, C., Merow, C., Miscicki, S., Mendoza, A.M., Moreno, V., Mukul, S.A., Mundhenk, P., Nava-Miranda, M.G., Neill, D., Neldner, V., Nevenic, R., Ngugi, M., Niklaus, P.A., Oleksyn, J., Ontikov, P., Ortiz-Malavasi, E., Pan, Y., Paquette, A., Parada-Gutierrez, A., Parfenova, E., Park, M., Parren, M., Parthasarathy, N., Peri, P.L., Pfautsch, S., Phillips, O.L., Picard, N., Piedade, M.T., Piotto, D., Pitman, N.C.A., Polo, I., Poorter, L., Poulsen, A.D., Poulsen, J.R., Pretzsch, H., Ramirez Arevalo, F., Restrepo-Correa, Z., Rodeghiero, M., Rolim, S., Roopsind, A., Rovero, F., Rutishauser, E., Saikia, P., Salas-Eljatib, C., Schall, P., Schepaschenko, D., Scherer-Lorenzen, M., Schmid, B., Schöngart, J., Searle, E.B., Šebeň, V., Serra-Diaz, J.M., Sheil, D., Shvidenko, A., Silva-Espejo, J., Silveira, M., Singh, J., Sist, P., Slik, F., Sonké, B., Souza, A.F., Stereńczak, K., Svenning, J., Svoboda, M., Swanepoel, B., Targhetta, N., Tchebakova, N., Thomas, R., Tikhonova, E., Umunay, P., Usoltsev, V., Valencia, R., Valladares, F., Van Der Plas, F., Tran, D.V., Van Nuland, M.E., Vasquez Martinez, R., Verbeeck, H., Viana, H., Vibrans, A.C., Vieira, S., Von Gadow, K., Wang, H., Watson, J., Werner, G.D.A., Wiser, S.K., Wittmann, F., Wortel, V., Zagt, R., Zawila-Niedzwiecki, T., Zhang, C., Zhao, X., Zhou, M., Zhu, Z., Zo-Bi, I.C., Crowther, T.W., 2023. Evenness mediates the global relationship between forest productivity and richness. Journal of Ecology 111, 1308–1326. https://doi.org/10.1111/1365-2745.14098

Horn, B.K.P., 1981. Hill shading and the reflectance map. Proc. IEEE 69, 14–47. https://doi.org/10.1109/PROC.1981.11918

Huang, H., Li, X., Chen, C., 2018. Individual Tree Crown Detection and Delineation From Very-High-Resolution UAV Images Based on Bias Field and Marker-Controlled Watershed Segmentation Algorithms. IEEE J. Sel. Top. Appl. Earth Observations Remote Sensing 11, 2253–2262. https://doi.org/10.1109/JSTARS.2018.2830410

Huang, K., Xia, J., 2019. High ecosystem stability of evergreen broadleaf forests under severe droughts. Global Change Biology 25, 3494–3503. https://doi.org/10.1111/gcb.14748

Huang, M., Xu, Y., Longo, M., Keller, M., Knox, R.G., Koven, C.D., Fisher, R.A., 2020. Assessing impacts of selective logging on water, energy, and carbon budgets and ecosystem dynamics in Amazon forests using the Functionally Assembled Terrestrial Ecosystem Simulator. Biogeosciences 17, 4999–5023. https://doi.org/10.5194/bg-17-4999-2020

Hubau, W., Lewis, S.L., Phillips, O.L., Affum-Baffoe, K., Beeckman, H., Cuní-Sanchez, A., Daniels, A.K., Ewango, C.E.N., Fauset, S., Mukinzi, J.M., Sheil, D., Sonké, B., Sullivan, M.J.P., Sunderland, T.C.H., Taedoumg, H., Thomas, S.C., White, L.J.T., Abernethy, K.A., Adu-Bredu, S., Amani, C.A., Baker, T.R., Banin, L.F., Baya, F., Begne, S.K., Bennett, A.C., Benedet, F., Bitariho, R., Bocko, Y.E., Boeckx, P., Boundja, P., Brienen, R.J.W., Brncic, T., Chezeaux, E., Chuyong, G.B., Clark, C.J., Collins, M., Comiskey, J.A., Coomes, D.A., Dargie, G.C., de Haulleville, T., Kamdem, M.N.D., Doucet, J.-L., Esquivel-Muelbert, A., Feldpausch, T.R., Fofanah, A., Foli, E.G., Gilpin, M., Gloor, E., Gonmadje, C., Gourlet-Fleury, S., Hall, J.S., Hamilton, A.C., Harris, D.J., Hart, T.B., Hockemba, M.B.N., Hladik, A., Ifo, S.A., Jeffery, K.J., Jucker, T., Yakusu, E.K., Kearsley, E., Kenfack, D., Koch, A., Leal, M.E., Levesley, A., Lindsell, J.A., Lisingo, J., Lopez-Gonzalez, G., Lovett, J.C., Makana, J.-R., Malhi, Y., Marshall, A.R., Martin, J., Martin, E.H., Mbayu, F.M., Medjibe, V.P., Mihindou, V., Mitchard, E.T.A., Moore, S., Munishi, P.K.T., Bengone, N.N., Ojo, L., Ondo, F.E., Peh, K.S.-H., Pickavance, G.C., Poulsen, A.D., Poulsen, J.R., Qie, L., Reitsma, J., Rovero, F., Swaine, M.D., Talbot, J., Taplin, J., Taylor, D.M., Thomas, D.W., Toirambe, B., Mukendi, J.T., Tuagben, D., Umunay, P.M., van der Heijden, G.M.F., Verbeeck, H., Vleminckx, J., Willcock, S., Wöll, H., Woods, J.T., Zemagho, L., 2020. Asynchronous carbon sink saturation in African and Amazonian tropical forests. Nature 579, 80–87. https://doi.org/10.1038/s41586-020-2035-0

Hunter, M.O., Keller, M., Victoria, D., Morton, D.C., 2013. Tree height and tropical forest biomass estimation. Biogeosciences 10, 8385–8399. https://doi.org/10.5194/bg-10-8385-2013

Huston, M.A., 1997. Hidden treatments in ecological experiments: re-evaluating the ecosystem function of biodiversity. Oecologia 110, 449–460. https://doi.org/10.1007/s004420050180

Hwang, K., Zhai, L., 2026. Structural diversity shifts from negative to positive associations with forest productivity via basal area, stand age, and precipitation thresholds. Journal of Ecology 114, e70200. https://doi.org/10.1111/1365-2745.70200

Hyyppä, J., Hyyppä, H., Leckie, D., Gougeon, F., Yu, X., Maltamo, M., 2008. Review of methods of small-footprint airborne laser scanning for extracting forest inventory data in boreal forests. International Journal of Remote Sensing 29, 1339–1366. https://doi.org/10.1080/01431160701736489

Igel, C., Oehmcke, S., 2023. Remember to Correct the Bias When Using Deep Learning for Regression! Künstl Intell 37, 33–40. https://doi.org/10.1007/s13218-023-00801-0

Illarionova, S., Shadrin, D., Ignatiev, V., Shayakhmetov, S., Trekin, A., Oseledets, I., 2022. Estimation of the Canopy Height Model From Multispectral Satellite

Imagery With Convolutional Neural Networks. IEEE Access 10, 34116–34132. https://doi.org/10.1109/ACCESS.2022.3161568

Imhoff, M.L., 1995. Radar Backscatter and Biomass Saturation: Ramifications for Global Biomass Inventory.

Isbell, F.I., Polley, H.W., Wilsey, B.J., 2009. Biodiversity, productivity and the temporal stability of productivity: patterns and processes. Ecology Letters 12, 443–451. https://doi.org/10.1111/j.1461-0248.2009.01299.x

Isensee, F., Jaeger, P.F., Kohl, S.A.A., Petersen, J., Maier-Hein, K.H., 2021. nnU-Net: a self-configuring method for deep learning-based biomedical image segmentation. Nat Methods 18, 203–211. https://doi.org/10.1038/s41592-020-01008-z

Jackson, T.D., Fischer, F.J., Vincent, G., Gorgens, E.B., Keller, M., Chave, J., Jucker, T., Coomes, D.A., 2024. Tall Bornean forests experience higher canopy disturbance rates than those in the eastern Amazon or Guiana shield. Global Change Biology 30, e17493. https://doi.org/10.1111/gcb.17493

Jelinski, D.E., Wu, J., 1996. The modifiable areal unit problem and implications for landscape ecology. Landscape Ecol 11, 129–140. https://doi.org/10.1007/BF02447512

Jucker, T., Bongalov, B., Burslem, D.F.R.P., Nilus, R., Dalponte, M., Lewis, S.L., Phillips, O.L., Qie, L., Coomes, D.A., 2018. Topography shapes the structure, composition and function of tropical forest landscapes. Ecol Lett 21, 989–1000. https://doi.org/10.1111/ele.12964

Jucker, T., Bouriaud, O., Coomes, D.A., 2015. Crown plasticity enables trees to optimize canopy packing in mixed-species forests. Functional Ecology 29, 1078–1086. https://doi.org/10.1111/1365-2435.12428

Jucker, T., Caspersen, J., Chave, J., Antin, C., Barbier, N., Bongers, F., Dalponte, M., Van Ewijk, K.Y., Forrester, D.I., Haeni, M., Higgins, S.I., Holdaway, R.J., Iida, Y., Lorimer, C., Marshall, P.L., Momo, S., Moncrieff, G.R., Ploton, P., Poorter, L., Rahman, K.A., Schlund, M., Sonké, B., Sterck, F.J., Trugman, A.T., Usoltsev, V.A., Vanderwel, M.C., Waldner, P., Wedeux, B.M.M., Wirth, C., Wöll, H., Woods, M., Xiang, W., Zimmermann, N.E., Coomes, D.A., 2017. Allometric equations for integrating remote sensing imagery into forest monitoring programmes. Global Change Biology 23, 177–190. https://doi.org/10.1111/gcb.13388

Juntu, J., Sijbers, J., Dyck, D., Gielen, J., 2005. Bias Field Correction for MRI Images, in: Kurzyński, M., Puchała, E., Woźniak, M., Żołnierek, A. (Eds.), Computer Recognition Systems, Advances in Soft Computing. Springer Berlin Heidelberg, Berlin, Heidelberg, pp. 543–551. https://doi.org/10.1007/3-540-32390-2_64

Kalacska, M., Calvo-Alvarado, J.C., Sanchez-Azofeifa, G.A., 2005. Calibration and assessment of seasonal changes in leaf area index of a tropical dry forest in different stages of succession. Tree Physiology 25, 733–744. https://doi.org/10.1093/treephys/25.6.733

Kashongwe, H.B., Roy, D.P., Skole, D.L., 2023. Examination of the amount of GEDI data required to characterize central Africa tropical forest aboveground biomass at REDD+ project scale in Mai Ndombe province. Science of Remote Sensing 7, 100091. https://doi.org/10.1016/j.srs.2023.100091

Kattge, J., Bönisch, G., Díaz, S., Lavorel, S., Prentice, I.C., Leadley, P., Tautenhahn, S., Werner, G.D.A., Aakala, T., Abedi, M., Acosta, A.T.R., Adamidis, G.C., Adamson, K., Aiba, M., Albert, C.H., Alcántara, J.M., Alcázar C, C., Aleixo, I., Ali, H., Amiaud, B., Ammer, C., Amoroso, M.M., Anand, M., Anderson, C., Anten, N., Antos, J., Apgaua, D.M.G., Ashman, T., Asmara, D.H., Asner, G.P., Aspinwall, M., Atkin, O., Aubin, I., Baastrup-Spohr, L., Bahalkeh, K., Bahn, M., Baker, T., Baker, W.J., Bakker, J.P., Baldocchi, D., Baltzer, J., Banerjee, A., Baranger, A., Barlow, J., Barneche, D.R., Baruch, Z., Bastianelli, D., Battles, J., Bauerle, W., Bauters, M., Bazzato, E., Beckmann, M., Beeckman, H., Beierkuhnlein, C., Bekker, R., Belfry, G., Belluau, M., Beloiu, M., Benavides, R., Benomar, L., Berdugo-Lattke, M.L., Berenguer, E., Bergamin, R., Bergmann, J., Bergmann Carlucci, M., Berner, L., Bernhardt-Römermann, M., Bigler, C., Bjorkman, A.D., Blackman, C., Blanco, C., Blonder, B., Blumenthal, D., Bocanegra-González, K.T., Boeckx, P., Bohlman, S., Böhning-Gaese, K., Boisvert-Marsh, L., Bond, W., Bond-Lamberty, B., Boom, A., Boonman, C.C.F., Bordin, K., Boughton, E.H., Boukili, V., Bowman, D.M.J.S., Bravo, S., Brendel, M.R., Broadley, M.R., Brown, K.A., Bruelheide, H., Brumnich, F., Bruun, H.H., Bruy, D., Buchanan, S.W., Bucher, S.F., Buchmann, N., Buitenwerf, R., Bunker, D.E., Bürger, J., Burrascano, S., Burslem, D.F.R.P., Butterfield, B.J., Byun, C., Marques, M., Scalon, M.C., Caccianiga, M., Cadotte, M., Cailleret, M., Camac, J., Camarero, J.J., Campany, C., Campetella, G., Campos, J.A., Cano-Arboleda, L., Canullo, R., Carbognani, M., Carvalho, F., Casanoves, F., Castagneyrol, B., Catford, J.A., Cavender-Bares, J., Cerabolini, B.E.L., Cervellini, M., Chacón-Madrigal, E., Chapin, K., Chapin, F.S., Chelli, S., Chen, S., Chen, A., Cherubini, P., Chianucci, F., Choat, B., Chung, K., Chytrý, M., Ciccarelli, D., Coll, L., Collins, C.G., Conti, L., Coomes, D., Cornelissen, J.H.C., Cornwell, W.K., Corona, P., Coyea, M., Craine, J., Craven, D., Cromsigt, J.P.G.M., Csecserits, A., Cufar, K., Cuntz, M., Da Silva, A.C., Dahlin, K.M., Dainese, M., Dalke, I., Dalle Fratte, M., Dang-Le, A.T., Danihelka, J., Dannoura, M., Dawson, S., De Beer, A.J., De Frutos, A., De Long, J.R., Dechant, B., Delagrange, S., Delpierre, N., Derroire, G., Dias, A.S., Diaz-Toribio, M.H., Dimitrakopoulos, P.G., Dobrowolski, M., Doktor, D., Dřevojan, P., Dong, N., Dransfield, J., Dressler, S., Duarte, L., Ducouret, E., Dullinger, S., Durka, W., Duursma, R., Dymova, O., E-Vojtkó, A., Eckstein, R.L., Ejtehadi, H., Elser, J., Emilio, T., Engemann, K., Erfanian, M.B., Erfmeier, A., Esquivel-Muelbert, A., Esser, G., Estiarte, M., Domingues, T.F., Fagan, W.F., Fagúndez, J., Falster, D.S., Fan, Y., Fang, J., Farris, E., Fazlioglu, F., Feng, Y., Fernandez-

Mendez, F., Ferrara, C., Ferreira, J., Fidelis, A., Finegan, B., Firn, J., Flowers, T.J., Flynn, D.F.B., Fontana, V., Forey, E., Forgiarini, C., François, L., Frangipani, M., Frank, D., Frenette-Dussault, C., Freschet, G.T., Fry, E.L., Fyllas, N.M., Mazzochini, G.G., Gachet, S., Gallagher, R., Ganade, G., Ganga, F., García-Palacios, P., Gargaglione, V., Garnier, E., Garrido, J.L., De Gasper, A.L., Gea-Izquierdo, G., Gibson, D., Gillison, A.N., Giroldo, A., Glasenhardt, M., Gleason, S., Gliesch, M., Goldberg, E., Göldel, B., Gonzalez-Akre, E., Gonzalez-Andujar, J.L., González-Melo, A., González-Robles, A., Graae, B.J., Granda, E., Graves, S., Green, W.A., Gregor, T., Gross, N., Guerin, G.R., Günther, A., Gutiérrez, A.G., Haddock, L., Haines, A., Hall, J., Hambuckers, A., Han, W., Harrison, S.P., Hattingh, W., Hawes, J.E., He, T., He, P., Heberling, J.M., Helm, A., Hempel, S., Hentschel, J., Hérault, B., Hereş, A., Herz, K., Heuertz, M., Hickler, T., Hietz, P., Higuchi, P., Hipp, A.L., Hirons, A., Hock, M., Hogan, J.A., Holl, K., Honnay, O., Hornstein, D., Hou, E., Hough-Snee, N., Hovstad, K.A., Ichie, T., Igić, B., Illa, E., Isaac, M., Ishihara, M., Ivanov, L., Ivanova, L., Iversen, C.M., Izquierdo, J., Jackson, R.B., Jackson, B., Jactel, H., Jagodzinski, A.M., Jandt, U., Jansen, S., Jenkins, T., Jentsch, A., Jespersen, J.R.P., Jiang, G., Johansen, J.L., Johnson, D., Jokela, E.J., Joly, C.A., Jordan, G.J., Joseph, G.S., Junaedi, D., Junker, R.R., Justes, E., Kabzems, R., Kane, J., Kaplan, Z., Kattenborn, T., Kavelenova, L., Kearsley, E., Kempel, A., Kenzo, T., Kerkhoff, A., Khalil, M.I., Kinlock, N.L., Kissling, W.D., Kitajima, K., Kitzberger, T., Kjøller, R., Klein, T., Kleyer, M., Klimešová, J., Klipel, J., Kloeppel, B., Klotz, S., Knops, J.M.H., Kohyama, T., Koike, F., Kollmann, J., Komac, B., Komatsu, K., König, C., Kraft, N.J.B., Kramer, K., Kreft, H., Kühn, I., Kumarathunge, D., Kuppler, J., Kurokawa, H., Kurosawa, Y., Kuyah, S., Laclau, J., Lafleur, B., Lallai, E., Lamb, E., Lamprecht, A., Larkin, D.J., Laughlin, D., Le Bagousse-Pinguet, Y., Le Maire, G., Le Roux, P.C., Le Roux, E., Lee, T., Lens, F., Lewis, S.L., Lhotsky, B., Li, Y., Li, X., Lichstein, J.W., Liebergesell, M., Lim, J.Y., Lin, Y., Linares, J.C., Liu, C., Liu, D., Liu, U., Livingstone, S., Llusià, J., Lohbeck, M., López-García, Á., Lopez-Gonzalez, G., Lososová, Z., Louault, F., Lukács, B.A., Lukeš, P., Luo, Y., Lussu, M., Ma, S., Maciel Rabelo Pereira, C., Mack, M., Maire, V., Mäkelä, A., Mäkinen, H., Malhado, A.C.M., Mallik, A., Manning, P., Manzoni, S., Marchetti, Z., Marchino, L., Marcilio-Silva, V., Marcon, E., Marignani, M., Markesteijn, L., Martin, A., Martínez-Garza, C., Martínez-Vilalta, J., Mašková, T., Mason, K., Mason, N., Massad, T.J., Masse, J., Mayrose, I., McCarthy, J., McCormack, M.L., McCulloh, K., McFadden, I.R., McGill, B.J., McPartland, M.Y., Medeiros, J.S., Medlyn, B., Meerts, P., Mehrabi, Z., Meir, P., Melo, F.P.L., Mencuccini, M., Meredieu, C., Messier, J., Mészáros, I., Metsaranta, J., Michaletz, S.T., Michelaki, C., Migalina, S., Milla, R., Miller, J.E.D., Minden, V., Ming, R., Mokany, K., Moles, A.T., Molnár, A., Molofsky, J., Molz, M., Montgomery, R.A., Monty, A., Moravcová, L., Moreno-Martínez, A., Moretti, M., Mori, A.S., Mori, S., Morris, D., Morrison, J., Mucina, L., Mueller, S., Muir, C.D., Müller, S.C., Munoz, F., Myers-Smith, I.H., Myster, R.W., Nagano, M., Naidu, S., Narayanan, A., Natesan, B., Negoita, L., Nelson, A.S., Neuschulz, E.L., Ni, J., Niedrist, G., Nieto, J., Niinemets, Ü., Nolan, R., Nottebrock, H., Nouvellon, Y., Novakovskiy, A., The Nutrient Network, Nystuen, K.O., O'Grady, A., O'Hara, K., O'Reilly-Nugent, A.,

Oakley, S., Oberhuber, W., Ohtsuka, T., Oliveira, R., Öllerer, K., Olson, M.E., Onipchenko, V., Onoda, Y., Onstein, R.E., Ordonez, J.C., Osada, N., Ostonen, I., Ottaviani, G., Otto, S., Overbeck, G.E., Ozinga, W.A., Pahl, A.T., Paine, C.E.T., Pakeman, R.J., Papageorgiou, A.C., Parfionova, E., Pärtel, M., Patacca, M., Paula, S., Paule, J., Pauli, H., Pausas, J.G., Peco, B., Penuelas, J., Perea, A., Peri, P.L., Petisco-Souza, A.C., Petraglia, A., Petritan, A.M., Phillips, O.L., Pierce, S., Pillar, V.D., Pisek, J., Pomogaybin, A., Poorter, H., Portsmuth, A., Poschlod, P., Potvin, C., Pounds, D., Powell, A.S., Power, S.A., Prinzing, A., Puglielli, G., Pyšek, P., Raevel, V., Rammig, A., Ransijn, J., Ray, C.A., Reich, P.B., Reichstein, M., Reid, D.E.B., Réjou-Méchain, M., De Dios, V.R., Ribeiro, S., Richardson, S., Riibak, K., Rillig, M.C., Riviera, F., Robert, E.M.R., Roberts, S., Robroek, B., Roddy, A., Rodrigues, A.V., Rogers, A., Rollinson, E., Rolo, V., Römermann, C., Ronzhina, D., Roscher, C., Rosell, J.A., Rosenfield, M.F., Rossi, C., Roy, D.B., Royer-Tardif, S., Rüger, N., Ruiz-Peinado, R., Rumpf, S.B., Rusch, G.M., Ryo, M., Sack, L., Saldaña, A., Salgado-Negret, B., Salguero-Gomez, R., Santa-Regina, I., Santacruz-García, A.C., Santos, J., Sardans, J., Schamp, B., Scherer-Lorenzen, M., Schleuning, M., Schmid, B., Schmidt, M., Schmitt, S., Schneider, J.V., Schowanek, S.D., Schrader, J., Schrodt, F., Schuldt, B., Schurr, F., Selaya Garvizu, G., Semchenko, M., Seymour, C., Sfair, J.C., Sharpe, J.M., Sheppard, C.S., Sheremetiev, S., Shiodera, S., Shipley, B., Shovon, T.A., Siebenkäs, A., Sierra, C., Silva, V., Silva, M., Sitzia, T., Sjöman, H., Slot, M., Smith, N.G., Sodhi, D., Soltis, P., Soltis, D., Somers, B., Sonnier, G., Sørensen, M.V., Sosinski, E.E., Soudzilovskaia, N.A., Souza, A.F., Spasojevic, M., Sperandii, M.G., Stan, A.B., Stegen, J., Steinbauer, K., Stephan, J.G., Sterck, F., Stojanovic, D.B., Strydom, T., Suarez, M.L., Svenning, J., Svitková, I., Svitok, M., Svoboda, M., Swaine, E., Swenson, N., Tabarelli, M., Takagi, K., Tappeiner, U., Tarifa, R., Tauugourdeau, S., Tavsanoglu, C., Te Beest, M., Tedersoo, L., Thiffault, N., Thom, D., Thomas, E., Thompson, K., Thornton, P.E., Thuiller, W., Tichý, L., Tissue, D., Tjoelker, M.G., Tng, D.Y.P., Tobias, J., Török, P., Tarin, T., Torres-Ruiz, J.M., Tóthmérész, B., Treurnicht, M., Trivellone, V., Trolliet, F., Trotsiuk, V., Tsakalos, J.L., Tsiripidis, I., Tysklind, N., Umehara, T., Usoltsev, V., Vadeboncoeur, M., Vaezi, J., Valladares, F., Vamosi, J., Van Bodegom, P.M., Van Breugel, M., Van Cleemput, E., Van De Weg, M., Van Der Merwe, S., Van Der Plas, F., Van Der Sande, M.T., Van Kleunen, M., Van Meerbeek, K., Vanderwel, M., Vanselow, K.A., Vårhammar, A., Varone, L., Vasquez Valderrama, M.Y., Vassilev, K., Vellend, M., Veneklaas, E.J., Verbeeck, H., Verheyen, K., Vibrans, A., Vieira, I., Villacís, J., Violle, C., Vivek, P., Wagner, K., Waldram, M., Waldron, A., Walker, A.P., Waller, M., Walther, G., Wang, H., Wang, F., Wang, W., Watkins, H., Watkins, J., Weber, U., Weedon, J.T., Wei, L., Weigelt, P., Weiher, E., Wells, A.W., Wellstein, C., Wenk, E., Westoby, M., Westwood, A., White, P.J., Whitten, M., Williams, M., Winkler, D.E., Winter, K., Womack, C., Wright, I.J., Wright, S.J., Wright, J., Pinho, B.X., Ximenes, F., Yamada, T., Yamaji, K., Yanai, R., Yankov, N., Yguel, B., Zanini, K.J., Zanne, A.E., Zelený, D., Zhao, Y., Zheng, Jingming, Zheng, Ji, Ziemińska, K., Zirbel, C.R., Zizka, G., Zo-Bi, I.C., Zotz, G., Wirth, C., 2020. TRY plant trait database –

enhanced coverage and open access. Global Change Biology 26, 119–188. https://doi.org/10.1111/gcb.14904

Kearsley, E., De Haulleville, T., Hufkens, K., Kidimbu, A., Toirambe, B., Baert, G., Huygens, D., Kebede, Y., Defourny, P., Bogaert, J., Beeckman, H., Steppe, K., Boeckx, P., Verbeeck, H., 2013. Conventional tree height–diameter relationships significantly overestimate aboveground carbon stocks in the Central Congo Basin. Nat Commun 4, 2269. https://doi.org/10.1038/ncomms3269

Kearsley, E., Hufkens, K., Verbeeck, H., Bauters, M., Beeckman, H., Boeckx, P., Huygens, D., 2019. Large-sized rare tree species contribute disproportionately to functional diversity in resource acquisition in African tropical forest. Ecology and Evolution 9, 4349–4361. https://doi.org/10.1002/ece3.4836

Kearsley, E., Verbeeck, H., Stoffelen, P., Janssens, S.B., Yakusu, E.K., Kosmala, M., De Mil, T., Bauters, M., Kitima, E.R., Ndiapo, J.M., Chuda, A.L., Richardson, A.D., Wingate, L., Ilondea, B.A., Beeckman, H., van den Bulcke, J., Boeckx, P., Hufkens, K., 2024. Historical tree phenology data reveal the seasonal rhythms of the Congo Basin rainforest. Plant Enviro Interactions 5, e10136. https://doi.org/10.1002/pei3.10136

Keeling, H.C., Phillips, O.L., 2007. The global relationship between forest productivity and biomass. Global Ecology and Biogeography 16, 618–631. https://doi.org/10.1111/j.1466-8238.2007.00314.x

Keränen, J., Maltamo, M., Packalen, P., 2016. Effect of flying altitude, scanning angle and scanning mode on the accuracy of ALS based forest inventory. International Journal of Applied Earth Observation and Geoinformation 52, 349–360. https://doi.org/10.1016/j.jag.2016.07.005

Khosravipour, A., Skidmore, A.K., Isenburg, M., 2016. Generating spike-free digital surface models using LiDAR raw point clouds: A new approach for forestry applications. International Journal of Applied Earth Observation and Geoinformation 52, 104–114. https://doi.org/10.1016/j.jag.2016.06.005

Kuenzer, C., Bluemel, A., Gebhardt, S., Quoc, T.V., Dech, S., 2011. Remote Sensing of Mangrove Ecosystems: A Review. Remote Sensing 3, 878–928. https://doi.org/10.3390/rs3050878

Lang, N., Kalischek, N., Armston, J., Schindler, K., Dubayah, R., Wegner, J.D., 2022. Global canopy height regression and uncertainty estimation from GEDI LIDAR waveforms with deep ensembles. Remote Sensing of Environment 268, 112760. https://doi.org/10.1016/j.rse.2021.112760

LaRue, E.A., Fahey, R., Fuson, T.L., Foster, J.R., Matthes, J.H., Krause, K., Hardiman, B.S., 2022. Evaluating the sensitivity of forest structural diversity characterization to LIDAR point density. Ecosphere 13, e4209. https://doi.org/10.1002/ecs2.4209

LaRue, E.A., Fahey, R.T., Alveshere, B.C., Atkins, J.W., Bhatt, P., Buma, B., Chen, A., Cousins, S., Elliott, J.M., Elmore, A.J., Hakkenberg, C.R., Hardiman, B.S., Johnson, J.S., Kashian, D.M., Koirala, A., Papeş, M., St Hilaire, J.B., Surasinghe, T.D., Zambrano, J., Zhai, L., Fei, S., 2023a. A theoretical framework for the ecological role of three-dimensional structural diversity. Frontiers in Ecol & Environ 21, 4–13. https://doi.org/10.1002/fee.2587

LaRue, E.A., Knott, J.A., Domke, G.M., Chen, H.Y., Guo, Q., Hisano, M., Oswalt, C., Oswalt, S., Kong, N., Potter, K.M., Fei, S., 2023b. Structural diversity as a reliable and novel predictor for ecosystem productivity. Frontiers in Ecol & Environ 21, 33–39. https://doi.org/10.1002/fee.2586

Lasky, J.R., Uriarte, M., Boukili, V.K., Erickson, D.L., John Kress, W., Chazdon, R.L., 2014. The relationship between tree biodiversity and biomass dynamics changes with tropical forest succession. Ecology Letters 17, 1158–1167. https://doi.org/10.1111/ele.12322

LeCun, Y.A., Bottou, L., Orr, G.B., Müller, K.-R., 2012. Efficient BackProp, in: Montavon, G., Orr, Geneviève B., Müller, K.-R. (Eds.), Neural Networks: Tricks of the Trade, Lecture Notes in Computer Science. Springer Berlin Heidelberg, Berlin, Heidelberg, pp. 9–48. https://doi.org/10.1007/978-3-642-35289-8_3

Lefsky, M.A., Cohen, W.B., Harding, D.J., Parker, G.G., Acker, S.A., Gower, S.T., 2002. Lidar remote sensing of above-ground biomass in three biomes. Global Ecology.

Legendre, P., 1993. Spatial Autocorrelation: Trouble or New Paradigm? Ecology 74, 1659–1673. https://doi.org/10.2307/1939924

Lewis, S.L., Lopez-Gonzalez, G., Sonké, B., Affum-Baffoe, K., Baker, T.R., Ojo, L.O., Phillips, O.L., Reitsma, J.M., White, L., Comiskey, J.A., K, M.-N.D., Ewango, C.E.N., Feldpausch, T.R., Hamilton, A.C., Gloor, M., Hart, T., Hladik, A., Lloyd, J., Lovett, J.C., Makana, J.-R., Malhi, Y., Mbago, F.M., Ndangalasi, H.J., Peacock, J., Peh, K.S.-H., Sheil, D., Sunderland, T., Swaine, M.D., Taplin, J., Taylor, D., Thomas, S.C., Votere, R., Wöll, H., 2009. Increasing carbon storage in intact African tropical forests. Nature 457, 1003–1006. https://doi.org/10.1038/nature07771

Li, H., Li, X., Kato, T., Hayashi, M., Fu, J., Hiroshima, T., 2024. Accuracy assessment of GEDI terrain elevation, canopy height, and aboveground biomass density estimates in Japanese artificial forests. Science of Remote Sensing 10, 100144. https://doi.org/10.1016/j.srs.2024.100144

Li, X., Wessels, K., Armston, J., Hancock, S., Mathieu, R., Main, R., Naidoo, L., Erasmus, B., Scholes, R., 2023. First validation of GEDI canopy heights in African savannas. Remote Sensing of Environment 285, 113402. https://doi.org/10.1016/j.rse.2022.113402

Lin, M., Lucas, H.C., Shmueli, G., 2013. Research Commentary —Too Big to Fail: Large Samples and the *p* -Value Problem. Information Systems Research 24, 906–917. https://doi.org/10.1287/isre.2013.0480

Liu, A., Chen, Y., Cheng, X., 2025. Improving Tropical Forest Canopy Height Mapping by Fusion of Sentinel-1/2 and Bias-Corrected ICESat-2–GEDI Data. Remote Sensing 17, 1968. https://doi.org/10.3390/rs17121968

Liu, A., Cheng, X., Chen, Z., 2021. Performance evaluation of GEDI and ICESat-2 laser altimeter data for terrain and canopy height retrievals. Remote Sensing of Environment 264, 112571. https://doi.org/10.1016/j.rse.2021.112571

Liu, J., Bowman, K.W., Schimel, D.S., Parazoo, N.C., Jiang, Z., Lee, M., Bloom, A.A., Wunch, D., Frankenberg, C., Sun, Y., O'Dell, C.W., Gurney, K.R., Menemenlis, D., Gierach, M., Crisp, D., Eldering, A., 2017. Contrasting carbon cycle responses of the tropical continents to the 2015–2016 El Niño. Science 358, eaam5690. https://doi.org/10.1126/science.aam5690

Liu, S., Csillik, O., Ordway, E.M., Chang, L.-L., Longo, M., Keller, M., Moorcroft, P.R., 2025. Environmental drivers of spatial variation in tropical forest canopy height: Insights from NASA's GEDI spaceborne LiDAR. Proc. Natl. Acad. Sci. U.S.A. 122, e2401755122. https://doi.org/10.1073/pnas.2401755122

Lloyd, J., Bird, M.I., Vellen, L., Miranda, A.C., Veenendaal, E.M., Djagbletey, G., Miranda, H.S., Cook, G., Farquhar, G.D., 2008. Contributions of woody and herbaceous vegetation to tropical savanna ecosystem productivity: a quasi-global estimate. Tree Physiology 28, 451–468. https://doi.org/10.1093/treephys/28.3.451

Lohbeck, M., Poorter, L., Martínez-Ramos, M., Rodriguez-Velázquez, J., Van Breugel, M., Bongers, F., 2014. Changing drivers of species dominance during tropical forest succession. Functional Ecology 28, 1052–1058. https://doi.org/10.1111/1365-2435.12240

Longo, M., Saatchi, S., Keller, M., Bowman, K., Ferraz, A., Moorcroft, P.R., Morton, D.C., Bonal, D., Brando, P., Burban, B., Derroire, G., dos-Santos, M.N., Meyer, V., Saleska, S., Trumbore, S., Vincent, G., 2020. Impacts of Degradation on Water, Energy, and Carbon Cycling of the Amazon Tropical Forests. JGR Biogeosciences 125, e2020JG005677. https://doi.org/10.1029/2020JG005677

Loreau, M., Hector, A., 2001. Partitioning selection and complementarity in biodiversity experiments. Nature 412, 72–76. https://doi.org/10.1038/35083573

Loubota Panzou, G.J., Fayolle, A., Jucker, T., Phillips, O.L., Bohlman, S., Banin, L.F., Lewis, S.L., Affum-Baffoe, K., Alves, L.F., Antin, C., Arets, E., Arroyo, L., Baker, T.R., Barbier, N., Beeckman, H., Berger, U., Bocko, Y.E., Bongers, F., Bowers, S., Brade, T., Brondizio, E.S., Chantrain, A., Chave, J., Compaore, H., Coomes,

D., Diallo, A., Dias, A.S., Dimobe, K., Djagbletey, G.D., Domingues, T., Doucet, J., Drouet, T., Forni, E., Godlee, J.L., Goodman, R.C., Gourlet-Fleury, S., Hien, F., Iida, Y., Ilondea, B.A., Ilunga Muledi, J., Jacques, P., Kuyah, S., López-Portillo, J., Loumeto, J.J., Marimon-Junior, B.H., Marimon, B.S., Mensah, S., Mitchard, E.T.A., Moncrieff, G.R., Narayanan, A., O'Brien, S.T., Ouedraogo, K., Palace, M.W., Pelissier, R., Ploton, P., Poorter, L., Ryan, C.M., Saiz, G., Santos, K., Schlund, M., Sellan, G., Sonke, B., Sterck, F., Thibaut, Q., Van Hoef, Y., Veenendaal, E., Vovides, A.G., Xu, Y., Yao, T.L., Feldpausch, T.R., 2021. Pantropical variability in tree crown allometry. Global Ecol. Biogeogr. 30, 459–475. https://doi.org/10.1111/geb.13231

Ma, J., Chen, L., Mi, X., Ren, H., Liu, X., Wang, Y., Wang, F., Yao, Y., Zhang, Y., Ma, K., 2023. The interactive effects of soil fertility and tree mycorrhizal association explain spatial variation of diversity–biomass relationships in a subtropical forest. Journal of Ecology 111, 1037–1049. https://doi.org/10.1111/1365-2745.14076

Ma, M., 2005. Species richness vs evenness: independent relationship and different responses to edaphic factors. Oikos 111, 192–198. https://doi.org/10.1111/j.0030-1299.2005.13049.x

MacArthur, R.H., MacArthur, J.W., 1961. On Bird Species Diversity. Ecology 42, 594–598. https://doi.org/10.2307/1932254

Malhi, Y., 2012. The productivity, metabolism and carbon cycle of tropical forest vegetation. Journal of Ecology 100, 65–75. https://doi.org/10.1111/j.1365-2745.2011.01916.x

Malhi, Y., Doughty, C., Galbraith, D., 2011. The allocation of ecosystem net primary productivity in tropical forests. Philosophical Transactions of the Royal Society B: Biological Sciences. https://doi.org/10.1098/rstb.2011.0062

Maraun, D., 2013. Bias Correction, Quantile Mapping, and Downscaling: Revisiting the Inflation Issue. Journal of Climate 26, 2137–2143. https://doi.org/10.1175/JCLI-D-12-00821.1

Mascaro, J., Detto, M., Asner, G.P., Muller-Landau, H.C., 2011. Evaluating uncertainty in mapping forest carbon with airborne LiDAR. Remote Sensing of Environment 115, 3770–3774. https://doi.org/10.1016/j.rse.2011.07.019

Matsuo, T., Poorter, L., Van Der Sande, M.T., Mohammed Abdul, S., Koyiba, D.W., Opoku, J., De Wit, B., Kuzee, T., Amissah, L., 2025. Drivers of biomass stocks and productivity of tropical secondary forests. Ecology 106, e4488. https://doi.org/10.1002/ecy.4488

Mayaux, P., Pekel, J.-F., Desclée, B., Donnay, F., Lupi, A., Achard, F., Clerici, M., Bodart, C., Brink, A., Nasi, R., Belward, A., 2013. State and evolution of the

African rainforests between 1990 and 2010. Phil. Trans. R. Soc. B 368, 20120300. https://doi.org/10.1098/rstb.2012.0300

Mayaux, P., Richards, T., Janodet, E., 1999. A vegetation map of Central Africa derived from satellite imagery. Journal of Biogeography 26, 353–366. https://doi.org/10.1046/j.1365-2699.1999.00270.x

McElhinny, C., Gibbons, P., Brack, C., Bauhus, J., 2005. Forest and woodland stand structural complexity: Its definition and measurement. Forest Ecology and Management 218, 1–24. https://doi.org/10.1016/j.foreco.2005.08.034

Miller, A.D., Roxburgh, S.H., Shea, K., 2012. Timing of disturbance alters competitive outcomes and mechanisms of coexistence in an annual plant model. Theor Ecol 5, 419–432. https://doi.org/10.1007/s12080-011-0133-1

Montgomery, R.A., Chazdon, R.L., 2001. FOREST STRUCTURE, CANOPY ARCHITECTURE, AND LIGHT TRANSMITTANCE IN TROPICAL WET FORESTS. Ecology 82, 2707–2718. https://doi.org/10.1890/0012-9658(2001)082%5B2707:FSCAAL%5D2.0.CO;2

Moudrý, V., Gábor, L., Marselis, S., Pracná, P., Barták, V., Prošek, J., Navrátilová, B., Novotný, J., Potůčková, M., Gdulová, K., Crespo-Peremarch, P., Komárek, J., Malavasi, M., Rocchini, D., Ruiz, L.A., Torralba, J., Torresani, M., Cazzolla Gatti, R., Wild, J., 2024a. Comparison of three global canopy height maps and their applicability to biodiversity modeling: Accuracy issues revealed. Ecosphere 15, e70026. https://doi.org/10.1002/ecs2.70026

Moudrý, V., Prošek, J., Marselis, S., Marešová, J., Šárovcová, E., Gdulová, K., Kozhoridze, G., Torresani, M., Rocchini, D., Eltner, A., Liu, X., Potůčková, M., Šedová, A., Crespo-Peremarch, P., Torralba, J., Ruiz, L.A., Perrone, M., Špatenková, O., Wild, J., 2024b. How to Find Accurate Terrain and Canopy Height GEDI Footprints in Temperate Forests and Grasslands? Earth and Space Science 11, e2024EA003709. https://doi.org/10.1029/2024EA003709

Murphy, B.A., May, J.A., Butterworth, B.J., Andresen, C.G., Desai, A.R., 2022. Unraveling Forest Complexity: Resource Use Efficiency, Disturbance, and the Structure-Function Relationship. JGR Biogeosciences 127, e2021JG006748. https://doi.org/10.1029/2021JG006748

Murphy, B.P., Bowman, D.M.J.S., 2012. What controls the distribution of tropical forest and savanna?: Tropical forest and savanna distribution. Ecology Letters 15, 748–758. https://doi.org/10.1111/j.1461-0248.2012.01771.x

Nesha, M.K., Hussin, Y.A., Van Leeuwen, L.M., Sulistioadi, Y.B., 2020. Modeling and mapping aboveground biomass of the restored mangroves using ALOS-2 PALSAR-2 in East Kalimantan, Indonesia. International Journal of Applied Earth

Observation and Geoinformation 91, 102158. https://doi.org/10.1016/j.jag.2020.102158

Niklaus, P.A., Baruffol, M., He, J., Ma, K., Schmid, B., 2017. Can niche plasticity promote biodiversity–productivity relationships through increased complementarity? Ecology 98, 1104–1116. https://doi.org/10.1002/ecy.1748

Nikparvar, B., Thill, J.-C., 2021. Machine Learning of Spatial Data. IJGI 10, 600. https://doi.org/10.3390/ijgi10090600

Noss, R.F., 1990. Indicators for Monitoring Biodiversity: A Hierarchical Approach. Conservation Biology 4, 355–364. https://doi.org/10.1111/j.1523-1739.1990.tb00309.x

Nunes, M.H., Muller-Landau, H.C., Görgens, E.B., Pascual, A., Dubayah, R., 2026. Heterogeneous climatic controls on tropical-forest biomass. Nature 656, 905–912. https://doi.org/10.1038/s41586-026-10880-2

Oliveras, I., Malhi, Y., 2016. Many shades of green: the dynamic tropical forest–savannah transition zones. Phil. Trans. R. Soc. B 371, 20150308. https://doi.org/10.1098/rstb.2015.0308

Ometto, J.P., Gorgens, E.B., De Souza Pereira, F.R., Sato, L., De Assis, M.L.R., Cantinho, R., Longo, M., Jacon, A.D., Keller, M., 2023. A biomass map of the Brazilian Amazon from multisource remote sensing. Sci Data 10, 668. https://doi.org/10.1038/s41597-023-02575-4

Oon, A., Ngo, K.D., Azhar, R., Ashton-Butt, A., Lechner, A.M., Azhar, B., 2019. Assessment of ALOS-2 PALSAR-2L-band and Sentinel-1 C-band SAR backscatter for discriminating between large-scale oil palm plantations and smallholdings on tropical peatlands. Remote Sensing Applications: Society and Environment 13, 183–190. https://doi.org/10.1016/j.rsase.2018.11.002

Osunkoya, O.O., Omar-Ali, K., Amit, N., Dayan, J., Daud, D.S., Sheng, T.K., 2007. Comparative height–crown allometry and mechanical design in 22 tree species of Kuala Belalong rainforest, Brunei, Borneo. American J of Botany 94, 1951–1962. https://doi.org/10.3732/ajb.94.12.1951

Paciorek, C.J., 2010. The Importance of Scale for Spatial-Confounding Bias and Precision of Spatial Regression Estimators. Statist. Sci. 25, 107–125. https://doi.org/10.1214/10-STS326

Pan, Y., Birdsey, R.A., Fang, J., Houghton, R., Kauppi, P.E., Kurz, W.A., Phillips, O.L., Shvidenko, A., Lewis, S.L., Canadell, J.G., Ciais, P., Jackson, R.B., Pacala, S.W., McGuire, A.D., Piao, S., Rautiainen, A., Sitch, S., Hayes, D., 2011. A Large and Persistent Carbon Sink in the World's Forests. Science 333, 988–993. https://doi.org/10.1126/science.1201609

Pan, Y., Birdsey, R.A., Phillips, O.L., Houghton, R.A., Fang, J., Kauppi, P.E., Keith, H., Kurz, W.A., Ito, A., Lewis, S.L., Nabuurs, G.-J., Shvidenko, A., Hashimoto, S., Lerink, B., Schepaschenko, D., Castanho, A., Murdiyarso, D., 2024. The enduring world forest carbon sink. Nature 631, 563–569. https://doi.org/10.1038/s41586-024-07602-x

Pattanayak, S.K., 2004. Valuing watershed services: concepts and empirics from southeast Asia. Agriculture, Ecosystems & Environment 104, 171–184. https://doi.org/10.1016/j.agee.2004.01.016

Patterson, P.L., Healey, S.P., Ståhl, G., Saarela, S., Holm, S., Andersen, H.-E., Dubayah, R.O., Duncanson, L., Hancock, S., Armston, J., Kellner, J.R., Cohen, W.B., Yang, Z., 2019. Statistical properties of hybrid estimators proposed for GEDI—NASA's global ecosystem dynamics investigation. Environ. Res. Lett. 14, 065007. https://doi.org/10.1088/1748-9326/ab18df

Pielawski, N., Wählby, C., 2020. Introducing Hann windows for reducing edge-effects in patch-based image segmentation. PLoS ONE 15, e0229839. https://doi.org/10.1371/journal.pone.0229839

Pisek, J., Govind, A., Arndt, S.K., Hocking, D., Wardlaw, T.J., Fang, H., Matteucci, G., Longdoz, B., 2015. Intercomparison of clumping index estimates from POLDER, MODIS, and MISR satellite data over reference sites. ISPRS Journal of Photogrammetry and Remote Sensing 101, 47–56. https://doi.org/10.1016/j.isprsjprs.2014.11.004

Ploton, P., Mortier, F., Réjou-Méchain, M., Barbier, N., Picard, N., Rossi, V., Dormann, C., Cornu, G., Viennois, G., Bayol, N., Lyapustin, A., Gourlet-Fleury, S., Pélissier, R., 2020. Spatial validation reveals poor predictive performance of large-scale ecological mapping models. Nat Commun 11, 4540. https://doi.org/10.1038/s41467-020-18321-y

Polley, H.W., Isbell, F.I., Wilsey, B.J., 2013. Plant functional traits improve diversity-based predictions of temporal stability of grassland productivity. Oikos 122, 1275–1282. https://doi.org/10.1111/j.1600-0706.2013.00338.x

Ponce De León, M.A., Bailey, B.N., 2024. Quantifying water-use efficiency in plant canopies with varying leaf angle and density distribution. Annals of Botany 133, 605–620. https://doi.org/10.1093/aob/mcae018

Poorter, L., Bongers, L., Bongers, F., 2006. ARCHITECTURE OF 54 MOIST-FOREST TREE SPECIES: TRAITS, TRADE-OFFS, AND FUNCTIONAL GROUPS. Ecology 87, 1289–1301. https://doi.org/10.1890/0012-9658(2006)87%5B1289:AOMTST%5D2.0.CO;2

Poorter, L., Craven, D., Jakovac, C.C., Van Der Sande, M.T., Amissah, L., Bongers, F., Chazdon, R.L., Farrior, C.E., Kambach, S., Meave, J.A., Muñoz, R., Norden, N.,

Rüger, N., Van Breugel, M., Almeyda Zambrano, A.M., Amani, B., Andrade, J.L., Brancalion, P.H.S., Broadbent, E.N., De Foresta, H., Dent, D.H., Derroire, G., DeWalt, S.J., Dupuy, J.M., Durán, S.M., Fantini, A.C., Finegan, B., Hernández-Jaramillo, A., Hernández-Stefanoni, J.L., Hietz, P., Junqueira, A.B., N'dja, J.K., Letcher, S.G., Lohbeck, M., López-Camacho, R., Martínez-Ramos, M., Melo, F.P.L., Mora, F., Müller, S.C., N'Guessan, A.E., Oberleitner, F., Ortiz-Malavassi, E., Pérez-García, E.A., Pinho, B.X., Piotto, D., Powers, J.S., Rodríguez-Buriticá, S., Rozendaal, D.M.A., Ruíz, J., Tabarelli, M., Teixeira, H.M., Valadares De Sá Barretto Sampaio, E., Van Der Wal, H., Villa, P.M., Fernandes, G.W., Santos, B.A., Aguilar-Cano, J., De Almeida-Cortez, J.S., Alvarez-Davila, E., Arreola-Villa, F., Balvanera, P., Becknell, J.M., Cabral, G.A.L., Castellanos-Castro, C., De Jong, B.H.J., Nieto, J.E., Espírito-Santo, M.M., Fandino, M.C., García, H., García-Villalobos, D., Hall, J.S., Idárraga, A., Jiménez-Montoya, J., Kennard, D., Marín-Spiotta, E., Mesquita, R., Nunes, Y.R.F., Ochoa-Gaona, S., Peña-Claros, M., Pérez-Cárdenas, N., Rodríguez-Velázquez, J., Villanueva, L.S., Schwartz, N.B., Steininger, M.K., Veloso, M.D.M., Vester, H.F.M., Vieira, I.C.G., Williamson, G.B., Zanini, K., Hérault, B., 2021. Multidimensional tropical forest recovery. Science 374, 1370–1376. https://doi.org/10.1126/science.abh3629

Potapov, P., Li, X., Hernandez-Serna, A., Tyukavina, A., Hansen, M.C., Kommareddy, A., Pickens, A., Turubanova, S., Tang, H., Silva, C.E., Armston, J., Dubayah, R., Blair, J.B., Hofton, M., 2021. Mapping global forest canopy height through integration of GEDI and Landsat data. Remote Sensing of Environment 253, 112165. https://doi.org/10.1016/j.rse.2020.112165

Pyles, M.V., Prado-Junior, J.A., Magnago, L.F.S., De Paula, A., Meira-Neto, J.A.A., 2018. Loss of biodiversity and shifts in aboveground biomass drivers in tropical rainforests with different disturbance histories. Biodivers Conserv 27, 3215–3231. https://doi.org/10.1007/s10531-018-1598-7

Ramo, R., Roteta, E., Bistinas, I., Van Wees, D., Bastarrika, A., Chuvieco, E., Van Der Werf, G.R., 2021. African burned area and fire carbon emissions are strongly impacted by small fires undetected by coarse resolution satellite data. Proc. Natl. Acad. Sci. U.S.A. 118, e2011160118. https://doi.org/10.1073/pnas.2011160118

Ranson, K.J., Guoqing Sun, 1994. Mapping biomass of a northern forest using multifrequency SAR data. IEEE Trans. Geosci. Remote Sensing 32, 388–396. https://doi.org/10.1109/36.295053

Réjou-Méchain, M., Barbier, N., Couteron, P., Ploton, P., Vincent, G., Herold, M., Mermoz, S., Saatchi, S., Chave, J., De Boissieu, F., Féret, J.-B., Takoudjou, S.M., Pélissier, R., 2019. Upscaling Forest Biomass from Field to Satellite Measurements: Sources of Errors and Ways to Reduce Them. Surv Geophys 40, 881–911. https://doi.org/10.1007/s10712-019-09532-0

Réjou-Méchain, M., Muller-Landau, H.C., Detto, M., Thomas, S.C., Le Toan, T., Saatchi, S.S., Barreto-Silva, J.S., Bourg, N.A., Bunyavejchewin, S., Butt, N.,

Brockelman, W.Y., Cao, M., Cárdenas, D., Chiang, J.-M., Chuyong, G.B., Clay, K., Condit, R., Dattaraja, H.S., Davies, S.J., Duque, A., Esufali, S., Ewango, C., Fernando, R.H.S., Fletcher, C.D., Gunatilleke, I.A.U.N., Hao, Z., Harms, K.E., Hart, T.B., Hérault, B., Howe, R.W., Hubbell, S.P., Johnson, D.J., Kenfack, D., Larson, A.J., Lin, L., Lin, Y., Lutz, J.A., Makana, J.-R., Malhi, Y., Marthews, T.R., McEwan, R.W., McMahon, S.M., McShea, W.J., Muscarella, R., Nathalang, A., Noor, N.S.M., Nytch, C.J., Oliveira, A.A., Phillips, R.P., Pongpattananurak, N., Punchi-Manage, R., Salim, R., Schurman, J., Sukumar, R., Suresh, H.S., Suwanvecho, U., Thomas, D.W., Thompson, J., Uríarte, M., Valencia, R., Vicentini, A., Wolf, A.T., Yap, S., Yuan, Z., Zartman, C.E., Zimmerman, J.K., Chave, J., 2014. Local spatial structure of forest biomass and its consequences for remote sensing of carbon stocks. Biogeosciences 11, 6827–6840. https://doi.org/10.5194/bg-11-6827-2014

Richardson, A.D., Dail, D.B., Hollinger, D.Y., 2011. Leaf area index uncertainty estimates for model–data fusion applications. Agricultural and Forest Meteorology 151, 1287–1292. https://doi.org/10.1016/j.agrformet.2011.05.009

Rishmawi, K., Huang, C., Zhan, X., 2021. Monitoring Key Forest Structure Attributes across the Conterminous United States by Integrating GEDI LiDAR Measurements and VIIRS Data. Remote Sensing 13, 442. https://doi.org/10.3390/rs13030442

Roberts, D.R., Bahn, V., Ciuti, S., Boyce, M.S., Elith, J., Guillera-Arroita, G., Hauenstein, S., Lahoz-Monfort, J.J., Schröder, B., Thuiller, W., Warton, D.I., Wintle, B.A., Hartig, F., Dormann, C.F., 2017. Cross-validation strategies for data with temporal, spatial, hierarchical, or phylogenetic structure. Ecography 40, 913–929. https://doi.org/10.1111/ecog.02881

Roberts, E., Jelsma, H.A., Hegna, T., 2015. Mesozoic Sedimentary Cover Sequences of the Congo Basin in the Kasai Region, Democratic Republic of Congo, in: De Wit, M.J., Guillocheau, F., De Wit, M.C.J. (Eds.), Geology and Resource Potential of the Congo Basin. Springer Berlin Heidelberg, Berlin, Heidelberg, pp. 163–191. https://doi.org/10.1007/978-3-642-29482-2_9

Robinson, C., Saatchi, S., Clark, D., Hurtado Astaiza, J., Hubel, A., Gillespie, T., 2018. Topography and Three-Dimensional Structure Can Estimate Tree Diversity along a Tropical Elevational Gradient in Costa Rica. Remote Sensing 10, 629. https://doi.org/10.3390/rs10040629

Rödig, E., Cuntz, M., Rammig, A., Fischer, R., Taubert, F., Huth, A., 2018. The importance of forest structure for carbon fluxes of the Amazon rainforest. Environ. Res. Lett. 13, 054013. https://doi.org/10.1088/1748-9326/aabc61

Ronneberger, O., Fischer, P., Brox, T., 2015. U-Net: Convolutional Networks for Biomedical Image Segmentation, in: Navab, N., Hornegger, J., Wells, W.M., Frangi, A.F. (Eds.), Medical Image Computing and Computer-Assisted

Intervention – MICCAI 2015, Lecture Notes in Computer Science. Springer International Publishing, Cham, pp. 234–241. https://doi.org/10.1007/978-3-319-24574-4_28

Roussel, J.-R., Béland, M., Caspersen, J., Achim, A., 2018. A mathematical framework to describe the effect of beam incidence angle on metrics derived from airborne LiDAR: The case of forest canopies approaching turbid medium behaviour. Remote Sensing of Environment 209, 824–834. https://doi.org/10.1016/j.rse.2017.12.006

Roussel, J.-R., Caspersen, J., Béland, M., Thomas, S., Achim, A., 2017. Removing bias from LiDAR-based estimates of canopy height: Accounting for the effects of pulse density and footprint size. Remote Sensing of Environment 198, 1–16. https://doi.org/10.1016/j.rse.2017.05.032

Rowland, L., Harper, A., Christoffersen, B.O., Galbraith, D.R., Imbuzeiro, H.M.A., Powell, T.L., Doughty, C., Levine, N.M., Malhi, Y., Saleska, S.R., Moorcroft, P.R., Meir, P., Williams, M., 2015. Modelling climate change responses in tropical forests: similar productivity estimates across five models, but different mechanisms and responses. Geosci. Model Dev. 8, 1097–1110. https://doi.org/10.5194/gmd-8-1097-2015

Saito, M., Luyssaert, S., Poulter, B., Williams, M., Ciais, P., Bellassen, V., Ryan, C.M., Yue, C., Cadule, P., Peylin, P., 2014. Fire regimes and variability in aboveground woody biomass in miombo woodland. JGR Biogeosciences 119, 1014–1029. https://doi.org/10.1002/2013JG002505

Sankaran, M., Hanan, N.P., Scholes, R.J., Ratnam, J., Augustine, D.J., Cade, B.S., Gignoux, J., Higgins, S.I., Le Roux, X., Ludwig, F., Ardo, J., Banyikwa, F., Bronn, A., Bucini, G., Caylor, K.K., Coughenour, M.B., Diouf, A., Ekaya, W., Feral, C.J., February, E.C., Frost, P.G.H., Hiernaux, P., Hrabar, H., Metzger, K.L., Prins, H.H.T., Ringrose, S., Sea, W., Tews, J., Worden, J., Zambatis, N., 2005. Determinants of woody cover in African savannas. Nature 438, 846–849. https://doi.org/10.1038/nature04070

Sarafian, R., Kloog, I., Sarafian, E., Hough, I., Rosenblatt, J.D., 2021. A Domain Adaptation Approach for Performance Estimation of Spatial Predictions. IEEE Trans. Geosci. Remote Sensing 59, 5197–5205. https://doi.org/10.1109/TGRS.2020.3012575

Schaaf, C.B., Xiaowen Li, Strahler, A.H., 1994. Topographic effects on bidirectional and hemispherical reflectances calculated with a geometric-optical canopy model. IEEE Trans. Geosci. Remote Sensing 32, 1186–1193. https://doi.org/10.1109/36.338367

Schlund, M., Wenzel, A., Camarretta, N., Stiegler, C., Erasmi, S., 2023. Vegetation canopy height estimation in dynamic tropical landscapes with TanDEM-X

supported by GEDI data. Methods Ecol Evol 14, 1639–1656. https://doi.org/10.1111/2041-210X.13933

Schnabel, F., Schwarz, J.A., Dănescu, A., Fichtner, A., Nock, C.A., Bauhus, J., Potvin, C., 2019. Drivers of productivity and its temporal stability in a tropical tree diversity experiment. Global Change Biology 25, 4257–4272. https://doi.org/10.1111/gcb.14792

Schneider, F.D., Dean, M., Ordway, E.M., Libalah, M.B., Ferraz, A., 2026a. Mapping the structural diversity of Central African and Western US forests using GEDI. Remote Sensing of Environment 334, 115215. https://doi.org/10.1016/j.rse.2025.115215

Schneider, F.D., Dean, M., Ordway, E.M., Libalah, M.B., Ferraz, A., 2026b. Forest Structural Diversity of Central Africa and the Western US mapped using GEDI. https://doi.org/10.3334/ORNLDAAC/2481

Schneider, F.D., Ferraz, A., Hancock, S., Duncanson, L.I., Dubayah, R.O., Pavlick, R.P., Schimel, D.S., 2020. Towards mapping the diversity of canopy structure from space with GEDI. Environ. Res. Lett. 15, 115006. https://doi.org/10.1088/1748-9326/ab9e99

Schneider, F.D., Longo, M., Paul-Limoges, E., Scholl, V.M., Schmid, B., Morsdorf, F., Pavlick, R.P., Schimel, D.S., Schaepman, M.E., Moorcroft, P.R., 2023. Remote Sensing-Based Forest Modeling Reveals Positive Effects of Functional Diversity on Productivity at Local Spatial Scale. JGR Biogeosciences 128, e2023JG007421. https://doi.org/10.1029/2023JG007421

Schneider, F.D., Morsdorf, F., Schmid, B., Petchey, O.L., Hueni, A., Schimel, D.S., Schaepman, M.E., 2017. Mapping functional diversity from remotely sensed morphological and physiological forest traits. Nat Commun 8, 1441. https://doi.org/10.1038/s41467-017-01530-3

Schwartz, M., Ciais, P., Ottlé, C., De Truchis, A., Vega, C., Fayad, I., Brandt, M., Fensholt, R., Baghdadi, N., Morneau, F., Morin, D., Guyon, D., Dayau, S., Wigneron, J.-P., 2024a. High-resolution canopy height map in the Landes forest (France) based on GEDI, Sentinel-1, and Sentinel-2 data with a deep learning approach. International Journal of Applied Earth Observation and Geoinformation 128, 103711. https://doi.org/10.1016/j.jag.2024.103711

Schwartz, M., Ciais, P., Ottlé, C., De Truchis, A., Vega, C., Fayad, I., Brandt, M., Fensholt, R., Baghdadi, N., Morneau, F., Morin, D., Guyon, D., Dayau, S., Wigneron, J.-P., 2024b. High-resolution canopy height map in the Landes forest (France) based on GEDI, Sentinel-1, and Sentinel-2 data with a deep learning approach. International Journal of Applied Earth Observation and Geoinformation 128, 103711. https://doi.org/10.1016/j.jag.2024.103711

Shannon, E.S., Finley, A.O., Hayes, D.J., Noralez, S.N., Weiskittel, A.R., Cook, B.D., Babcock, C., 2024. Quantifying and correcting geolocation error in spaceborne LiDAR forest canopy observations using high spatial accuracy data: A Bayesian model approach. Environmetrics 35, e2840. https://doi.org/10.1002/env.2840

Shea, K., Roxburgh, S.H., Rauschert, E.S.J., 2004. Moving from pattern to process: coexistence mechanisms under intermediate disturbance regimes. Ecology Letters 7, 491–508. https://doi.org/10.1111/j.1461-0248.2004.00600.x

Shimada, M., Itoh, T., Motooka, T., Watanabe, M., Shiraishi, T., Thapa, R., Lucas, R., 2014. New global forest/non-forest maps from ALOS PALSAR data (2007–2010). Remote Sensing of Environment 155, 13–31. https://doi.org/10.1016/j.rse.2014.04.014

Siddique, N., Paheding, S., Elkin, C.P., Devabhaktuni, V., 2021. U-Net and Its Variants for Medical Image Segmentation: A Review of Theory and Applications. IEEE Access 9, 82031–82057. https://doi.org/10.1109/ACCESS.2021.3086020

Silva, C.A., Hamamura, C., Valbuena, R., Cardil, A., Broadbent, E.N., Almeida, D., Silva Junior, C., Klauberg, C., 2022. rGEDI: NASA's Global Ecosystem Dynamics Investigation (GEDI) Data Visualization and Processing.

Silva Dias, M. a. F., Rutledge, S., Kabat, P., Silva Dias, P.L., Nobre, C., Fisch, G., Dolman, A.J., Zipser, E., Garstang, M., Manzi, A.O., Fuentes, J.D., Rocha, H.R., Marengo, J., Plana-Fattori, A., Sá, L.D.A., Alvalá, R.. c. S., Andreae, M.O., Artaxo, P., Gielow, R., Gatti, L., 2002. Cloud and rain processes in a biosphere-atmosphere interaction context in the Amazon Region. Journal of Geophysical Research: Atmospheres 107, LBA 39-1-LBA 39-18. https://doi.org/10.1029/2001JD000335

Silva, G.F., Carneiro, G.B., Doth, R., Amaral, L.A., Azevedo, D.F.G.D., 2018. Near real-time shadow detection and removal in aerial motion imagery application. ISPRS Journal of Photogrammetry and Remote Sensing 140, 104–121. https://doi.org/10.1016/j.isprsjprs.2017.11.005

Silva Pedro, M., Rammer, W., Seidl, R., 2017. Disentangling the effects of compositional and structural diversity on forest productivity. J Vegetation Science 28, 649–658. https://doi.org/10.1111/jvs.12505

Silva Pedro, M., Rammer, W., Seidl, R., 2016. A disturbance-induced increase in tree species diversity facilitates forest productivity. Landscape Ecol 31, 989–1004. https://doi.org/10.1007/s10980-015-0317-y

Slik, J.W.F., Arroyo-Rodríguez, V., Aiba, S.-I., Alvarez-Loayza, P., Alves, L.F., Ashton, P., Balvanera, P., Bastian, M.L., Bellingham, P.J., Van Den Berg, E., Bernacci, L., Da Conceição Bispo, P., Blanc, L., Böhning-Gaese, K., Boeckx, P., Bongers, F., Boyle, B., Bradford, M., Brearley, F.Q., Breuer-Ndoundou Hockemba, M.,

Bunyavejchewin, S., Calderado Leal Matos, D., Castillo-Santiago, M., Catharino, E.L.M., Chai, S.-L., Chen, Y., Colwell, R.K., Chazdon, R.L., Clark, C., Clark, D.B., Clark, D.A., Culmsee, H., Damas, K., Dattaraja, H.S., Dauby, G., Davidar, P., DeWalt, S.J., Doucet, J.-L., Duque, A., Durigan, G., Eichhorn, K.A.O., Eisenlohr, P.V., Eler, E., Ewango, C., Farwig, N., Feeley, K.J., Ferreira, L., Field, R., De Oliveira Filho, A.T., Fletcher, C., Forshed, O., Franco, G., Fredriksson, G., Gillespie, T., Gillet, J.-F., Amarnath, G., Griffith, D.M., Grogan, J., Gunatilleke, N., Harris, D., Harrison, R., Hector, A., Homeier, J., Imai, N., Itoh, A., Jansen, P.A., Joly, C.A., De Jong, B.H.J., Kartawinata, K., Kearsley, E., Kelly, D.L., Kenfack, D., Kessler, M., Kitayama, K., Kooyman, R., Larney, E., Laumonier, Y., Laurance, S., Laurance, W.F., Lawes, M.J., Amaral, I.L.D., Letcher, S.G., Lindsell, J., Lu, X., Mansor, A., Marjokorpi, A., Martin, E.H., Meilby, H., Melo, F.P.L., Metcalfe, D.J., Medjibe, V.P., Metzger, J.P., Millet, J., Mohandass, D., Montero, J.C., De Morisson Valeriano, M., Mugerwa, B., Nagamasu, H., Nilus, R., Ochoa-Gaona, S., Onrizal, Page, N., Parolin, P., Parren, M., Parthasarathy, N., Paudel, E., Permana, A., Piedade, M.T.F., Pitman, N.C.A., Poorter, L., Poulsen, A.D., Poulsen, J., Powers, J., Prasad, R.C., Puyravaud, J.-P., Razafimahaimodison, J.-C., Reitsma, J., Dos Santos, J.R., Roberto Spironello, W., Romero-Saltos, H., Rovero, F., Rozak, A.H., Ruokolainen, K., Rutishauser, E., Saiter, F., Saner, P., Santos, B.A., Santos, F., Sarker, S.K., Satdichanh, M., Schmitt, C.B., Schöngart, J., Schulze, M., Suganuma, M.S., Sheil, D., Da Silva Pinheiro, E., Sist, P., Stevart, T., Sukumar, R., Sun, I.-F., Sunderland, T., Suresh, H.S., Suzuki, E., Tabarelli, M., Tang, J., Targhetta, N., Theilade, I., Thomas, D.W., Tchouto, P., Hurtado, J., Valencia, R., Van Valkenburg, J.L.C.H., Van Do, T., Vasquez, R., Verbeeck, H., Adekunle, V., Vieira, S.A., Webb, C.O., Whitfeld, T., Wich, S.A., Williams, J., Wittmann, F., Wöll, H., Yang, X., Adou Yao, C.Y., Yap, S.L., Yoneda, T., Zahawi, R.A., Zakaria, R., Zang, R., De Assis, R.L., Garcia Luize, B., Venticinque, E.M., 2015. An estimate of the number of tropical tree species. Proc. Natl. Acad. Sci. U.S.A. 112, 7472–7477. https://doi.org/10.1073/pnas.1423147112

Spadavecchia, L., Williams, M., Bell, R., Stoy, P.C., Huntley, B., Van Wijk, M.T., 2008. Topographic controls on the leaf area index and plant functional type of a tundra ecosystem. Journal of Ecology 96, 1238–1251. https://doi.org/10.1111/j.1365-2745.2008.01424.x

Sterck, F.J., Bongers, F., 2001. Crown development in tropical rain forest trees: patterns with tree height and light availability. Journal of Ecology 89, 1–13. https://doi.org/10.1046/j.1365-2745.2001.00525.x

Stirling, G., Wilsey, B., 2001. Empirical Relationships between Species Richness, Evenness, and Proportional Diversity.

Storch, F., Boch, S., Gossner, M.M., Feldhaar, H., Ammer, C., Schall, P., Polle, A., Kroiher, F., Müller, J., Bauhus, J., 2023. Linking structure and species richness to

support forest biodiversity monitoring at large scales. Annals of Forest Science 80, 3. https://doi.org/10.1186/s13595-022-01169-1

Sullivan, M.J.P., Talbot, J., Lewis, S.L., Phillips, O.L., Qie, L., Begne, S.K., Chave, J., Cuni-Sanchez, A., Hubau, W., Lopez-Gonzalez, G., Miles, L., Monteagudo-Mendoza, A., Sonké, B., Sunderland, T., Ter Steege, H., White, L.J.T., Affum-Baffoe, K., Aiba, S., De Almeida, E.C., De Oliveira, E.A., Alvarez-Loayza, P., Dávila, E.Á., Andrade, A., Aragão, L.E.O.C., Ashton, P., Aymard C., G.A., Baker, T.R., Balinga, M., Banin, L.F., Baraloto, C., Bastin, J.-F., Berry, N., Bogaert, J., Bonal, D., Bongers, F., Brienen, R., Camargo, J.L.C., Cerón, C., Moscoso, V.C., Chezeaux, E., Clark, C.J., Pacheco, Á.C., Comiskey, J.A., Valverde, F.C., Coronado, E.N.H., Dargie, G., Davies, S.J., De Canniere, C., Djuikouo K., M.N., Doucet, J.-L., Erwin, T.L., Espejo, J.S., Ewango, C.E.N., Fauset, S., Feldpausch, T.R., Herrera, R., Gilpin, M., Gloor, E., Hall, J.S., Harris, D.J., Hart, T.B., Kartawinata, K., Kho, L.K., Kitayama, K., Laurance, S.G.W., Laurance, W.F., Leal, M.E., Lovejoy, T., Lovett, J.C., Lukasu, F.M., Makana, J.-R., Malhi, Y., Maracahipes, L., Marimon, B.S., Junior, B.H.M., Marshall, A.R., Morandi, P.S., Mukendi, J.T., Mukinzi, J., Nilus, R., Vargas, P.N., Camacho, N.C.P., Pardo, G., Peña-Claros, M., Pétronelli, P., Pickavance, G.C., Poulsen, A.D., Poulsen, J.R., Primack, R.B., Priyadi, H., Quesada, C.A., Reitsma, J., Réjou-Méchain, M., Restrepo, Z., Rutishauser, E., Salim, K.A., Salomão, R.P., Samsoedin, I., Sheil, D., Sierra, R., Silveira, M., Slik, J.W.F., Steel, L., Taedoumg, H., Tan, S., Terborgh, J.W., Thomas, S.C., Toledo, M., Umunay, P.M., Gamarra, L.V., Vieira, I.C.G., Vos, V.A., Wang, O., Willcock, S., Zemagho, L., 2017. Diversity and carbon storage across the tropical forest biome. Sci Rep 7, 39102. https://doi.org/10.1038/srep39102

Takeda, H., 2004. GROUND SURFACE ESTIMATION IN DENSE FOREST.

Takyu, M., Aiba, S.-I., Kitayama, K., 2002. Effects of topography on tropical lower montane forests under different geological conditions on Mount Kinabalu, Borneo. Plant Ecology 159, 35–49. https://doi.org/10.1023/A:1015512400074

Tang, H., Armston, J., 2019. GEDI L2B Footprint Canopy Cover and Vertical Profile Metrics.

Tang, H., Stoker, J., Luthcke, S., Armston, J., Lee, K., Blair, B., Hofton, M., 2023. Evaluating and mitigating the impact of systematic geolocation error on canopy height measurement performance of GEDI. Remote Sensing of Environment 291, 113571. https://doi.org/10.1016/j.rse.2023.113571

Thomas, R.Q., Hurtt, G.C., Dubayah, R., Schilz, M.H., 2008. Using lidar data and a height-structured ecosystem model to estimate forest carbon stocks and fluxes over mountainous terrain. Canadian Journal of Remote Sensing 34, S351–S363. https://doi.org/10.5589/m08-036

Tinkham, W.T., Smith, A.M.S., Hoffman, C., Hudak, A.T., Falkowski, M.J., Swanson, M.E., Gessler, P.E., 2012. Investigating the influence of LiDAR ground surface errors on the utility of derived forest inventories. Can. J. For. Res. 42, 413–422. https://doi.org/10.1139/x11-193

Tolan, J., Yang, H.-I., Nosarzewski, B., Couairon, G., Vo, H.V., Brandt, J., Spore, J., Majumdar, S., Haziza, D., Vamaraju, J., Moutakanni, T., Bojanowski, P., Johns, T., White, B., Tiecke, T., Couprie, C., 2024. Very high resolution canopy height maps from RGB imagery using self-supervised vision transformer and convolutional decoder trained on aerial lidar. Remote Sensing of Environment 300, 113888. https://doi.org/10.1016/j.rse.2023.113888

Tyukavina, A., Hansen, M.C., Potapov, P., Parker, D., Okpa, C., Stehman, S.V., Kommareddy, I., Turubanova, S., 2018. Congo Basin forest loss dominated by increasing smallholder clearing. Sci. Adv. 4, eaat2993. https://doi.org/10.1126/sciadv.aat2993

Urbazaev, M., Hess, L.L., Hancock, S., Sato, L.Y., Ometto, J.P., Thiel, C., Dubois, C., Heckel, K., Urban, M., Adam, M., Schmullius, C., 2022. Assessment of terrain elevation estimates from ICESat-2 and GEDI spaceborne LiDAR missions across different land cover and forest types. Science of Remote Sensing 6, 100067. https://doi.org/10.1016/j.srs.2022.100067

Van Cleemput, E., Adler, P.B., Suding, K.N., Rebelo, A.J., Poulter, B., Dee, L.E., 2025. Scaling-up ecological understanding with remote sensing and causal inference. Trends in Ecology & Evolution 40, 122–135. https://doi.org/10.1016/j.tree.2024.09.006

Vancutsem, C., Achard, F., Pekel, J.-F., Vieilledent, G., Carboni, S., Simonetti, D., Gallego, J., Aragão, L.E.O.C., Nasi, R., 2021. Long-term (1990–2019) monitoring of forest cover changes in the humid tropics. Sci. Adv. 7, eabe1603. https://doi.org/10.1126/sciadv.abe1603

Vancutsem, C., Pekel, J.-F., Evrard, C., Malaisse, F., Defourny, P., 2009. Mapping and characterizing the vegetation types of the Democratic Republic of Congo using SPOT VEGETATION time series. International Journal of Applied Earth Observation and Geoinformation 11, 62–76. https://doi.org/10.1016/j.jag.2008.08.001

Vargas-Larreta, B., López-Martínez, J.O., González, E.J., Corral-Rivas, J.J., Hernández, F.J., 2021. Assessing above-ground biomass-functional diversity relationships in temperate forests in northern Mexico. For. Ecosyst. 8, 8. https://doi.org/10.1186/s40663-021-00282-3

Veenendaal, E.M., Torello-Raventos, M., Feldpausch, T.R., Domingues, T.F., Gerard, F., Schrodt, F., Saiz, G., Quesada, C.A., Djagbletey, G., Ford, A., Kemp, J., Marimon, B.S., Marimon-Junior, B.H., Lenza, E., Ratter, J.A., Maracahipes, L.,

Sasaki, D., Sonké, B., Zapfack, L., Villarroel, D., Schwarz, M., Yoko Ishida, F., Gilpin, M., Nardoto, G.B., Affum-Baffoe, K., Arroyo, L., Bloomfield, K., Ceca, G., Compaore, H., Davies, K., Diallo, A., Fyllas, N.M., Gignoux, J., Hien, F., Johnson, M., Mougin, E., Hiernaux, P., Killeen, T., Metcalfe, D., Miranda, H.S., Steininger, M., Sykora, K., Bird, M.I., Grace, J., Lewis, S., Phillips, O.L., Lloyd, J., 2015. Structural, physiognomic and above-ground biomass variation in savanna–forest transition zones on three continents – how different are co-occurring savanna and forest formations? Biogeosciences 12, 2927–2951. https://doi.org/10.5194/bg-12-2927-2015

Verhegghen, A., Mayaux, P., De Wasseige, C., Defourny, P., 2012. Mapping Congo Basin vegetation types from 300 m and 1 km multi-sensor time series for carbon stocks and forest areas estimation. Biogeosciences 9, 5061–5079. https://doi.org/10.5194/bg-9-5061-2012

Vicente-Serrano, S., Perezcabello, F., Lasanta, T., 2008. Assessment of radiometric correction techniques in analyzing vegetation variability and change using time series of Landsat images. Remote Sensing of Environment 112, 3916–3934. https://doi.org/10.1016/j.rse.2008.06.011

Villard, L., Le Toan, T., Ho Tong Minh, D., Mermoz, S., Bouvet, A., 2016. Forest Biomass From Radar Remote Sensing, in: Land Surface Remote Sensing in Agriculture and Forest. Elsevier, pp. 363–425. https://doi.org/10.1016/B978-1-78548-103-1.50009-1

Wagner, F.H., Dalagnol, R., Carter, G., Hirye, M.C.M., Gill, S., Takougoum, L.B.S., Favrichon, S., Keller, M., Ometto, J.P.H.B., Alves, L., Creze, C., George-Chacon, S.P., Li, S., Liu, Z., Mullissa, A., Yang, Y., Santos, E.G., Worden, S.R., Brandt, M., Ciais, P., Hagen, S.C., Saatchi, S., 2026. Wall-to-wall Amazon forest height mapping with Planet NICFI , Aerial LIDAR , and a U-Net regression model. Remote Sens Ecol Conserv 12, 323–348. https://doi.org/10.1002/rse2.70041

Wang, C., Elmore, A.J., Numata, I., Cochrane, M.A., Shaogang, L., Huang, J., Zhao, Y., Li, Y., 2022. Factors affecting relative height and ground elevation estimations of GEDI among forest types across the conterminous USA. GIScience & Remote Sensing 59, 975–999. https://doi.org/10.1080/15481603.2022.2085354

Wang, Y., Fang, H., 2020. Estimation of LAI with the LiDAR Technology: A Review. Remote Sensing 12, 3457. https://doi.org/10.3390/rs12203457

Wang, Z., Zhou, Y., Wang, F., Wang, S., Qin, G., Zhu, J., 2024. Shadow Detection and Reconstruction of High-Resolution Remote Sensing Images in Mountainous and Hilly Environments. IEEE J. Sel. Top. Appl. Earth Observations Remote Sensing 17, 1233–1243. https://doi.org/10.1109/JSTARS.2023.3338976

Watson, J.E.M., Evans, T., Venter, O., Williams, B., Tulloch, A., Stewart, C., Thompson, I., Ray, J.C., Murray, K., Salazar, A., McAlpine, C., Potapov, P., Walston, J.,

Robinson, J.G., Painter, M., Wilkie, D., Filardi, C., Laurance, W.F., Houghton, R.A., Maxwell, S., Grantham, H., Samper, C., Wang, S., Laestadius, L., Runting, R.K., Silva-Chávez, G.A., Ervin, J., Lindenmayer, D., 2018. The exceptional value of intact forest ecosystems. Nat Ecol Evol 2, 599–610. https://doi.org/10.1038/s41559-018-0490-x

White, L.J.T., Masudi, E.B., Ndongo, J.D., Matondo, R., Soudan-Nonault, A., Ngomanda, A., Averti, I.S., Ewango, C.E.N., Sonké, B., Lewis, S.L., 2021. Congo Basin rainforest — invest US$150 million in science. Nature 598, 411–414. https://doi.org/10.1038/d41586-021-02818-7

Whitley, E., Ball, J., 2002. Statistics review 6: Nonparametric methods. Crit Care 6, 509. https://doi.org/10.1186/cc1820

Williams, L.J., Paquette, A., Cavender-Bares, J., Messier, C., Reich, P.B., 2017. Spatial complementarity in tree crowns explains overyielding in species mixtures. Nat Ecol Evol 1, 0063. https://doi.org/10.1038/s41559-016-0063

Wilsey, B.J., Chalcraft, D.R., Bowles, C.M., Willig, M.R., 2005. RELATIONSHIPS AMONG INDICES SUGGEST THAT RICHNESS IS AN INCOMPLETE SURROGATE FOR GRASSLAND BIODIVERSITY. Ecology 86, 1178–1184. https://doi.org/10.1890/04-0394

Wood, S.N., 2017. Generalized Additive Models: An Introduction with R, 2nd ed. Chapman and Hall/CRC. https://doi.org/10.1201/9781315370279

Wu, N., Jastrze, S., Cho, K., Geras, K.J., 2022. Characterizing and Overcoming the Greedy Nature of Learning in Multi-modal Deep Neural Networks.

Wu, X., Wang, X., Tang, Z., Shen, Z., Zheng, C., Xia, X., Fang, J., 2015. The relationship between species richness and biomass changes from boreal to subtropical forests in China. Ecography 38, 602–613. https://doi.org/10.1111/ecog.00940

Xiao, Z., Liang, S., Wang, J., Chen, P., Yin, X., Zhang, L., Song, J., 2014. Use of General Regression Neural Networks for Generating the GLASS Leaf Area Index Product From Time-Series MODIS Surface Reflectance. IEEE Trans. Geosci. Remote Sensing 52, 209–223. https://doi.org/10.1109/TGRS.2013.2237780

Xu, L., Saatchi, S.S., Shapiro, A., Meyer, V., Ferraz, A., Yang, Y., Bastin, J.-F., Banks, N., Boeckx, P., Verbeeck, H., Lewis, S.L., Muanza, E.T., Bongwele, E., Kayembe, F., Mbenza, D., Kalau, L., Mukendi, F., Ilunga, F., Ebuta, D., 2017. Spatial Distribution of Carbon Stored in Forests of the Democratic Republic of Congo. Sci Rep 7, 15030. https://doi.org/10.1038/s41598-017-15050-z

Xu, Y., Chen, H.Y.H., Xiao, Z., Wan, D., Liu, F., Guo, Y., Qiao, X., Jiang, M., 2022. Species Richness Promotes Productivity through Tree Crown Spatial

Complementarity in a Species-Rich Natural Forest. Forests 13, 1604. https://doi.org/10.3390/f13101604

Yachi, S., Loreau, M., 2007. Does complementary resource use enhance ecosystem functioning? A model of light competition in plant communities. Ecology Letters 10, 54–62. https://doi.org/10.1111/j.1461-0248.2006.00994.x

Yalcin, I., Kocaman, S., Saunier, S., Albinet, C., 2021. RADIOMETRIC QUALITY ASSESSMENT FOR MAXAR HD IMAGERY. Int. Arch. Photogramm. Remote Sens. Spatial Inf. Sci. XLIII-B3-2021, 797–804. https://doi.org/10.5194/isprs-archives-XLIII-B3-2021-797-2021

Yan, K., Park, T., Chen, C., Xu, B., Song, W., Yang, B., Zeng, Y., Liu, Z., Yan, G., Knyazikhin, Y., Myneni, R.B., 2018. Generating Global Products of LAI and FPAR From SNPP-VIIRS Data: Theoretical Background and Implementation. IEEE Trans. Geosci. Remote Sensing 56, 2119–2137. https://doi.org/10.1109/TGRS.2017.2775247

Yang, Y., Saatchi, S.S., Xu, L., Yu, Y., Lefsky, M.A., White, L., Knyazikhin, Y., Myneni, R.B., 2016. Abiotic Controls on Macroscale Variations of Humid Tropical Forest Height. Remote Sensing 8, 494. https://doi.org/10.3390/rs8060494

Yosinski, J., Clune, J., Bengio, Y., Lipson, H., 2014. How transferable are features in deep neural networks? https://doi.org/10.48550/arXiv.1411.1792

Yu, K., Liu, S., Zhao, Y., 2016. CPBAC: A quick atmospheric correction method using the topographic information. Remote Sensing of Environment 186, 262–274. https://doi.org/10.1016/j.rse.2016.08.010

Yu, Y., Saatchi, S., 2016. Sensitivity of L-Band SAR Backscatter to Aboveground Biomass of Global Forests. Remote Sensing 8, 522. https://doi.org/10.3390/rs8060522

Zhang, G., Zhao, H., Yu, Y., Poupart, P., 2021. Quantifying and Improving Transferability in Domain Generalization.

Zhang, W., Xi, Y., Brandt, M., Ren, C., Bai, J., Ma, Q., Fensholt, R., 2024. Stand structure of tropical forests is strongly associated with primary productivity. Commun Earth Environ 5, 796. https://doi.org/10.1038/s43247-024-01984-6

Zhang, Y., Chen, H.Y.H., 2015. Individual size inequality links forest diversity and above-ground biomass. Journal of Ecology 103, 1245–1252. https://doi.org/10.1111/1365-2745.12425

Zhang, Y., Chen, H.Y.H., Reich, P.B., 2012. Forest productivity increases with evenness, species richness and trait variation: a global meta-analysis. Journal of Ecology 100, 742–749. https://doi.org/10.1111/j.1365-2745.2011.01944.x

Zhang, Y., He, H., Shi, L., Peñuelas, J., Sardans, J., Bai, Y., Li, C., Pei, J., 2026. Stand structural attributes exert stronger and scale-dependent control on forest biomass than tree diversity across typical forest ecosystems in China. Plant Diversity S2468265926000296. https://doi.org/10.1016/j.pld.2026.01.001

Zhao, X., Feng, Y., Xu, K., Cao, M., Hu, S., Yang, Q., Liu, X., Ma, Q., Hu, T., Kelly, M., Guo, Q., Su, Y., 2023. Canopy structure: An intermediate factor regulating grassland diversity-function relationships under human disturbances. Fundamental Research 3, 179–187. https://doi.org/10.1016/j.fmre.2022.10.007